Computational Methods for Non-planar Vortex Wake Flow Fields With Applications to Conventional and Rotating Wings

by

Paul Michael Stremel

B.S. Aerospace Engineering, University of Colorado (1977)

SUBMITTED TO THE DEPARTMENT OF AERONAUTICS AND ASTRONAUTICS IN PARTIAL FULFILLMENT OF THE REQUIREMENTS OF THE DEGREE OF

MASTER OF SCIENCE IN AERONAUTICS AND ASTRONAUTICS

at the

MASSACHUSETTS INSTITUTE OF TECHNOLOGY

February 1982

Signature of Author_____
Department of Aeronautics and Astronautics

Certified by_____
Earll M. Murman
Thesis Supervisor

Accepted by_____
Harold Y. Wachman
Chairman, Department Graduate Committee

COMPUTATIONAL METHODS FOR NON-PLANAR VORTEX WAKE FLOW FIELDS WITH APPLICATIONS TO CONVENTIONAL AND ROTATING WINGS

by

Paul Michael Stremel

Submitted to the Department of Aeronautics and Astronautics on February 1, 1982 in partial fulfillment of the requirements for the Degree of Master of Science in Aeronautics and Astronautics

ABSTRACT

Newly developed techniques for the computation of non-planar vortex flow fields are presented. These techniques are designed to track point vortices in an incompressible, inviscid and irrotational fluid. In this method, the point vortices are tracked by Lagrangian methods while the flow field velocity, induced by the singularities, is calculated on an Eulerian mesh. This technique is termed the Eulerian-Lagrangian Method. Solutions to non-planar vortex wake flow fields for conventional wings are obtained by representing the flow field as a two-dimensional time dependent problem. Calculations are conducted on the Trefftz plane. Solutions to non-planar vortex wake flow fields for rotating wings are obtained from a two-dimensional model of the three-dimensional rotor wake. Calculations are conducted on an Eulerian mesh for the rotating wing analysis. The point vortices defining the vortex sheet are redistributed on the Eulerian mesh by use of the "Cloud in Cell" technique.

Calculations representing conventional and rotating wing load distributions are presented. In particular, the rollup of the vortex wake generated by an elliptically loaded wing and the wake for a load distribution simulating a wing with a deflected flap are included. The rollup of the vortex wake for a rotating wing in the hover condition is shown. Results of computational experiments to determine the effects of grid size, number of vortex points in the wake definition and type of singularity representation (constant circulation strength or constant incremental spacing along the span) are presented.

Results indicate the ability of the method to calculate vortex flow fields consisting of single vortex wakes with one or several rolled up vortex cores and flow fields consisting of numerous wake representations, each containing several vortex cores. Predicted locations of the rolled up vortex cores are compared with the theoretical results of Betz and have been found to be in close agreement for an elliptical load distribution. Predictions of the location and structure of the wake for a rotating wing in hover are compared and contrasted with the findings of Miller [19].

Thesis Supervisor: Dr. Earll M. Murman

Title: Professor of Aeronautical Engineering

ACKNOWLEDGEMENTS

Special expressions of gratitude are extended to Professor E. M. Murman for his continual guidance, enthusiasm and confidence. Always, when times seemed darkest, Professor Murman provided inspiration to continue.

I would also like to thank Professor R.H. Miller for his many hours spent discussing the characteristics of rotating wing flow fields.

Special thanks to Marilyn Evans for her efficient typing of this manuscript and especially for her patience and understanding.

This research was funded under NASA grant NAG2-105.

TABLE OF CONTENTS

LIST OF ILLUSTRATIONS

LIST OF SYMBOLS

a,A	Semi-span
A1 A2 A3 A4	Areas used in "CIC" scheme
$F(z')$	Complex potential
j	Computational mesh index
k	Computational mesh index
m	Integer value, 0, ±1, ±2, ...
N	Summation index for point vortices on computational mesh
NF	Summation index for the far wake model
NI	Summation index for the intermediate wake model
n	Integer value, 0, ±1, ±2, ...
R	Rotor blade tip radius
t	Time
Δ t	Time increment
v, V	Velocity component in y direction
w, W	Velocity component in z direction
W_o	Initial W velocity
x, X	Cartesian coordinate, positive downstream
y, Y	Cartesian coordinate, positive out right wing
Δ y	Computational mesh spacing in y direction
y ,y	End points of span increment
y_t	Cartesian coordinate of tip vortex centroid
z, Z	Cartesian coordinate, positive up
z_n	Cartesian coordinate of far wake vortex centroid

Δz	Computational mesh spacing in z direction
Δz_n	Wake spacing in far wake
Δz_w	Wake spacing
β	Angle in far wake analysis
γ	Blade separation angle
Γ	Circulation
Γ_i	Circulation of ith point vortex
Γ_w	Circulation of lifting surface
Γ_{w_o}	Circulation of lifting surface at symmetry plane (y=0)
θ	Position angle from point vortex to flow field
λ	Dimensionless velocity, $\lambda = \frac{w}{\Omega R}$
ϕ	Velocity potential
ψ	Stream function
Ω	Angular velocity
ω	Vorticity
∞	Infinity
$\bar{(\ )}$	Non-unique value at branch cut
$(\ )^*$	Dimensionless quantity
$(\ )'$	Quantity used in complex plane
$(\ )^+$	Value above branch cut
$(\ )^-$	Value below branch cut
$o(\ )$	Order of
$(\ )_r$	Reflected quantity

SECTION 1

INTRODUCTION

1.1 Importance of Non-planar Vortex Wake Analysis

The design and analysis of conventional and rotating wing vehicles are restricted by inadequate means of computing the development of non-planar vortex wakes. The majority of design codes developed to date utilize a linear wake model to represent the vortex wake generated by a lifting wing. In reality, the vortex wake rolls up into concentrated vortex cores within a short distance downstream of the trailing edge. For an isolated wing and body, the induced velocity distribution at the wing plane, except perhaps at the wing tip, varies insignificantly due to the redistribution of the vorticity in the rolled up wake. For this reason, the development of wing-body codes has not been limited significantly by the linear wake model. Unlike the wing-body configuration, for many configurations, this is strictly not so. Some important ones are.

1. Empennage: Vortex wakes shed from the wing propagate downstream very near the empennage. For a transport aircraft at cruise condition, the influence of the non-planar vortex wake may not be significant due to the location of the tip vortex core outboard away from the horizontal tail. However, during pitch-up and maneuver, when the wing is highly

loaded, the wake quickly rolls up into concentrated vortex cores which will be much closer to the empennage. The non-planar vortex wake should be modeled.

2. Canard-Wing: The vortex wake generated by a canard wing will interact directly with the wing flow field. The non-planar vortex wake should be modeled to provide accurate loading distributions on the wing.

3. Delta Wings: The flow at the leading edge of a delta wing separates at moderate to high incidence and develops into a vortex wake above the wing. The non-planar wake model is essential in this analysis.

4. Helicopter Rotors: Design of rotating wing vehicles is significantly limited by accoustic and vibration constraints. Blade-vortex wake interaction contributes the major influence on these constraints. Non-planar vortex wake models are needed to correctly predict this interaction.

Non-planar vortex wake models will enhance the analysis of many aircraft configurations. For some configurations, non-planar vortex wake models are a necessity. It is therefore desirable to develop methodologies to treat non-planar vortex wakes. This report presents such a method for simplified problems and, hopefully, represents the first

step in the development of a method for the above mentioned configurations.

1.2 Previous Investigations

1.2.1 Vortex Flows and Conventional Wings

Analysis of the incompressible, inviscid interaction and propagation of isolated singularities (point vortices) in an otherwise irrotational flow field dates back to the early work of Rosenhead [1] and has received considerable attention in the past ten years. When the fluid is considered ideal, except for isolated singularities, the theorems of Helmholtz and Kelvin are applicable to a control surface convected with the flow and encompassing the singularities. In accordance with these theorems, the transport or convection of the vorticity throughout the control surface is determined by the local fluid velocity which, in turn, is induced in the flow field by the point vortices. This approach was utilized by Rosenhead and formed the foundation for a number of investigations that followed. In this approach, with knowledge of the location and circulation strengths of the point vortices, the velocity field induced by the point singularities can be calculated by use of the Biot-Savart relation. Since the flow is ideal and the problem is linear, the solution of the flow field for any number of vortex points may be determined through superimposing the induced velocities of the individual singularities. A point vortex does not induce a velocity on itself. The point vortices are convected by the local flow field velocity. After

which, at a short time interval later, a new induced flow field emerges and the point vortices are convected again. This point tracking or Langrangian method is applied to convect the point vortices while the velocity field is determined by summing the effects of the point vortices.

The work of Rosenhead and, more recently, Moore [2] approximates a vortex wake by a finite number of point vortices or vortex markers and determines the three-dimensional rollup of the non-planar vortex wake through a two-dimensional time dependent solution. This two-dimensional plane, which is convected with the free stream velocity, is called the Trefftz plane and remains perpendicular to the free stream (see Figure 1.1). The two-dimensional time dependent solution using the point vortices and the Biot-Savart relation often resulted in instabilities and chaotic vortex motion. The instabilities stem from the singular nature of the vortex points. In a paper by Chorin et al [3], the nature of the singularities was investigated. In this paper, it was shown that if the point vortices are smoothed out or given a finite radius, the instabilities disappear and the vortex rollup is smooth.

The previously described full Lagrangian approach has significant inherent computational burdens. In the above method, for N point vortices, a number of operations of order N^2 are required to determine the flow field. This condition puts a burden on the number of point vortices used to define

the vortex sheet. Instead of isolating each point vortex, increased computational efficiency can be achieved by grouping a number of the point vortices together. After which, the velocity field is then calculated. This concept leads to the concept of "Vortex in Cell" or "Cloud in Cell" and suggests the Eulerian-Lagrangian approach to the solution.

The Eulerian-Lagrangian approach, coupled with the "Cloud in Cell" technique, has been employed by a number of authors [see for example, [4,5,6]]. The solution to the point vortex convection remains Lagrangian, but the velocity field is determined from the stream function in an Eulerian manner. The stream function is determined on the Eulerian mesh as the solution to Poisson's equation. In this method, the vorticity is redistributed to the mesh nodes using a bilinear interpolation scheme. The Poisson equation for the stream function can now be solved with the vorticity on the right-hand side of the equation. The velocity field is determined from the stream function and then bilinearly interpolated to the point vortices. The point vortices can now be convected. The redistribution scheme or "Cloud in Cell" technique of this method accomplishes a result similar to that of Chorin [3]. The point vortices are smoothed and the instabilities are suppressed.

Baker [4] completed extensive investigations on the rollup of vortex wakes generated by elliptically loaded wings and by wing loadings simulating deflected flap configurations.

Typically, in his investigations, Baker represented the vortex wake by 2,000 point vortices. Instabilities are shown in the tip vortex core and in some portions of the vortex wake in some of the results. Christiansen [5] demonstrated the utility of the technique through numerous applications.

Three-dimensional calculations of the non-planar vortex rollup problem are, for the most part, determined through the use of panel methods. In general, the analysis is conducted to more fully understand flow characteristics about wings and wing-body combinations with leading edge vortex separation. Johnson et al [7] used panel methods to model the development of vortex structures shed from the leading edge of delta wings. Here again, the vortex sheet is tracked in a Lagrangian fashion and the influence of the vortex singularities is included in the calculation of the velocity field. Owing to the complexity of the three-dimensional problem, the shed vortex wake is parameterized and the vortex wake singularity strengths are determined as part of the singularity solution. The findings of Johnson [7] indicate that if the real flow deviates significantly from the single vortex structure predicted by the flow model, the analysis will generally tend to fail.

1.2.2 Rotating Wings

Applications of vortex methods to understand and, consequently, alleviate the accoustical and vibratory patterns associated with rotary wing vehicles have increased significantly in the past five years. Extensive surveys of numerical analysis applied to rotating wings are presented in [8] and [9] and are highlighted here for completeness. Emphasis on the distorted wake analysis is presented here.

The development of the "semi-rigid" wake concept was initiated by Miller [10] and marked the inception of the distorted wake analysis. Previously, the undistorted wake was represented by a semi-infinite cylinder emerging from the tips of the rotor blades. This cylindrical model implies an infinite number of blades and, therefore, will yield no information about the periodic vortex wake known to exist. Accoustical and vibratory analysis is not possible for the cylindrical wake model, but the "semi-rigid" wake would provide a wake model needed for this analysis.

Several authors [11-13] investigated further the "semi-rigid" wake concept to represent the structure of the rolled up tip vortex and to estimate the influence of the vortex on the rotor blade loading. This model has fallen short of representing the real wake. Large discrepancies between the calculated and measured wake geometries have been shown by Ham [13]. More accurate wake models were needed. Simplified methods using vortex rings of constant circulation to represent

the wake geometry were developed by Brady and Crimi [14]. Extensions of the vortex ring model and a method to include the rollup of the two concentrated tip vortices was developed by Levinsky [15].

A more complex method used to calculate the effects of the wake geometry, which is free to distort under the influence of the flow field, was developed by Landgrebe [16, 17]. For this method, the vortex wake is represented by a finite number of vortex "filaments" which convect and interact under the influence of the local velocity field. However, in this analysis, the wake is allowed to distort only after the wake has been predescribed. Landgrebe [17] predescribes the wake as being grouped into a strong rolled up tip vortex filament and several weaker filaments representing the inboard portion of the vortex wake. Knowledge of the predescribed location of the vortex filaments is gained from experimental results and will limit the analysis owing to this empiricism. Summa and Clark [18] have represented the blade lifting surface through the use of vortex lattice techniques. The wake is described with techniques reported by Landgrebe.

At present, the work of Miller [19] is the only investigation devoted to the free wake analysis of rotating wing devices which is not restricted by the empiricisms associated with the wake geometry. In this analysis, the wake geometry is divided into three sections: the near wake; the intermediate wake; and a far wake. The near wake consists of

straight semi-infinite vortex filaments extending from the rotor blade trailing edge. Using the Betz [22] approximation, this wake is rolled up into three concentrated vortices for the three regions of the load distribution as shown in Figure 1.2. These three vortices, whose initial position is given by the Betz approximation, are used to represent the intermediate wake. For the Betz approximations, the tip vortex is represented by the wake rollup from the tip to the maximum circulation and a second vortex is represented by the rollup from this maximum to the point where the slope of the loading tends to zero. The root vortex is represented by the remaining portion of the load distribution. The far wake is represented by a semi-infinite vortex cylinder for the three-dimensional analysis and by two semi-infinite vortex wakes for the two-dimensional analysis (see Figure 1.3).

A new distribution of the intermediate wake is determined from the induced flow field velocities. Induced flow field velocities at the rotor blade plane are then calculated from the influence of the near wake, intermediate wake and the far wake. The vortex wake shed from the blade is then recalculated and the cycle repeats. The iterative process continues until the induced velocities at the blade location have reached convergence. In Miller's analysis [19] and in predictions by Betz's theory, the emergence of a mid-span vortex is shown. While experimental results clearly

indicate a strong tip vortex, at present, the mid-span vortex has not been measured. The effect of this vortex on the blade loading at large distances may be small, but when the vortex is in close proximity of the blade, significant errors in the predicted blade loading may appear. Analysis to verify the existence of the mid-span vortex is needed.

This survey is intended to bring to light the current status of rotating wing wake analysis and to motivate the current analysis in order that a better model of the vortex wake may be obtained.

1.3 Current Investigation

The two-dimensional time dependent solution for the rollup of non-planar vortex wakes with use of the existing Eulerian-Lagrangian method [4, 5] is restricted in that an extension of the analysis to three-dimensions is not possible. In order to investigate the development of non-planar vortex wakes in three-dimensions, the flow field must be described by use of the velocity potential rather than the stream function. While this paper does not deal directly with the three-dimensional problem, the first step in the analysis (two-dimensional time dependent problem for conventional wings or two-dimensional steady state problem for rotating wings) is presented.

1.3.1 Vortex Flows and Conventional Wings

In this section, an introduction is given for the problem solved in the present investigation. Detailed development of the theoretical and numerical treatment is given in Sections 2 and 3.

1) Governing Equations, Boundary Conditions, Initial Conditions and Jump Conditions

In order to specify the problem, the governing equations and boundary conditions must be clearly stated. The calculations of the flow field are performed on the Trefftz plane for an ideal fluid. The vorticity is considered here to be scalar and corresponding to a vorticity vector directed parallel to the free stream. The vorticity vector is a doubly infinite line vortex. The vortex wake is represented by distributing point vortices along the width of the vortex wake on the Trefftz plane. Everywhere in this investigation, a vortex wake symmetric about the y=0 plane is modeled. Owing to this symmetry, calculations are necessary on the Trefftz Plane for $y \geq 0$ only. The influence of the reflected wake is modeled through the boundary conditions. Laplace's equation for the velocity potential governs the flow field. Boundary conditions on the velocity potential are determined from the flow field induced by line vortices (see for example, Batchelor [21]). Initially, the vorticity is

distributed along a z = constant line and has extent $0 \leq y \leq 1$.

In contrast to the flow field solution using the stream function, solutions obtained using the velocity potential will be multivalued. (See for example [20]) In order to retain a unique solution, it is necessary to construct branch cuts extending from the singularities to $+\infty$ and to apply appropriate jump conditions at this cut. To illustrate this condition, consider the figure below.

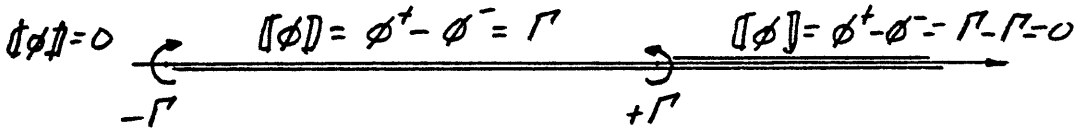

As illustrated in this figure, the jump conditions are needed between the reflected vortices only (the jump conditions cancel identically to the right of the right vortex for a reflected pair of vortices). (Appendix A)

The velocity field is determined from the gradient of the potential and the motion of the point vortices is calculated from the trajectory equations of motion. These topics are discussed fully in Section 2.1.

2) Singularity Redistribution and Velocity Determination

For the solution of the velocity field on the Eulerian mesh, the vorticity must be redistributed if it is to be accurately included in the analysis. An

adaptation of the "Cloud in Cell" technique is used to redistribute the vorticity. The vorticity is redistributed to the centroids of the four nearest mesh cells. See figure below.

"CIC" Redistribution

$\Gamma_1 = A_1 \Gamma_i$
$\Gamma_2 = A_2 \Gamma_i$
$\Gamma_3 = A_3 \Gamma_i$
$\Gamma_4 = A_4 \Gamma_i$

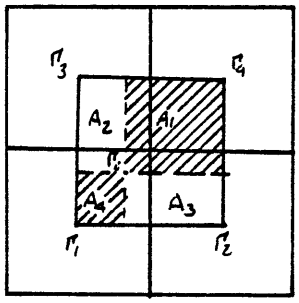

New branch cuts are constructed for each of the newly redistributed points. After the potential field is solved, the velocity at the location of the point vortex markers is determined using bilinear interpolation from the velocities of the four nearest mesh centroids. Only information from mesh cells affected during the vorticity redistribution is used in the velocity determination (see Appendix B).

3) Method

Solutions to the non-dimensional forms of the governing equations, the boundary conditions and the initial conditions are determined through the use of finite difference techniques.

Initially, the input vorticity is distributed along the z=0 axis. The vorticity is redistributed to the centroids of the mesh cells and the boundary conditions determined from the new distribution of vorticity.

The components of the flow field velocity are set everywhere to zero at t=0. Laplace's equation for the velocity potential is now replaced by a central difference equation. Jump conditions for the new distribution of vorticity are calculated and introduced into the finite difference forms of the Laplace equation and the w velocity equation. The difference equations are solved using successive line over-relaxation (SLOR) or a direct solver for elliptic partial differential equations [24]. The flow field velocities are determined from the gradient of the potential. The motion of the point vortices are calculated according to the equations of motion, after which, the vorticity is convected and the Trefftz plane is stepped forward (downstream) in time. The new vortex wake is redistributed and the cycle repeats. A flow chart is shown in Figure 1.4.

1.3.2 Rotating Wings

The solution to the non-planar vortex wake flow field for rotating wings is obtained on an Eulerian mesh. Unlike the two-dimensional time dependent problem for conventional wings, we week the steady state solution to the flow field for the rotating wing problem. By steady state, we mean that the helical rotor wake below the rotor blade is invariant with blade rotation for a given blade loading.

In this analysis, as in the analysis for conventional wings, the vortex wake or wakes on the computational plane are represented by intersections of doubly infinite line vortices with that plane. The time dependent solution for conventional wing analysis (Trefftz plane representation) was obtained by integrating along the vortex trajectories with respect to time. In the steady state solution for rotating wing flow fields, the wake geometry below the rotor blade is obtained by integrating along the helical rotor wake with respect to arc length. Consider a single point vortex illustrated below.

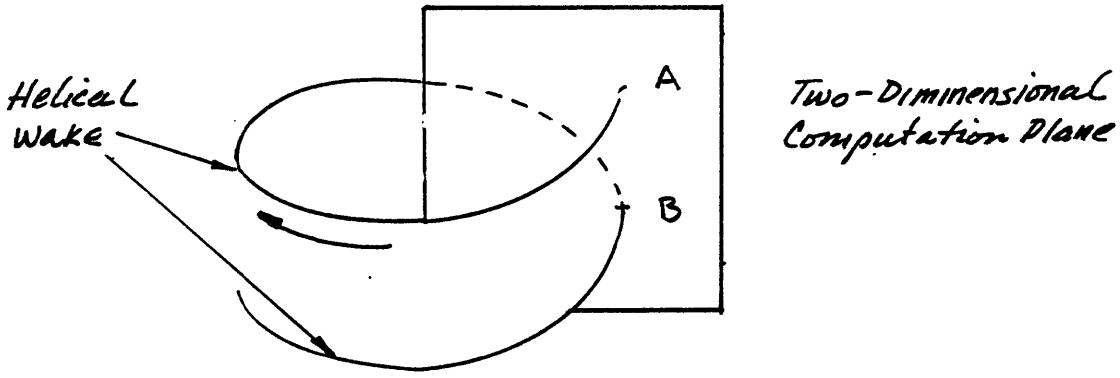

If the location of A is known, the position of B can be determined by integrating the trajectory equation of motion along the helical path. This will be discussed further in Section 2.1.2.

1) Governing Equations, Boundary Conditions, Initial Conditions and Jump Conditions

Here, again, the flow of an ideal fluid is investigated. The solution to the rotating wing flow

field is obtained on a computational plane illustrated in the figure below.

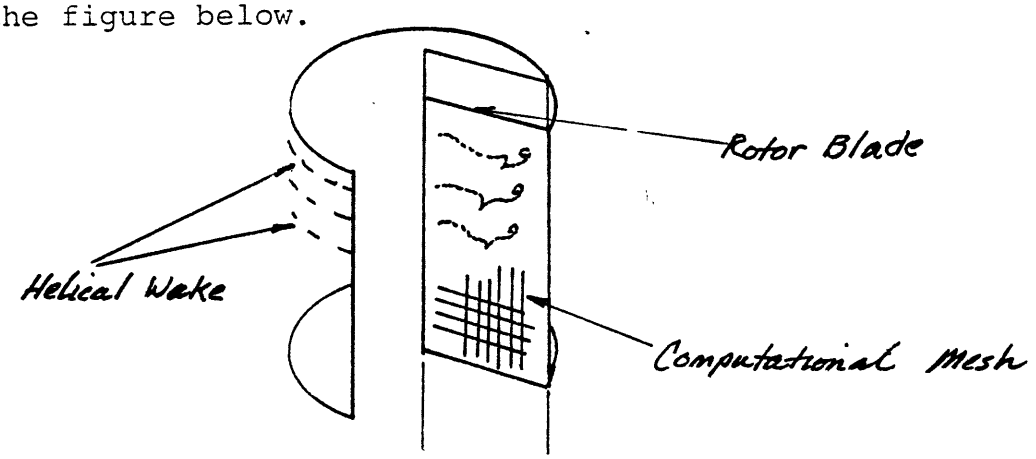

Vortex wakes representing the rotor blade and the intersections of the helical rotor blade wake with the computational plane are distributed on this plane. The computational plane extends from just above the vortex wake representing the rotor blade to negative infinity below the rotor blade.

On this plane, three distinct regions representing the helical rotor wake are modeled. The three regions will be termed; the near wake, the intermediate wake and the far wake. See figure below.

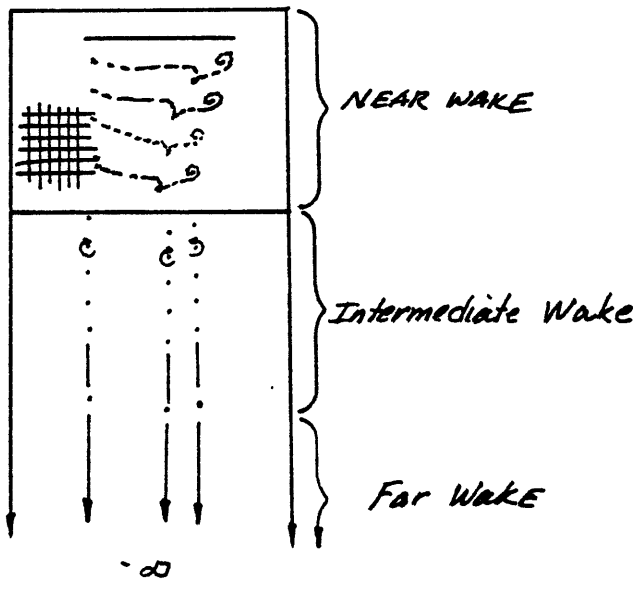

The near wake represents the rotor blade and the first four intersections of the helical rotor wake with the computational plane. The computational mesh is constructed on the computational plane and, in general, will encompass the near wake only.

The intermediate wake is represented, initially, by concentrated point vortices of strengths and locations predicted by Betz [22] theory. The intermediate wake represents the next ten intersections of the helical wake with the computational plane. The far wake is similar to the intermediate wake, but extends to $-\infty$. The intermediate wake will generally be outside the computational mesh and the far wake will always lie outside the mesh. Boundary conditions for the near and intermediate wakes are calculated in the usual way and represent the influence of line vortices. The influence of the far wake on the boundary conditions is modeled using an asymptotic expansion over the length of the far wake. See Figures 1.5 and 1.6. Further development of the intermediate and far wake models can be found in Appendix C.

Initially, the input vorticity on the computational mesh will be distributed along lines of constant z or axial distance. These distributions represent the near wake. The spacing of this tiered structure (see Figure 1.7) is determined from the flow velocity through the

rotor. Miller [19] determined that the solution was not sensitive to the number of input wakes beyond a minimum of four plus the blade representation. The flow field velocities and the potential are set similarly to values described before. These topics are discussed further in Section 2.1.

2) Singularity Redistribution and Velocity Determination

The singularity redistribution technique and methods for determining the velocities of the point vortices are directly extended to N vortices and are exactly those described in the previous section (also see Appendix B).

3) Method

A) Initially, the vorticity is input in the previously described tier structure and represents the shed wake for the rotor blade loading. The vorticity in the wake is represented by point vortices at the intersection points of the doubly infinite line vortices with the computational plane. The first or uppermost (z=0) wake represents the blade. This first wake or blade wake is considered fixed on the computational mesh and does not rollup, but retains the signature of the blade loading.

B) The vorticity is redistributed and the boundary conditions calculated from the influence of this and the intermediate and far wake

vorticity. Jump conditions are calculated in the usual way (Appendix A). Laplace's equation for the velocity potential is again solved using SLOR or a direct method [24] and the velocity field calculated from the potential.

C) The induced velocities at the blade location, $z=0$, are calculated and examined for convergence. If the velocities have converged, the steady state rotor wake flow field is known. If the induced velocities have not converged, a new distribution of vorticity is calculated and control returns to B. The new distribution of vorticity in the near wake below the rotor blade is determined by integrating along the helical vortex trajectories from the fixed rotor blade location to each vortex wake. For a two-bladed rotor, the first wake below the rotor blade would be obtained by integrating from 0 to π, the second wake by integrating from 0 to 2π and so forth. A flow chart is shown in Figure 1.8.

SECTION 2

FORMULATION OF PROBLEM

The two-dimensional flow field for an incompressible, inviscid and irrotational (except for isolated vortex singularities) fluid can be represented by a potential function ϕ . Here ϕ is the velocity potential and, for the fluid described above, satisfies Laplace's equation everywhere in the defined flow field. The velocity in the flow field can be calculated directly as the gradient of the potential.

When the problem is solved on a two-dimensional plane, such as the Trefftz plane, the problem is thought of as a boundary value problem. The boundary conditions are determined uniquely from the vorticity distributed on the plane. The continuous distribution of vorticity on the plane is often represented by a finite number of point (line) vortices. This representation creates a singularity problem which was not present in the continuous definition of the vorticity. The point vortices are branch points and branch cuts must be extended from each singularity. Jump conditions are applied across the cuts in order that the solution remain unique.

This section will present the development of the governing equations, dimensionless forms of the equations and restrictions on the potential to ensure a unique solution.

2.1 Governing Equations

2.1.1 Conventional Wings

For the two-dimensional, incompressible, inviscid fluid flow under consideration, the governing equation can be described by the Eulerian equations:

$$\nabla^2 \phi = 0 \tag{2.1}$$

$$\vec{V} = \partial\phi/\partial y \quad , \quad \vec{W} = \frac{\partial \phi}{\partial z} \tag{2.2 a, b}$$

together with the boundary condition:

$$\phi = \frac{1}{2\pi} \sum_{N}^{i} \Gamma_i \, \theta_i \tag{2.3}$$

where Γ_i is the circulation of the ith point vortex and θ_i is the angle from the positive y axis to the boundary point. (See Figure 2.1) Here, the summation over N represents the contributions of the point vortices on the computational plane and the corresponding reflected image vortices.

The initial conditions for the vortex wake are determined from the wing loading or circulation, $\Gamma_w(y)$. If we consider the wake vorticity to be given by $\Gamma(t,y,z)$, then for the continuous (non-discretized) problem, the initial wake vorticity is given by:

$$\Gamma(0,y,0) = -\int_0^y \frac{d\Gamma_w}{dy}\, dy \qquad 0 \le y \le 1$$

$$\Gamma(0,y,z) = 0 \qquad \text{Everywhere else.}$$

For the numerical problem, this continuous vorticity distribution is lumped into discrete vortex markers, each designated by the index i where i=1,N and N is the number of markers. The strength of each marker is:

$$\Gamma_i(0, y_i, 0) = -\int_{y_1}^{y_2} \frac{d\Gamma_w}{dy}\, dy = -\left[\Gamma_w(y_2) - \Gamma_w(y_1)\right] \qquad (2.4)$$

where Γ_i = circulation of ith vortex in wake

Γ_w = load distribution on lifting surface

y_1, y_2 = limits on span increment defining

y_i = position of ith vortex y = $\frac{y_1 + y_2}{2}$

The solution to equations 2.1-2.4 is termed the Eulerian problem. Instead of solving for the transport of vorticity on the Eulerian mesh, a discrete point or Lagrangian method is utilized. In the Lagrangian method, the trajectory equations of motion are solved to determine the convection of the point vortices. They have the form:

$$\frac{dy_i}{dt} = V(y_i, z_i) \quad , \quad \frac{dz_i}{dt} = W(y_i, z_i) \qquad (2.5a, b)$$

where y_i, z_i are the coordinates representing the ith point vortex location. The solution to equations 2.1-2.5 is termed the Eulerian-Lagrangian method and is the foundation for this investigation.

2.1.2 Potating Wings

The solution to vortex wakes of rotating wings is calculated on a computational plane (Figure 1.5) and is governed by equations 2.1 and 2.2. The time dependent trajectory equations of equation 2.5 are not applicable to the steady state solution for rotating wing flow fields. The trajectory equations used in this steady state solution are defined later in this subsection. The boundary conditions and initial conditions differ from those for conventional wings.

For rotating wings in the hover condition, a helical vortex wake structure extends from the rotor disk to $z=-\infty$. The wake near the rotor disk is represented by individual vortex wakes, each composed of many vortex markers. The remainder of the wake is approximated by the semi-infinite vortex wake model (see Figure 1.6). The boundary condition for the potential on the computational domain is calculated by superimposing the effects of the individual wakes and the semi-infinite vortex wake. The vortex wakes on the computational mesh are represented by point vortices which have the boundary condition of equation 2.3. The boundary condition for the intermediate vortex wake has the form:

$$\phi = \frac{1}{2\pi} \sum_{NI} \Gamma_i \cdot \theta_i \qquad (2.6)$$

where NI is the total number of point vortices in the intermediate wake and the corresponding reflected image vortices.

The boundary condition for the far wake is developed in Appendix C and is given by equation C.9.

As with the conventional wing, the rotor loading distribution is discretized to give the strength of the wake vortex markers. However, markers must be initially placed not only at the rotor trailing edge, but also in wakes spaced apart below the rotor.

The initial vortex wake definition on the computational mesh is then:

$$\Gamma_i(0, y_i, 0) = \Gamma_i(0, y_i, -\Delta z_w)$$

$$= \Gamma_i(0, y_i, -2\Delta z_w) =$$

$$-\int_{y_1}^{y_2} \frac{d\Gamma_w}{dy}\, dy = -\Gamma_w(y_2) + \Gamma_w(y_1) \qquad (2.7)$$

where the notation is that following equation 2.4 and Δz_w is determined from the flow through the rotor.

Miller [19] has determined that the solution is insensitive to the number of input wakes beyond a minimum of four. In this analysis, four input wakes plus the blade representation are modeled.

The trajectory equations of motion are now spatially dependent rather than time dependent as was shown in equation 2.5. Here, the trajectory equations of motion define the helical trajectory of each vortex marker in the near wake definition. The spatially dependent trajectory equations of motion are obtained from equation 2.5 as follows:

$$\frac{dy_i}{dt} = V(y_i, z_i) \quad , \quad \frac{dz_i}{dt} = W(y_i, z_i)$$

where dt represents the time for the next rotor blade passage.

Then: $$dt = \gamma / \Omega$$

Where γ is the blade separation angle in radians and is equal to π for a two-bladed rotor, for instance.

The trajectory equations become:

$$dy_i = \gamma/\pi \; V(y_i, z_i), \quad dz_i = \gamma/2\pi \; W(y_i, z_i) \tag{2.8}$$

2.1.3 Betz Approximations

Theoretical methods to determine the location of fully rolled up vortex structures generated by lifting wings were derived by Betz [22] and elaborated on by Donaldson [23]. The theory relates the loading on the wing to the fully developed vortex structure by utilizing three conservation laws. The conservation laws satisfied are: conservation of circulation; invariant spanwise centroid of vorticity; and conservation of the second moment of vorticity. Development of the theory is outlined in Donaldson [23] and the results are shown here for convenience.

Consider the load distribution shown in Figure 2.2. The load distribution will generate three separate vortex cores. We assume that all the vorticity shed outboard of point A will roll up into the tip vortex, that the vorticity between points A and B will roll up into the mid-span or flap vortex and all vorticity between B and the aircraft symmetry plane, y=0, will roll up into the inboard vortex.

The centroid of the rolled up vorticity for region A-B is defined by:

$$\bar{y}_B \int_{y_B}^{y_A} \frac{d\Gamma_w}{dy}\, dy = \int_{y_B}^{y_A} y \frac{d\Gamma_w}{dy}\, dy \qquad (2.9)$$

where Γ_w is the circulation of the wing loading.

The total circulation of the vortex is equal to:

$$\Gamma_B = -\int_{y_B}^{y_A} \frac{d\Gamma_w}{dy}\, dy$$

$$\Gamma_B = -\left(\Gamma_w(A) - \Gamma_w(B)\right) \tag{2.10}$$

These results will be used later to compare the centroids of vorticity with those predicted by the current investigation.

2.2 Dimensionless Forms of the Equations

The dimensionless forms of the governing equations are developed in this section. The non-dimensionalization of the conventional wing and rotating wing problems are slightly different, corresponding to the different notations used in the respective literatures.

2.2.1 Conventional Wings

Dimensionless forms of the equations of Section 2.1 may be obtained by introducing the following dimensionless parameters:

$$y^* = y/a \;,\quad z^* = z/a \;,\quad \Gamma_i^* = \Gamma_i/\Gamma_{w_0}$$

$$V^* = V/w_0 \;,\quad w^* = w/w_0 \;,\quad w_0 = \Gamma_{w_0}/2\pi a \tag{2.11}$$

$$\phi^* = \phi/w_0 a \;,\quad t^* = t/a/w_0$$

where, a = semi-span

Γ_{w_o} = circulation at wing root section

w_o = initial downwash at the semi-span location due to a vortex of strength Γ_{w_o} at y=0.

Using the conventions of equation 2.11, the governing equations take the form:

$$\nabla^2 \phi^* = 0 \tag{2.12}$$

$$V^* = \frac{\partial \phi^*}{\partial y^*} \quad , \quad W^* = \frac{\partial \phi^*}{\partial z^*} \tag{2.13 a, b}$$

On the boundary,

$$\phi^* = \sum_N \Gamma_i^* \theta_i \tag{2.14}$$

where N is the sum over the point vortices and the corresponding reflected images. The trajectory equations for the vortex markers become:

$$\frac{dy_i^*}{dt^*} = V^*(y_i^*, z_i^*), \quad \frac{dz_i^*}{dt^*} = W^*(y_i^*, z_i^*) \tag{2.15}$$

Equations 2.12 and 2.13b will have different forms at the branch cuts. See equations A.16 and A.17, Appendix A.

2.2.2 Rotating Wings

Dimensionless forms of the equations of Section 2.1 can be obtained by introducing the following dimensionless parameters:

$$y^* = y/R \,, \quad z^* = z/R \,, \quad \Gamma_i^* = \Gamma_i/\Omega R^2$$

$$V^* = V/w_o \,, \quad w^* = w/w_o \,, \quad w_o = \Omega R \tag{2.16}$$

$$\phi^* = \phi/\Omega R^2 \,, \quad t^* = \Omega t$$

where R = rotary disk radius

Ω = angular velocity

w_o = tip speed.

With the convention of equation 2.16, the governing equations become:

$$\nabla^2 \phi^* = 0 \tag{2.17}$$

$$V^* = \frac{\partial \phi^*}{\partial y^*} \,, \quad w^* = \frac{\partial \phi^*}{\partial z^*} \tag{2.18 a, b}$$

On the boundary for the near and intermediate wakes.

$$\phi^* = \frac{1}{2\pi} \sum_{N+NI} \Gamma_i^* \theta_i \tag{2.19}$$

where N+NI is the sum over the point vortices and the corresponding reflected images in the near and intermediate wakes.

On the boundary for the far wake.

$$\phi^* = \sum_{i=1}^{3} \frac{\Gamma_i^*}{2\pi} \left[\frac{2y_n^*}{\Delta z_n^{*2}} \right] \left[\frac{3cy^{*2}}{\Delta z_n^{*2}} - a - \frac{2bz^*}{\Delta z_n^*} - \frac{3cz^{*2}}{\Delta z_n^{*2}} + \frac{cy_n^{*2}}{\Delta z_n^{*2}} \right] \tag{2.20}$$

Here, the summation represents the summation over the three point vortices defining the far wake and a, b, c are given in equation C.10.

The trajectory equations of motion become:

$$dy_i^* = \gamma V^*(y_i^*, z_i^*), \quad dz_i^* = \gamma W^*(y_i^*, z_i^*) \tag{2.21}$$

where γ is the blade separation angle (radians).

The variation by a constant between the dimensionless forms of the governing equations for conventional and rotating wings results from the dimensionless conventions for each configuration.

The description of the dimensionless forms of equations 2.17 and 2.18b at the singularity branch cut will be discussed in Section 2.3 and later in Section 3.1. See equations A.18 and A.19, Appendix A.

2.3 Single Value Restrictions on the Velocity Potential

The distributed point vortices representing the vortex wake are branch point singularities. When the flow field is described by use of the velocity potential, the solution will be non-unique unless restrictions on the potential are imposed. After each full cycle around a vortex singularity, the potential will either be increased or decreased by the strength of the vortex singularity (the sign of the change depends on the direction of the path and the direction of the circulatory flow). For the potential to remain single valued, jump conditions are included in the analysis to compensate for this change in the potential. A summary of these conditions follows. Full details are presented in Appendix A.

The complex potential generated by a point vortex at $z'=0$ can be written:

$$F(z') = -i\frac{\Gamma_i}{2\pi}\log(z') \qquad (2.22)$$

$i=\sqrt{-1}$

where Γ_i is strength of the circulatory flow, the flow is counterclockwise for $\Gamma_i > 0$.

The extension of equation 2.22 to a pair of vortices of equal and opposite strengths with positions $z' = \pm a$ is represented by:

$$F(z') = -\frac{i\Gamma_i}{2\pi}\log(z'-a) + \frac{i\Gamma_i}{2\pi}\log(z'+a) \qquad (2.23)$$

then $$\phi = \frac{\Gamma_i}{2\pi}\left((\theta_+' + 2\pi m) - (\theta_-' + 2\pi n)\right)$$

where θ_+', θ_-' are position angles from $z' = \pm a$ to point z' and m,n are integer values.

It follows from equation 2.23 that the velocity potential will be an infinitely many valued function. In order to investigate this further, we construct branch cuts from each point vortex to $+\infty$ along the real axis. Then, if a simple closed contour is constructed around each point vortex and the closed contour is traversed in the counterclockwise direction starting at the branch cut, the following is found (see figure below).

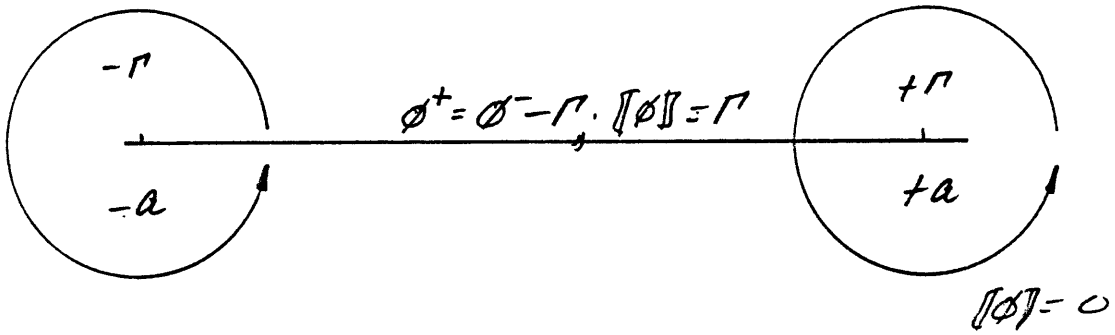

As the traverse approaches 2π (m=1, n=1), the velocity potential is decreased by Γ on the segment $-a \leq y \leq \infty$ due to the left vortex and increased on the segment $a \leq y \leq \infty$ due to the right vortex. Then, the sum of these effects cancel on $a \leq y \leq +\infty$ and are due to the left vortex only on $-a \leq y \leq a$. In order that the velocity potential remains single valued, the jump condition, $[\![\phi]\!] = \phi^+ - \phi^- = \Gamma$, must be applied on the section $-a \leq y \leq a$.

SECTION 3

NUMERICAL SCHEME

Solutions to the non-planar vortex wake flow fields are obtained from the solutions of finite difference approximations for the governing equations. In this section, finite difference forms of the governing equations, method of solution and accuracy of the method will be discussed.

3.1 Finite Difference Forms

Finite difference forms of the governing equations are evaluated on an Eulerian mesh. The mesh is to be rectangular and have constant incremental spacing along the y and z axes (i.e., Δy=constant, Δz=constant). The analysis considers the vortex wake solutions to wings of span $2a$ and evaluates one half of the wake with the influence of the mirror image wake included in the boundary conditions.

3.1.1 Governing Equations

To obtain the velocity potential, a five-point centered difference approximation is made to equation 2.1. The equation is generally Laplace in form due to localized vorticity. However, at the singularity branch cuts, the equation has a Poisson form due to the jump conditions. Equation 2.1 has the forms:

$$\frac{\phi^*_{j+1,k} - 2\phi^*_{j,k} + \phi^*_{j-1,k}}{\Delta y^{*2}} - \frac{\phi^*_{j,k+1} - 2\phi^*_{j,k} + \phi^*_{j,k-1}}{\Delta z^{*2}} = 0 \qquad (3.1)$$

and

$$\frac{\phi^*_{j+1,k} - 2\phi^*_{j,k} + \phi^*_{j-1,k}}{\Delta y^{*2}} - \frac{\phi^*_{j,k+1} - 2\phi^*_{j,k} + \phi^*_{j,k-1}}{\Delta z^{*2}} =$$

$$\frac{2\pi}{\Delta z^{*2}} \sum_{l=j}^{J} \Gamma^*_{l+1/2,k+1/2} - \Gamma^*_{l+1/2,k-1/2} \qquad (3.2)$$

where $\Gamma_{l+1/2,k\pm1/2}$ is the dimensionless circulation of the redistributed vorticity. The differencing is illustrated on the figure below.

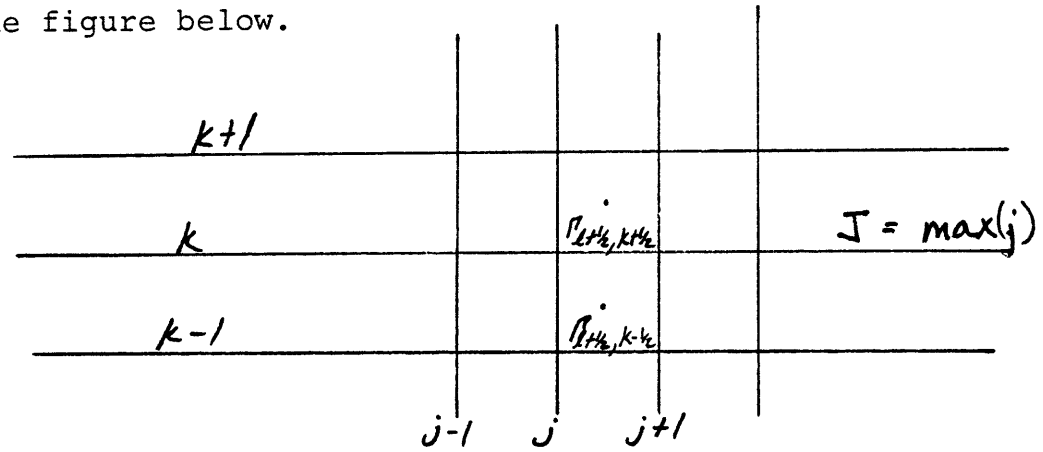

Equations 3.1 and 3.2 are dimensionless forms of equation 2.1 and represent the flow field equations off and on the branch cuts for non-rotating wings.

For rotating wing flow fields, equation 3.1 is applied off the branch cut and the form near the branch cut is now:

$$\frac{\phi^*_{j+1,k} - 2\phi^*_{j,k} + \phi^*_{j-1,k}}{\Delta y^{*2}} - \frac{\phi^*_{j,k+1} - 2\phi^*_{j,k} + \phi^*_{j,k-1}}{\Delta z^{*2}} = \frac{1}{\Delta z^{*2}} \sum_{j=\ell}^{J} \Gamma^*_{\ell+\frac{1}{2},k+\frac{1}{2}} - \Gamma^*_{\ell+\frac{1}{2},k-\frac{1}{2}} \tag{3.3}$$

The variation in the right-hand side of equations 3.2 and 3.3 originates from the dimensionless conventions of equations 2.11 and 2.16.

The v and w components of the velocity at the mesh nodes are determined using central difference approximations to the gradient of the velocity potential. This central difference is taken over two mesh cells. The calculation of the v component of velocity will be indifferent to the existence of the branch cuts. However, jump conditions must be applied at the cut when central differences of the velocity potential with respect to z are calculated.

The difference equations for the flow field velocities have the forms:

For conventional wings:

$$V^*_{j,k} = \frac{\phi^*_{j+1,k} - \phi^*_{j-1,k}}{2\Delta y^*} \tag{3.4}$$

$$W^*_{j,k} = \frac{\phi^*_{j,k+1} - \phi^*_{j,k-1}}{2\Delta z^*} \tag{3.5}$$

At the branch cut, 3.5 becomes:

$$W^*_{j,k} = \frac{\phi^*_{j,k+1} - \phi^*_{j,k-1}}{2\Delta z^*} - \frac{\pi}{\Delta z^*} \sum \Gamma^*_{k+\frac{1}{2}, k+\frac{1}{2}} + \Gamma^*_{k+\frac{1}{2}, k-\frac{1}{2}} \quad (3.6)$$

For rotating wing flow fields, equations 3.4 and 3.5 are unchanged and equation 3.6 has the form:

$$W^*_{j,k} = \frac{\phi^*_{j,k+1} - \phi^*_{j,k-1}}{2\Delta z^*} - \frac{1}{2\Delta z^*} \sum \Gamma^*_{k+\frac{1}{2}, k+\frac{1}{2}} + \Gamma^*_{k-\frac{1}{2}, k-\frac{1}{2}} \quad (3.7)$$

Development of the dimensionless forms of the equations appropriate at the branch cut may be found in Appendix A.

The convection of the vortex markers throughout the flow field is calculated from the trajectory equations of motion 2.15 and 2.21. The expressions are different for conventional and rotating wing flow fields and will be discussed separately.

Equation 2.15 may be written:

$$dy_i^* = V^*(y_i^*, z_i^*)\, dt^* \quad (3.8)$$

Equation 3.8 is then integrated over a small time interval with the velocity held constant for this interval. If the initial time is represented by n and the final time by n+1, then:

$$y_i^{*\,n+1} - y_i^{*\,n} = V^{*\,n}(y_i^*, z_i^*)\left(t^{*\,n+1} - t^{*\,n}\right) \qquad (3.9a)$$

$$y_i^{*\,n+1} = y_i^{*\,n} + \Delta t\, V^{*\,n}(y_i^*, z_i^*)$$

and

$$z_i^{*\,n+1} = z_i^{*\,n} + \Delta t\, W^{*\,n}(y_i^*, z_i^*) \qquad (3.9b)$$

where v_i^*, w_i^* are the velocities at the location of the point vortex

and $$\Delta t < \max\left[{}^{\Delta y^*}/_{V_{j,k}^*},\ {}^{\Delta z^*}/_{W_{j,k}^*} \right]$$

This forward Euler time integration scheme used by Baker has been adopted without investigating further any other schemes.

Equation 2.21 may be written:

$$dy_i^* = \gamma V^*(y_i^*, z_i^*) \tag{3.10}$$

where γ is the blade separation angle in radians. A similar expression holds for z^*.

If equation 3.10 is integrated along the helical wake over the blade separation angle, the following is found:

$$y_i^{*\,k+1} = y_i^k + \gamma V_i^{*\,k+1/2} \tag{3.11}$$

where $V_i^{*\,k+1/2}$ is considered constant and equal to the average velocity between k and k+1,

$$V_i^{*\,k+1/2} = \left(V_i^{*\,k+1} + V_i^{*\,k}\right)/2.$$

The velocity of the point vortex is calculated from information at only the nodes of mesh cells affected by the redistribution of the point vortex. This is discussed further in Sections 3.2 and 3.3.

Boundary conditions on the velocity potential are calculated from the redistributed vorticity on the computational mesh, plus, for rotating wing analysis, the influence of the semi-infinite vortex wake represented by the intermediate and far wake models. Baker [4] approximated the boundary condition by lumping together neighboring point vortices into local centroids and then calculating the boundary condition using these centroids. This technique will greatly reduce the computation time. However, in the present

investigation, the boundary condition is calculated exactly from the redistributed circulation in order to evaluate the method.

The influence of the redistributed vorticity on the boundary values of the potential is related to equations 2.14 and 2.19 for conventional and rotating wing flow fields, respectively. The potential on the boundary is calculated from the summed influence of the redistributed point (line) vortices. The effect of the semi-infinite vortex wake is represented by equations 2.19 and 2.20 or C.1 and C.10.

3.2 "Cloud in Cell" (CIC) Redistribution Scheme

In order to solve equations 3.1 and 3.3 with the appropriate jump conditions across the branch cuts, the point vortices representing the vortex wake must be redistributed on the computational mesh. A modified version of the method known as "CIC" is utilized to redistribute the circulation of the point vortices.

In order to accurately model the branch cuts throughout the computational mesh, the circulation of each point vortex is redistributed to the centroid of the four nearest mesh cells, rather than to the nearest mesh nodes [4, 5]. It would be equally accurate to redistribute the circulation to the mesh nodes, but the redistribution of circulation to the nearest mesh cell centroids was chosen in order to model the branch cut at equal distances from mesh nodes above and below the cut. The method "area weights" the region encompassed by

the four centroids and determines the amount of circulation to be applied at each centroid. Circulation is conserved within a contour surrounding the four centroids.

The velocity at the point vortex is obtained in the reverse of the circulation redistribution. See figure below.

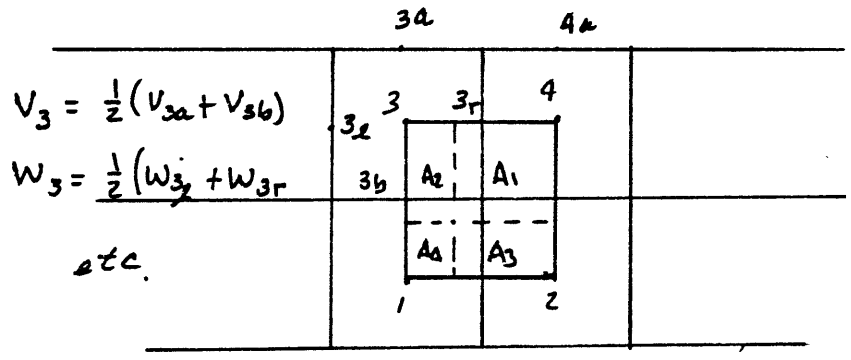

The velocity at the point vortex location is calculated from information at only the nodes of mesh cells affected by the redistribution of circulation. Because the circulation was redistributed to the centroids of mesh cells, it is important to first calculate the velocity at these centroids. The velocity at the centroid can then be bilinearly interpolated to the point vortex location.

The velocities at the center of each mesh cell edge are calculated using central differences approximations of equation 2.2a, b over one mesh cell. The velocities at the centroids are taken to be the averages of the values at opposing mesh edges. The centroid values are then bilinearly interpolated to the point vortex location. See Appendix B.

3.3 Numerical Solution

This subsection describes the methods and numerical schemes used to solve the finite difference forms of the governing equations. Flow charts describing the method of solution for conventional and rotating wing flow fields are shown in Figures 1.4 and 1.8, respectively. Clarification between the methods for conventional wings and rotating wings is presented when appropriate. The method is summarized as follows:

1) Consider an array of N point vortices located at coordinates (y_i, z_i) and distributed on the computational mesh; the strength of each vortex being Γ_i and representing the shed vorticity from a lifting surface. This strength is given by equation 2.4 or 2.7. The point vorticity is initially along lines of constant z and distributed along this line in one of two ways: a) the vortex wake is represented by equally spaced point vortices with varying strength; or b) a distribution of constant vortex strength (Γ_i = constant) and unequal spacing is used. In either case, the contour integral around the shed wake remains constant. For conventional wing analysis, a single vortex wake is input at z=0, $0 \leq y \leq a$. In the analysis of rotating wings, a minimum of four vortex wakes is input, excluding the blade

representation. Again, each wake is located on a line of constant z, with the wake spacing (in z) determined from the flow through the rotor (momentum theory). For no variation in the velocity across the wake, momentum theory provides:

$$C_T = 2\lambda^2 \tag{3.12}$$

where $\lambda = \frac{w}{\Omega R}$ and C_T is the thrust coefficient. See Figure 1.7. For both analyses, the reflected vortex wake images ($-a \leq y \leq 0$) are excluded from the computational mesh and included in the analysis mathematically. The point vorticity contained in the vortex wake representation is redistributed next.

2) The point vortex or circulation redistribution scheme is obtained from a modified version of the "Cloud in Cell" technique. Due to the singularity branch cuts, the circulation is redistributed to the mesh centroids, rather than the mesh nodes (as in [4]). The jump conditions of the redistributed circulation are represented by the right-hand side of equations A.16-A.19. See Appendix A. The influence of the redistributed vorticity on the value of the velocity potential at the boundary can then be calculated.

3) The vorticity at the centroid of the mesh cells affected by the redistribution is represented by point vortices and the influence on the flow field parameters calculated accordingly. The boundary condition for the point vorticity on the mesh and that represented by the reflected images is calculated directly from equations 2.14 and 2.19 for conventional and rotating wing flow fields, respectively. This represents the total contribution to the boundary condition for conventional wing analysis. However, for rotating wing flow fields, the effect of the semi-infinite helical wake below the mesh must be taken into account. See Appendix C. Superposition of these effects determines the boundary condition on the velocity potential. Solutions to equations 3.1 and 3.2 or 3.3 are now obtainable.

4) Solutions to equations 3.1 and 3.2 or 3.3 are determined. Iterative and noniterative (direct) methods are available for solving the equations. Preliminary solutions were obtained using SLOR (successive line over-relaxation). A direct method of solution has been applied in order to increase computational efficiency. This method is described in reference [24]. After the velocity potential is determined, the flow field velocity components are

determined from equations 3.4, 3.5 and 3.6 or 3.7 for conventional and rotating wing flow fields, respectively.

5) Next, the distribution of vorticity at a later time $(t+\Delta t)$, for conventional wings, or at the next iteration for rotating wings, is determined from the local velocity components and the previous vorticity distribution. Convection of the vorticity is determined from the local induced velocities and the equations of motion, equations 3.9 or 3.11. Equation 3.9 represents the time dependent form of the trajectory equations of motion and is applicable to the conventional wing problem. Equation 3.11 is the spatial dependent form of the trajectory equations and is used in the rotating wing analysis. The integration of equation 3.11 was found to be generally unstable. An under-relaxation scheme was applied during integration as a stabilizing factor. The induced velocity components at the ith point vortex location are calculated from the values of the velocity potential at nodes of mesh cells affected by the redistribution of the ith point vortex circulation. This method of determining the ith point vortex velocity is essentially a reverse application of the modified "Cloud in Cell"

technique described in step 2 above. The method of this step is applicable to conventional as well as rotating wing wake analysis.

6) For conventional wing analysis, the flow field velocity components and the geometry and orientation of the nonlinear vortex wake are now known at $t+\Delta t$. If the solution is to advance to a later time and, therefore, a greater distance downstream, control will return to step 2 and the cycle will repeat. Otherwise, the solution terminates at this step. At this point in the computation, the rotating wing wake is evaluated for convergence by examining the induced velocities at the rotor blade location. If the wake has not yet converged, the iteration counter is advanced and control returns to step 2.

3.4 Accuracy, Stability

In the solution of non-planar vortex wake flow fields on an Eulerian mesh, finite difference approximations to the governing equations were evaluated. Due to the finite limits on the Eulerian mesh spacing ($\Delta y, \Delta z \neq 0$) and the utilization of finite difference approximations, the "modeled" flow field will differ from the "real" flow field by a truncation error. This truncation error is determined by expanding the finite difference equations in Taylor series and is related to the mesh spacing, as expected. There will also be errors

associated with the redistribution scheme and these must be assessed. In this subsection, the magnitude of these errors will be discussed. In addition, the stability restriction on the time step Δt will be stated. See Appendix D.

The accuracy of equations 3.1-3.3 and 3.4-3.7 can be determined easily from Taylor series expansions of the velocity potential. The equations are found to be second order accurate in Δy, Δz.

In order to investigate the accuracy of the redistribution of vorticity, two errors were evaluated: first, the error associated with the induced velocity at the ith point vortex location due to the redistributed point vortices of the ith point vortex; and second, the error in calculating the velocity of the ith point vortex from values of velocity at the four nearest mesh cell centroids. See Appendix D. The errors are found to have the following forms for induced velocity at (y_i, z_i) due to redistributing the vorticity:

$$V_i \leq o(\Delta) \quad , \quad \Delta y = \Delta z = \Delta$$

and velocity from mesh cell information:

$$\frac{A_1 V_1 + A_2 V_2 + A_3 V_3 + A_4 V_4}{\Delta y \, \Delta z} = V_i + o(\Delta y^2) + o(\Delta z^2)$$

(see notation of Appendix D).

The stability limitation on Δt is determined from the equations of motion which are related to the vorticity transport equation:

$$\frac{\partial \bar{\omega}}{\partial t} + v\frac{\partial \bar{\omega}}{\partial y} + w\frac{\partial \bar{\omega}}{\partial z} = 0 \qquad (3.12)$$

The equations of motion are a multistep representation of equation 3.12 and have related stability limitations [4].

The step size is chosen to satisfy:

$$\Delta t < \max\left[\frac{\Delta y^*}{v^*_{jk}}, \frac{\Delta z^*}{w^*_{jk}}\right] . \qquad (3.13)$$

SECTION 4

COMPUTATIONAL EXPERIMENTS

Computational experiments using the numerical scheme and finite difference equations of Section 3 were conducted to determine the ability of the scheme to predict the development of non-planar vortex wakes. In this section, descriptions and results of three numerical applications are discussed. The three applications include vortex wakes shed from: 1) conventional wings represented by elliptical load distributions; 2) conventional wings having load distributions representative of deflected flaps; and 3) helicopter rotor blades. Included in this section are experiments to investigate the effects of mesh variation and initial input wake definitions. Graphic representations of the vortex wake geometry, velocity profiles through the wake and variations in the centroids of vorticity with time will be presented.

4.1 Conventional Wings - Elliptical Load Distribution

4.1.1 Input Description

Consider for the first application an elliptically loaded wing of extent $-a \leq y \leq a$ located at the plane $z=0$. The strength of the vortex wake shed at the trailing edge is related directly to the lifting line representation of the bound circulation. For an elliptical load distribution, the wing circulation is represented by:

$$\Gamma_w(y) = \Gamma_{w_0}\left(1-(y/a)^2\right)^{1/2} \tag{4.1}$$

where Γ_{w_0} is the circulation at the symmetry plane y=0. See Figure 4.1.

If the non-dimensional convention of equation 2.11 is introduced, equation 4.1 takes the dimensionless form:

$$\Gamma_w^*(y^*) = \left(1-y^{*2}\right)^{1/2} \tag{4.2}$$

The initial vortex wake is defined by one of two methods: 1) constant point vortex circulation; or 2) constant spacing between the point vortices. In each method, the point vortex is located at the center of the span increment represented by the point vortex. The strengths and locations of the point vortices are determined directly from equation 4.2 and equation 2.4 which has the form:

$$\Gamma_i^*(0,y_i^*,0) = -\Gamma_w^*(y_2^*) + \Gamma_w^*(y_1) \tag{4.3}$$

$$y_i^* = \left(y_1^* + y_2^*\right)/2.$$

The extent of the initial vortex wake is represented on the interval $0 \leq y \leq a$. The flow field to the left of the plan y=0 is represented by a mirror image of the right-hand plane.

4.1.2 Input and Mesh Variations

Variations in the input vortex wake description are obtained by varying the number of point vortices in the wake or by changing the representation of the wake vorticity. The vorticity in the wake can be represented by constant strength point vortices or by point vortices equally spaced along the semi-span. This subsection is presented in three parts. First, results of vortex wakes represented by point vortices of constant strength and constant spacing are presented. Secondly, the vortex wake defined by constant strength vortices using a different number of input point vortices will be shown. In the third part, the effects of varying the mesh spacing for the velocity calculation will be presented. In each part, graphs illustrating the vortex wake geometry and velocity profiles through the vortex wake will be presented.

In this first part, the vortex wake is defined by two methods: a) constant strength point vortices; and b) point vortices of constant semi-span spacing with varying strength. For both definitions, 120 points are used to define the wake. The computational grid is 31x31 with an equal mesh spacing of .05 in y and z. In the development of the rolled up vortex wake, the large scale characteristics of the wake emerge as

the wake rolls up. First, a reverse "hook" at the tip region develops and second, the emergence of small scale structures in the vortex core can be seen at larger times (Figure 4.2e).

The reverse "hook" is generated due to the scheme used to redistribute the vorticity. At the tip region, the vorticity in the last mesh cell will be redistributed beyond the wake definition. (See figure below.)

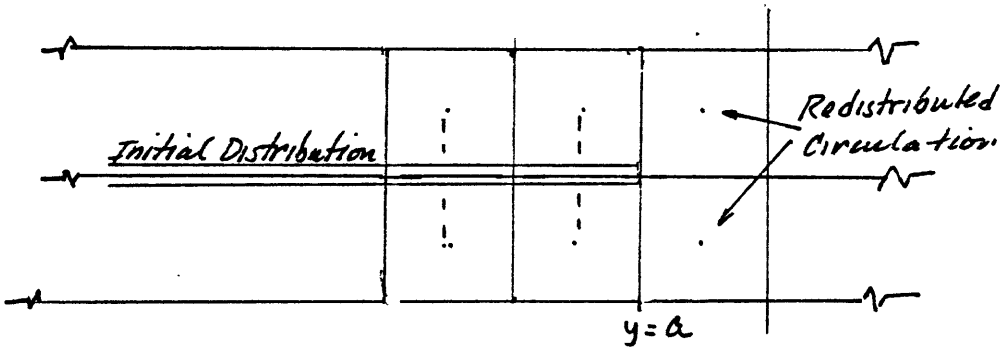

This new distribution of vorticity will tend to retard the rollup from the tip and will create the "hook" shown in the results. The "hook" does not appear in the results of Baker [4], but with the wake defined by 2,000 points, it is not clear from the figures if the "hook" exists.

The second small scale structures are the results of the vortex sheet rolling up on itself. This effect is dependent on the mesh spacing and becomes more predominant as the mesh is refined.

The velocity profiles for the v and w components of velocity are shown in Figures 4.3 and 4.4. The velocity profiles are shown at locations of constant y and z for the v and w velocity components, respectively. Initially, the v velocity represents the velocity through the undistorted

wake (Figure 4.3a) and at a later time (Figure 4.3b), the v velocity through the vortex core is shown. • Initially, the w velocity represents the velocity along the undistorted wake (Figure 4.4a), while Figure 4.4b presents the w velocity through the rolled up vortex core. A small variation in the downwash near y=0 is shown in Figure 4.4a and is the result of the sparse distribution of vorticity in this region.

The rollup of the vortex wake defined by equally spaced point vortices is shown in Figure 4.5. Initially (Figures 4.5a, b, c), there are virtually no differences in the vortex wake geometry from the geometry shown in Figure 4.2. The rollup schedule is similar and the emergence of the "hook" at the tip region is shown. Unlike the vortex wake defined by constant strength point vortices, the present definition results in instabilities in the vortex core at later times (Figures 4.5d, e, f).

In Figures 4.5d, e, f, the large scale structure of the vortex wake remains stable and is virtually identical to the constant strength case. However, it is not clear that this condition will persist. In Figure 4.5f, the interior structure of the vortex core is beginning to disturb the outer portion of the vortex sheet defining the vortex core. At large times ($t^* \sim 1$), the large scale structure of the vortex wake does indeed remain stable and is shown in Figure 4.5g. Numerous small scale structures in the vortex core can be seen. The velocity profiles for the v and w velocity

components are shown in Figures 4.6 and 4.7. At t* = 0, the v velocity profile (Figure 4.6a) is unchanged from that of Figure 4.3a, but the irregularity in the w velocity profile of Figure 4.4a has been smoothed out and does not appear in Figure 4.7a. This is the result of a more uniform point vortex spacing near y=0. The results of Figures 4.6b and 4.7b are similar to those shown previously (4.3b, 4.4b) with the exception that the velocities in the core are irregular due to the vortex instabilities within the vortex core.

The effects of varying the number of point vortices in the definition of the vortex wake are presented next. For this case, the overall dimensions of the computational mesh are unaltered from the previous results. Here, the vortex wake is defined by 60 point vortices of constant strength. The results are compared with those of Figure 4.2. The vortex wake geometry is presented in Figure 4.8 and the velocity profiles are shown in Figures 4.9 and 4.10. No significant differences in the vortex wake geometry from that shown in Figure 4.2 appear. Irregularities in the w velocity component near y=0 can be seen in Figure 4.10a. Again, this is due to the sparse definition of the vortex wake in that region.

Variations in the mesh definition are obtained by refining the mesh spacing. For this case, the mesh spacing is decreased by a factor of 2 with the computational boundaries remaining unchanged. The computational grid is

now 61x61. The development of the vortex wake modeled by 120 constant strength point vortices is shown in Figure 4.11. The solution is stopped at a time less than that shown in the previous examples due to the length of computation and reduced time step for this case. The predominant change in the vortex wake is the rollup schedule. As the computational mesh is refined, velocities more representative of the vortex core are modeled and the rollup adjusts accordingly. Small scale structures in the vortex core can be seen in Figures 4.11d and 4.11e. The velocity profiles are shown in Figures 4.12 and 4.13 and are representative of the increased velocity associated with the refined mesh. In Figure 4.13a, the local velocity profile between point vortices near y=0 can be seen.

The variation in the centroid of vorticity with time is shown in Figure 4.14. The y location of the centroid is determined by equation 2.9 with a similar expression for the z location. The calculated centroid of vorticity is shown to be in close agreement with the Betz predictions. The vertical variation of the vortex centroid with time is shown in Figure 4.15.

4.2 Conventional Wings - Deflected Flap Load Distribution

4.2.1 Input Description

As a second application, consider a load distribution representing a deflected trailing edge flap configuration. The flap model [4] representing the load distribution is

separated into three sections along the semi-span. The functions representing the circulation distribution are chosen and constrained by equating circulation value and derivative at the section end points. See Figure 4.16. Then, from [4]:

$$0 \le y \le A$$

$$\Gamma_w(y) = \Gamma_{w_0} + 3/A^2 \left(\Gamma_{w_1} - \Gamma_{w_0}\right) y^2 - 2/A^3 \left(\Gamma_{w_1} - \Gamma_{w_0}\right) y^3 \quad (4.4)$$

for, $A \le y \le B$, the form is chosen:

$$\Gamma_w(y) = ay^3 + by^2 + cy + d \quad (4.5)$$

and $B \le y \le 1$:

$$\Gamma_w(y) = (1 - y^2)^{1/2} \quad (4.6)$$

where:

$$a = \frac{-2(\Gamma_{w_1} - \beta)}{(A-B)^3} - \frac{B}{(A-B)^2 \beta}$$

$$b = \frac{-B}{2\beta(B-A)} - \frac{3a(B+A)}{2}$$

$$c = -3aA^2 - 2bA$$

$$d = \Gamma_{w_1} + 2aA^3 + bA^2$$

$$\beta = (1 - B^2)^{1/2}$$

The expression for b in reference [4] has the form:

$$b = \frac{-B}{2\beta(B-A)} - \frac{3A(B+A)}{2}$$

which is a misprint. The expression should be of the form shown previously.

Equations 4.4-4.6 are non-dimensionalized, using the value of circulation Γ_{w_0} . The constraints are chosen to be A=.3, B=.7, Γ_{w_0}=1.4, Γ_{w_1}=2.0. Equations 4.4-4.6, together with equation 2.4, determine directly the circulation of the vortex wake.

4.2.2 Input and Mesh Variations

Results obtained by varying the input description and the mesh spacing for the simulated flap loading are presented in this subsection. The variations in the input description are identical to those of Section 4.1.2 and are related to the type of point vortex (constant strength or equally spaced) and the number of point vortices used to define the vortex wake. This subsection is presented in three parts. First, the results of varying the point vortex description are presented. Next, the results obtained from varying the number of input point vortices will be shown and, finally, results obtained by varying the mesh spacing will be presented.

Results obtained by varying the input point vortex description are shown in Figures 4.17 through 4.22. In these results 120 input point vortices are used to define the vortex wake. The computational grid is 31x31 with equal mesh spacing of .05 in y and z. Figure 4.17 illustrates the development of the vortex wake generated by the simulated flap loading. In this figure, the vortex wake is represented by three symbols with each symbol corresponding to a different section of the input load distribution of Figure 4.16. The vortex wake quickly rolls up into three distinct vortex cores (Figures 4.17a-4.17c). The development of the reverse "hook" in the tip vortex core is shown in Figures 4.17b and 4.17c. Here again, as in the results for the elliptical loading, the "hook" is the result of smearing the highly loaded tip region of the wake by the bilinear interpolation scheme. See figure in text of section 4.1.2. At later times, Figures 4.17d and 4.17e, the vortex cores become more distinctive and the tip vortex begins to rotate about the mid-span vortex. It is clear that the demarcation point between the inboard and the mid-span vortex is accurately represented in Figure 4.16. The demarcation point between the mid-span vortex and the tip vortex varies from that of Figure 4.16 insignificantly. Baker [4] has shown similar results, but care must be taken in comparing the results. It is not clear how Baker non-dimensionalized his problem.

Velocity profiles through the vortex wake are shown in Figures 4.18 and 4.19. The components of velocity v and w are shown at centroids of local vorticity defined by equation 2.9 for the y location and a similar expression for the z location. The velocity profiles are shown for the initial and final times of Figure 4.17.

The velocity profiles for the v component of velocity are shown in Figure 4.18 and represent the velocity along lines of constant y. Initially (Figure 4.18a), the velocity through the undistorted vortex wake is shown and represents the strength and sign of velocity in the three regions of the wake. At a later time (Figure 4.18b), the velocity profiles through the vortex cores can be seen. The velocity profiles for the w component of velocity are shown in Figures 4.19a and 4.19b, and represent the downwash at positions of constant z. The centroids of vorticity are represented in the legend of each figure.

Development of the vortex wake defined by equally spaced point vortices is shown in Figure 4.20. Here again, the wake is represented by 130 point vortices and the grid is 31x31. The overall structure shown varies only slightly from that shown in Figure 4.17 and only in regions of the vortex cores or on the wake between the large scale structures. Variations in the position of the demarcation points are shown. Velocity profiles are shown in Figures 4.21 and 4.22 and indicate insignificant variations from those shown in

Figures 4.18 and 4.19. In comparing the predicted centroids of vorticity (shown in the legend of each figure), only small changes are shown.

The development of the vortex wake defined by 60 constant strength point vortices is shown in Figure 4.23. The grid is 31x31. The large scale structures remain invariant from the previous results and the positions of the demarcation points are in closer agreement with the results of Figure 4.17 than those shown in Figure 4.20. The cross-over of the lines in the figures do not represent instabilities, but are rather the result of the sparse definition of the curved portions of the vortex wake. Velocity profiles are shown in Figures 4.24 and 4.25 and indicate insignificant variations from the results shown previously.

Results of the vortex wake development on a refined mesh are shown in Figure 4.26. Here, the vortex wake is defined by 130 constant strength point vortices on a grid equal to 61x61. The development of the wake is not shown for the later times of the previous figures. The large scale structure of the vortex wake is similar to that shown in the previous results with the exception that the vortex cores are more highly concentrated in Figure 4.26. This results from the ability of the refined mesh to resolve the larger velocities near the vortex core. Small scale structures can be seen within the large scale structures of Figures 4.26c

and 4.26d. Similar structures are presented in [4]. The velocity profiles are shown in Figures 4.27 and 4.28, and indicate the increased velocities associated with the smaller point vortex core (on the order of the mesh spacing).

The variation in the spanwise position of the vortex centroids with time for the simulated flap loading are shown in Figure 4.29. Initially, the positions of the centroids are in close agreement with those predicted by Donaldson [23], but disagree significantly at later times. This trend results from the inability of the Betz theory to predict the interaction of several vortex structures within the wake. The Betz theory only predicts the spanwise location of the vortex centroids. The vertical variation of the vortex centroids with time are shown in Figure 4.30.

4.3 Rotating Wings

4.3.1 Input Description

Consider the rotating wing load distribution illustrated in Figure 4.31. This load distribution was taken from Figure 2 in [19]. The load distribution is represented by three distinct regions and will generate three concentrated vortex cores [23]. The three regions of Figure 4.31 are modeled mathematically as:

$$.1 \leq y^* \leq A$$

$$\Gamma^*(y^*) = \Gamma_w^*(A)\sqrt{1-\left[\frac{(y^*-A)}{(A-.1)}\right]^2} \qquad (4.7)$$

where $\Gamma_w(A)$ is chosen to be .0152.

On the interval A $\leq y^* \leq$ B, a cubic equation is used to describe the load distribution and has the form:

$$\Gamma_w^*(y^*) = a y^{*3} + b y^{*2} + c y^* + d \tag{4.8}$$

where a, b, c, d are determined by matching value the of circulation Γ_w and the slope of the load distribution at points A and B. The values become:

$$a = \frac{2(\Gamma_{w_0} - \Gamma_w)(A-B)}{DET\,A}$$

$$b = \frac{-3}{2}(A+B)a$$

$$c = 3ABa$$

$$d = \Gamma_1 + \frac{a}{2} B^2(B-3A)$$

$$DET = AB(4A^2 + 4B^2 - 6AB) - (B^4 + A^4)$$

for B $\leq y^* \leq$ 1, the form chosen is:

$$\Gamma_w^*(y^*) = (1 - y^{*2})^{1/3} \tag{4.9}$$

Here, the values are chosen to be: A =.8, B=.9, Γ_w (A) =.0152 and Γ_w (B)=.022.

The equations 4.7 through 4.9 are in dimensionless forms. The shed vorticity for this load distribution can be calculated directly from equation 2.4.

4.3.2 Results

Preliminary results representing the non-planar vortex wake generated by a rotating wing load distribution are presented. The results are termed preliminary because the locations of the point vortices in the wake have not fully converged. However, in the results presented, the predicted locations of the vortex wakes are in close agreement with those of Miller [19]. The results represent two methods of defining the near wake model. First, the near wake is modeled by concentrated point vortices (similar to Miller's method) and second, the near wake is represented by many point vortices distributed on each vortex wake.

In both definitions, the computational grid is equal to 61x81 with equal mesh spacing of .025 in y and z. The initial wake spacing in the near wake is determined from equation 3.12 with $C_T = 4.42 \times 10^{-3}$ (Miller [19]) for both near wake definitions.

Results obtained by modeling the near wake as point vortices are shown in Figure 4.32. The relaxation coefficient used in the numerical integration of equation 2.8 was chosen to be .1. The initial locations of the point vortices are determined from the method of Section 2.1.3 and the initial wake spacing (Figure 4.32a). The wake geometry after ten and twenty iterations are shown in Figures 4.32b and 4.32c, respectively. The figures indicate the rapid contraction of the rotor wake and the increased flow through

the rotor near the tip vortex location. The results for wake iterations thirty and forty are shown in Figures 4.32d and 4.32e, respectively, and indicate further contraction of the rotor wake. Results in Figure 4.32e are compared with the results in Figure 2.0 of [19]. The results of this investigation are in close agreement with those of Miller [19], but are not considered fully converged.

Results obtained for a near wake model consisting of many point vortices are shown in Figure 4.33. Here, the relaxation coefficient in the numerical integration of equation 2.8 was chosen to be .2. This value was chosen to reduce the computation time. Each vortex wake in the near wake model is represented by thirty constant strength point vortices. The initial wake spacing is equal to that described above. Initially, the vortex wakes in the near wake model are planar and undistorted (Figure 4.33a). Development of the vortex wake geometries are shown in Figures 4.33b through 4.33e and indicate the rapid rollup of the tip and root vortices. The core definition of the vortex just inboard of the tip vortex is not clearly defined, but the circulatory flow associated with this vortex is clearly shown.

SECTION 5

SUMMARY

This report presents a computational method for the prediction of non-planar vortex wake flow fields generated by conventional and rotating wings. Results are shown for the non-planar vortex wake geometry and the velocity fields induced by the vortex wakes.

The numerical scheme has demonstrated the ability to predict the vortex wake geometry for an elliptical load distribution, a load distribution representing a deflected flap configuration and a load distribution representative of rotating wings.

Results for conventional wing indicate that, for a given load distribution, the large scale structures (the rolled up vortex) are relatively insensitive to input variations (constant strength or constant spaced point vortices) and mesh refinement. The small scale structures are sensitive to both input definitions and mesh refinement.

Preliminary results for the rotating wing wake show promise, but further study is needed to provide a fully converged wake.

Recommendations for further investigations include:

1) Evaluate alternative circulation redistribution schemes.

2) Utilize far field approximations to the boundary condition in order to increase computational efficiency.

3) Evaluate alternative integration schemes for the spatially dependent forms of the trajectory equations of motion.

4) Investigate the time dependent solution for the rotating wing vortex wake.

REFERENCES

1) Rosenhead, L., "The Formation of Vortices from a Surface of Discontinuity," Proc. Roy. Soc., Series A, V134 (1931), 170.

2) Moore, D.W., "The Discrete Vortex Approximation of a Finite Vortex Sheet," California Institute of Technology Report AFSOR-1804-69, 1971.

3) Chorin, A.J. and Bernard, P.S., "Discretization of a Vortex Sheet With an Example of Roll-Up," J. Comp. Physics, V13 (1973), 423-429.

4) Baker, G.R., "The 'Cloud in Cell' Technique Applied to the Rollup of Vortex Sheets," J. Comp. Physics, V31 (1979), 76-95.

5) Christiansen, J.P., "Numerical Simulation of Hydrodynamics by the Method of Point Vortices," J. Comp. Physics, V13 (1973), 363-379.

6) Meng, J.C.S. and Thomson, J.A.L., "Numerical Studies of Some Nonlinear Hydrodynamic Problems by Discrete Vortex Element Methods," J. Fluid Mech., V84 (1978), 433-453.

7) Johnson, F.T., Tinoco, E.N., Lu, P. and Epton, M.A.,, "Three-Dimensional Flow Over Wings With Leading-Edge Separation," AIAA J., V18, no. 4 (1980), 367-380.

8) Landgrebe, A.J., "Rotor Wakes - Key to Performance Predictions," Proceedings of Symposium on Status of Testing and Modeling Techniques for V/STOL Aircraft," AHS Mid-East Region, October 1972.

9) Johnson, W. and Scully, M.P., "Aerodynamic Problems in the Calculation of Helicopter Airloads," Proceedings of Symposium on Status of Testing and Modeling Techniques for V/STOL Aircraft, AHS Mid-East Region, October 1972.

10) Miller, R., "Rotor Blade Harmonic Air Loading," AIAA J., V2, no. 7, July 1964.

11) Piziali, R.A., "Method for Solution of the Aeroelastic Response Problem for Rotating Wings," Jl. Sound and Vibration, V4, no. 3, 1966.

12) Brandt, D.E., "Investigation of Rotor Blade Dynamics During Equilibrium Transition Flight," M.S. Thesis, Massachusetts Institute of Technology, 1962.

13) Ham, N., "An Experimental Investigation of the Effect of a Non-Rigid Wake on Rotor Blade Airloads in Transition Flight," Proceedings CAL/TRECOM Symposium, V.I., June 1963.

14) Brady, W.G. and Crimi, P., "Representation of Propeller Wakes by Systems of Finite Core Vortices," Cornell Aeronautical Lab. Report No. BB-1665-S-2, Feb. 1965.

15) Levinsky, E.S. and Strand, T., "A Method for Calculating Helicopter Vortex Paths and Wake Velocities," Air Force Flight Dynamics Laboratory, Technical Report AFFDL-TR-69-113, July 1970.

16) Landgrebe, A.J., "An Analytical Method for Predicting Rotor Wake Geometry," J2., AHS, V 14, no. 4, October 1969.

17) Landgrebe, A.J., "The Wake Geometry of a Hovering Helicopter Rotor and Its Influence on Rotor Performance," 28th Annual Forum, AHS, May 1972.

18) Summa, J.M. and Clark, D.R., "A Lifting-Surface Method for Hover/Climb Airloads," 35th Annual National Forum, AHS, May 1979.

19) Miller, R.H., "Simplified Free Wake Analyses for Rotors," Aeroelastic and Structural Research Lab. Report TR 194-3, Aug. 1981, Massachusetts Institute of Technology.

20) Milne, L.M. and Thomson, C.B.E., "Theoretical Hydrodynamics," The Macmillan Company, New York.

21) Batchelor, G.K., "An Introduction to Fluid Dynamics," Cambridge University Press.

22) Betz, A., "Behavior of Vortex Systems," Zeitschrift fur angewandte Mathemathik and Mechanik, V. 12, no. 3, June 1932; also TM 713, June 1933, NACA.

23) Donaldson, C., duP., Snedeker, R.S. and Sullivan, R.D., "Calculation of Aircraft Wake Velocity Profiles and Comparison With Experimental Measurements," J. Aircraft, V. 11, no. 9, Sept. 1974.

24) Swarztrauber, P.N., Sweet, R.A., "Algorithm 541 Efficient Fortran Subprograms for the Solution of Separable Elliptic Partial Differential Equations [D3]," ACM Transactions on Mathematical Software, V5, no. 3, Sept. 1979, 352-364.

25) Beyer, W.H., "CRC Standard Mathematical Tables," 25th ed, CRC Press, Inc.

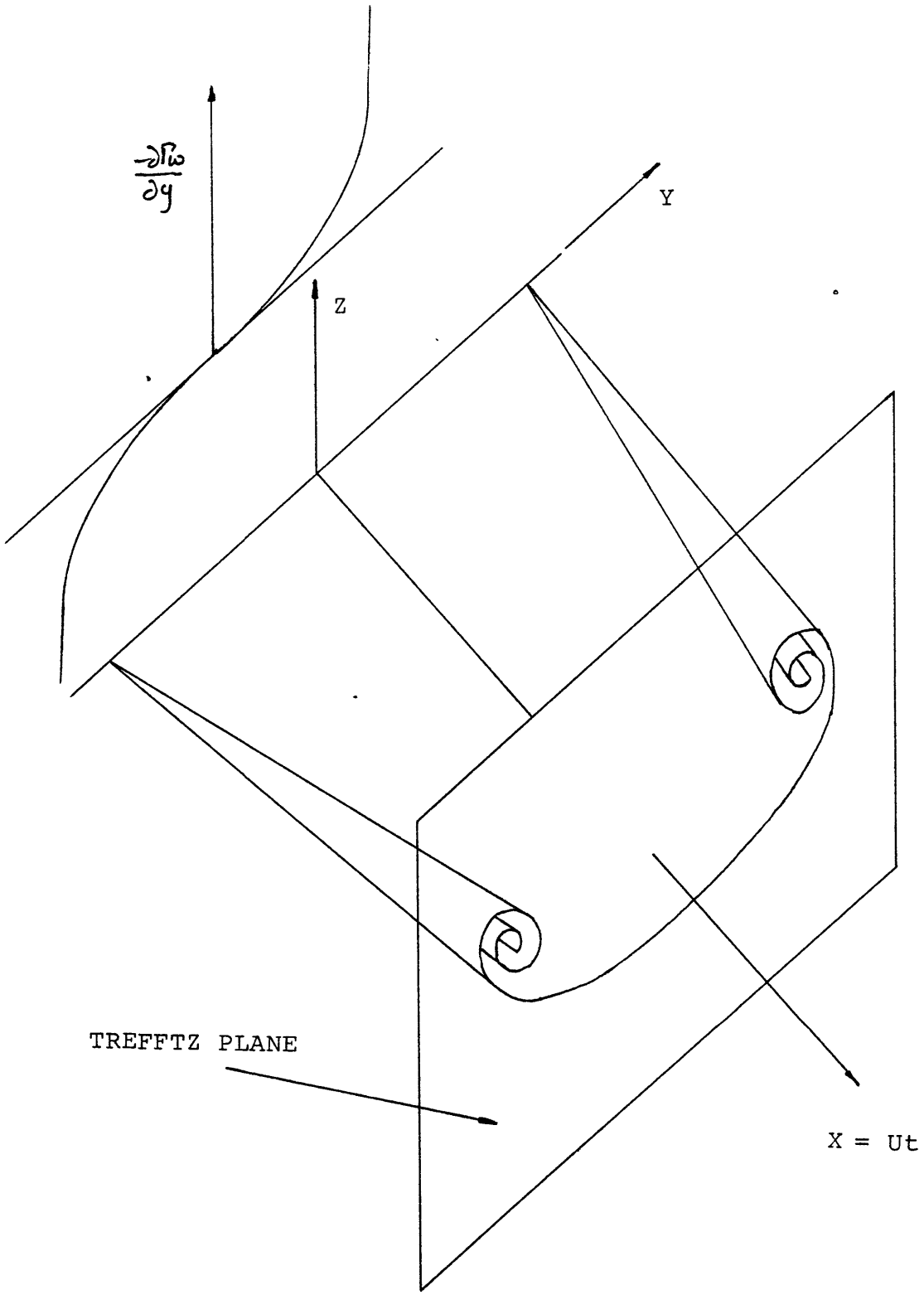

FIGURE 1.1 - COMPUTATIONAL PLANE REPRESENTATION

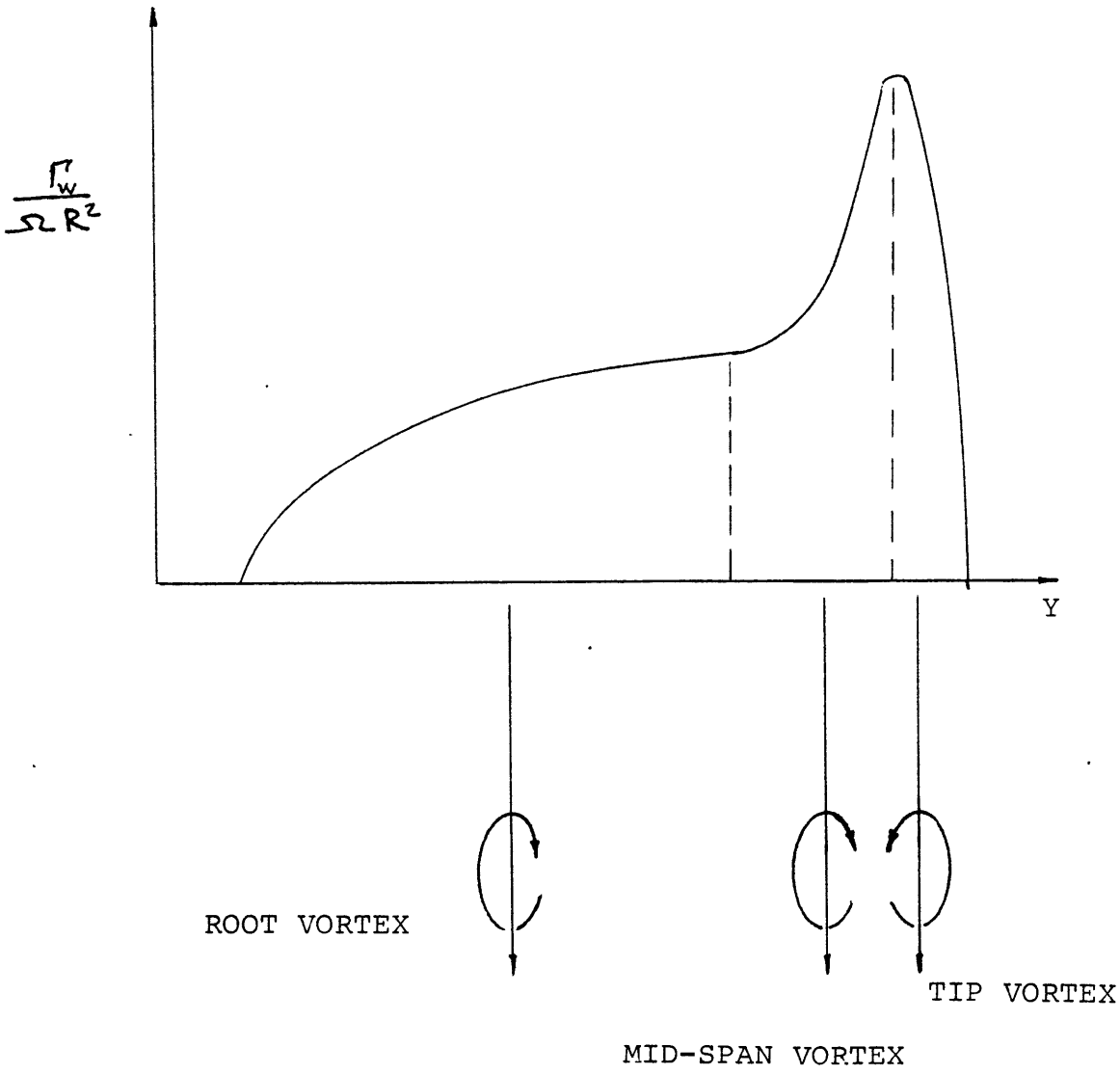

FIGURE 1.2 - BETZ APPROXIMATIONS TO ROTATING WING LOAD DISTRIBUTIONS

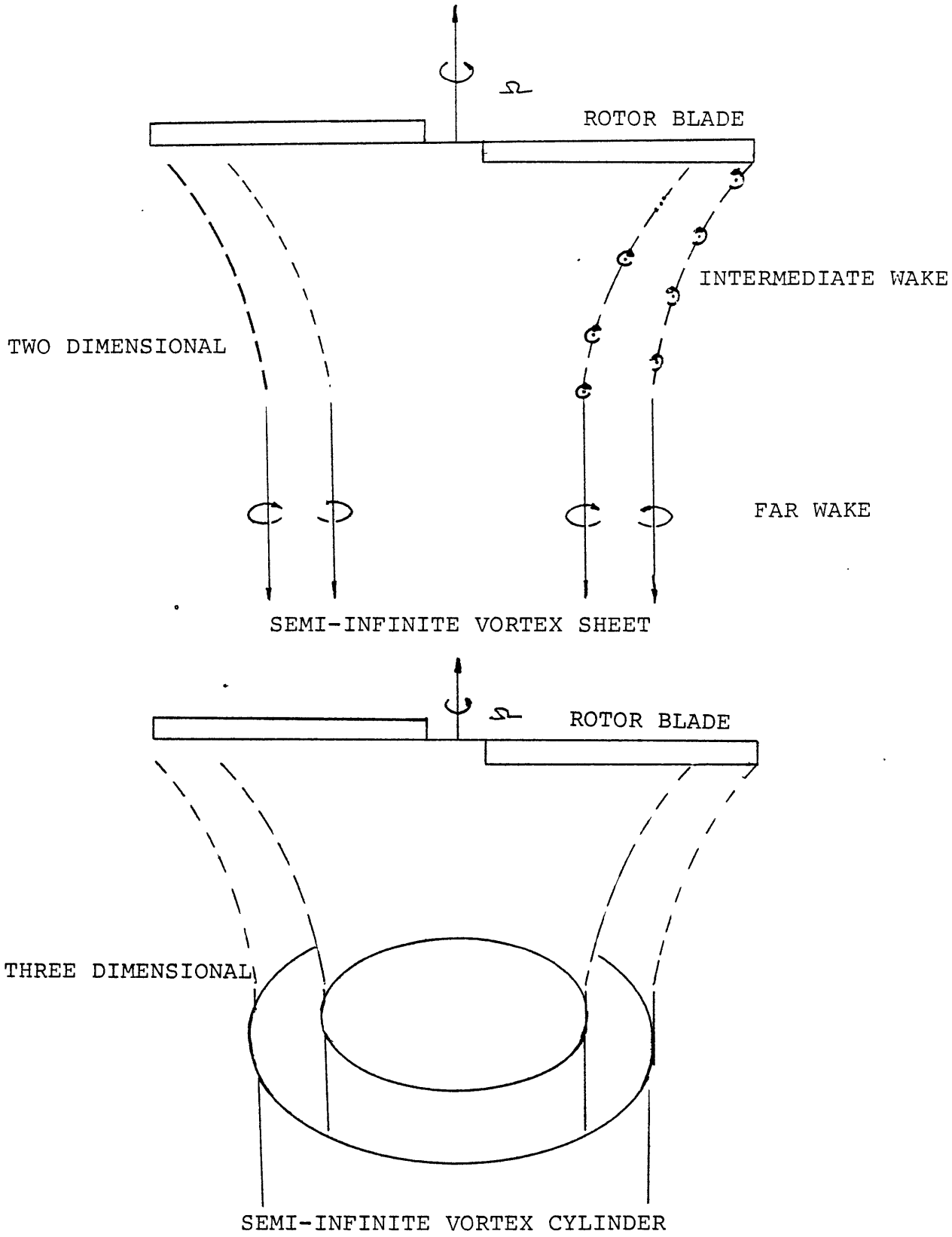

FIGURE 1.3 - FAR WAKE MODELS FOR ROTATING WING ANALYSIS (MILLER)

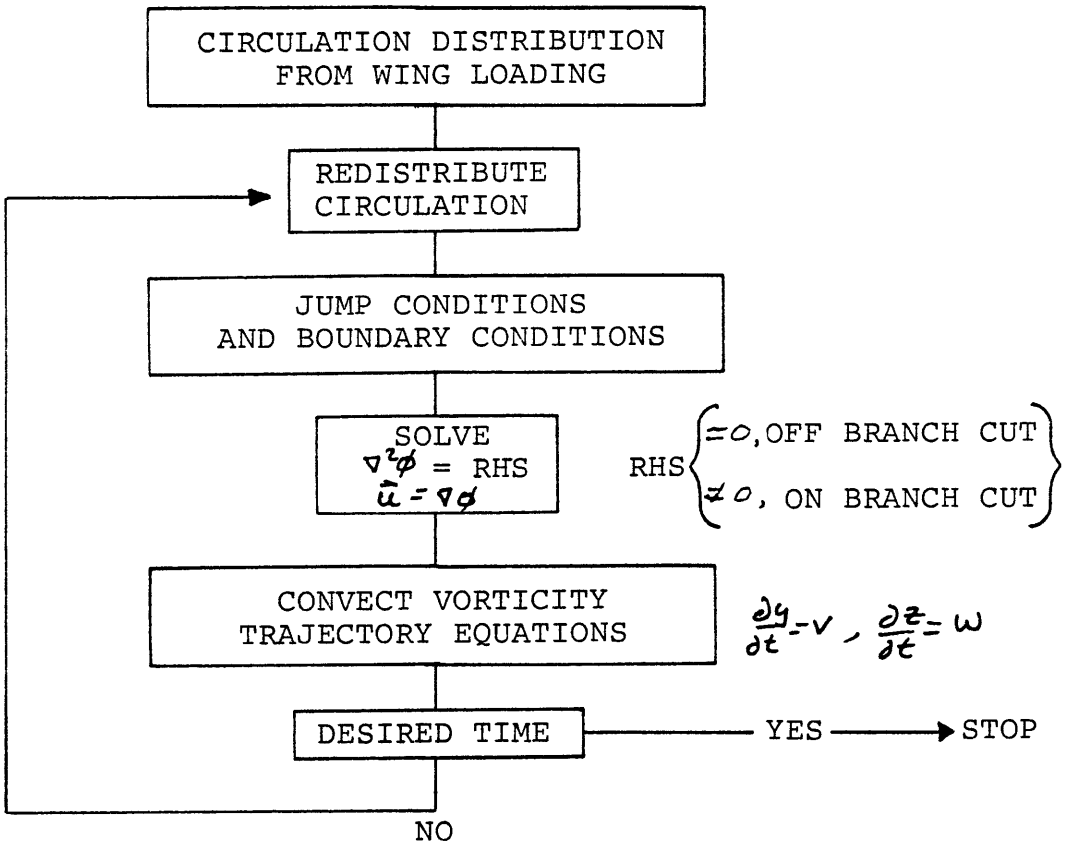

FIGURE 1.4 - FLOW CHART - CONVENTIONAL WING ANALYSIS

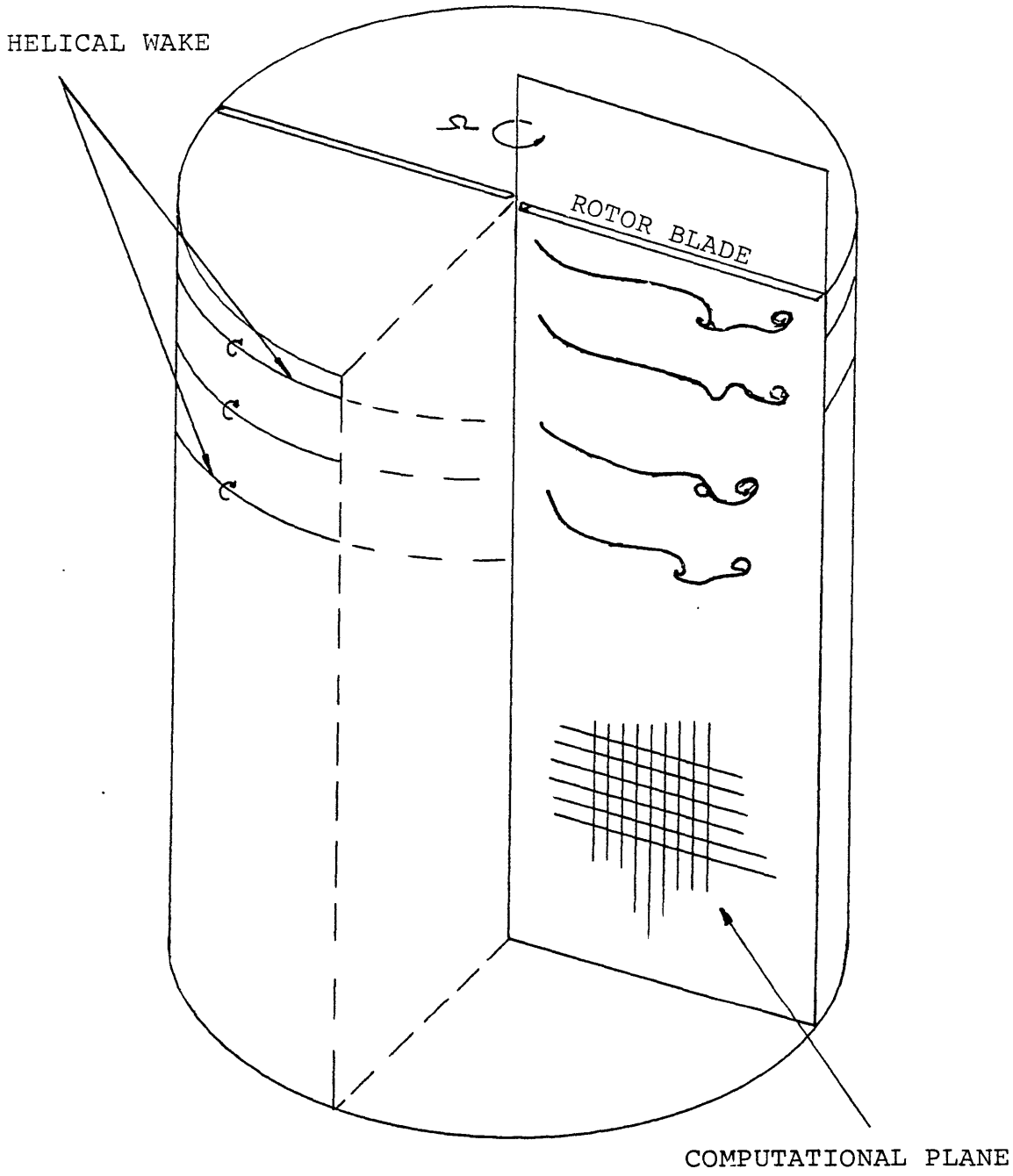

FIGURE 1.5 - COMPUTATIONAL PLANE REPRESENTATION FOR ROTATING WING ANALYSIS

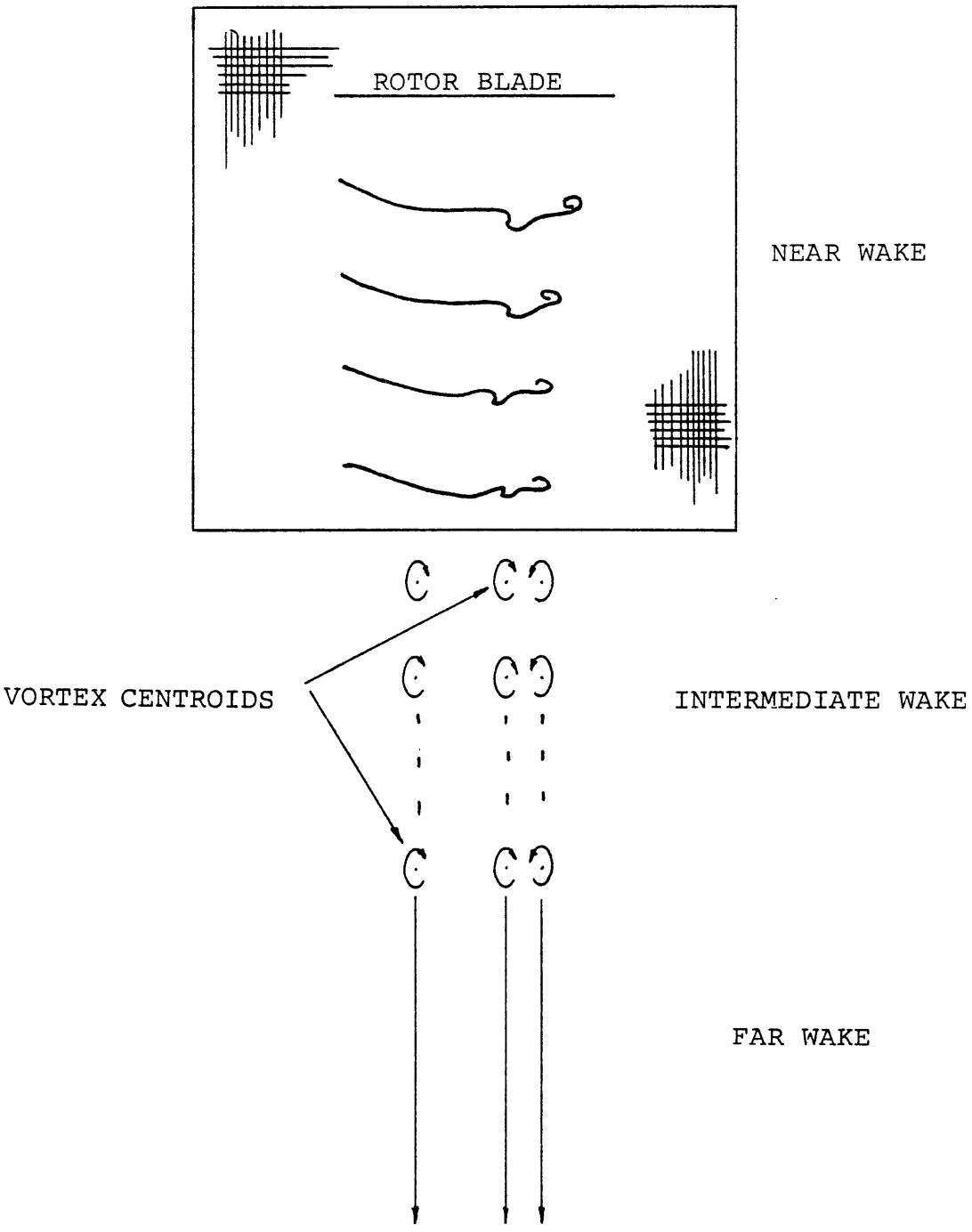

FIGURE 1.6 - INTERMEDIATE AND FAR WAKE MODELS

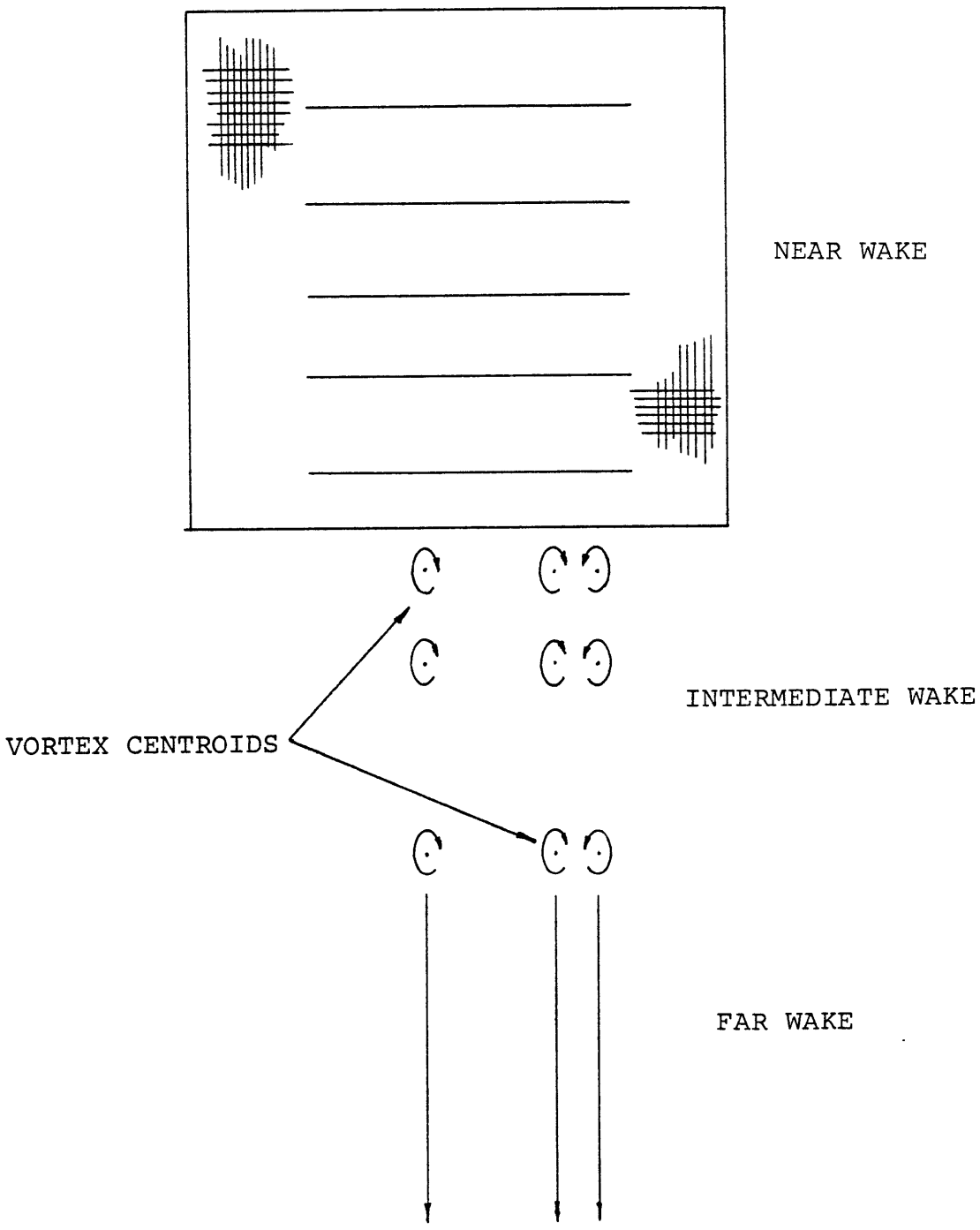

FIGURE 1.7 - GEOMETRY OF INPUT - ROTATING WING

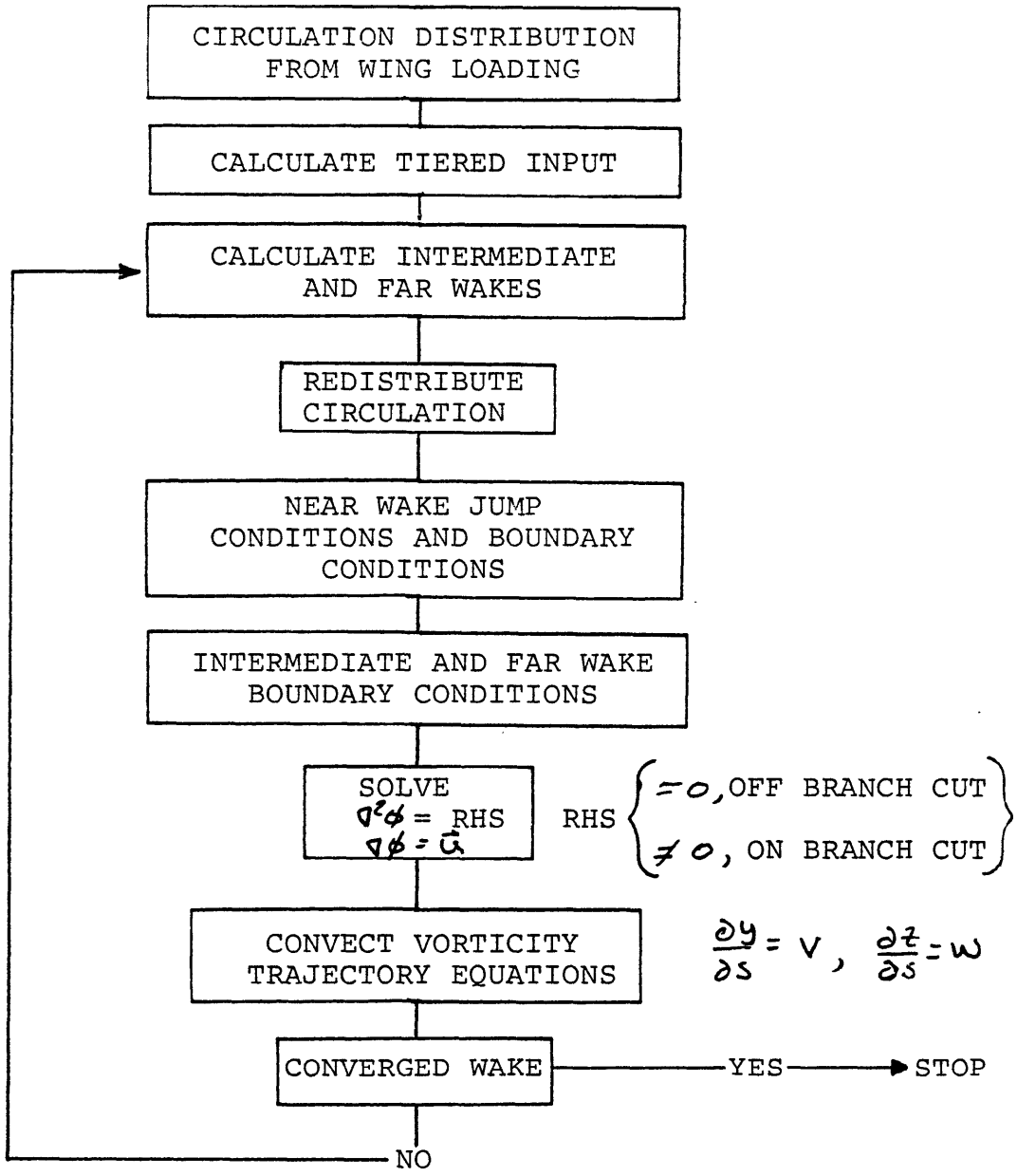

FIGURE 1.8 - FLOW CHART - ROTATING WING ANALYSIS

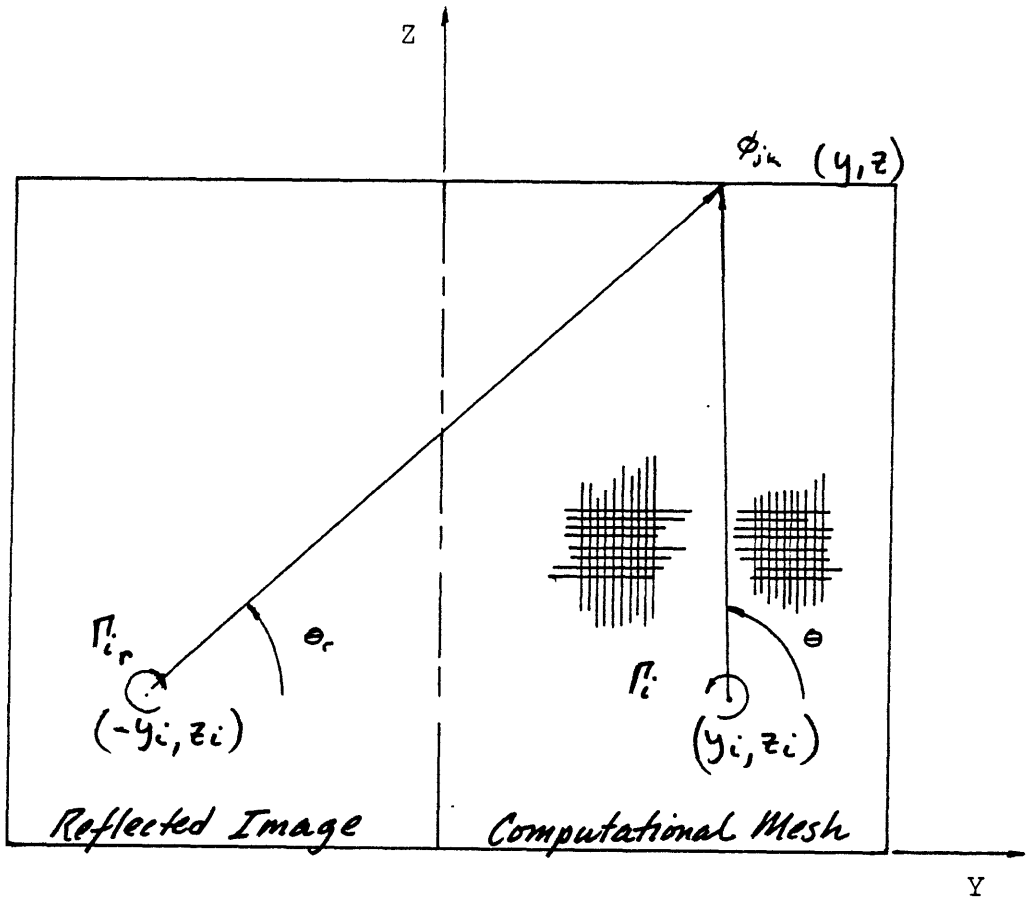

$$\Gamma_i = -\Gamma_{ir} \quad , \quad \Gamma_i > 0$$

$$\theta = \tan^{-1}\left(y - y_i / z - z_i\right)$$

$$\theta_r = \tan^{-1}\left(y + y_i / z - z_i\right)$$

$$\phi(y,z) = \frac{\Gamma_i}{2\pi}\left(\theta - \theta_r\right)$$

FIGURE 2.1 - SCHEMATIC OF BOUNDARY CONDITION ON THE VELOCITY POTENTIAL

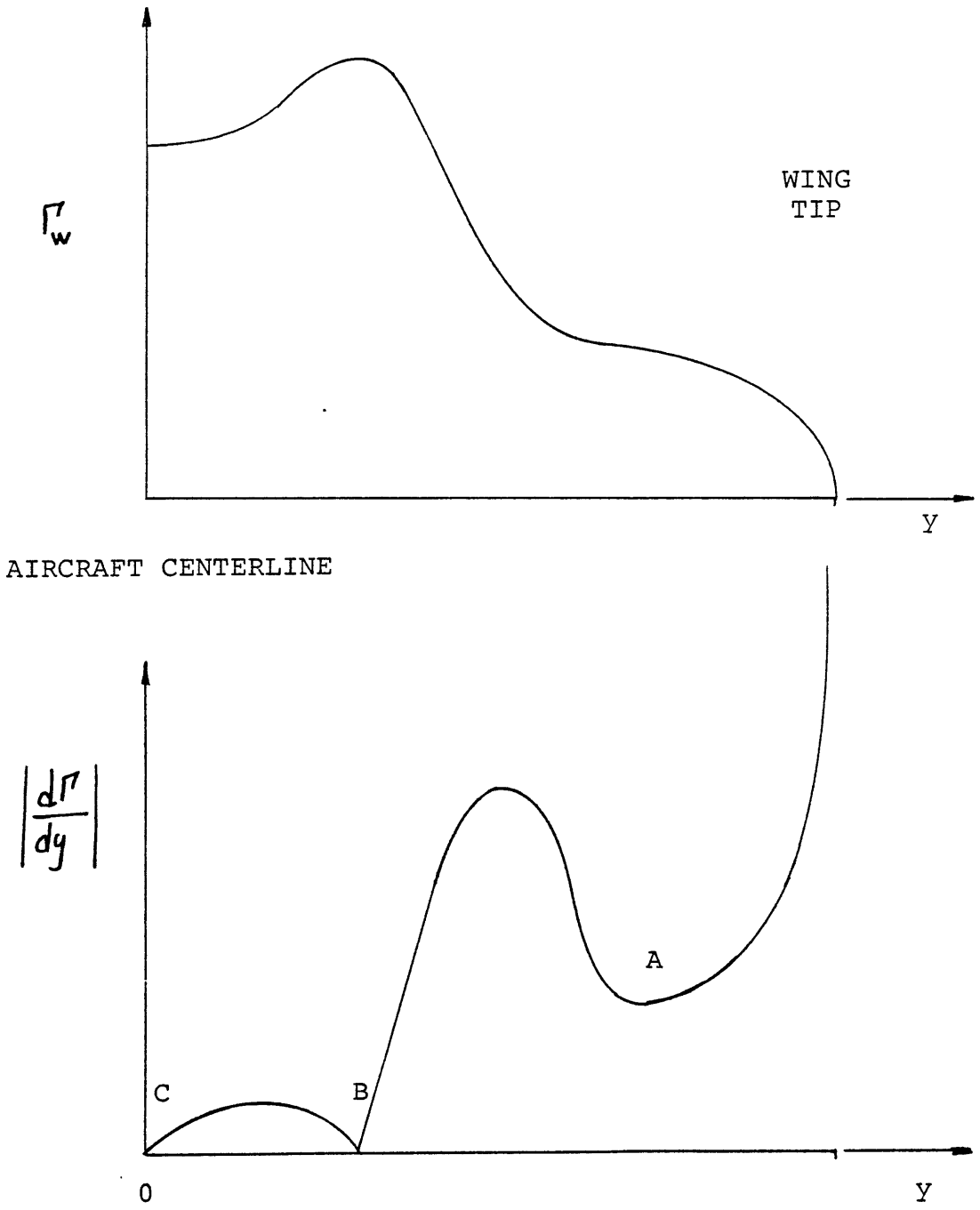

FIGURE 2.2 - DONALDSON'S METHOD FOR ROLLED UP VORTEX CORES

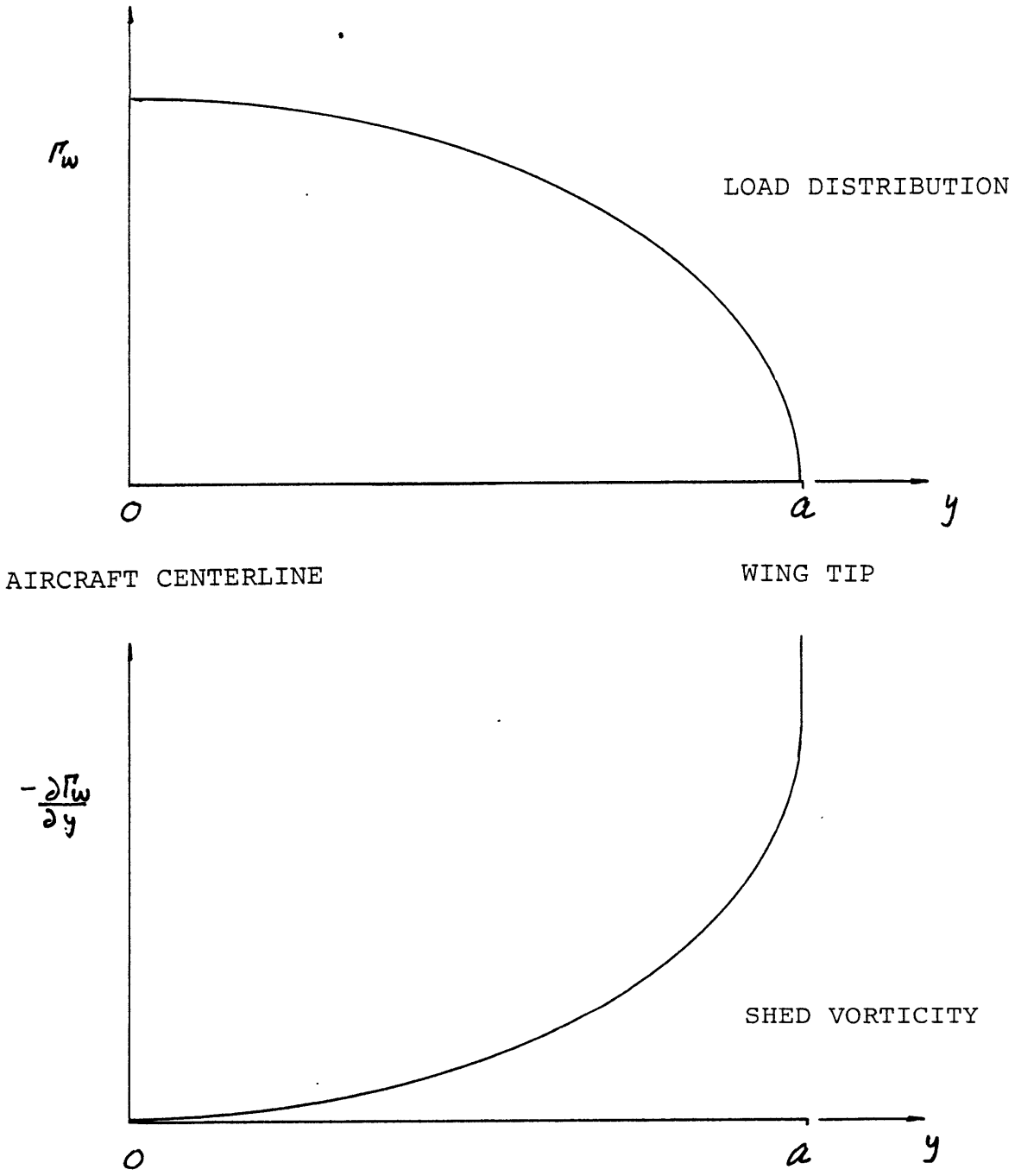

FIGURE 4.1 - WING LOADING AND SHED WAKE STRENGTH - ELLIPTICALLY LOADED WING

VORTEX ROLLUP

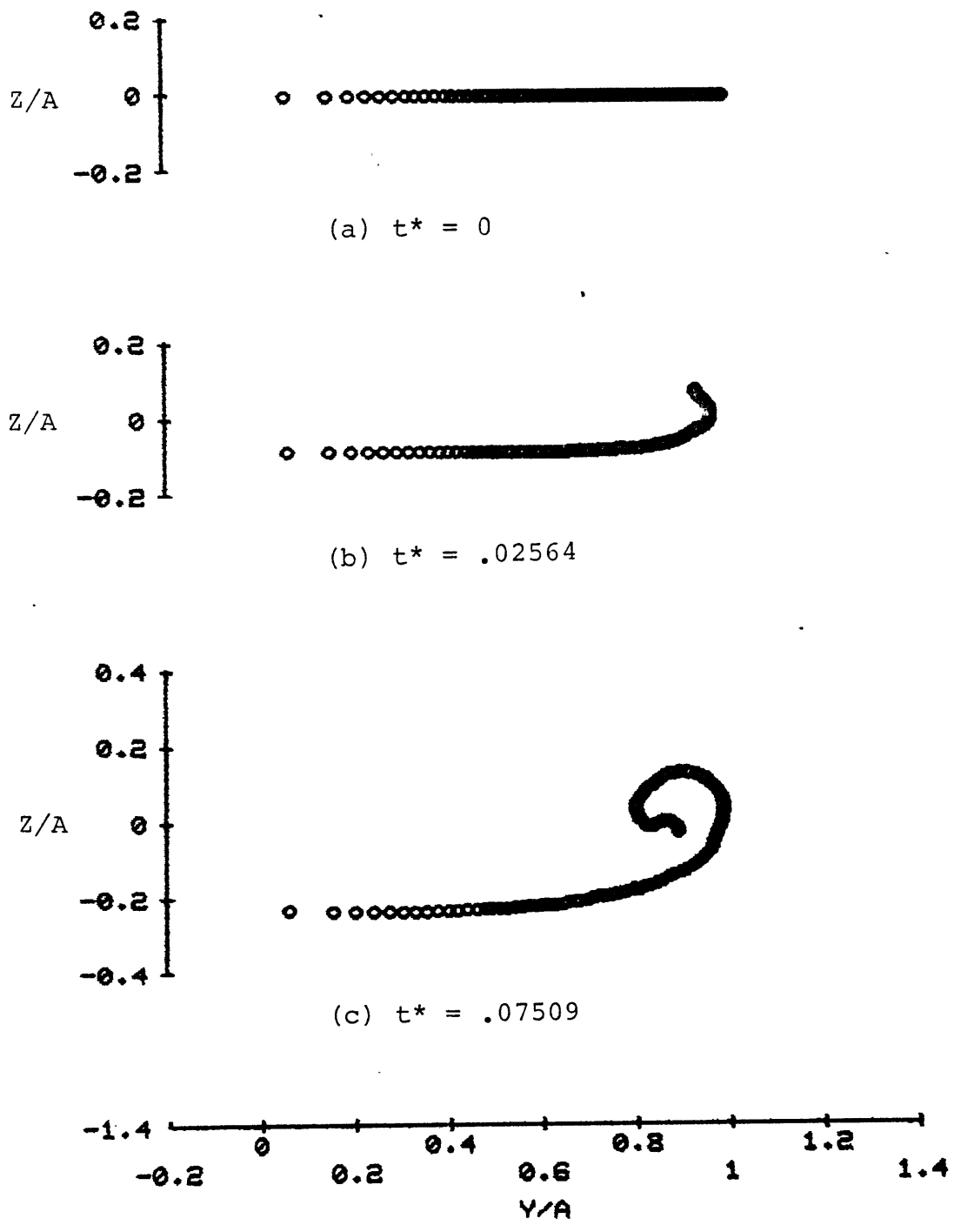

FIGURE 4.2 - ELLIPTICAL LOAD DISTRIBUTION - VORTEX WAKE GEOMETRY, CONSTANT STRENGTH POINT VORTICES, 120 POINTS, GRID = 31x31

VORTEX ROLLUP

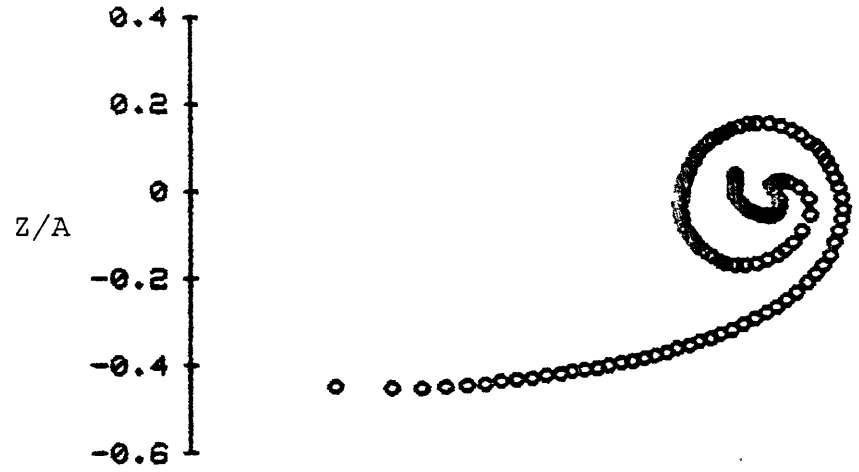

(d) t* = .15730

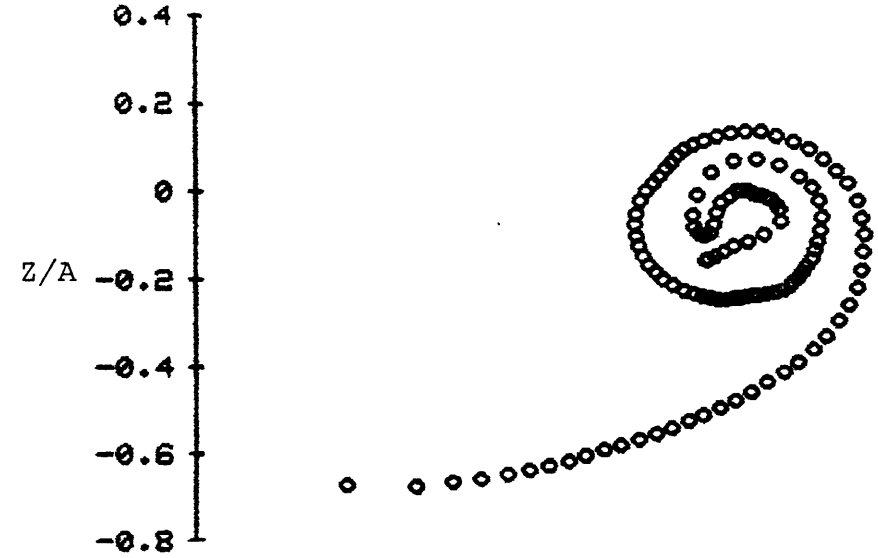

(e) t* = .25590

FIGURE 4.2 CONTINUED

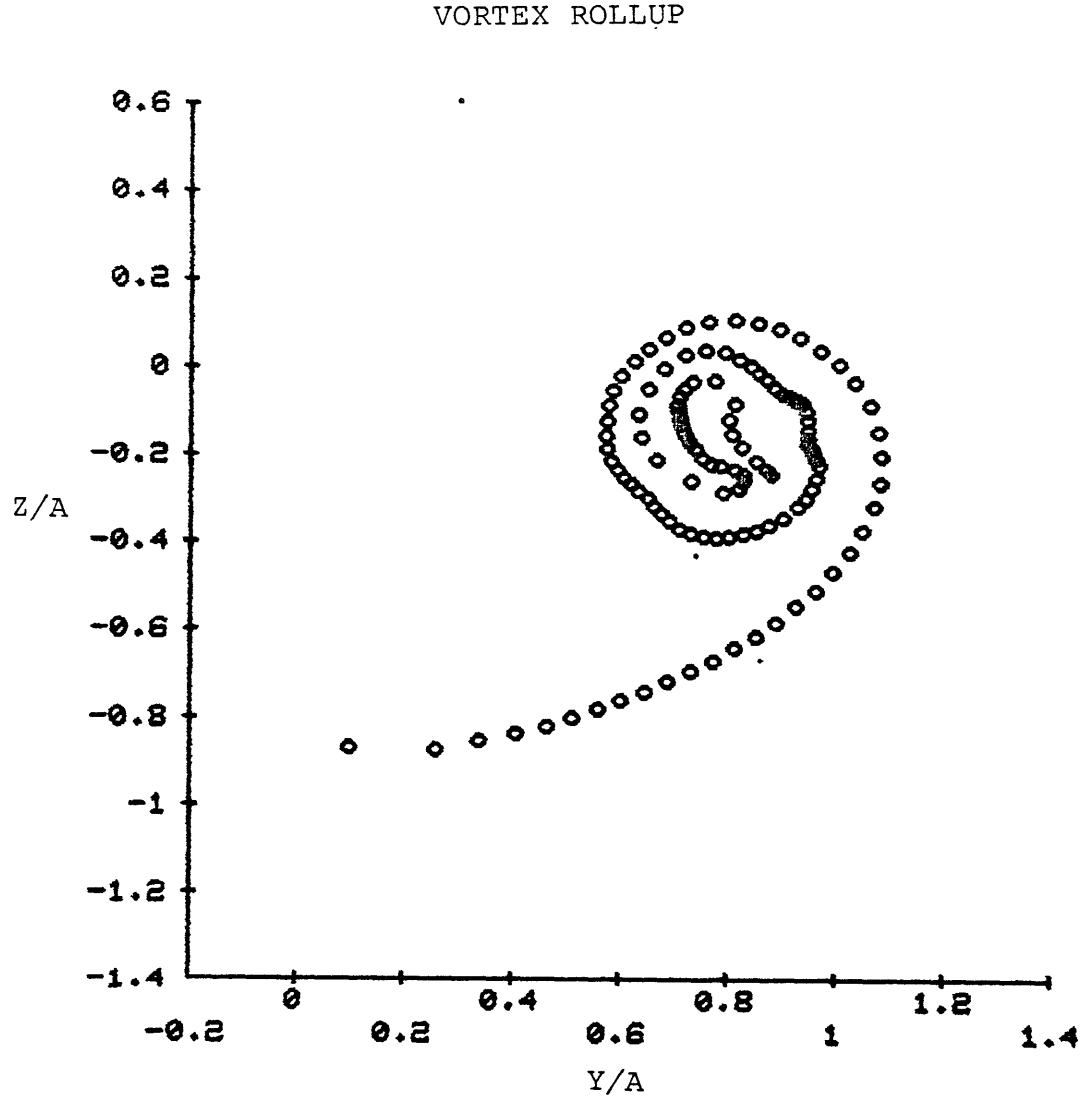

(f) t* = .36168

FIGURE 4.2 CONTINUED

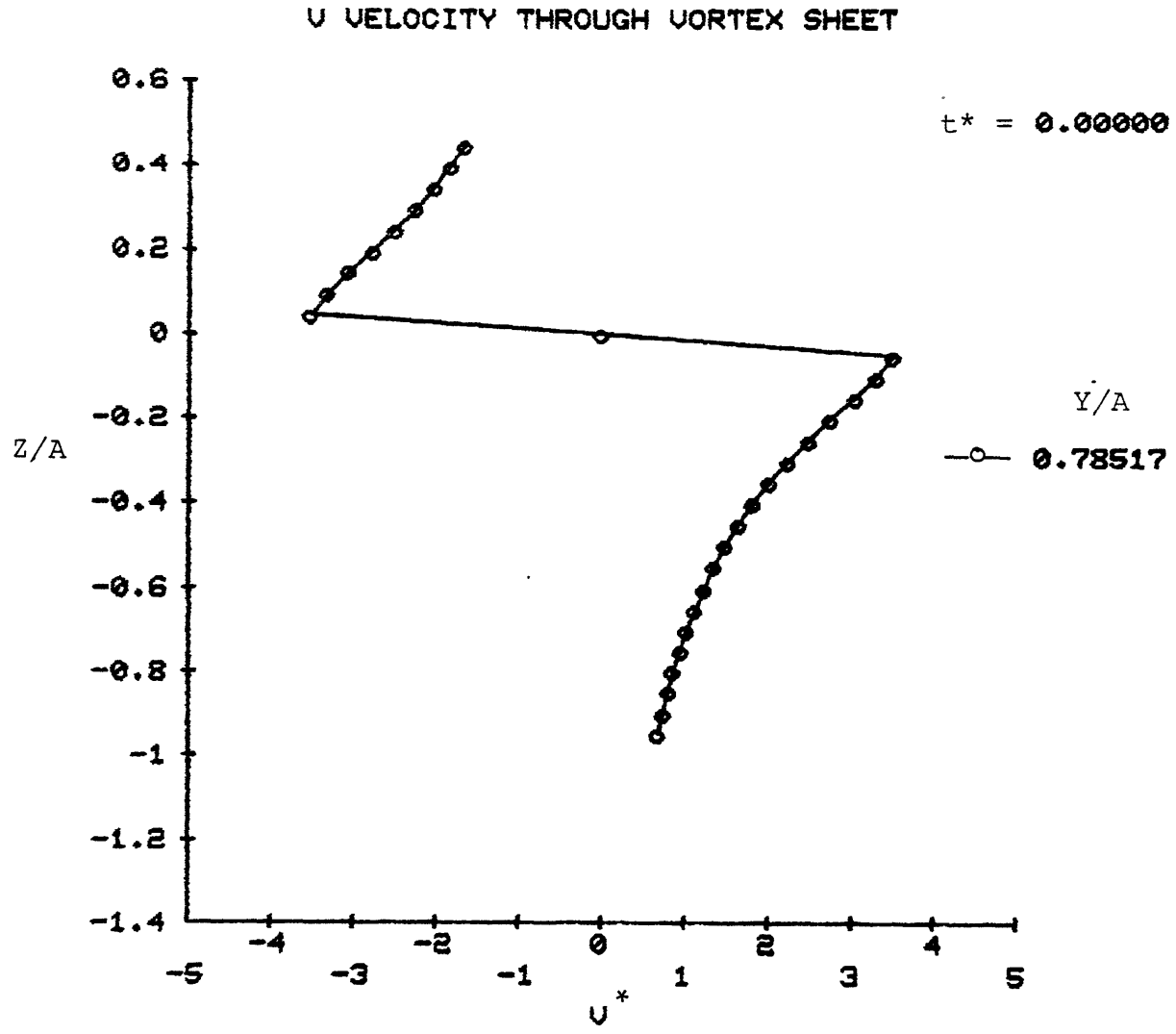

FIGURE 4.3a - ELLIPTICAL LOAD DISTRIBUTION - V VELOCITY PROFILE, CONSTANT STRENGTH POINT VORTICES, 120 POINTS, GRID = 31x31, t* = 0

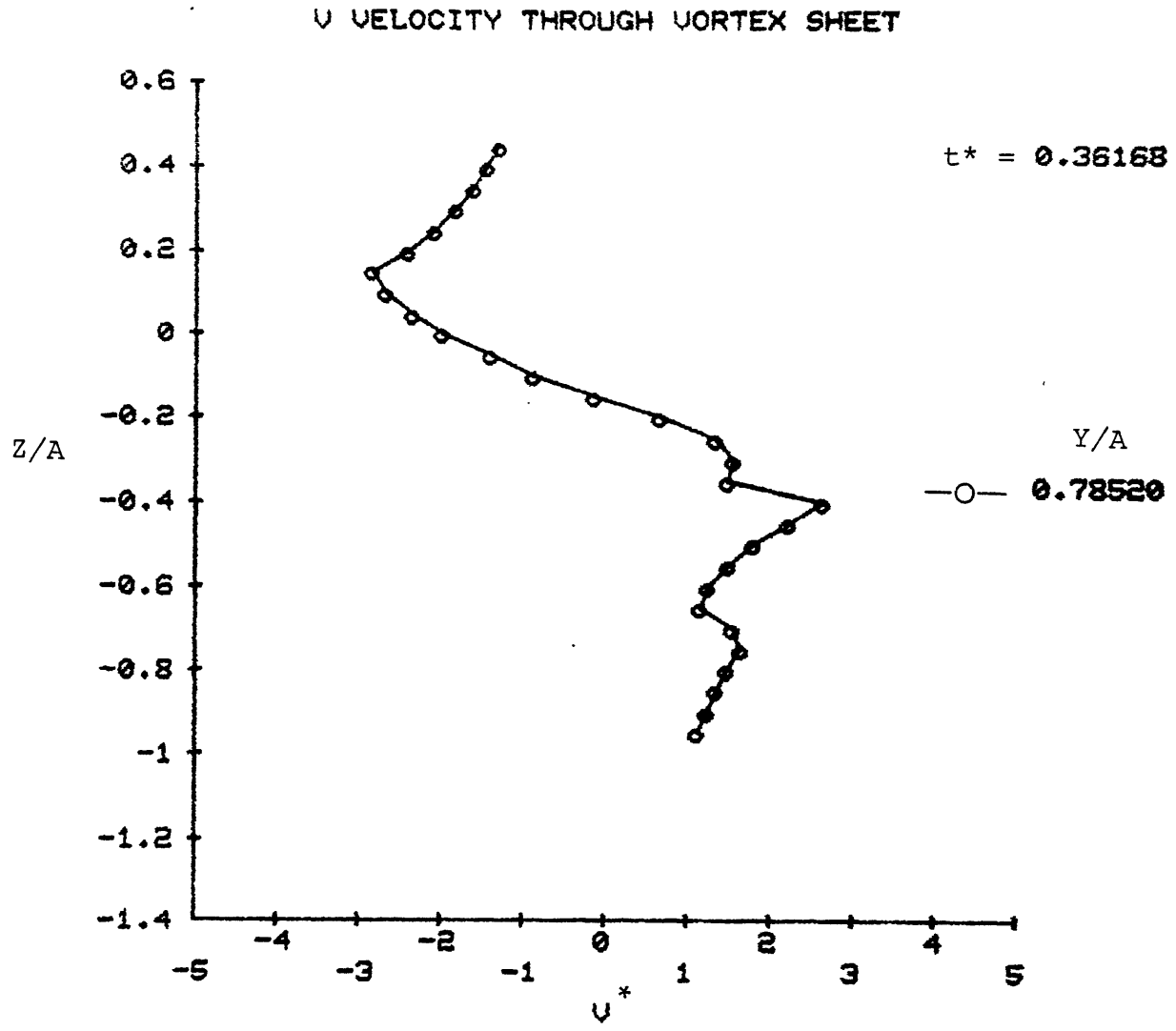

FIGURE 4.3b - ELLIPTICAL LOAD DISTRIBUTION - V VELOCITY PROFILE, CONSTANT STRENGTH POINT VORTICES 120 POINTS, GRID = 31x31, t* = .36168

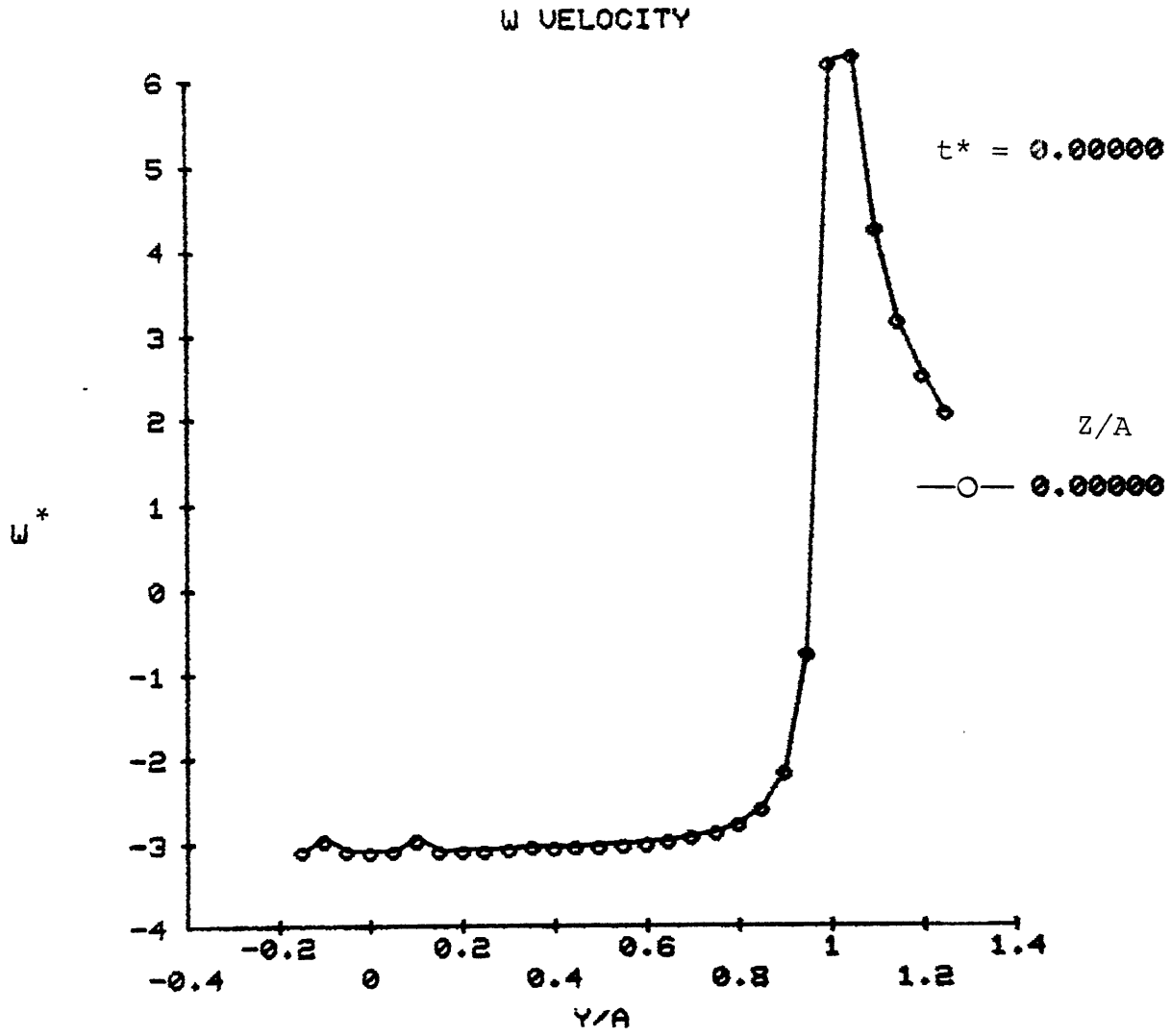

FIGURE 4.4a - ELLIPTICAL LOAD DISTRIBUTION - W VELOCITY PROFILE, CONSTANT STRENGTH POINT VORTICES, 120 POINTS, GRID = 31x31, t* = 0

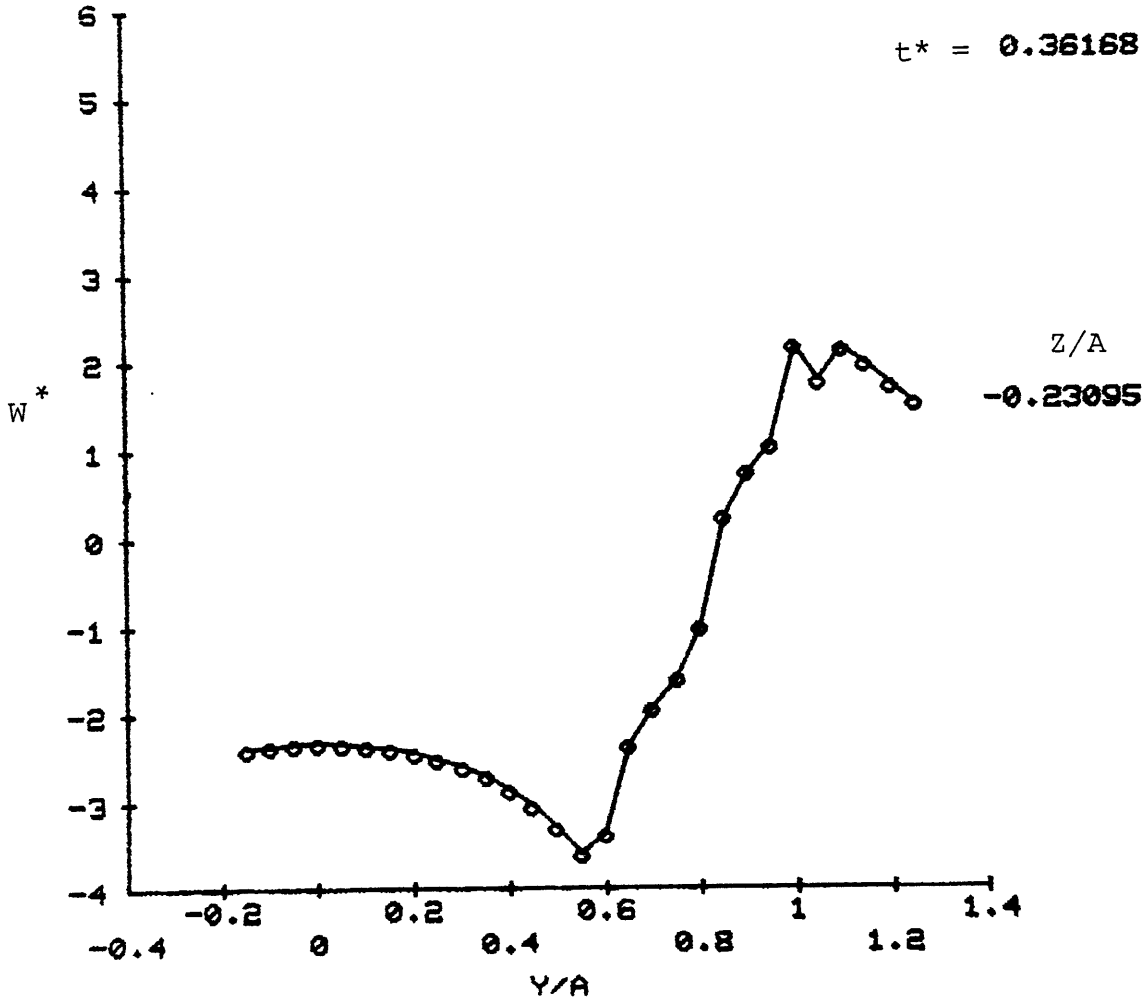

FIGURE 4.4b - ELLIPTICAL LOAD DISTRIBUTION - W VELOCITY PROFILE, CONSTANT STRENGTH POINT VORTICES, 120 POINTS, GRID = 31x31, t* = .36168

VORTEX ROLLUP

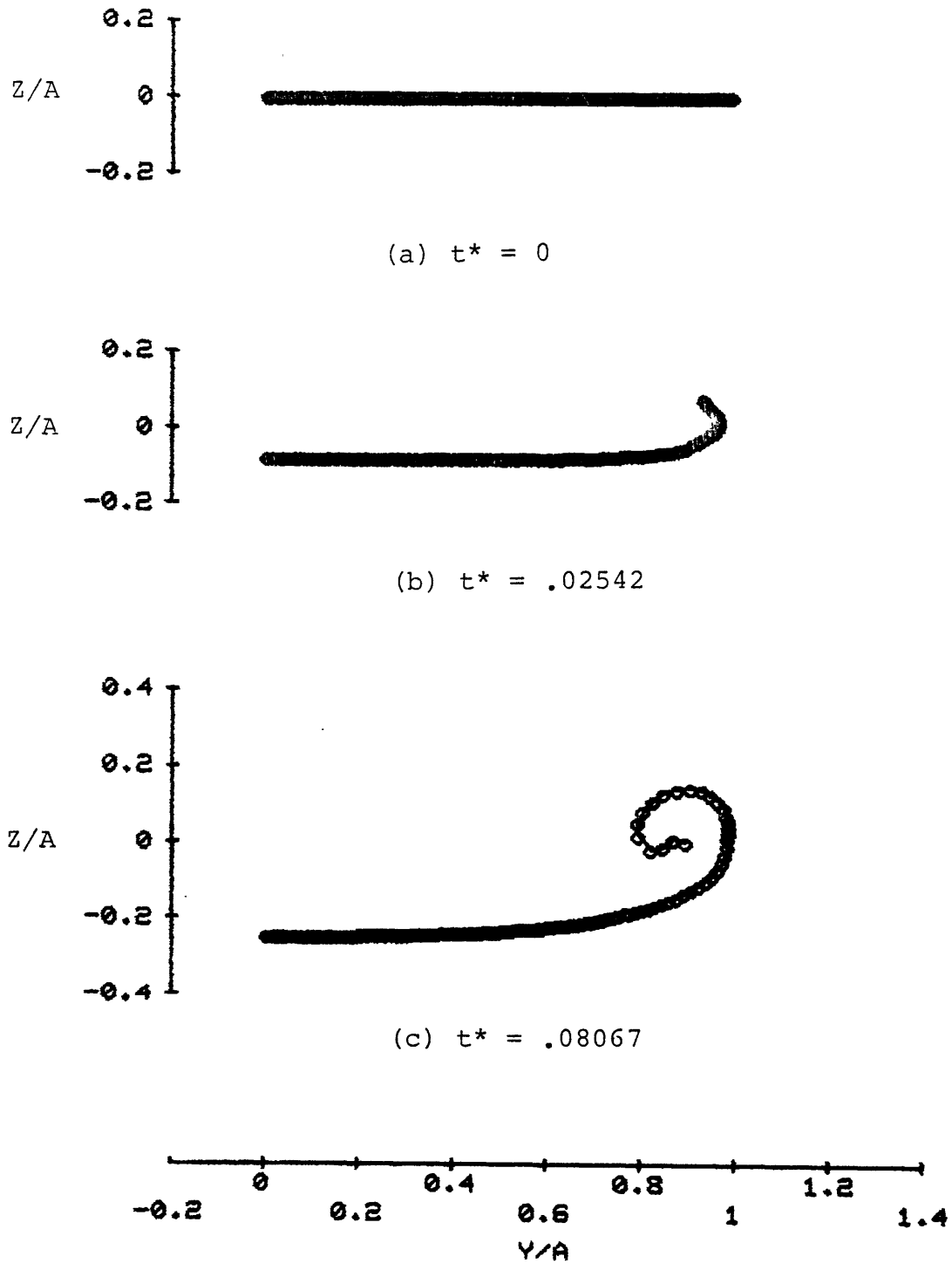

FIGURE 4.5 - ELLIPTICAL LOAD DISTRIBUTION - VORTEX WAKE GEOMETRY, EQUALLY SPACED POINT VORTICES, 120 POINTS, GRID = 31x31

VORTEX ROLLUP

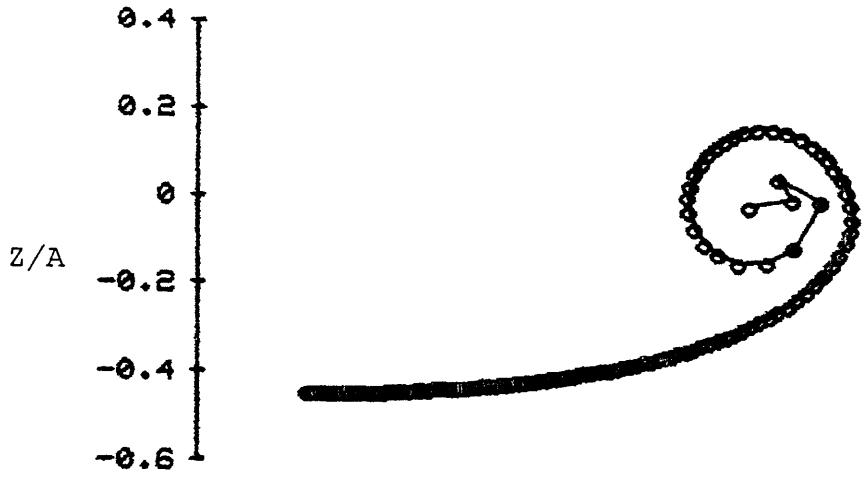

(d) t* = .15537

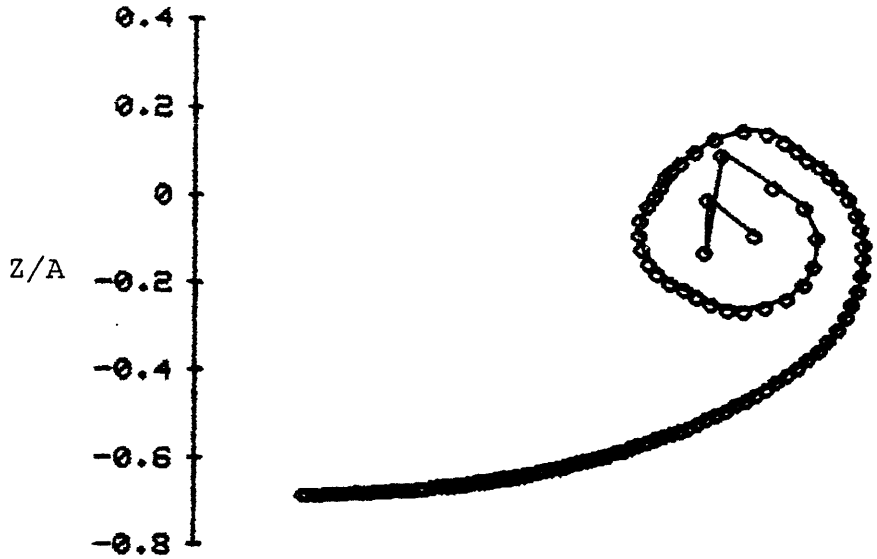

(e) t* = .25381

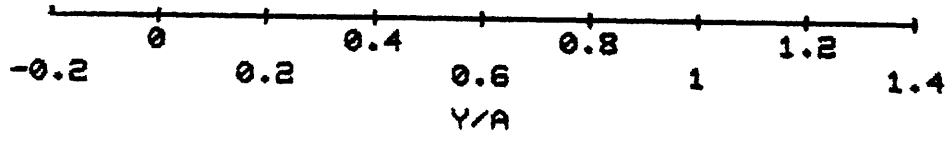

FIGURE 4.5 CONTINUED

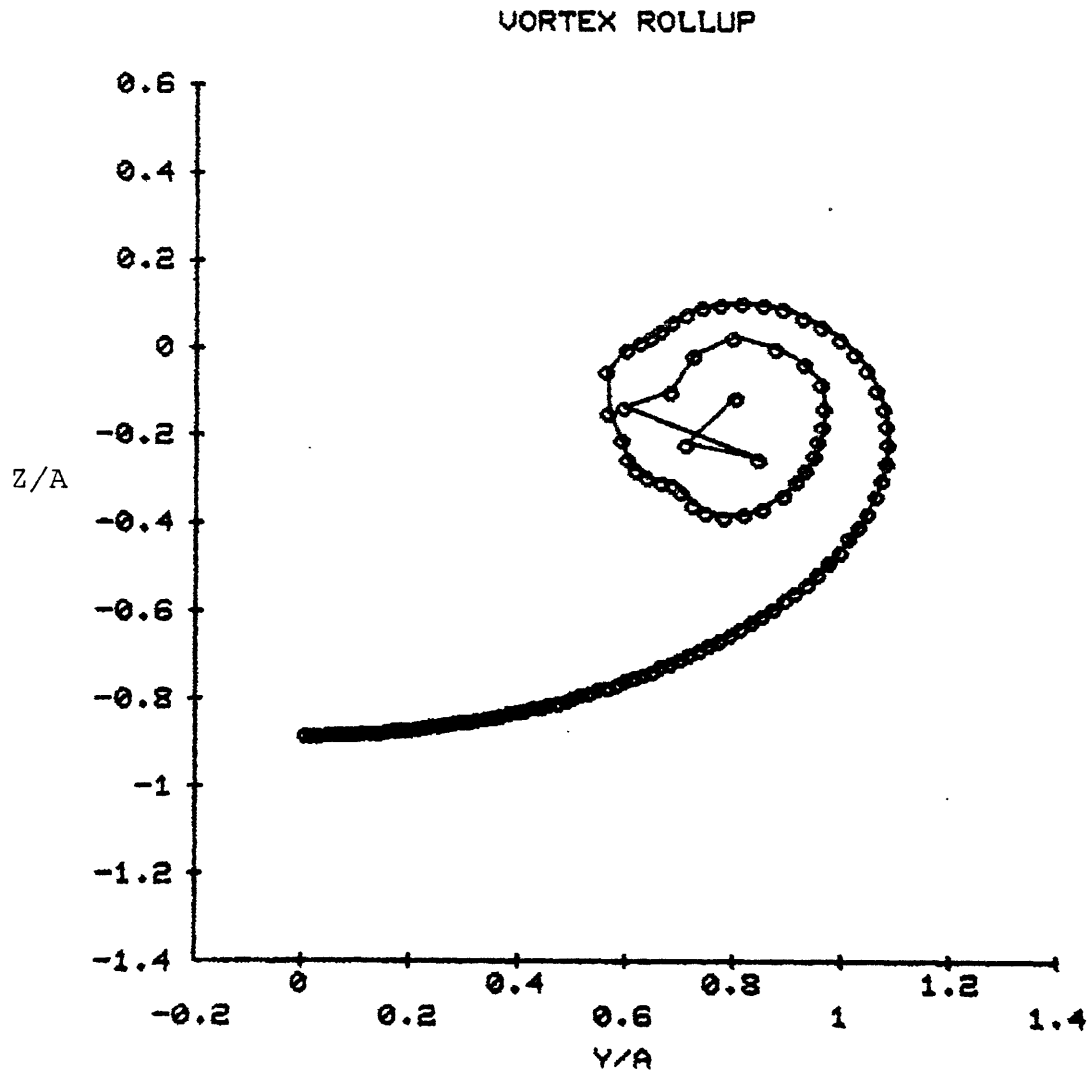

(f) t* = .35863

FIGURE 4.5 CONTINUED

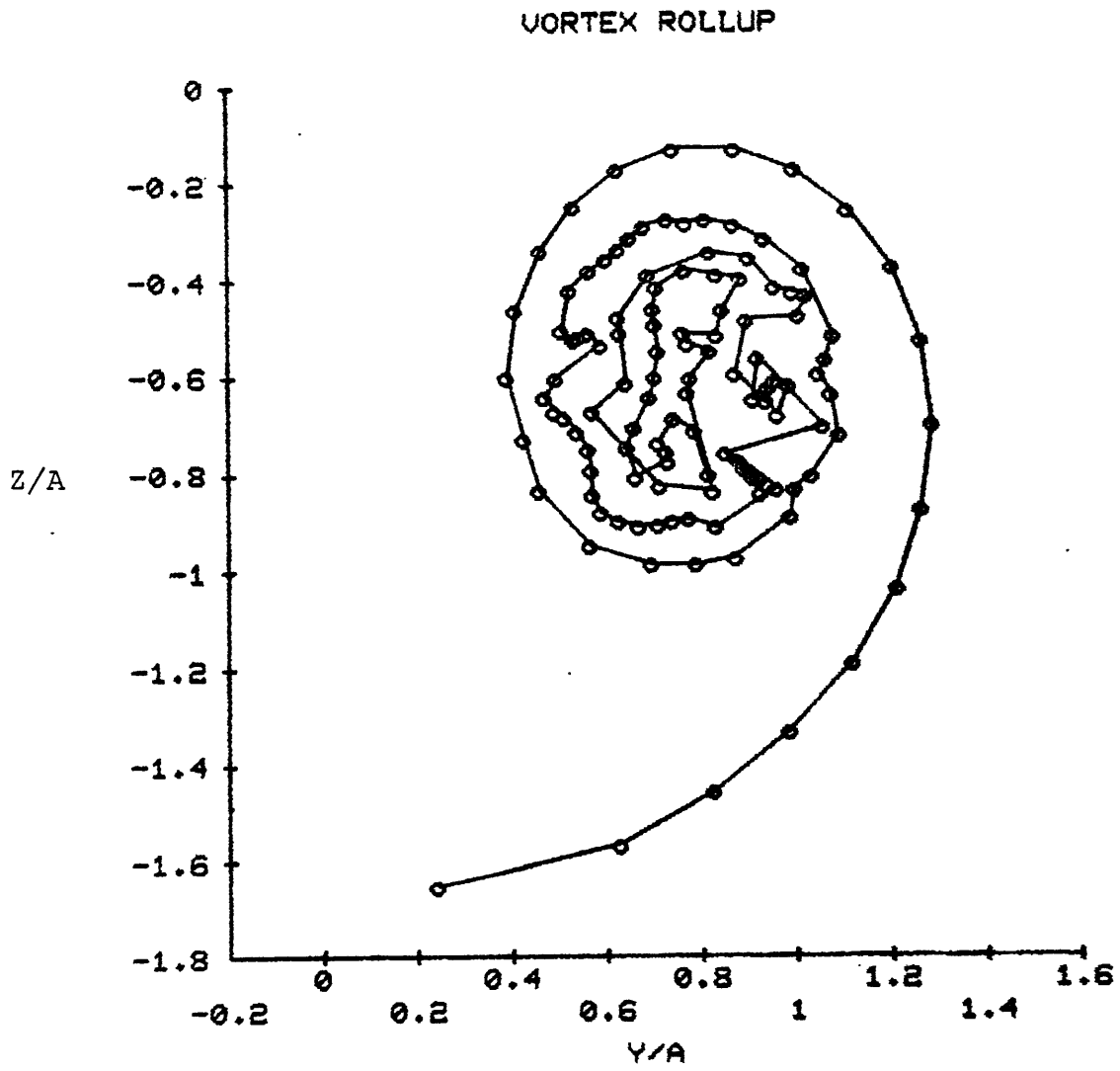

(g) t* = 1.01033

FIGURE 4.5 CONTINUED

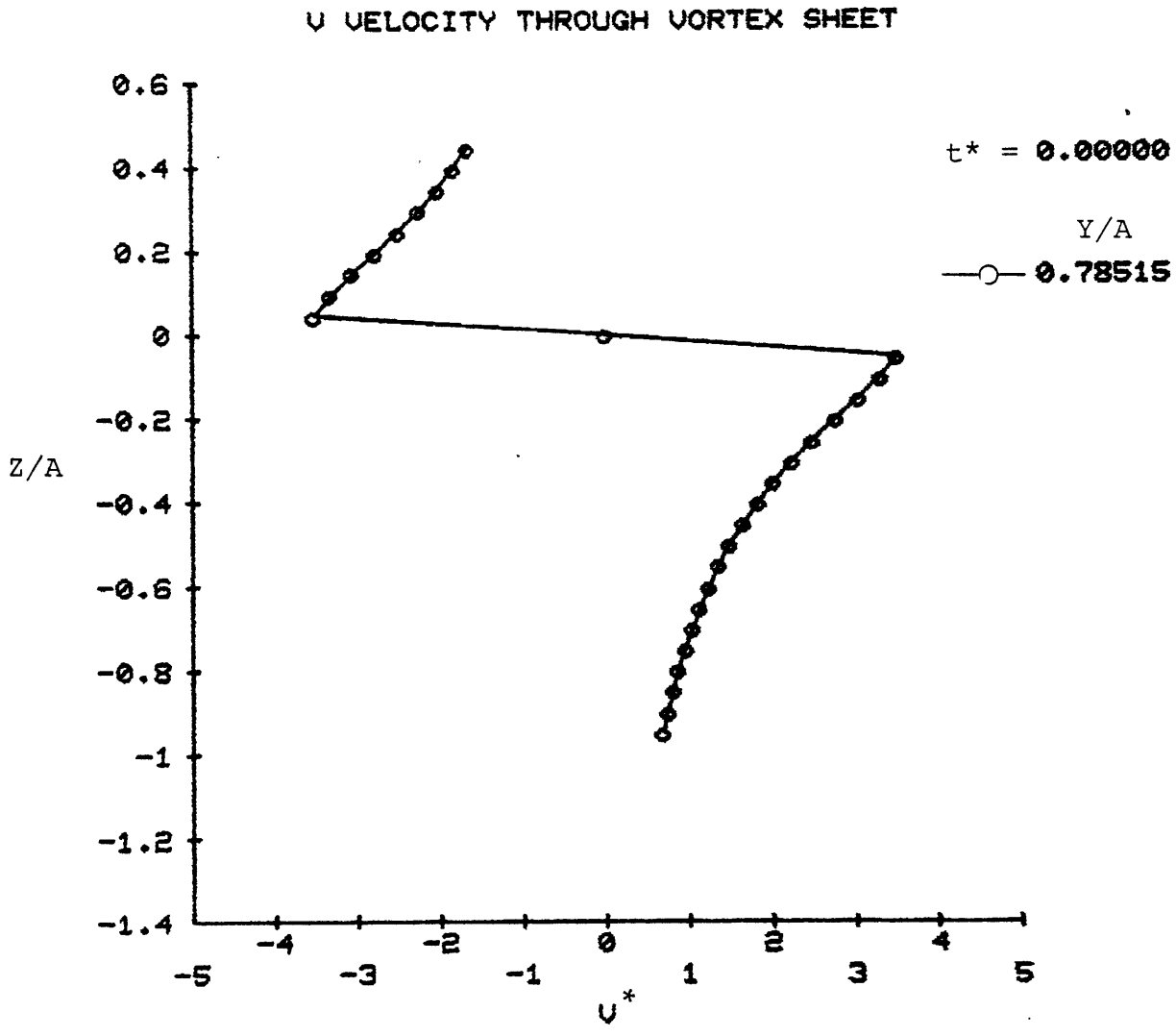

FIGURE 4.6a - ELLIPTICAL LOAD DISTRIBUTION - V VELOCITY PROFILE, EQUALLY SPACED POINT VORTICES, 120 POINTS, GRID = 31x31, t* = 0

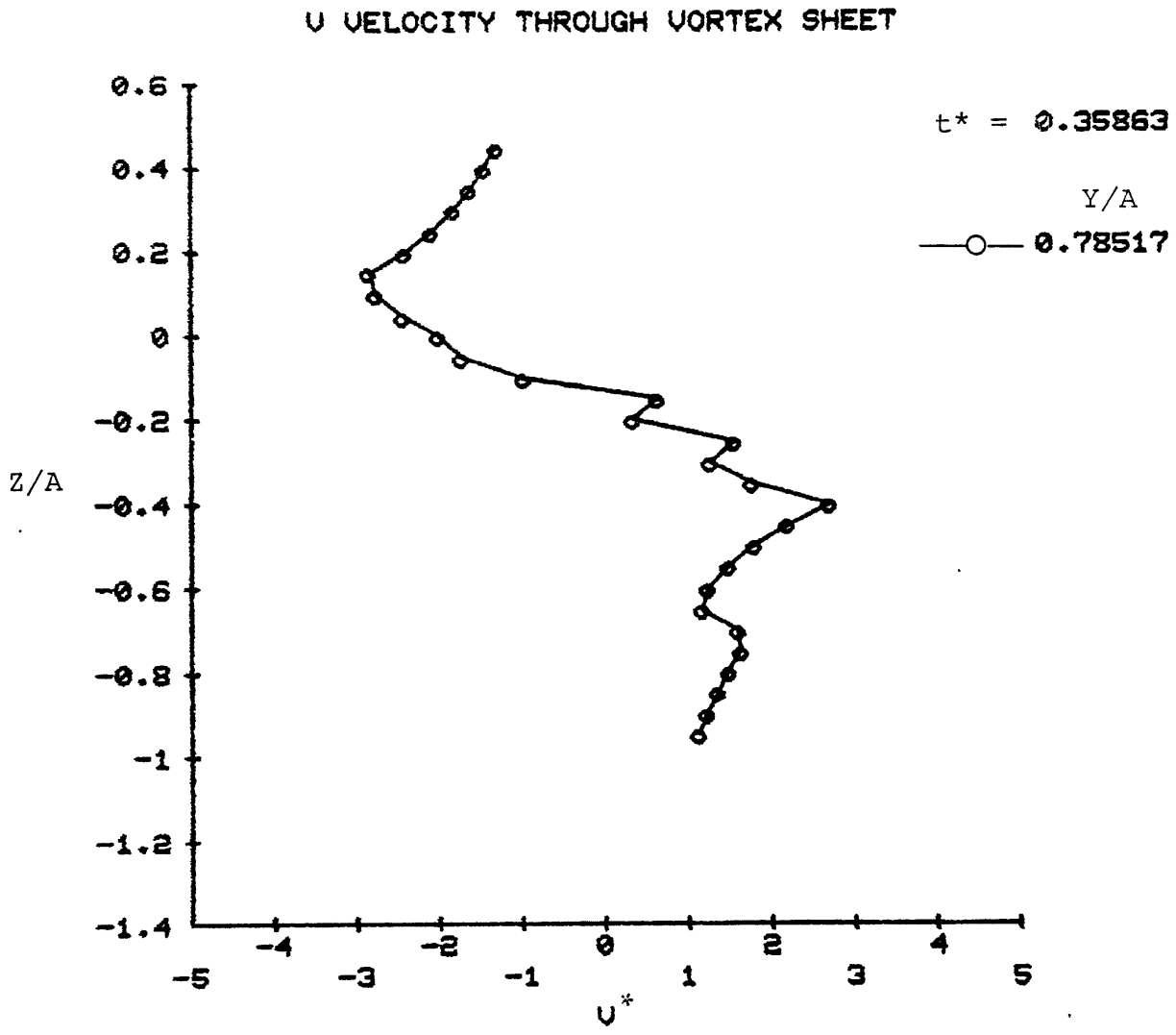

FIGURE 4.6b - ELLIPTICAL LOAD DISTRIBUTION - V VELOCITY PROFILE, EQUALLY SPACED POINT VORTICES, 120 POINTS, GRID = 31x31, t* = .35863

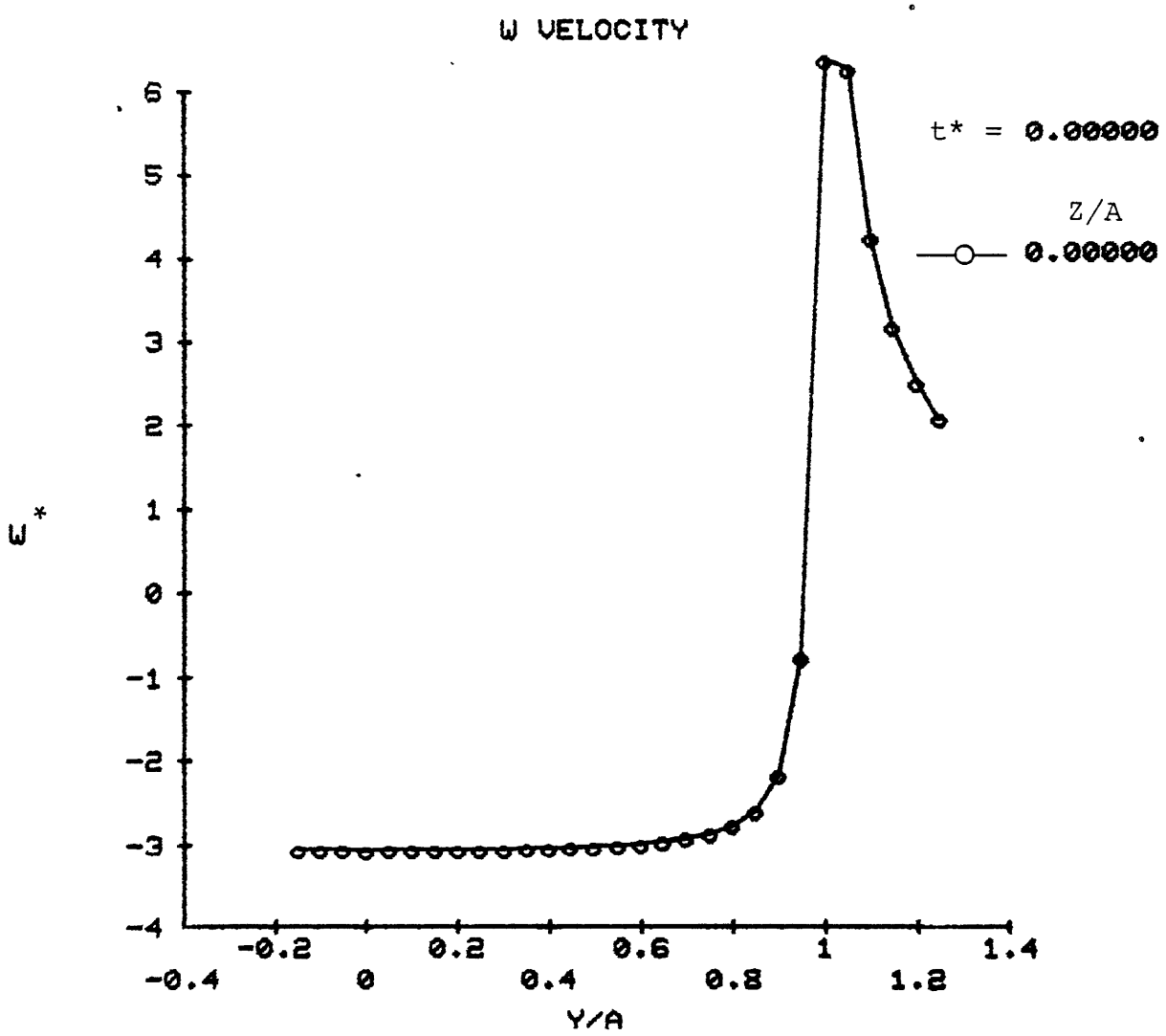

FIGURE 4.7a - ELLIPTICAL LOAD DISTRIBUTION - W VELOCITY PROFILE, EQUALLY SPACED POINT VORTICES, 120 POINTS, GRID = 31x31, t* = 0

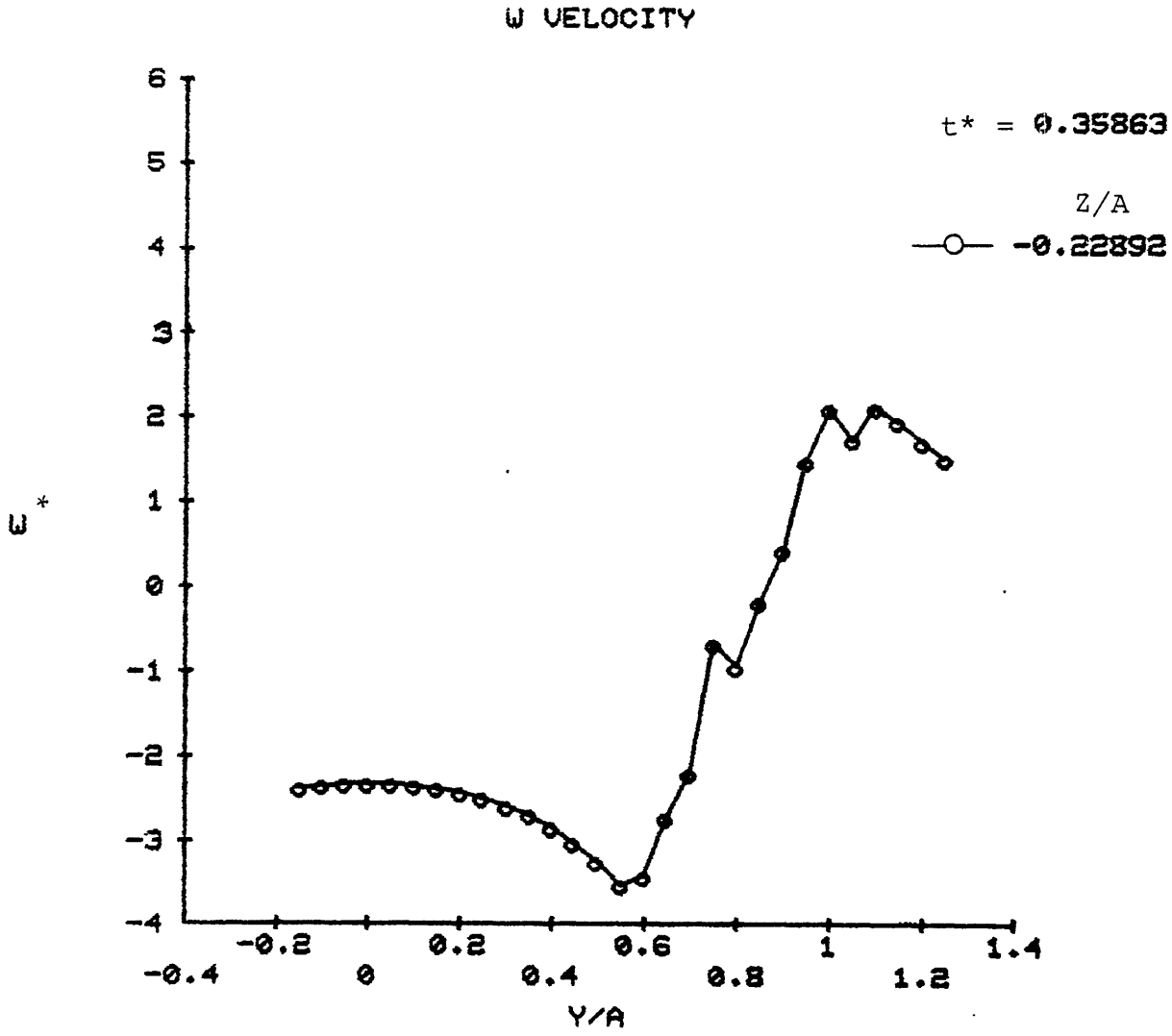

FIGURE 4.7b - ELLIPTICAL LOAD DISTRIBUTION - W VELOCITY PROFILE, EQUALLY SPACED POINT VORTICES, 120 POINTS, GRID = 31x31, t* = .35863

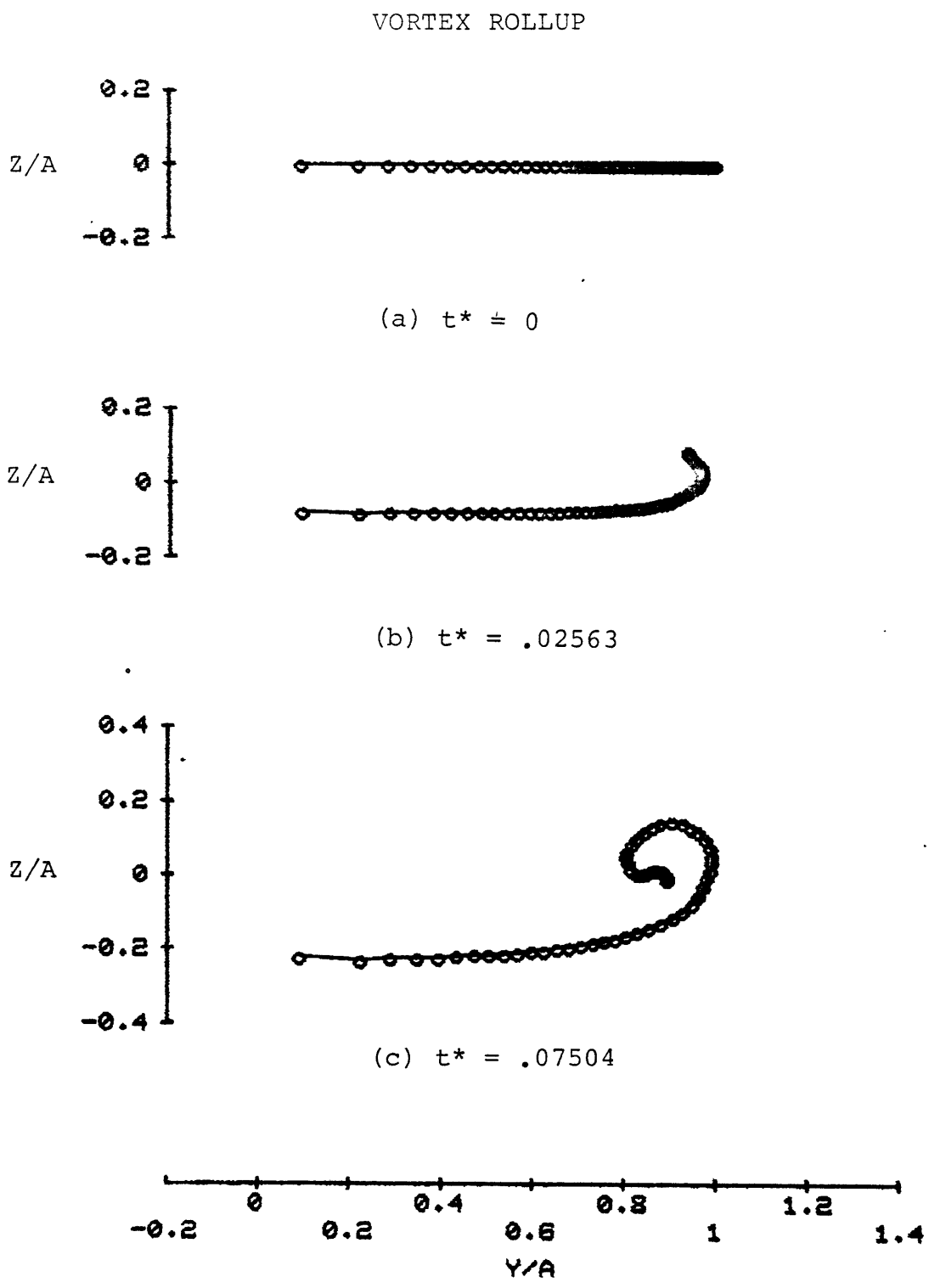

FIGURE 4.8 - ELLIPTICAL LOAD DISTRIBUTION - VORTEX WAKE GEOMETRY, CONSTANT STRENGTH POINT VORTICES, 60 POINTS, GRID = 31x31

VORTEX ROLLUP

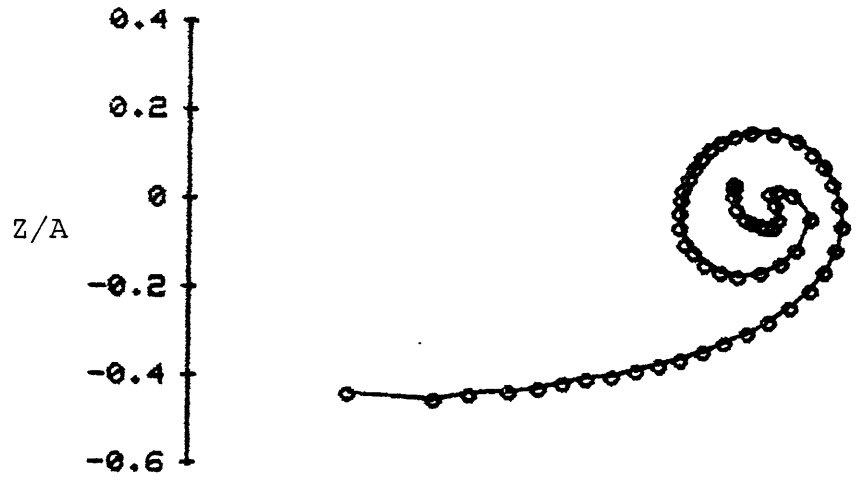

(d) t* = .15714

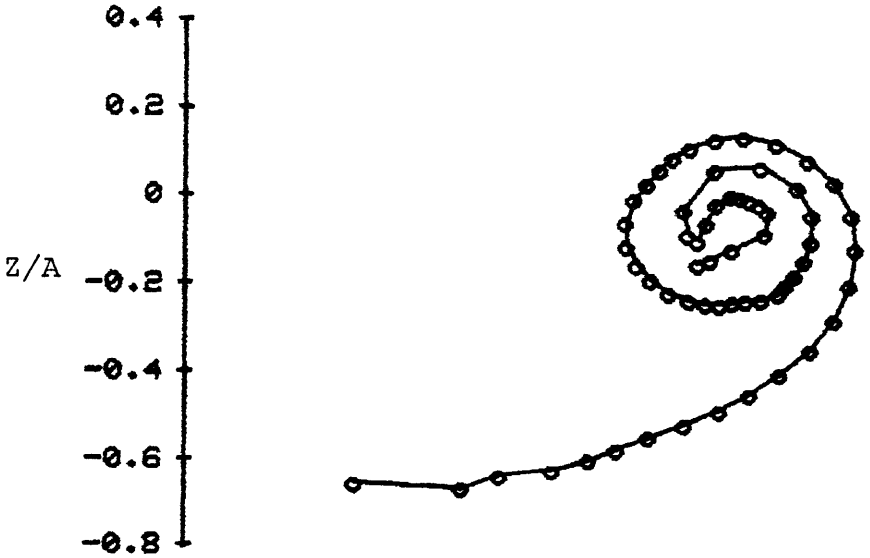

(e) t* = .25539

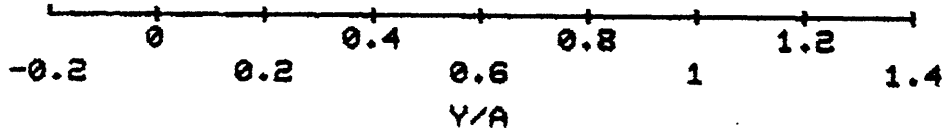

FIGURE 4.8 CONTINUED

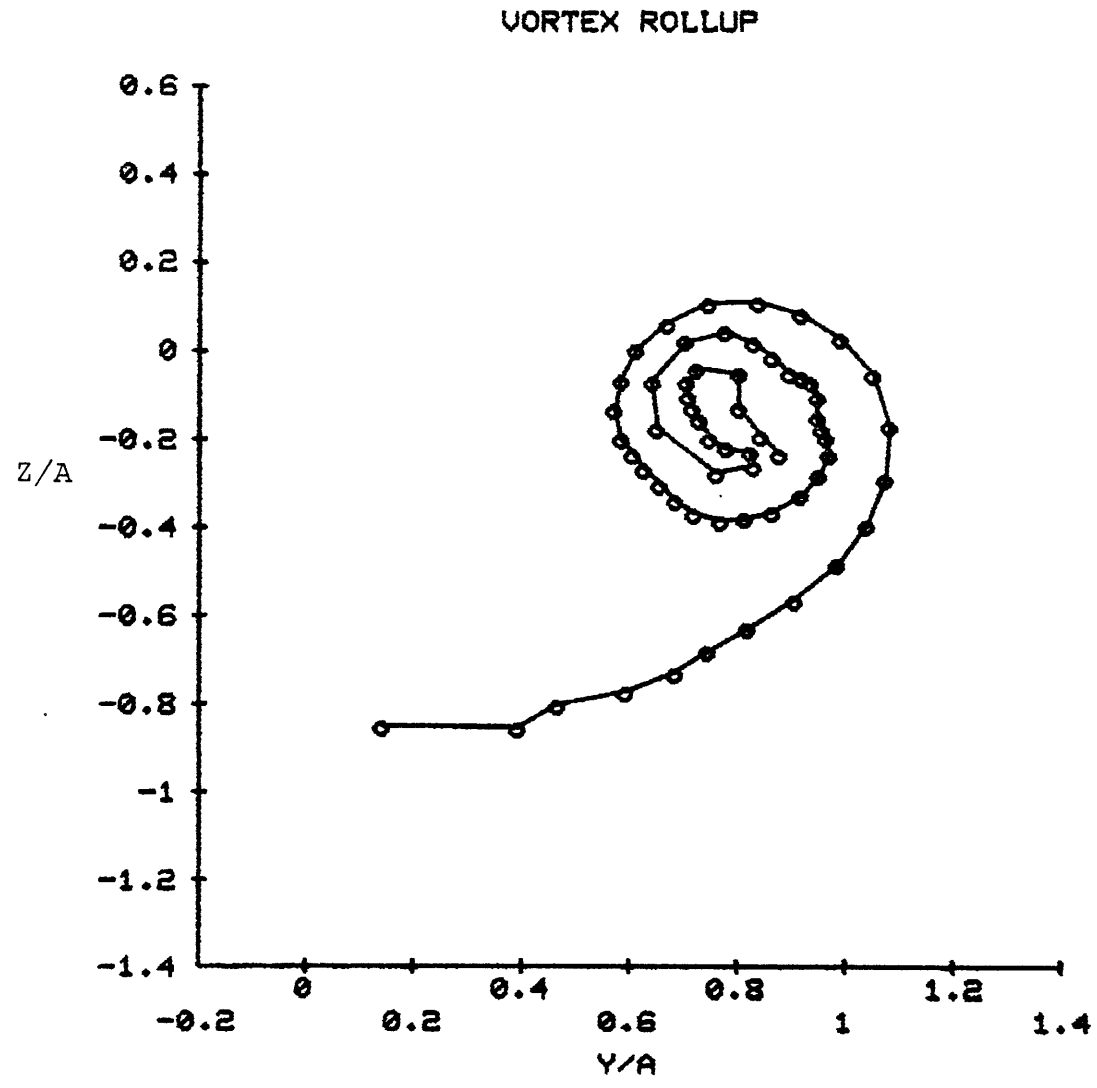

(f) t* = .36155

FIGURE 4.8 CONTINUED

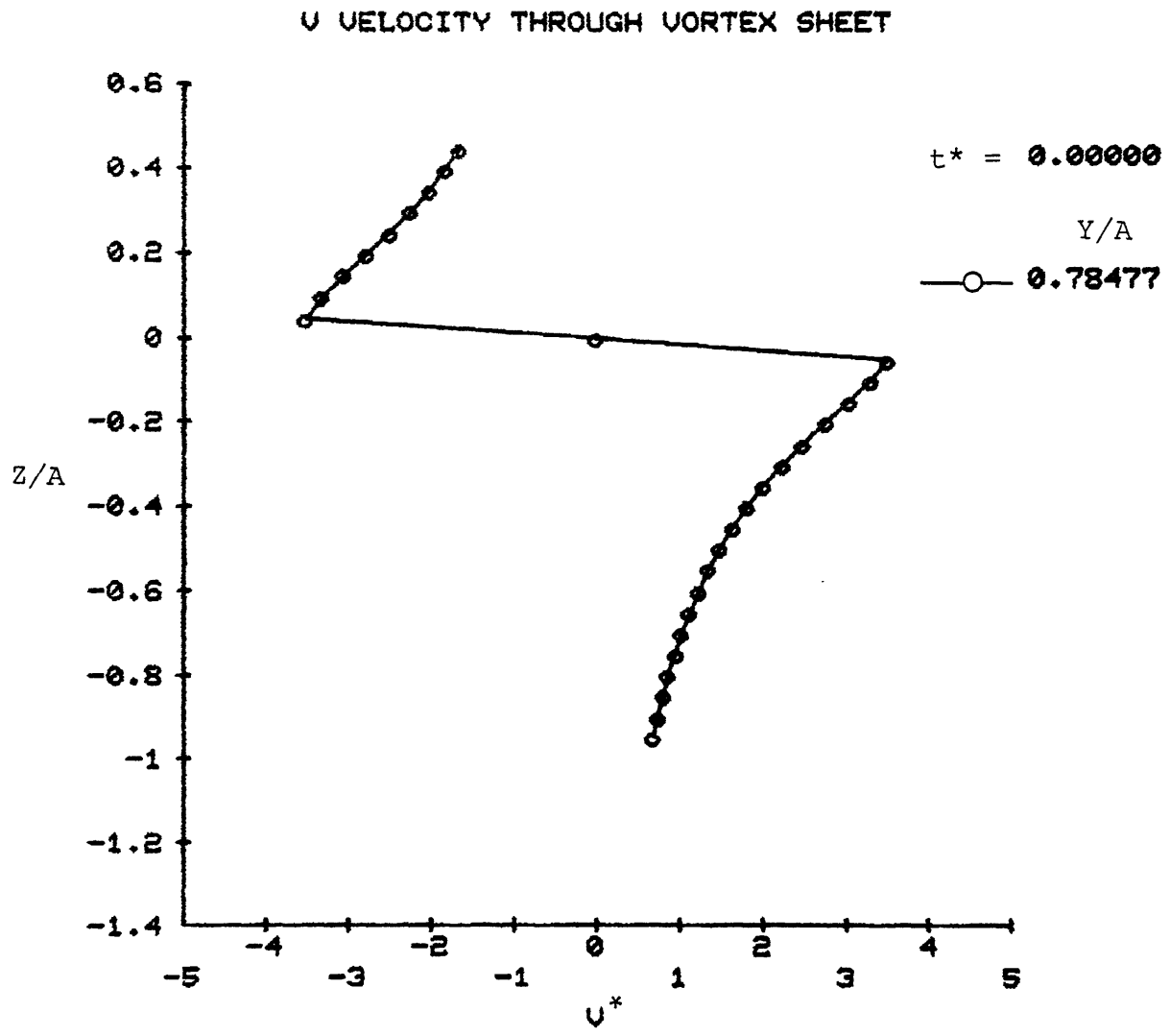

FIGURE 4.9a - ELLIPTICAL LOAD DISTRIBUTION - V VELOCITY PROFILE, CONSTANT STRENGTH POINT VORTICES, 60 POINTS, GRID = 31x31, t* = 0

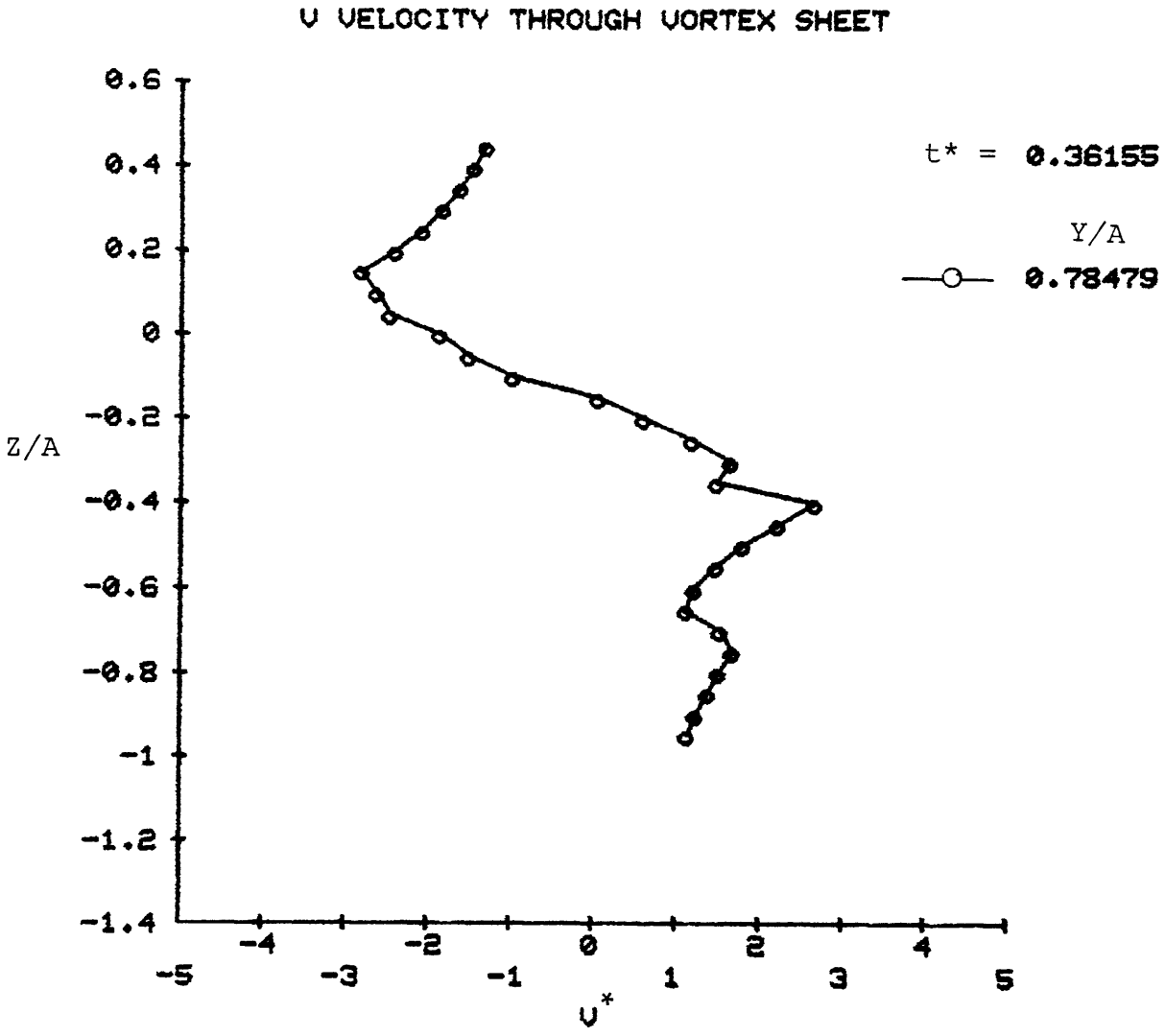

FIGURE 4.9b - ELLIPTICAL LOAD DISTRIBUTION - V VELOCITY PROFILE, CONSTANT STRENGTH POINT VORTICES, 60 POINTS, GRID = 31x31, t* = .36155

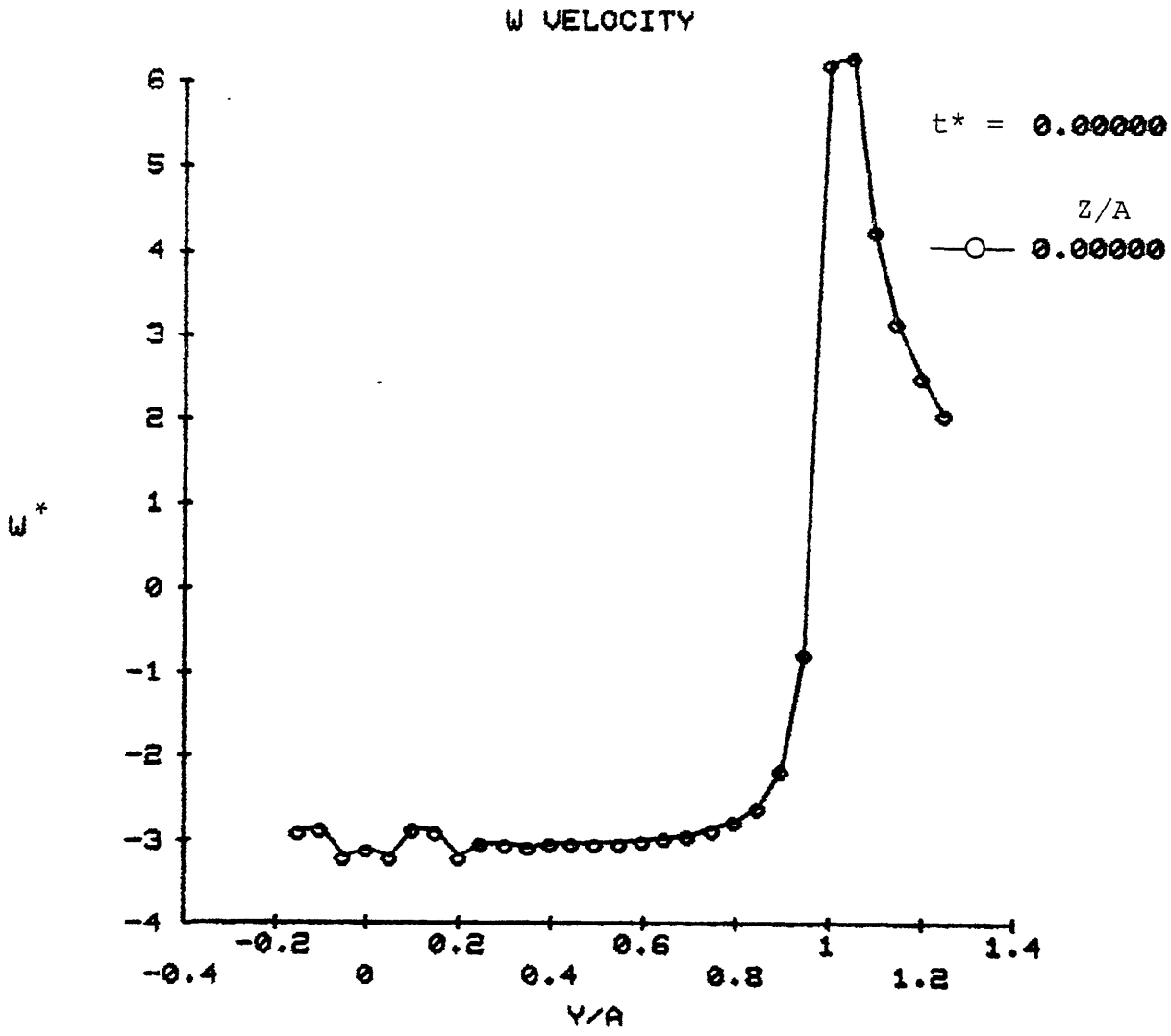

FIGURE 4.10a - ELLIPTICAL LOAD DISTRIBUTION - W VELOCITY PROFILE, CONSTANT STRENGTH POINT VORTICES, 60 POINTS, GRID = 31x31, t* = 0

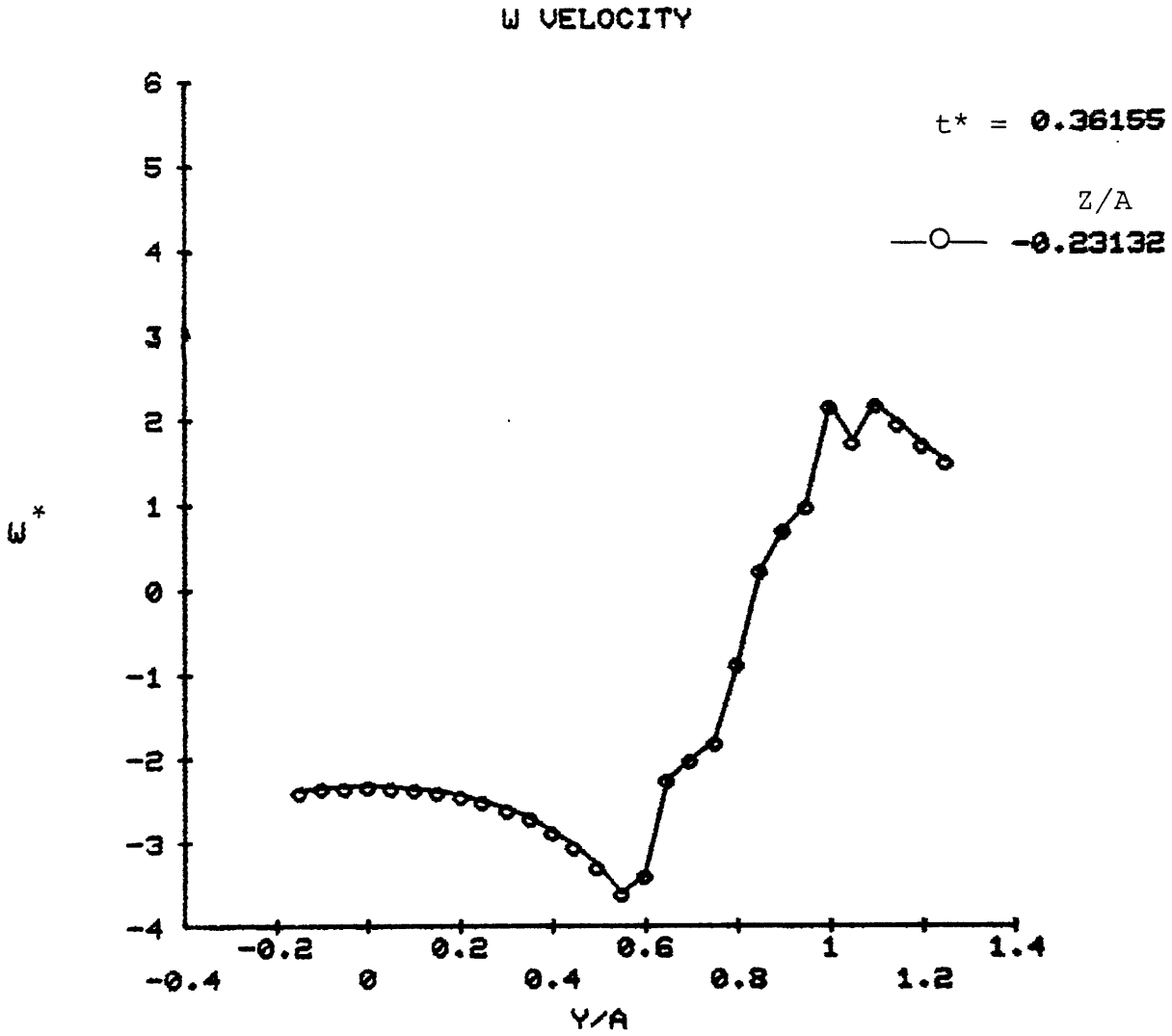

FIGURE 4.10b - ELLIPTICAL LOAD DISTRIBUTION - W VELOCITY PROFILE, CONSTANT STRENGTH POINT VORTICES, 60 POINTS, GRID = 31x31, t* = .36155

VORTEX ROLLUP

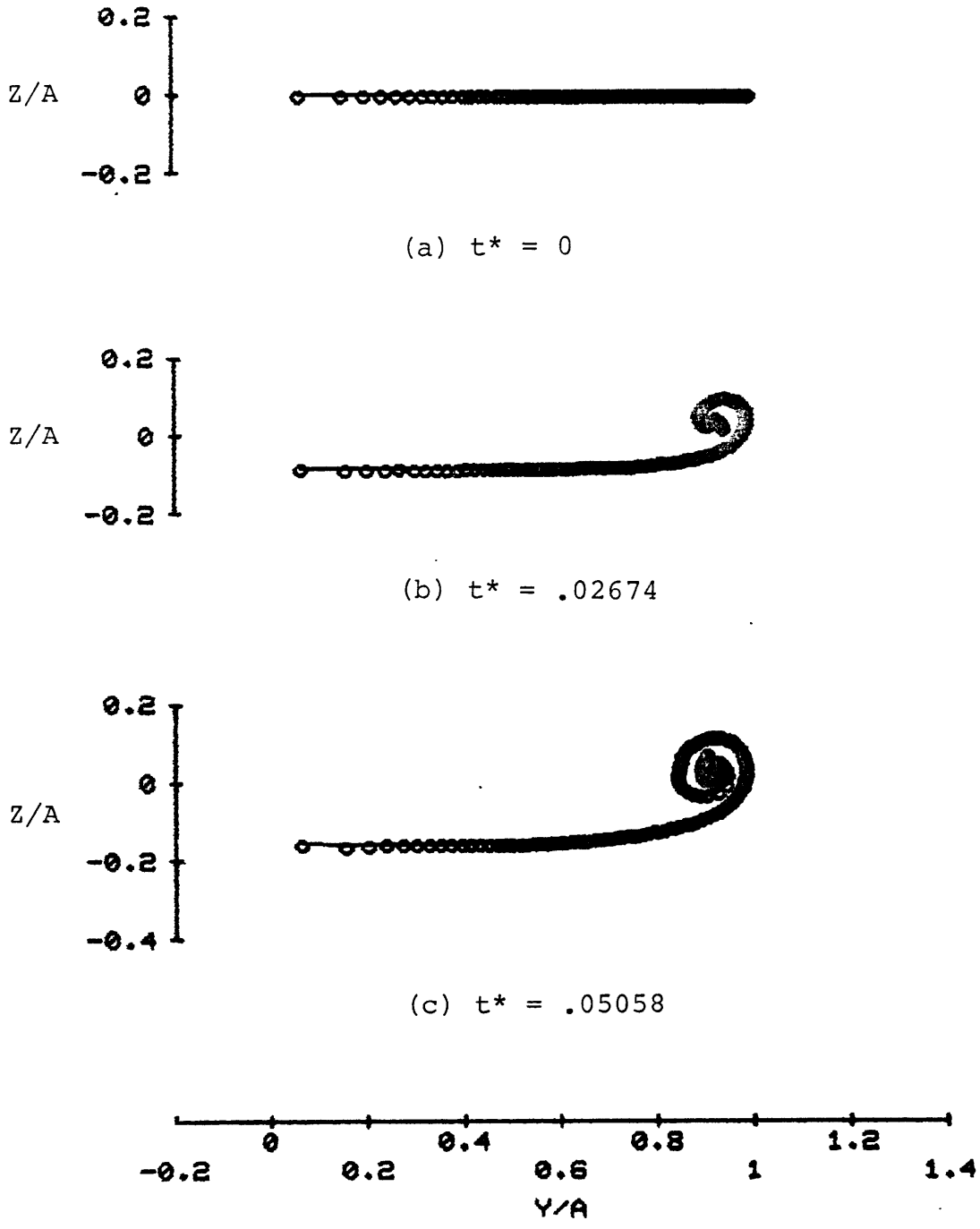

FIGURE 4.11 - ELLIPTICAL LOAD DISTRIBUTION - VORTEX WAKE GEOMETRY, CONSTANT STRENGTH POINT VORTICES, 120 POINTS, GRID = 61x61

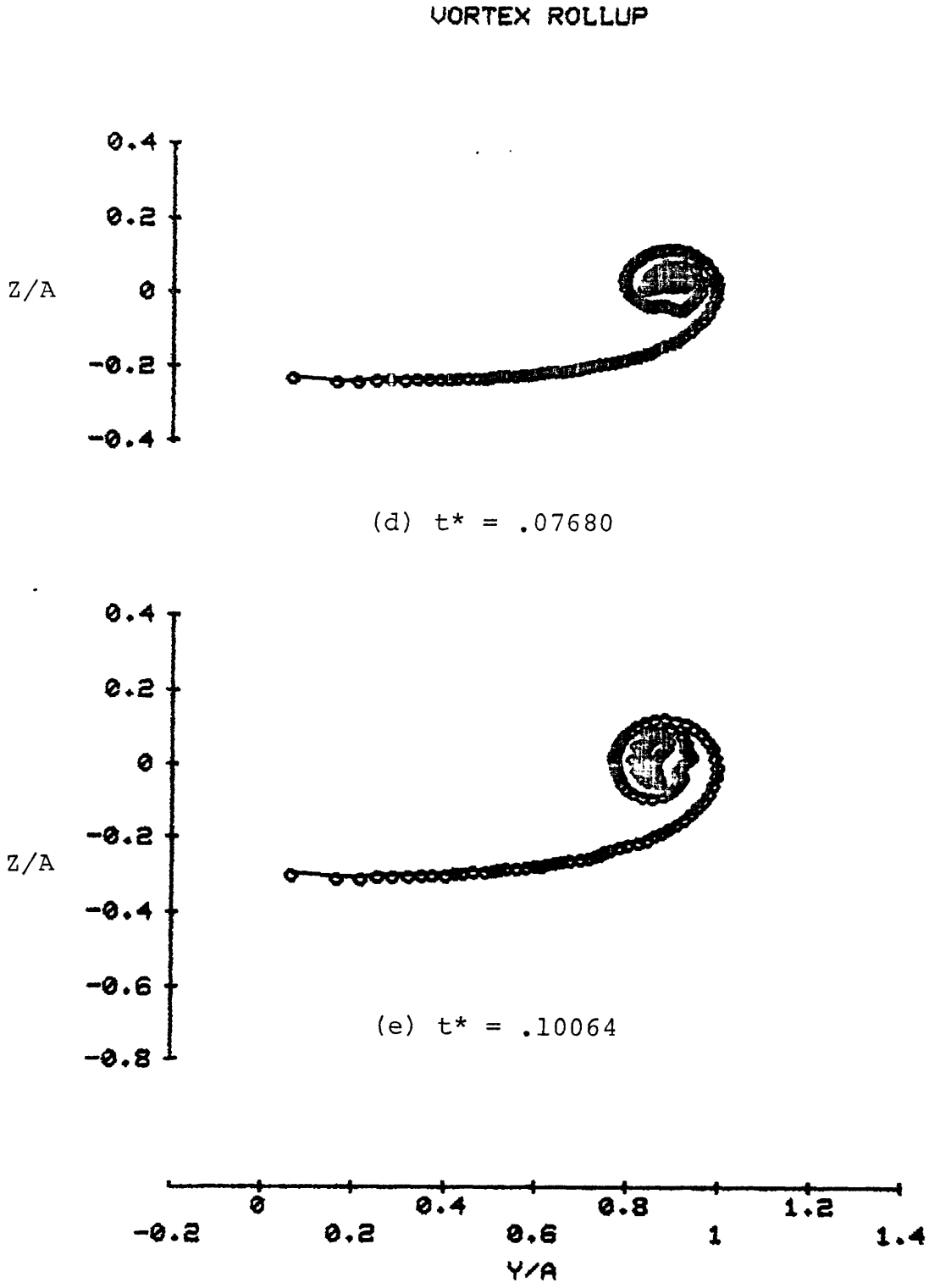

FIGURE 4.11 CONTINUED

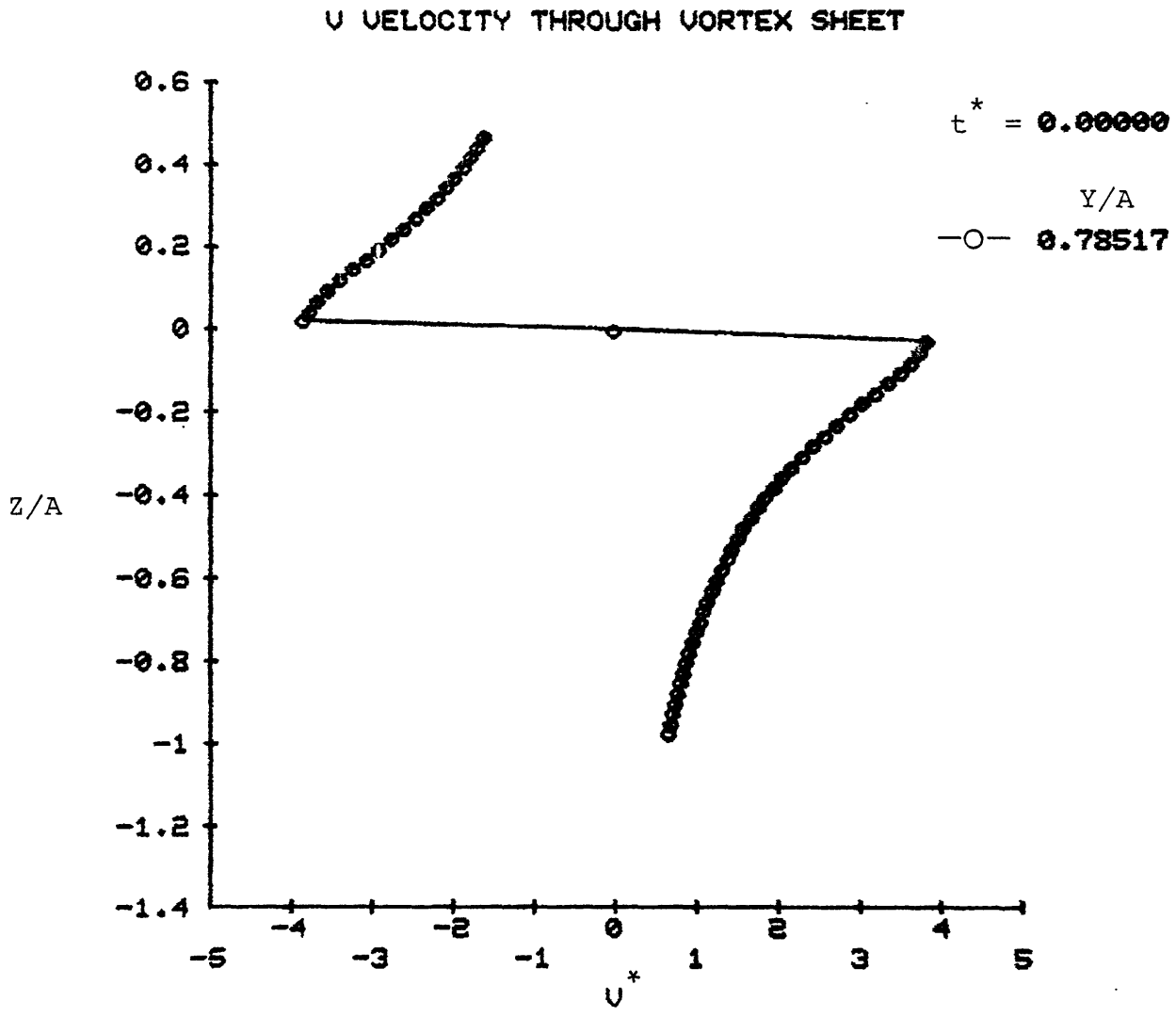

FIGURE 4.12a - ELLIPTICAL LOAD DISTRIBUTION - V VELOCITY PROFILE, CONSTANT STRENGTH POINT VORTICES, 120 POINTS, GRID = 61x61, t* = 0

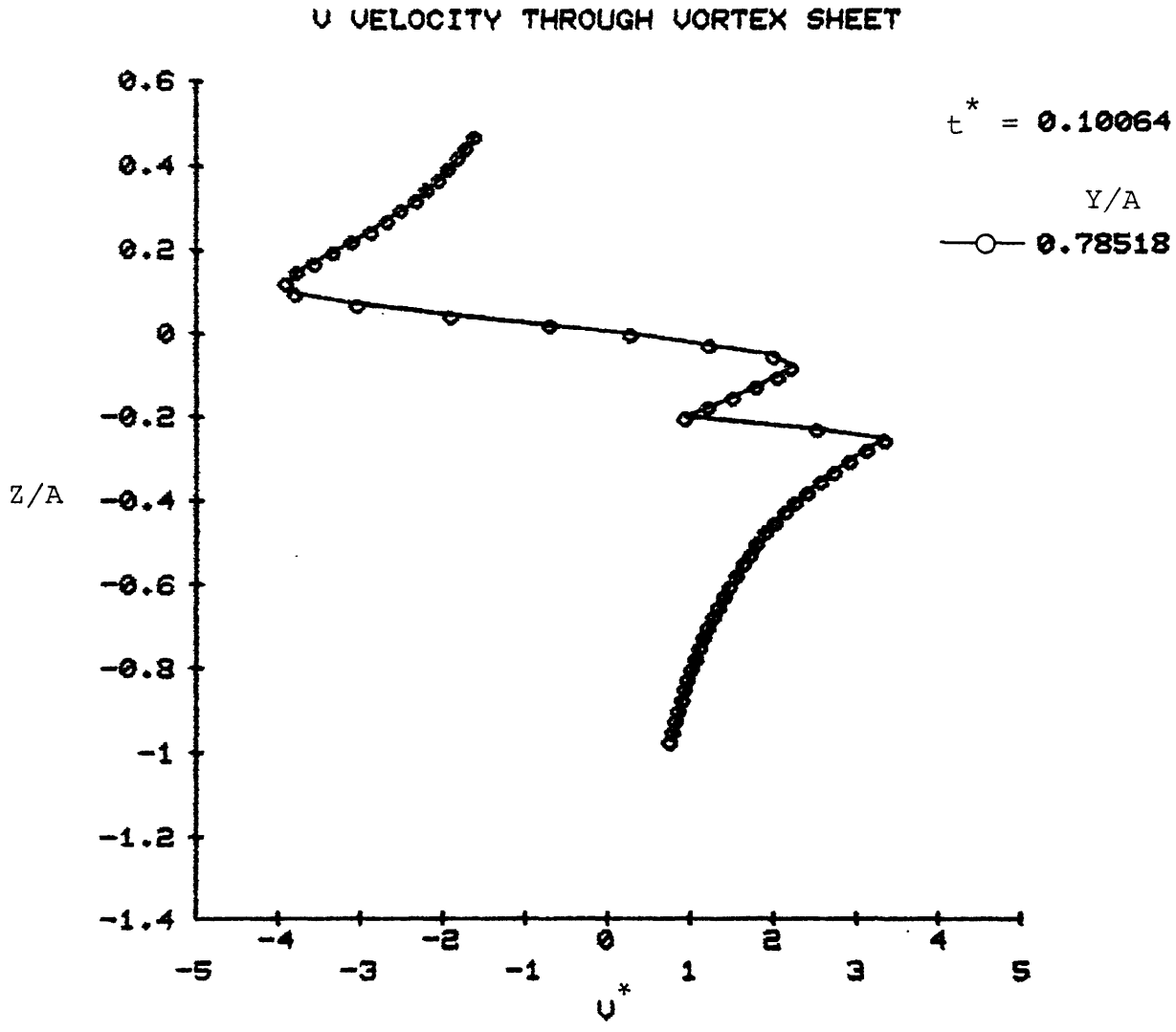

FIGURE 4.12b - ELLIPTICAL LOAD DISTRIBUTION - V VELOCITY PROFILE, CONSTANT STRENGTH POINT VORTICES, 120 POINTS, GRID = 61x61, t* = .10064

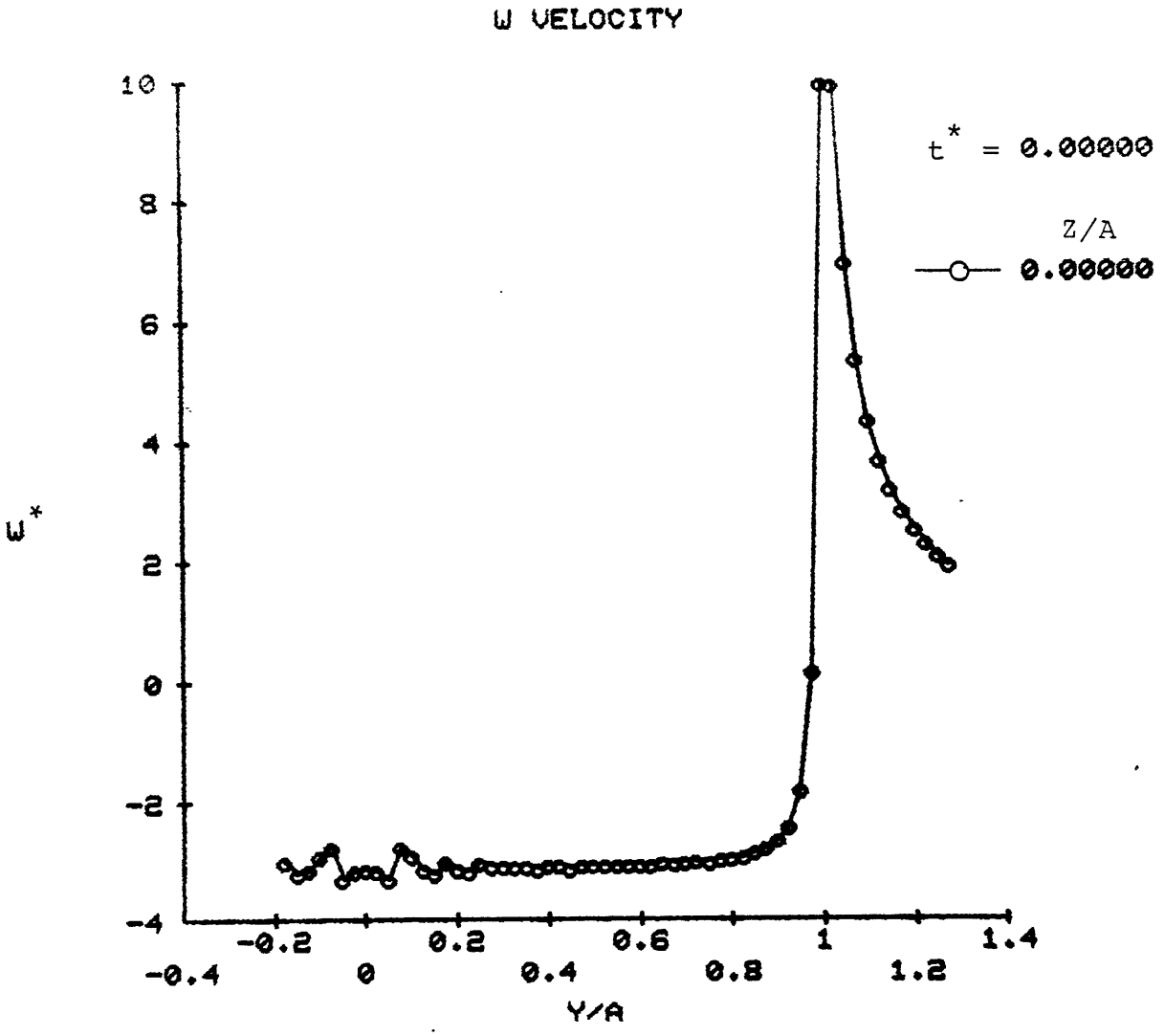

FIGURE 4.13a - ELLIPTICAL LOAD DISTRIBUTION - W VELOCITY PROFILE, CONSTANT STRENGTH POINT VORTICES, 120 POINTS, GRID = 61x61, t* = 0

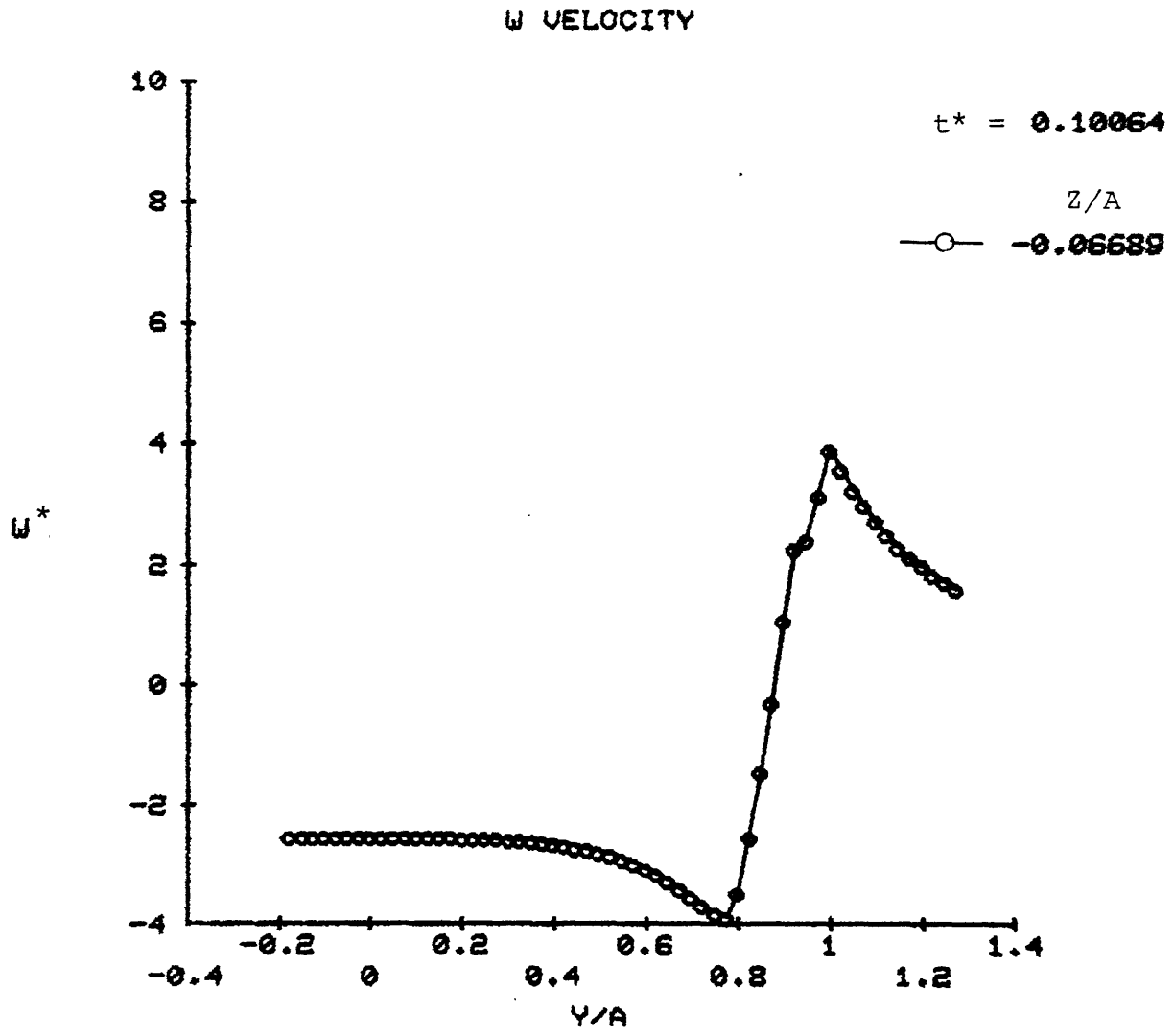

FIGURE 4.13b - ELLIPTICAL LOAD DISTRIBUTION - W VELOCITY PROFILE, CONSTANT STRENGTH POINT VORTICES, 120 POINTS, GRID = 61x61, t* = .10064

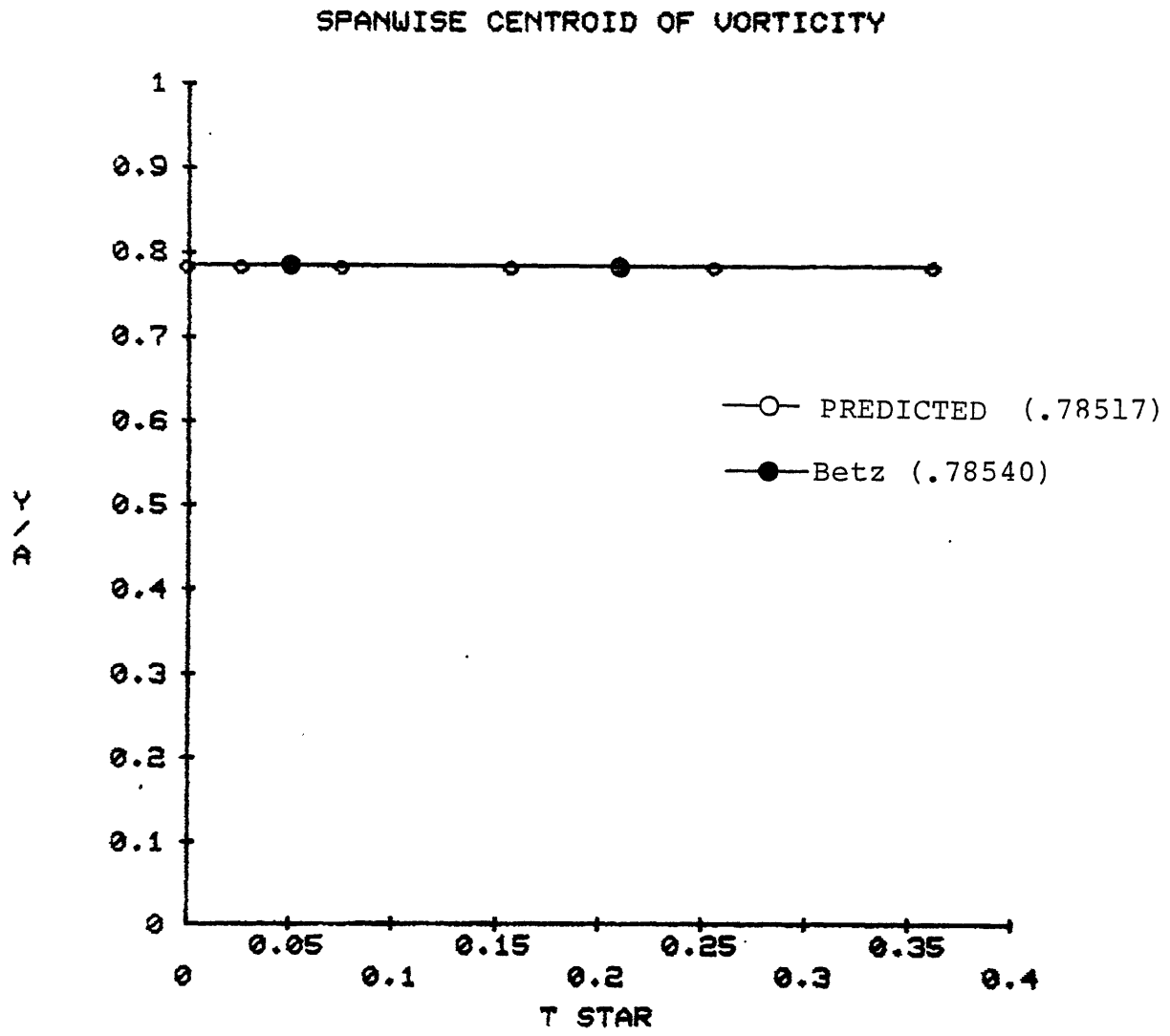

FIGURE 4.14 - ELLIPTICAL LOAD DISTRIBUTION - SPANWISE VARIATION OF VORTEX CENTROID WITH TIME

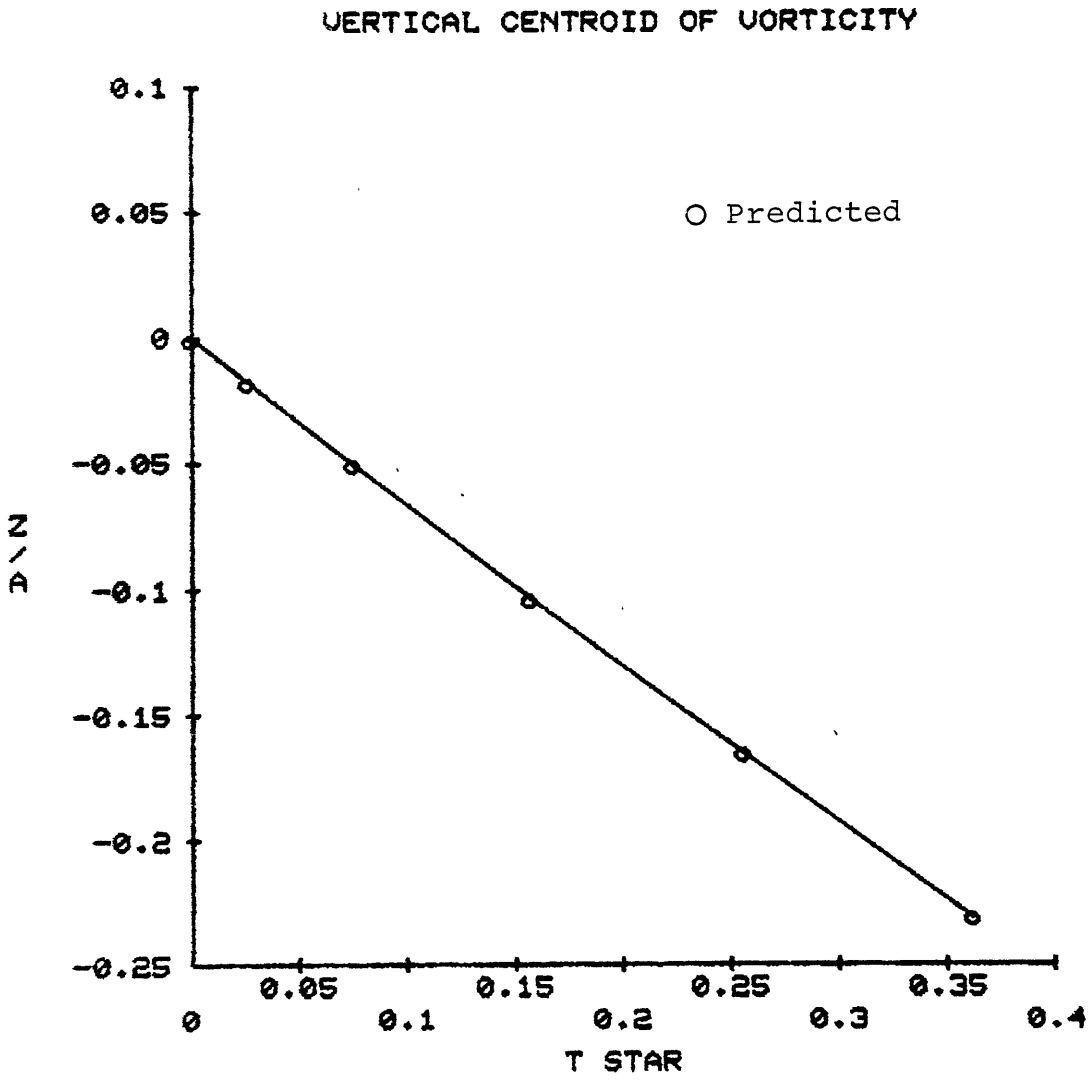

FIGURE 4.15 - ELLIPTICAL LOAD DISTRIBUTION - VERTICAL VARIATION OF VORTEX CENTROID WITH TIME

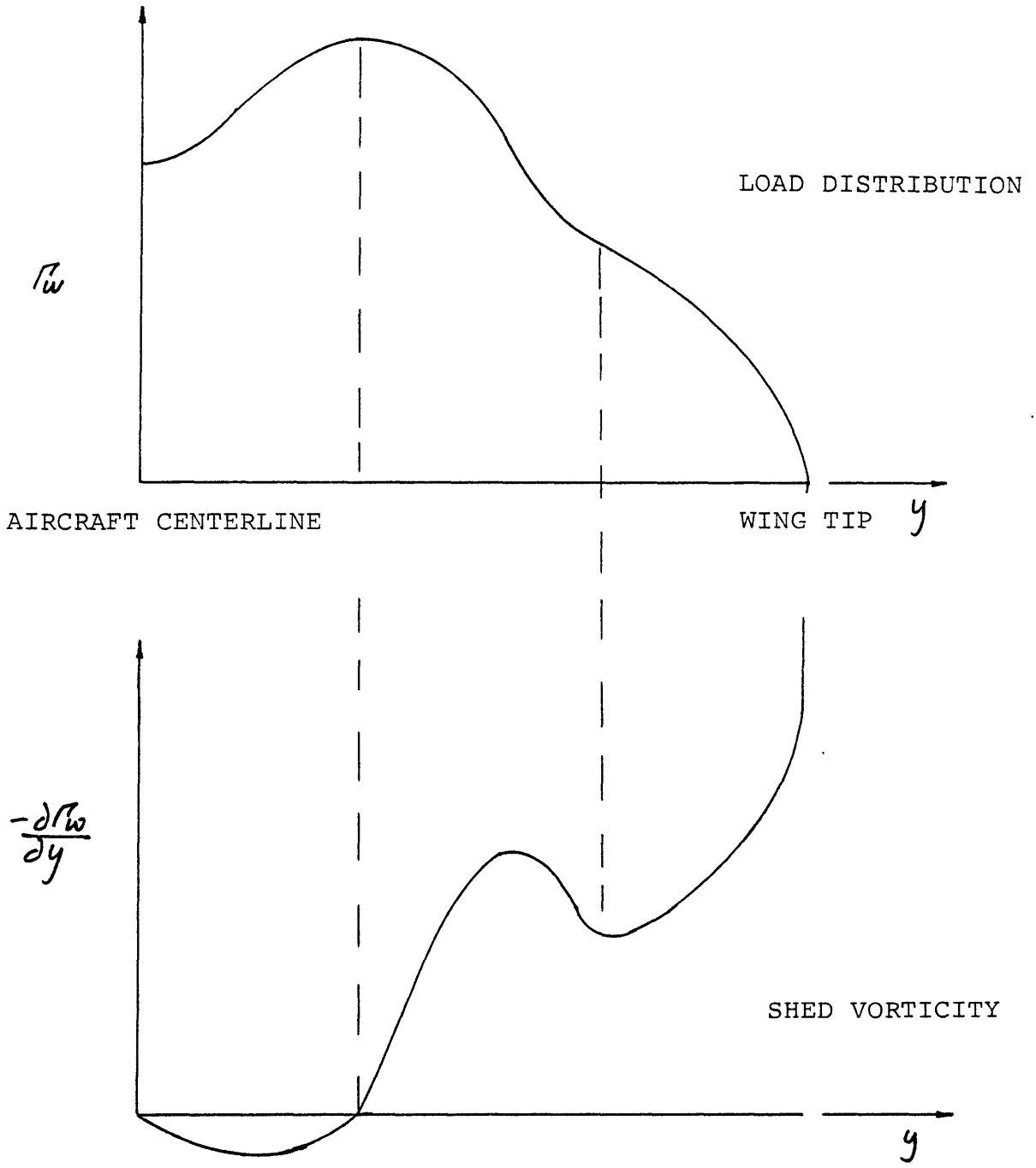

FIGURE 4.16 - WING LOADING AND SHED WAKE STRENGTH - SIMULATED FLAP LOADING

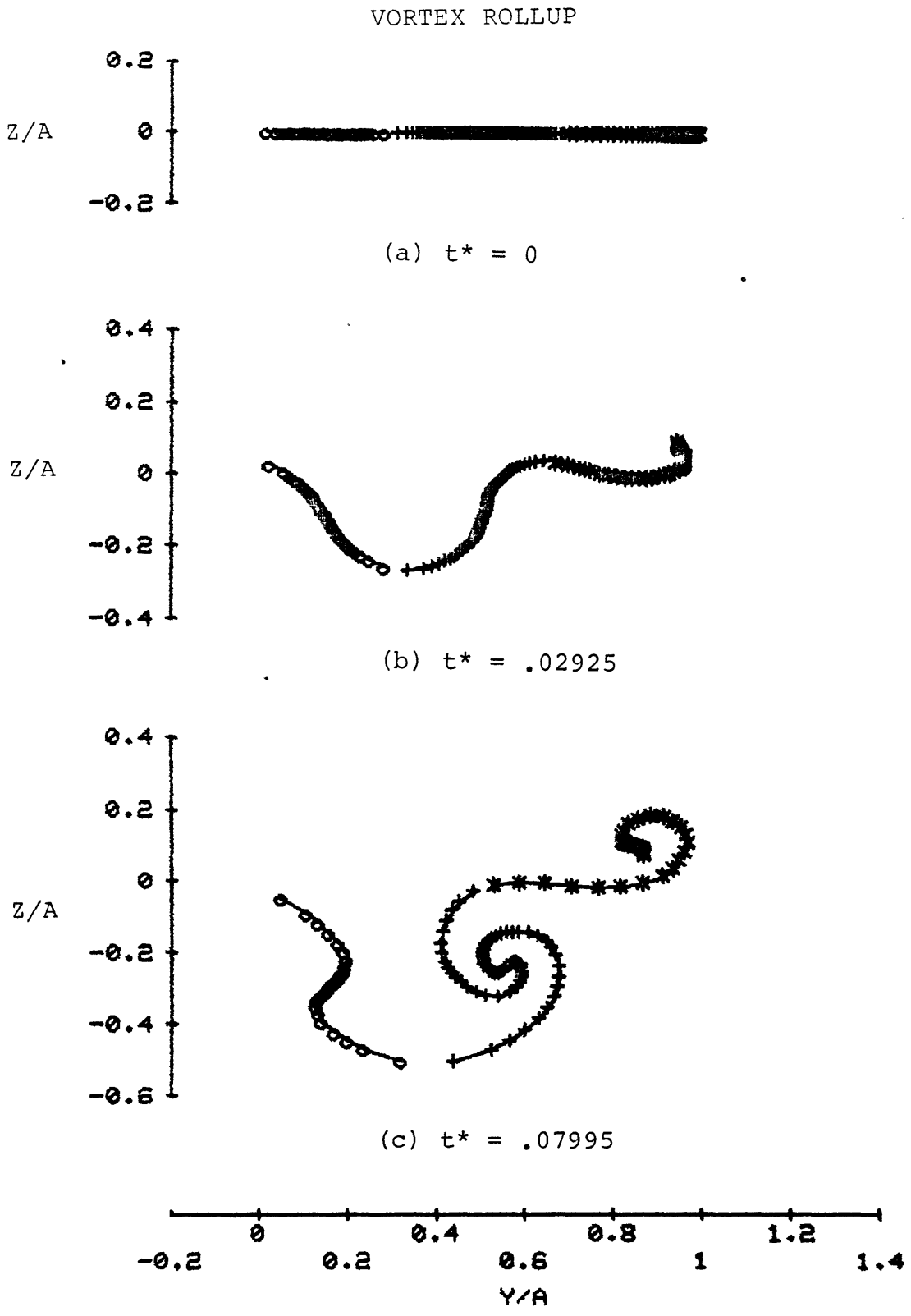

FIGURE 4.17 - SIMULATED FLAP LOADING - VORTEX WAKE GEOMETRY, CONSTANT STRENGTH POINT VORTICES, 130 POINTS, GRID = 31x31

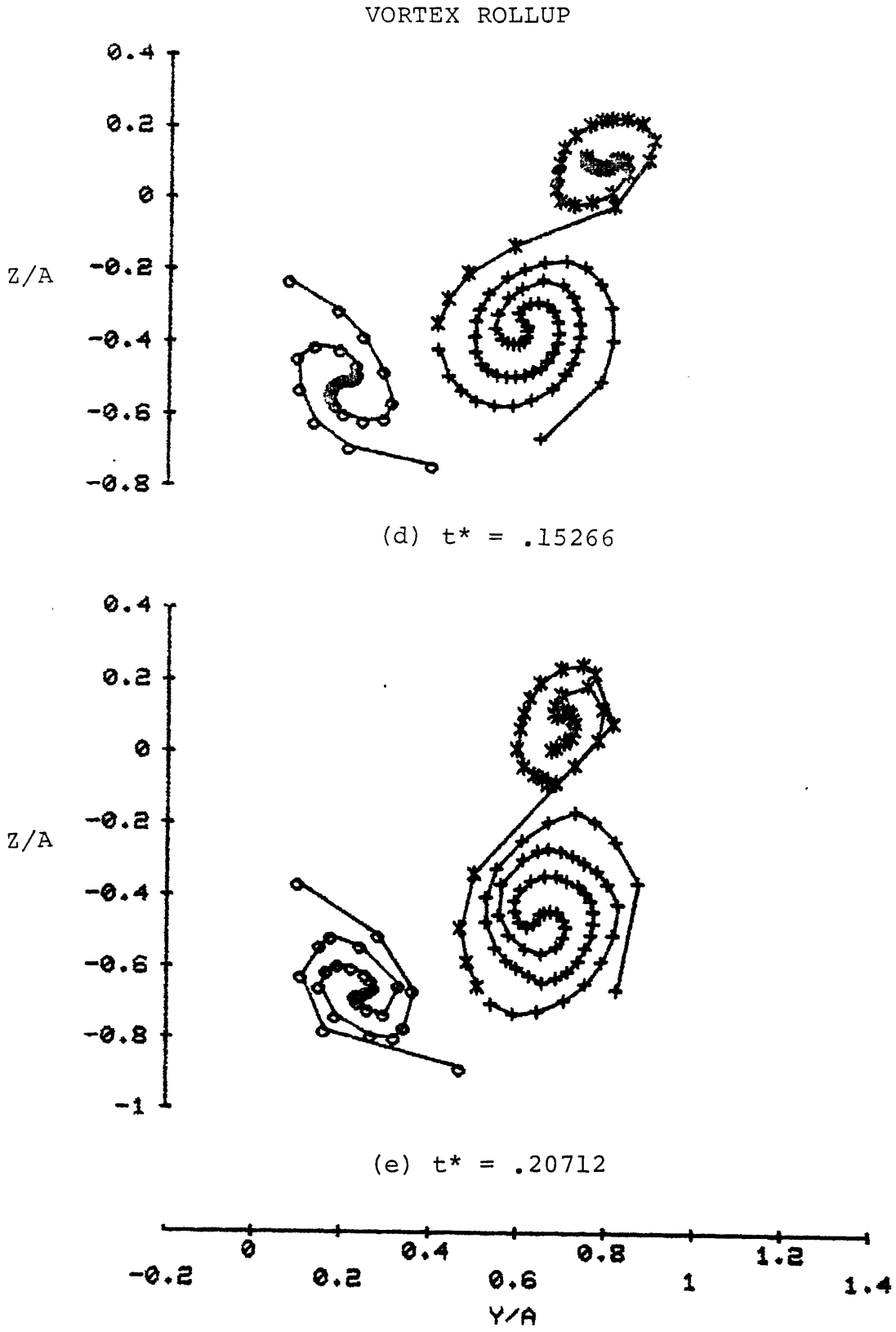

FIGURE 4.17 CONTINUED

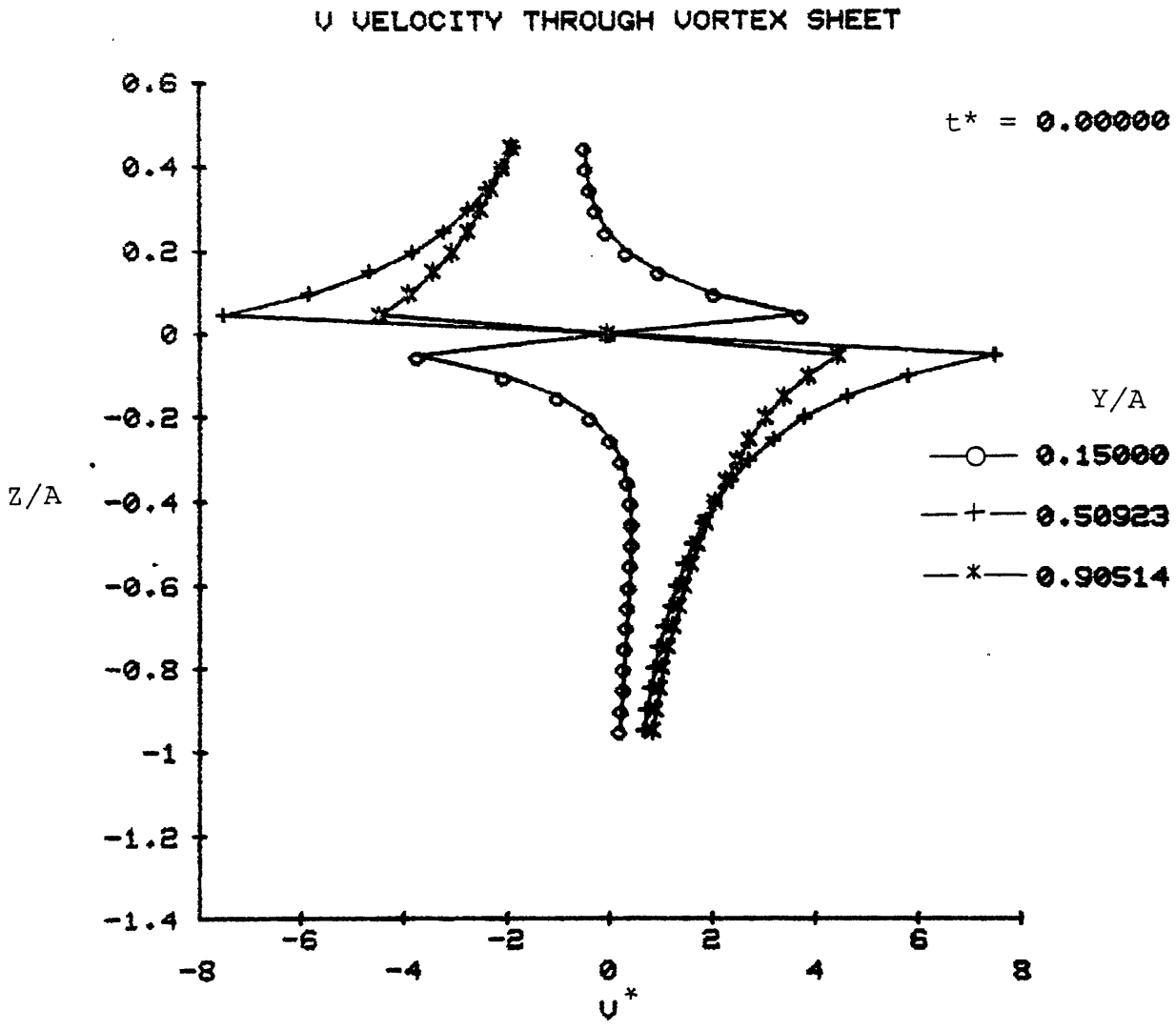

FIGURE 4.18a - SIMULATED FLAP LOADING - V VELOCITY PROFILE, CONSTANT STRENGTH POINT VORTICES, 130 POINTS, GRID = 31x31, t* = 0

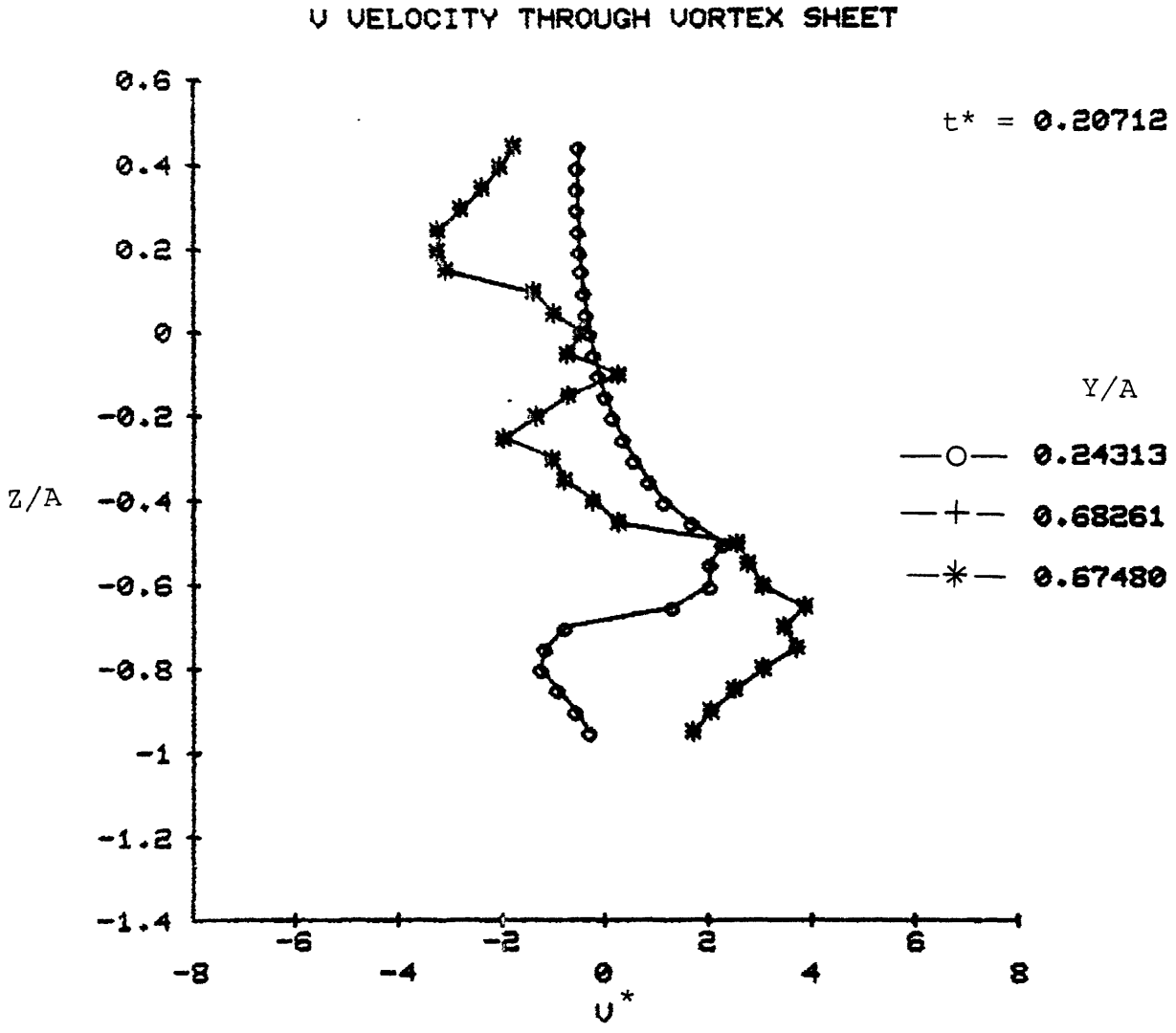

FIGURE 4.18b - SIMULATED FLAP LOADING - V VELOCITY PROFILE, CONSTANT STRENGTH POINT VORTICES, 130 POINTS, GRID = 31x31, t* = .20712

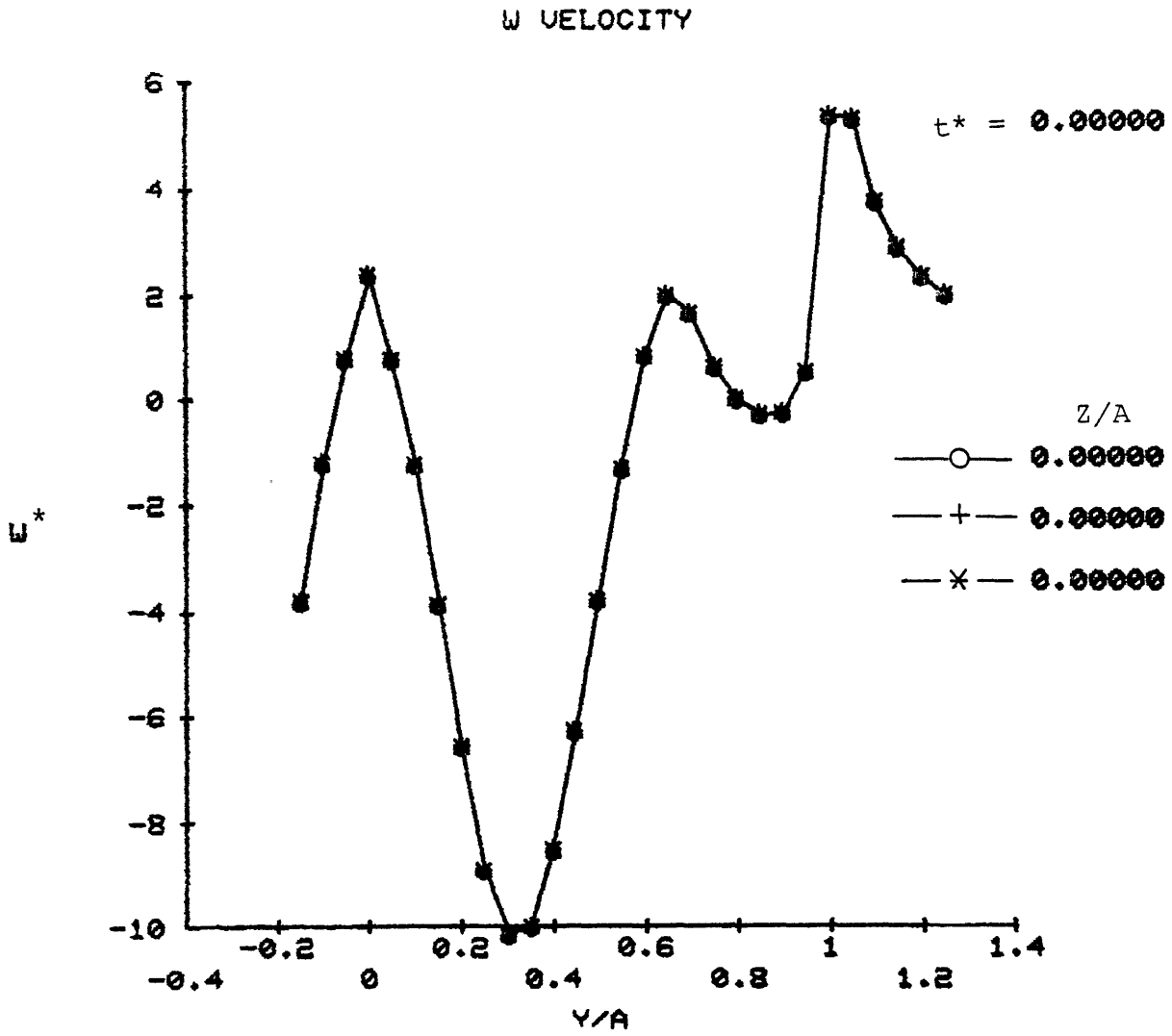

FIGURE 4.19a - SIMULATED FLAP LOADING - W VELOCITY PROFILE, CONSTANT STRENGTH POINT VORTICES, 130 POINTS, GRID = 31x31, t* = 0

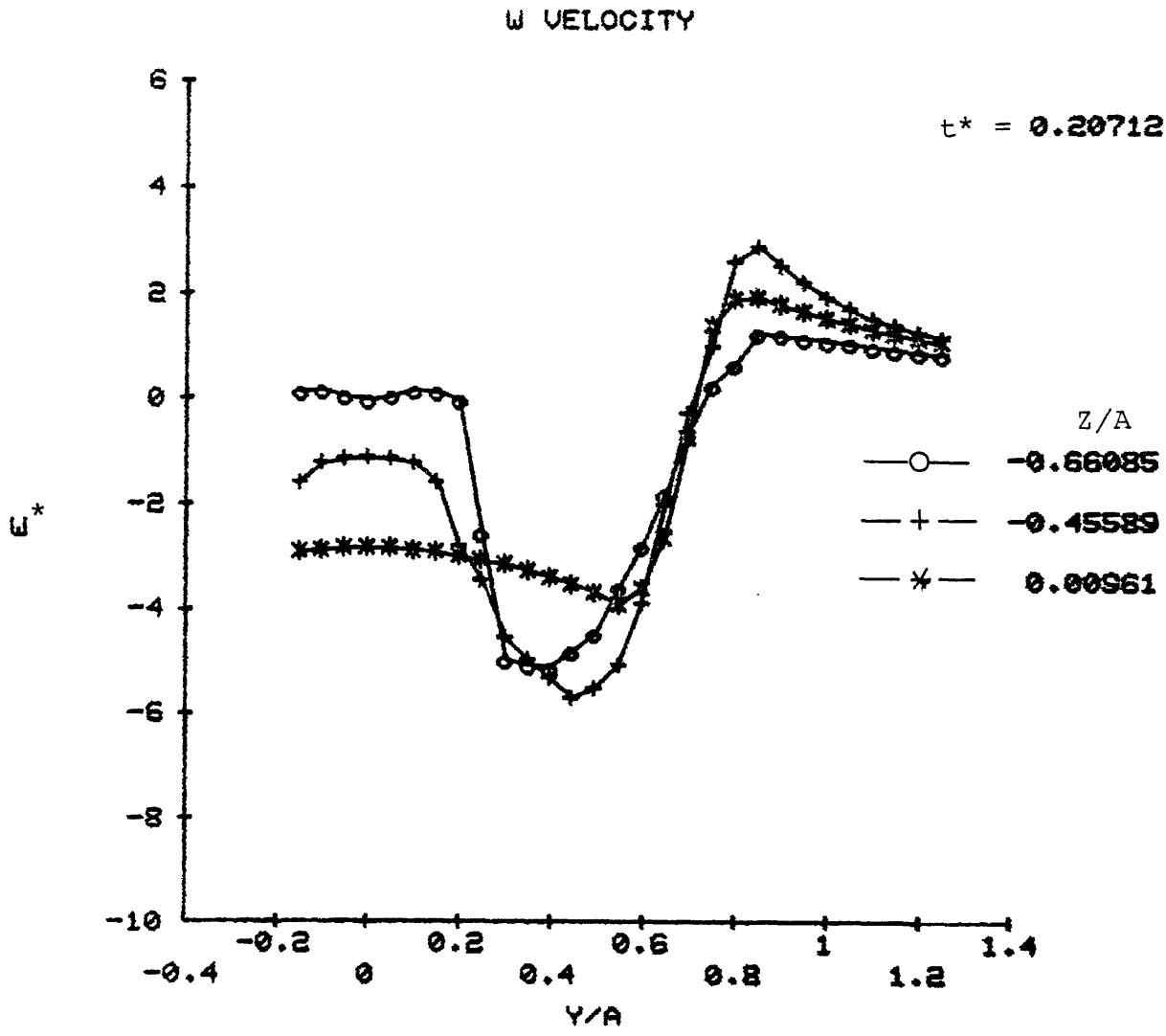

FIGURE 4.19b - SIMULATED FLAP LOADING - W VELOCITY PROFILE, CONSTANT STRENGTH POINT VORTICES, 130 POINTS, GRID = 31x31, t* = .20712

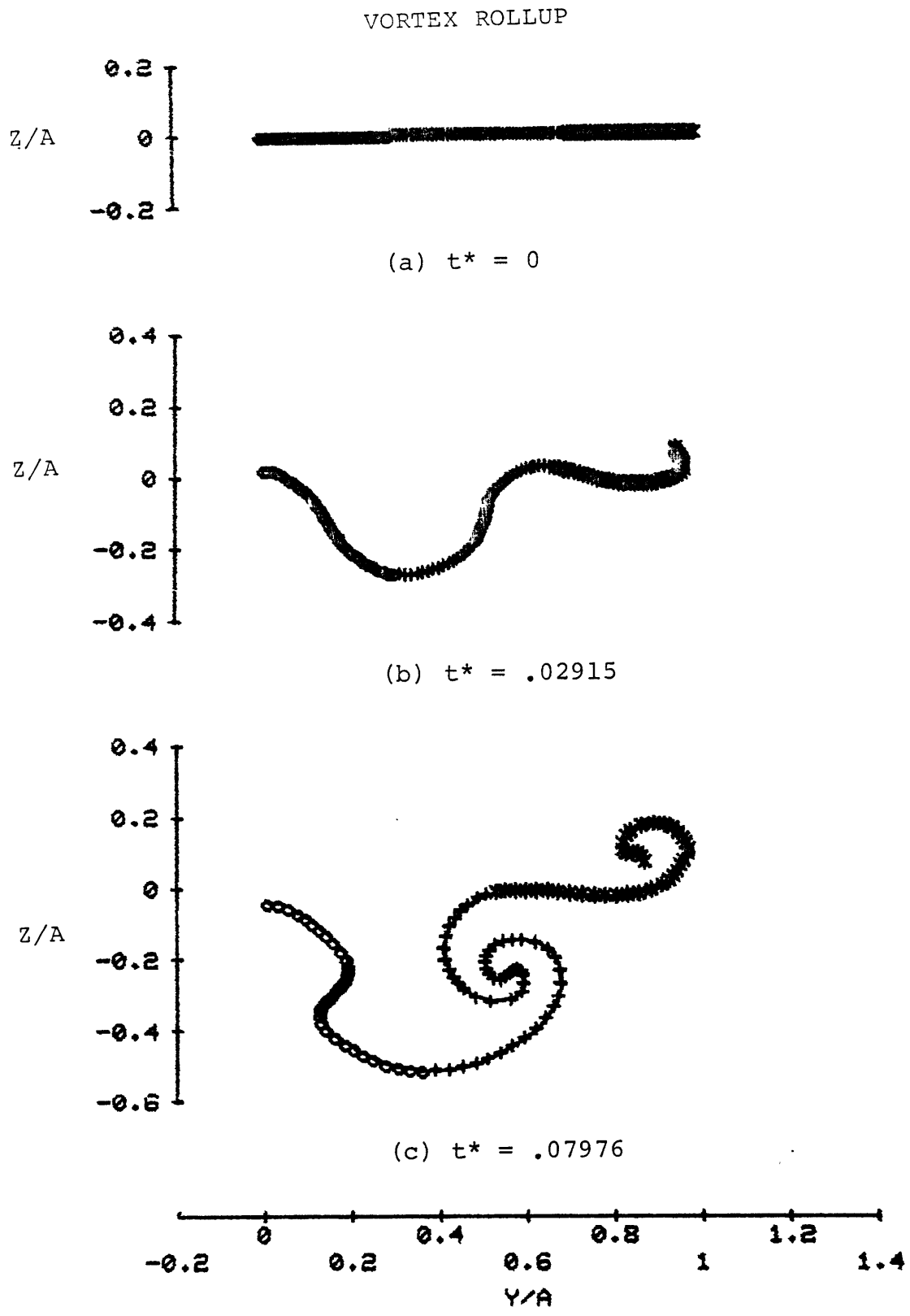

FIGURE 4.20 - SIMULATED FLAP LOADING - VORTEX WAKE GEOMETRY, EQUALLY SPACED POINT VORTICES, 130 POINTS, GRID = 31x31

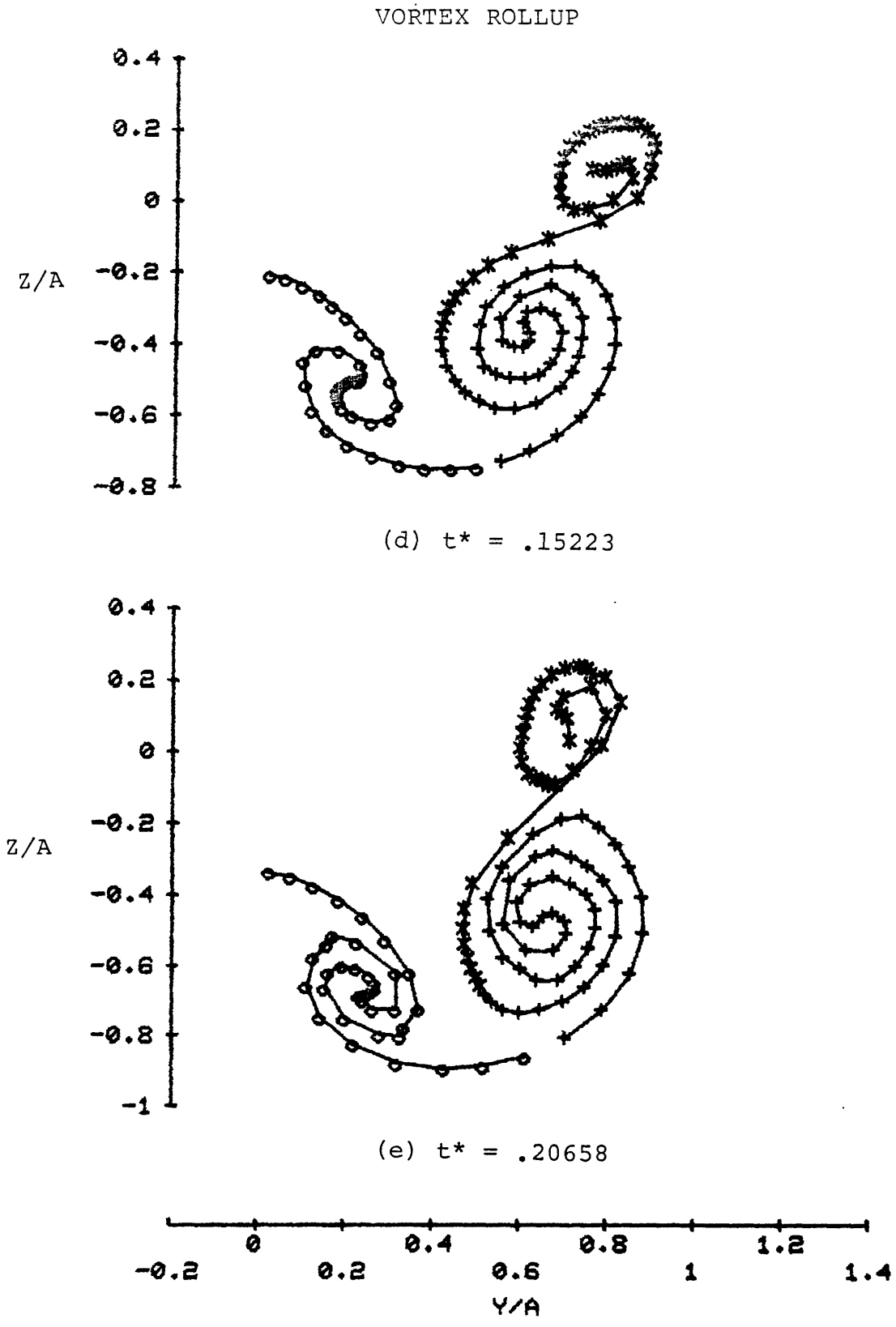

FIGURE 4.20 CONTINUED

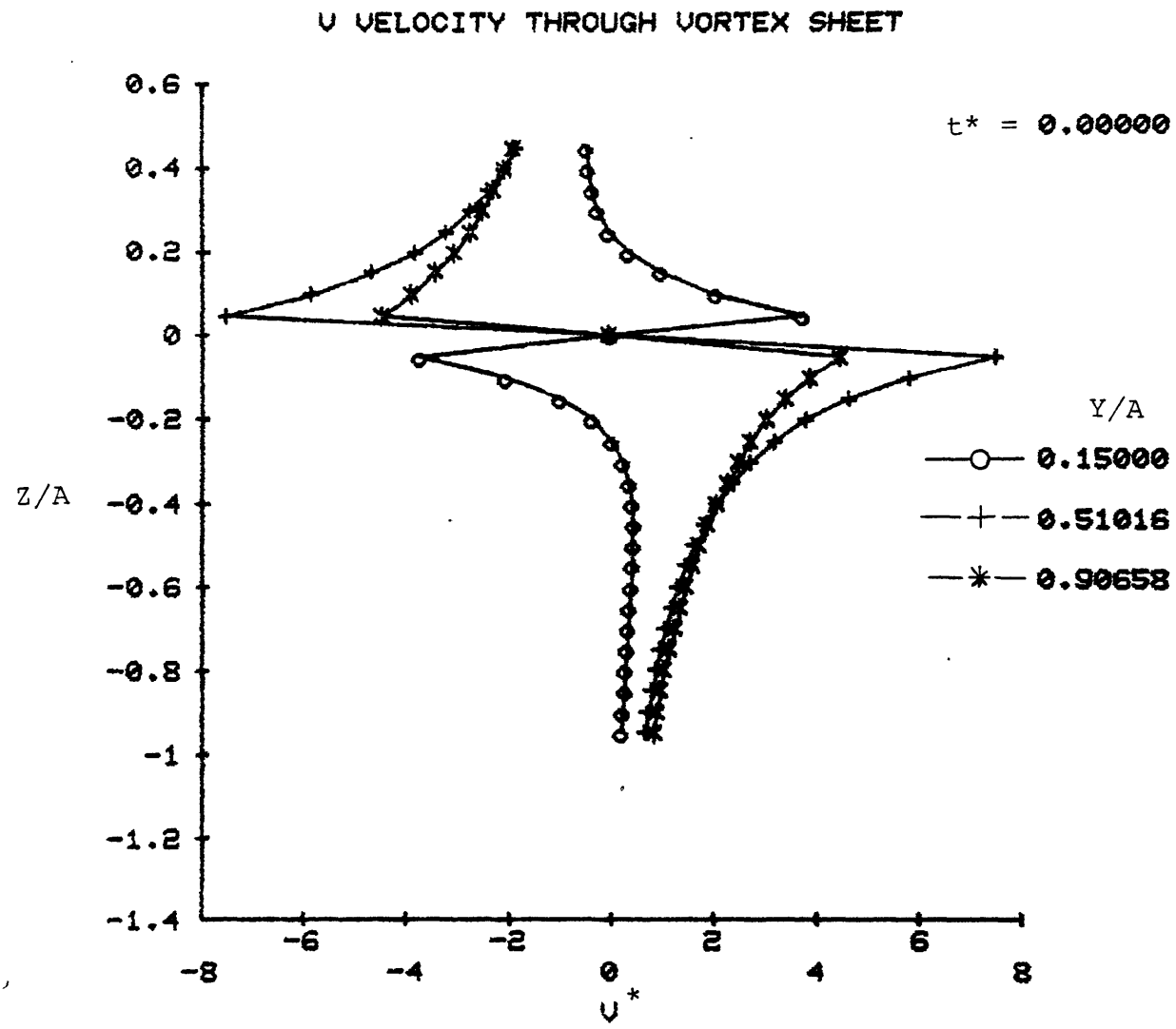

FIGURE 4.21a - SIMULATED FLAP LOADING - V VELOCITY PROFILE, EQUALLY SPACED POINT VORTICES, 130 POINTS, GRID = 31x31, t* = 0

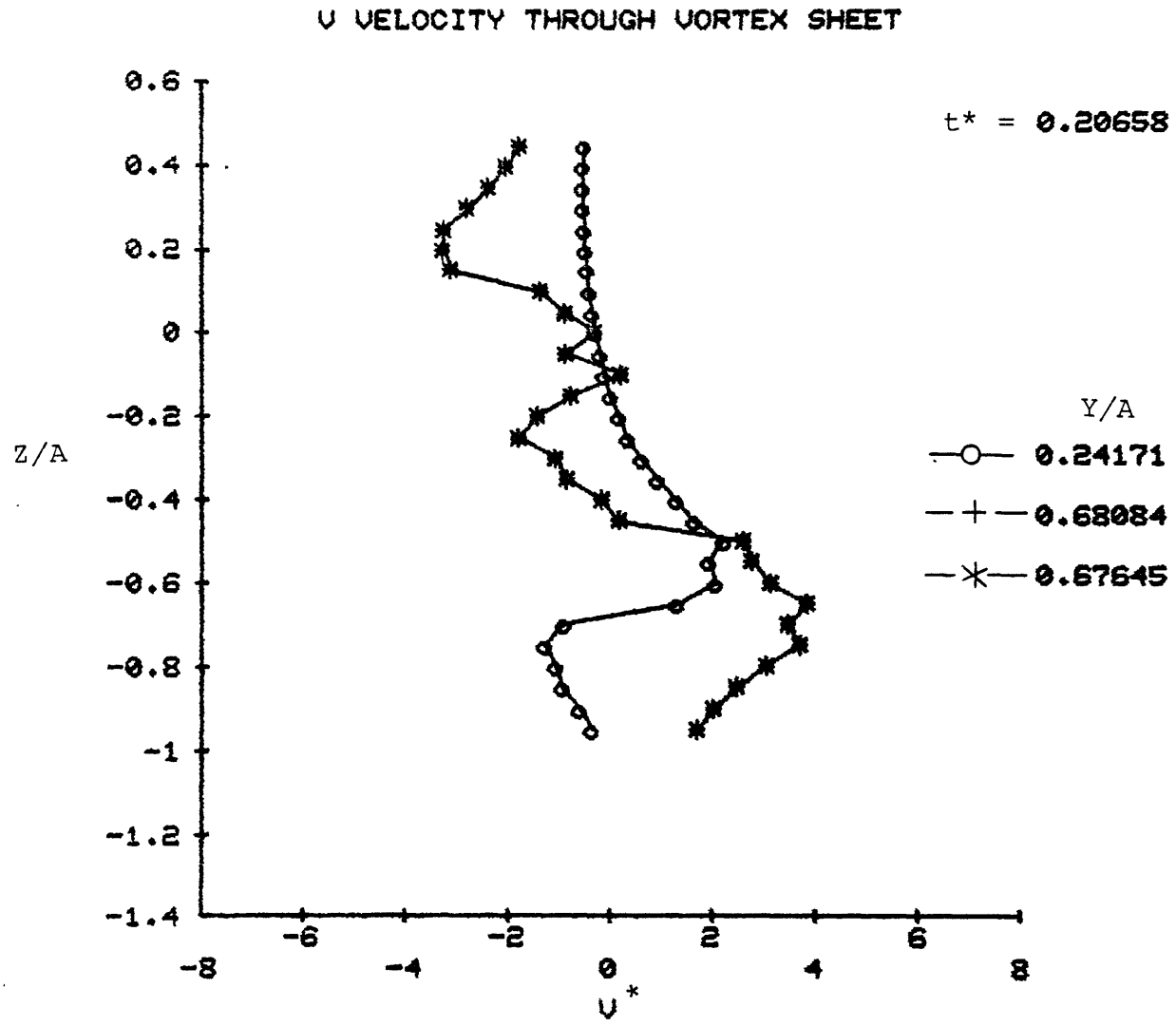

FIGURE 4.21b - SIMULATED FLAP LOADING - V VELOCITY PROFILE, EQUALLY SPACED POINT VORTICES, 130 POINTS, GRID = 31x31, t* = .20658

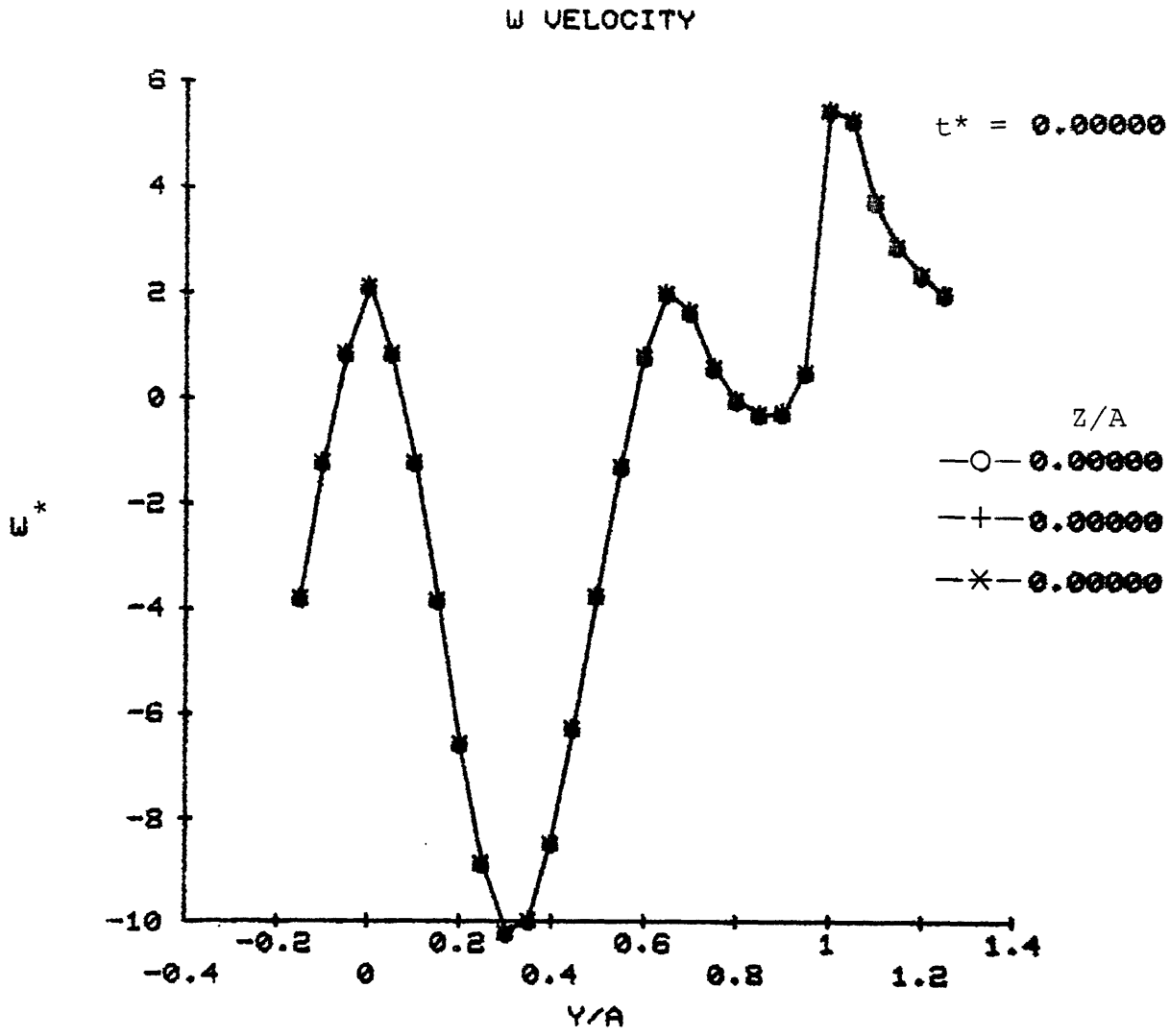

FIGURE 4.22a - SIMULATED FLAP LOADING - W VELOCITY PROFILE, EQUALLY SPACED POINT VORTICES, 130 POINTS, GRID = 31x31, t* = 0

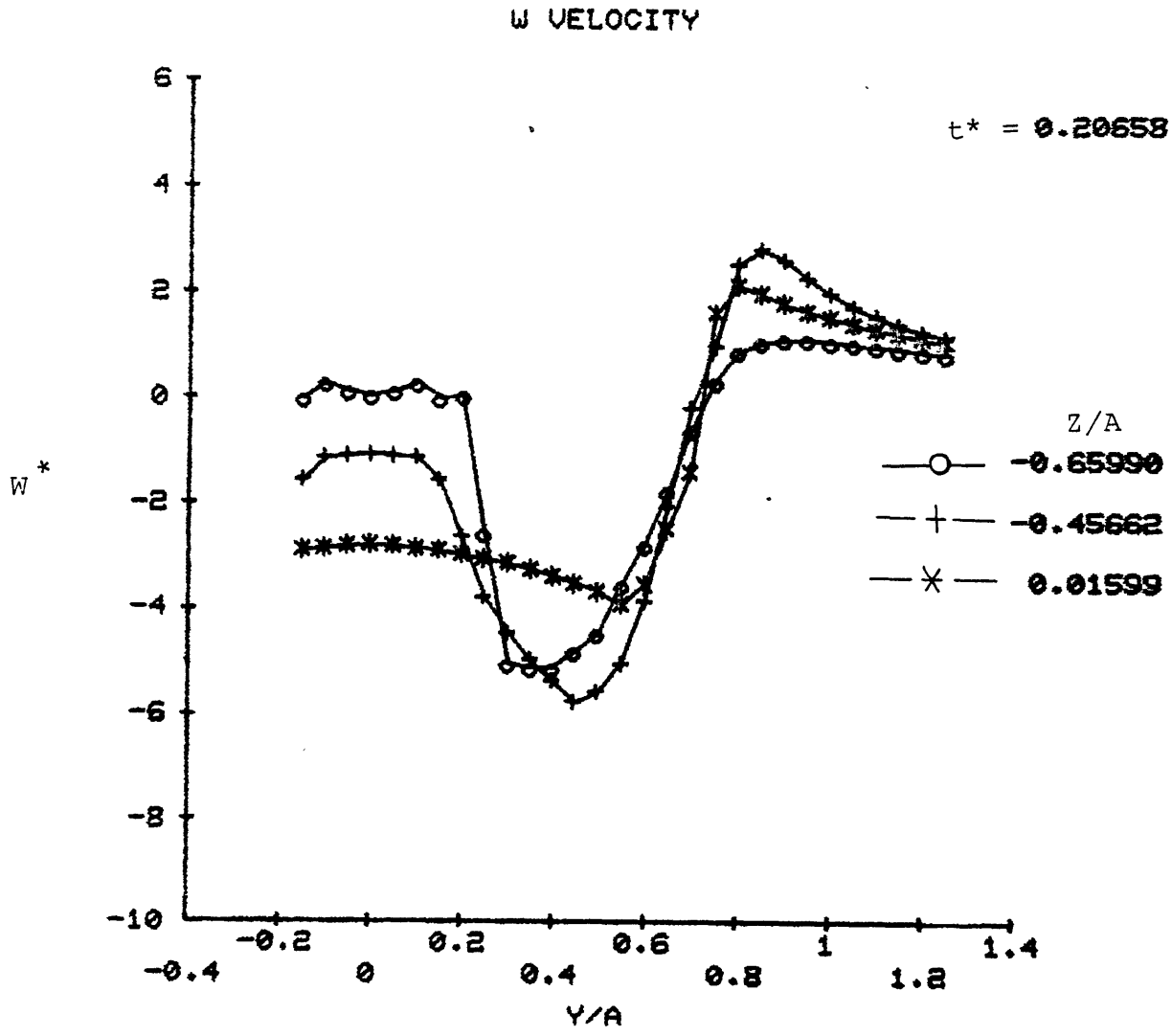

FIGURE 4.22b - SIMULATED FLAP LOADING - W VELOCITY PROFILE, EQUALLY SPACED POINT VORTICES, 130 POINTS, GRID = 31x31, t* = .20658

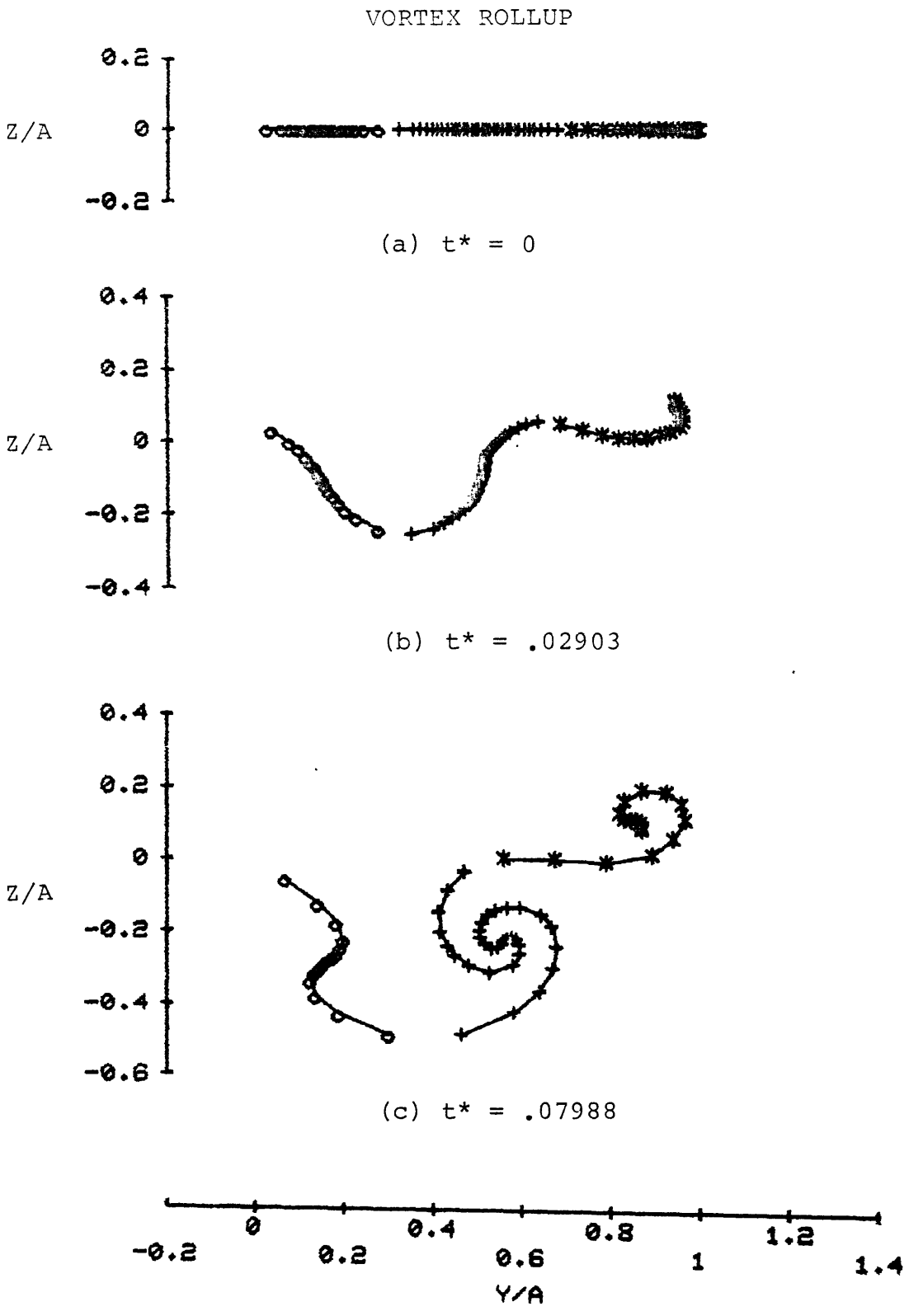

FIGURE 4.23 - SIMULATED FLAP LOADING - VORTEX WAKE GEOMETRY, CONSTANT STRENGTH POINT VORTICES, 65 POINTS, GRID = 31x31

VORTEX ROLLUP

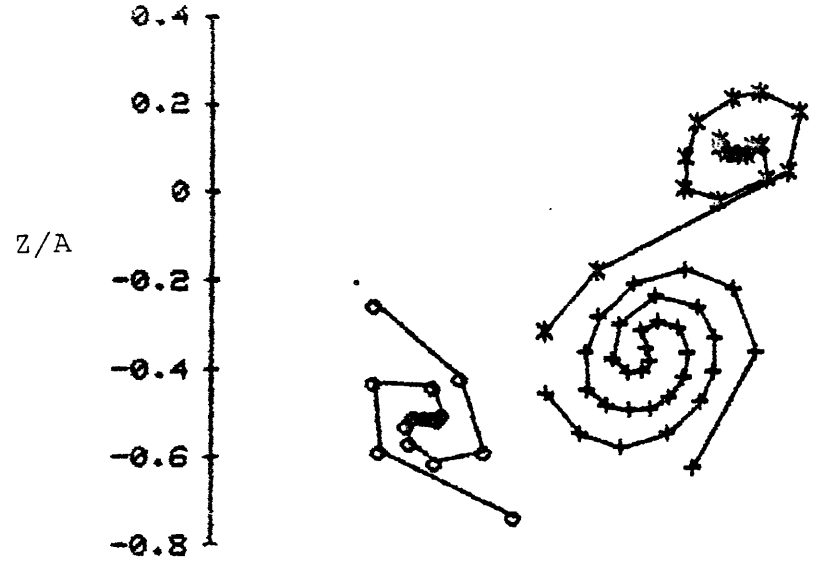

(d) t* = .15276

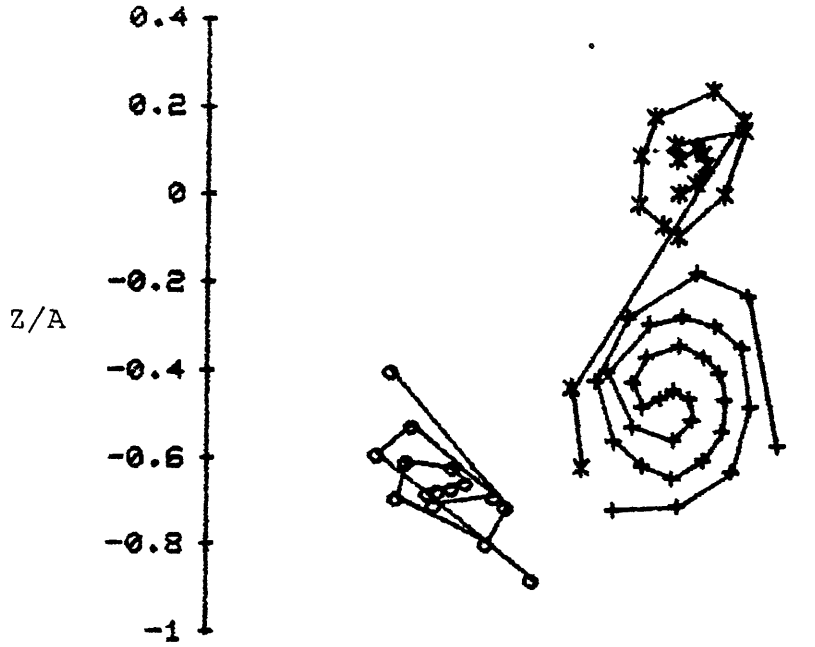

(e) t* = .20659

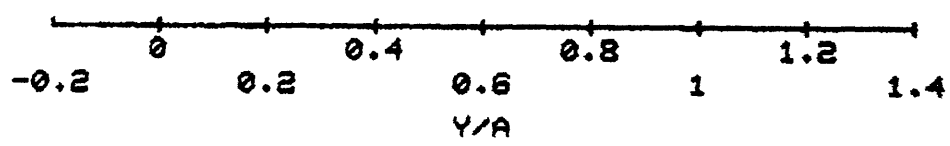

FIGURE 4.23 CONTINUED

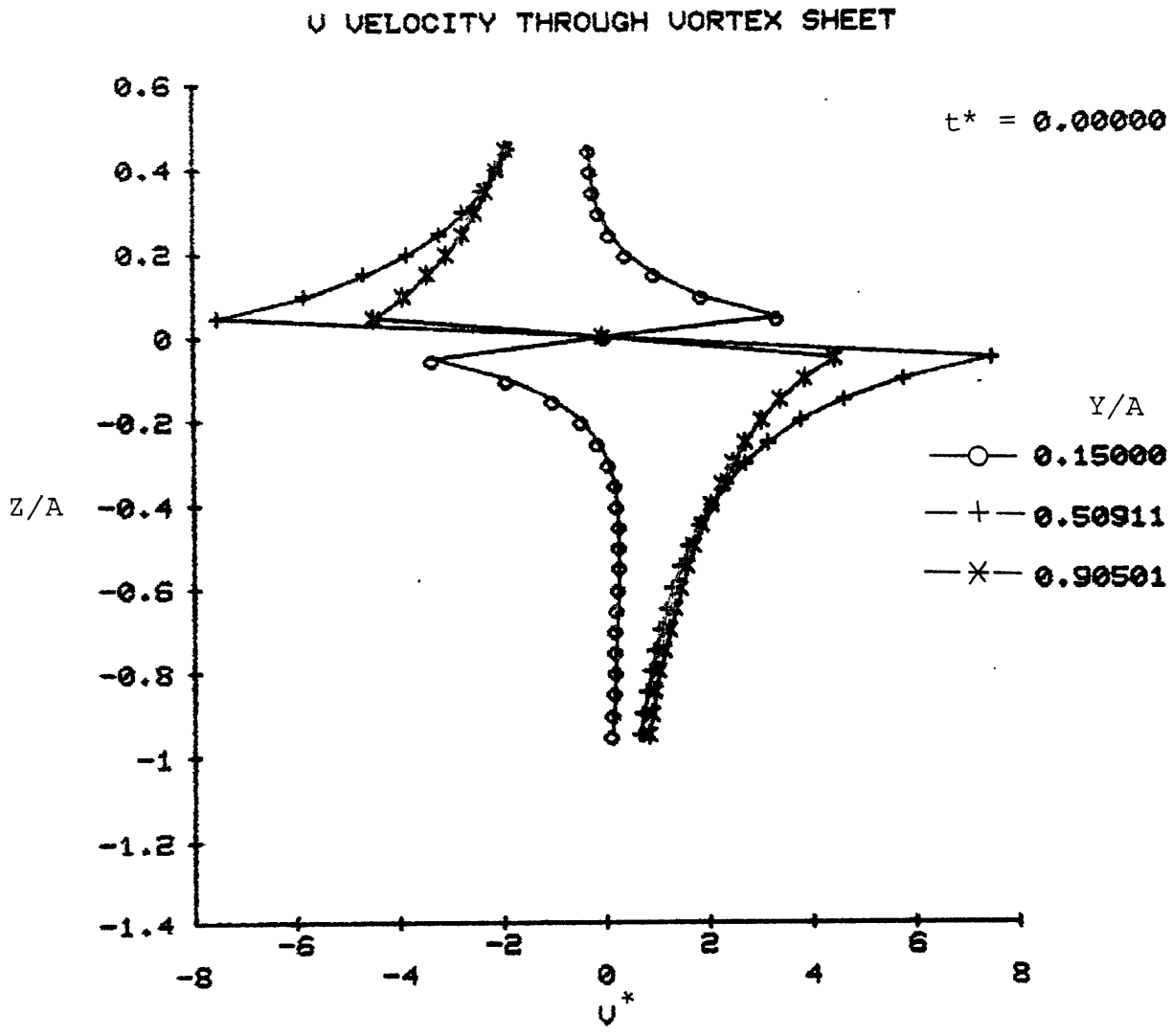

FIGURE 4.24a - SIMULATED FLAP LOADING - V VELOCITY PROFILE, CONSTANT STRENGTH POINT VORTICES, 65 POINTS, GRID = 31x31, t* = 0

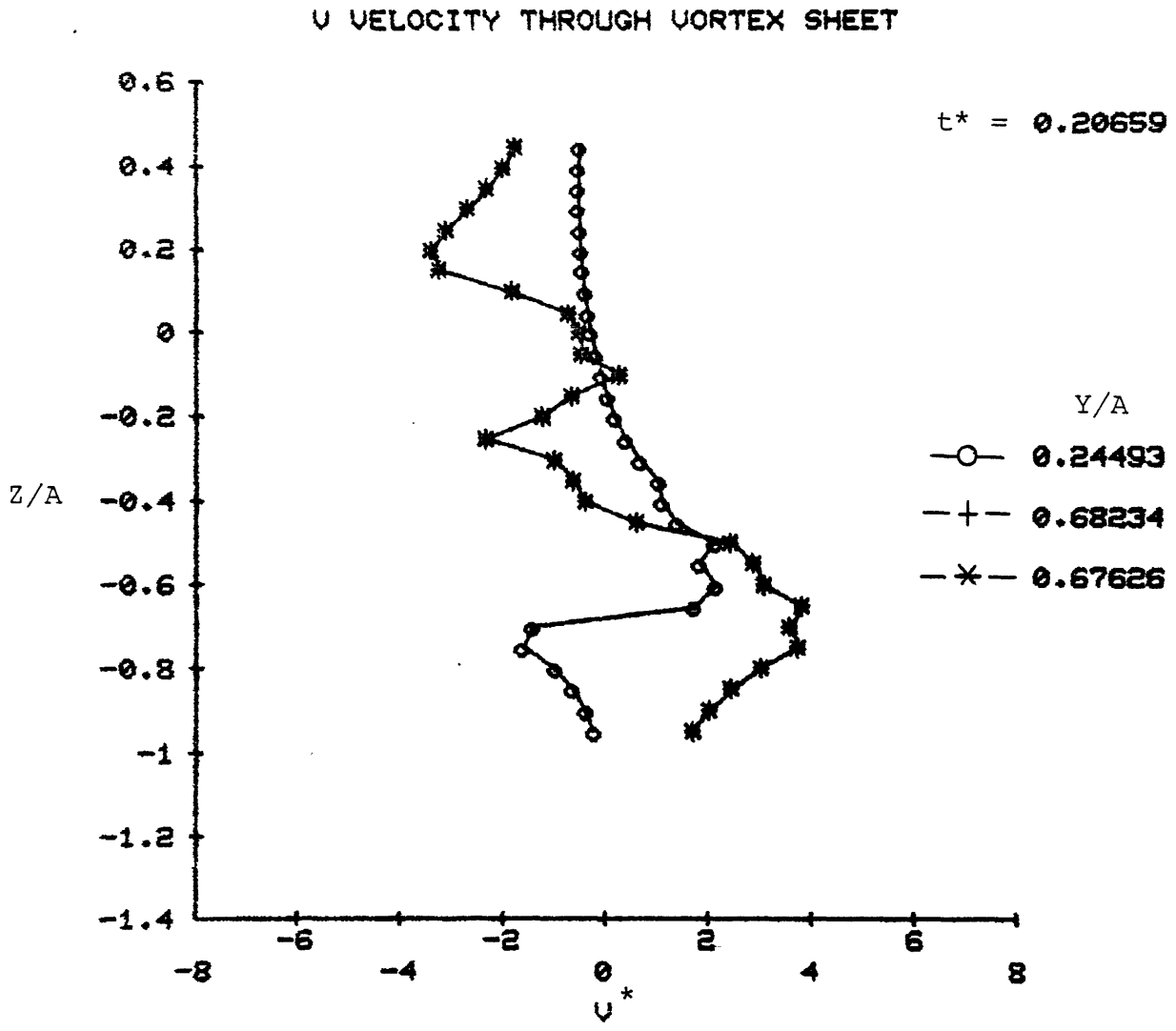

FIGURE 4.24b - SIMULATED FLAP LOADING - V VELOCITY PROFILE, CONSTANT STRENGTH POINT VORTICES, 65 POINTS, GRID = 31x31, t* = .20659

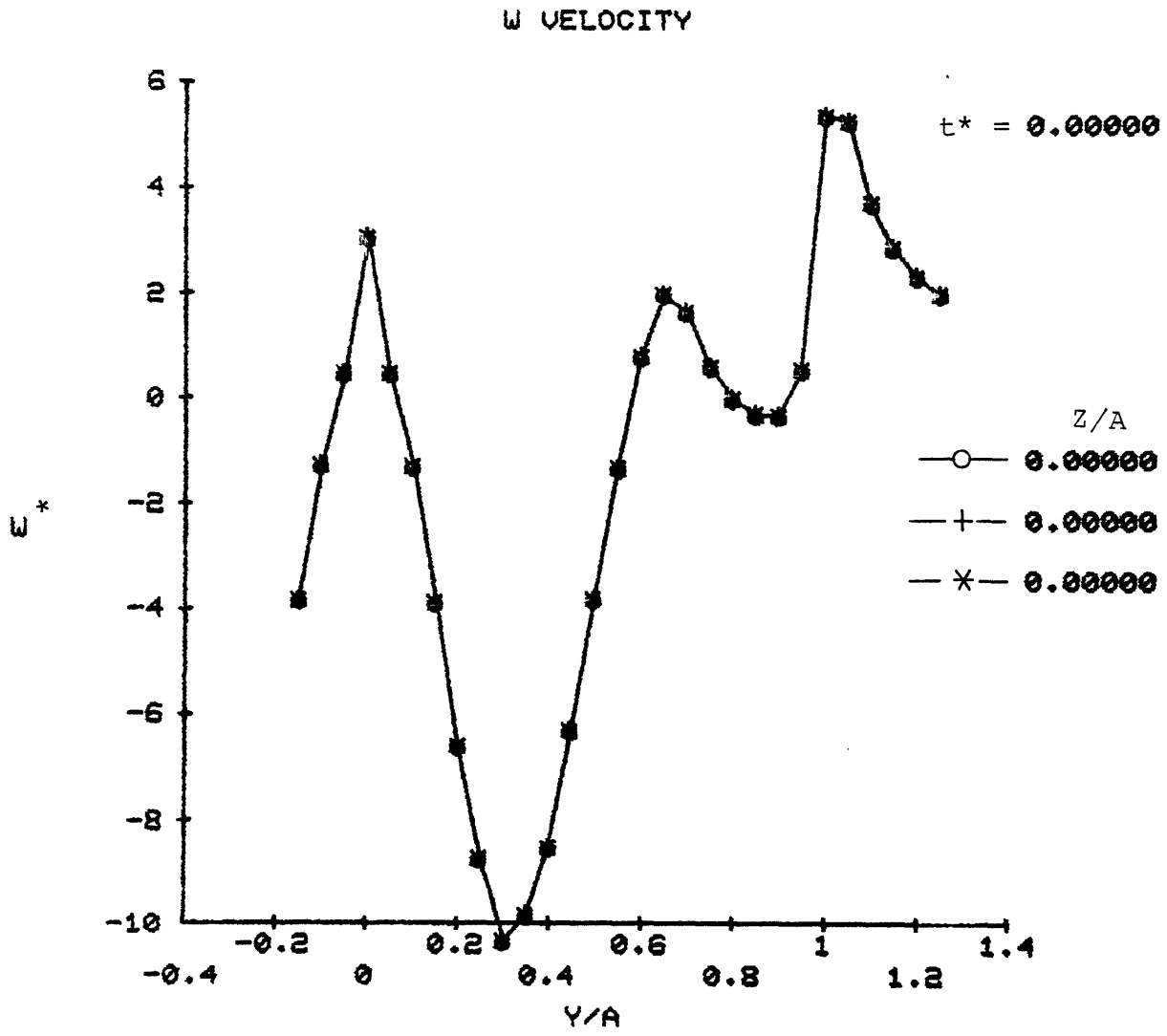

FIGURE 4.25a - SIMULATED FLAP LOADING - W VELOCITY PROFILE, CONSTANT STRENGTH POINT VORTICES, 65 POINTS, GRID = 31x31, t* = 0

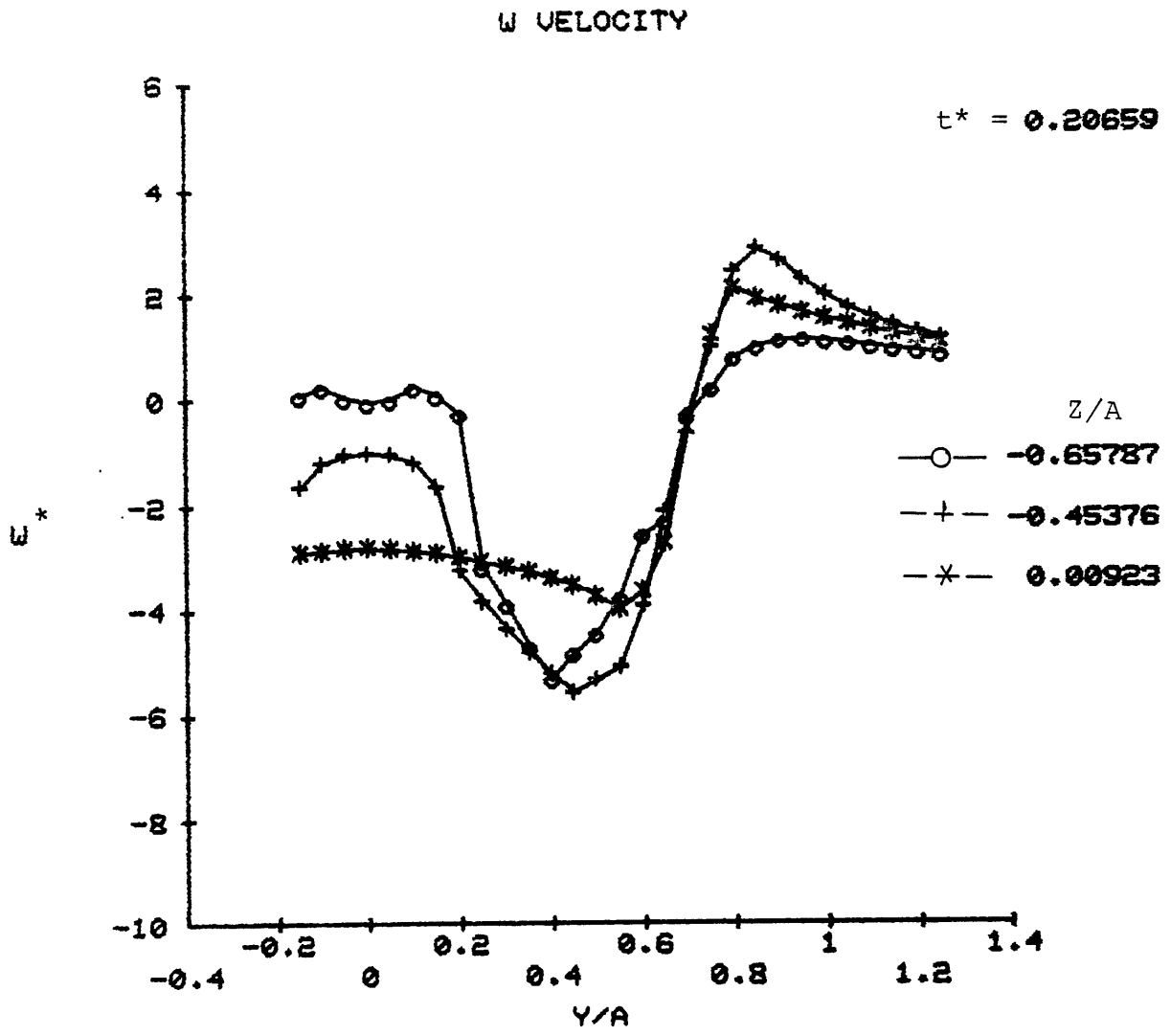

FIGURE 4.25b - SIMULATED FLAP LOADING - W VELOCITY PROFILE, CONSTANT STRENGTH POINT VORTICES, 65 POINTS, GRID = 31x31, t* = .20659

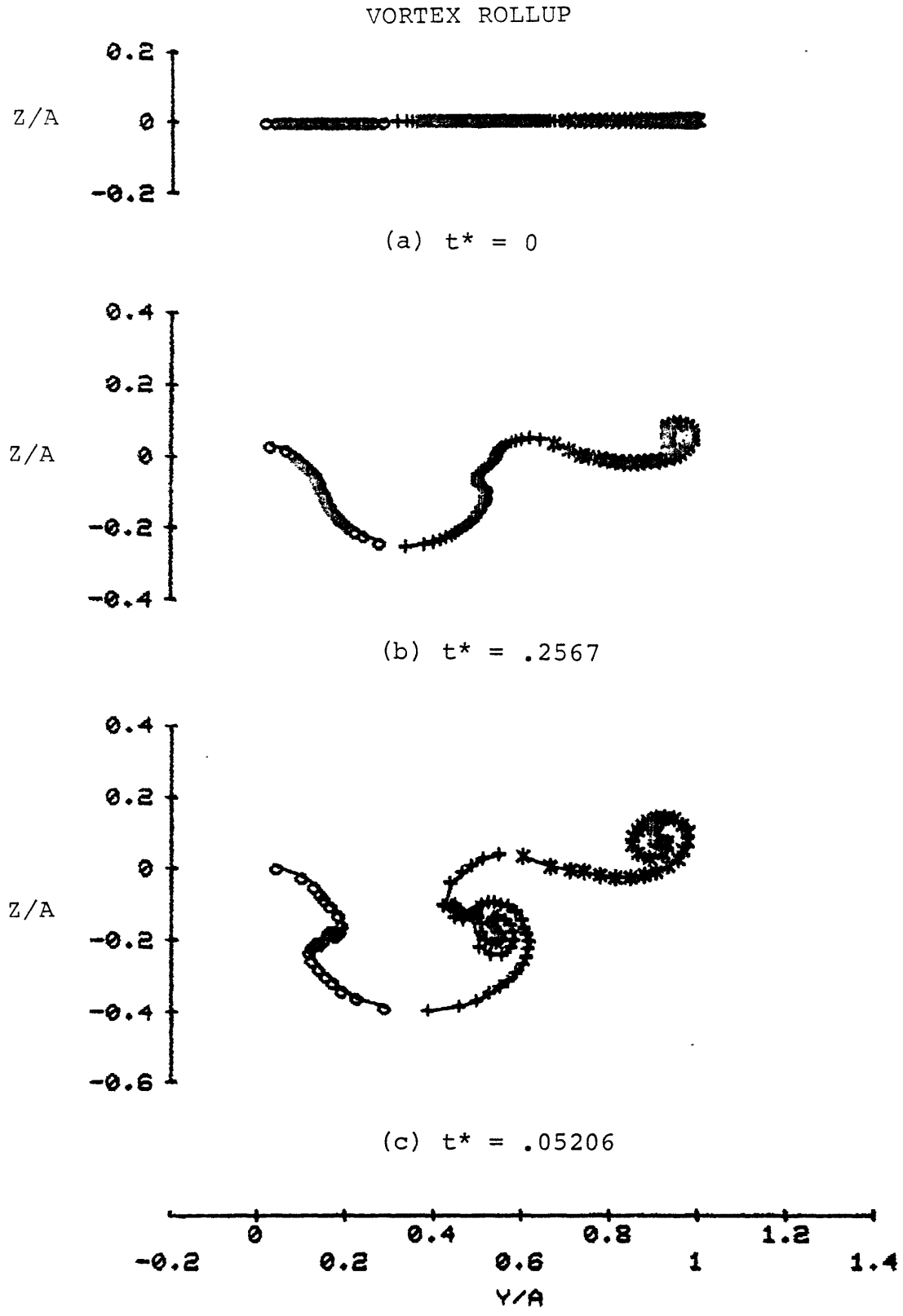

FIGURE 4.26 - SIMULATED FLAP LOADING - VORTEX WAKE GEOMETRY, CONSTANT STRENGTH POINT VORTICES, 130 POINTS, GRID 61x61

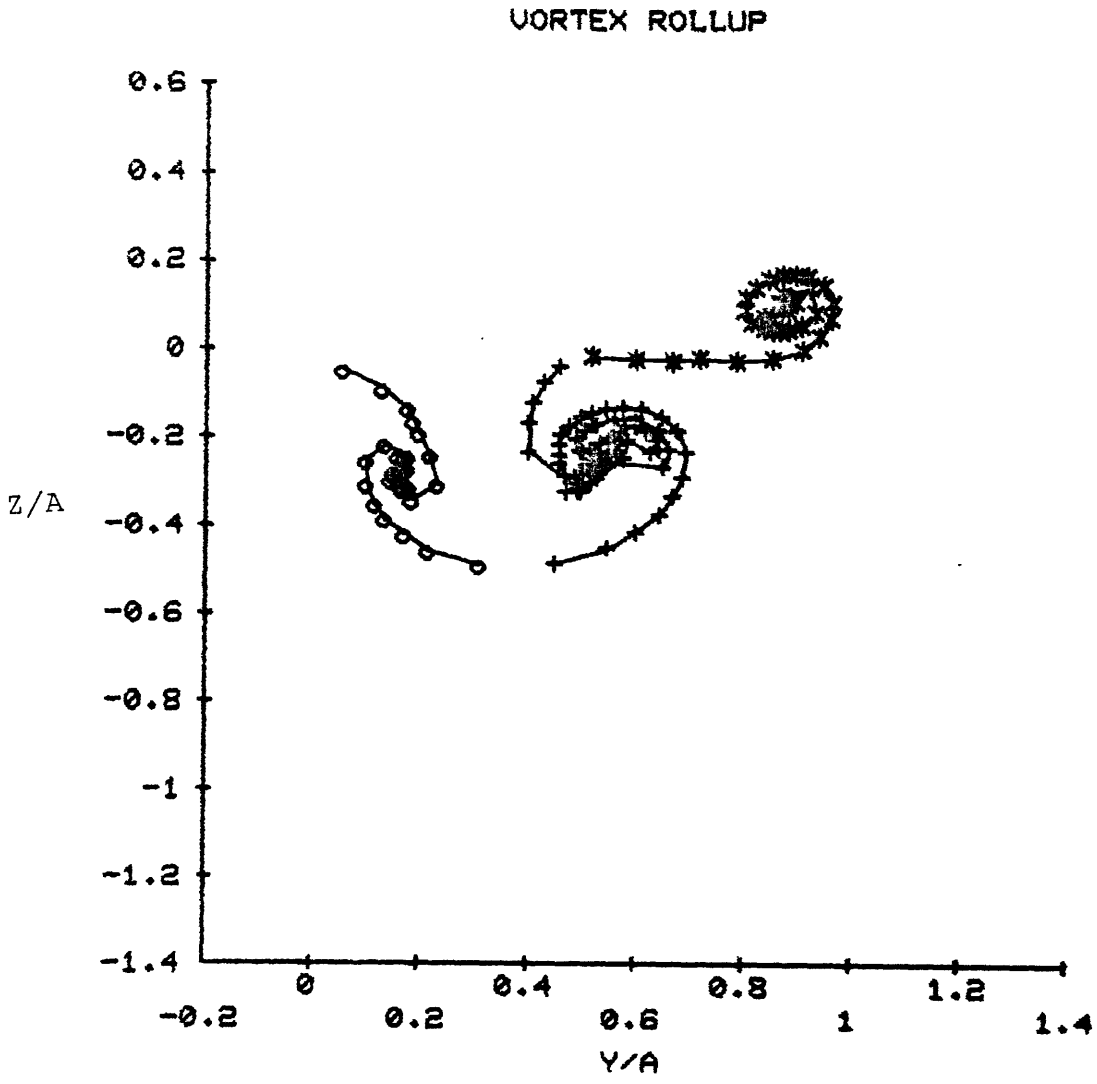

(d) t* = .07749

FIGURE 4.26 CONTINUED

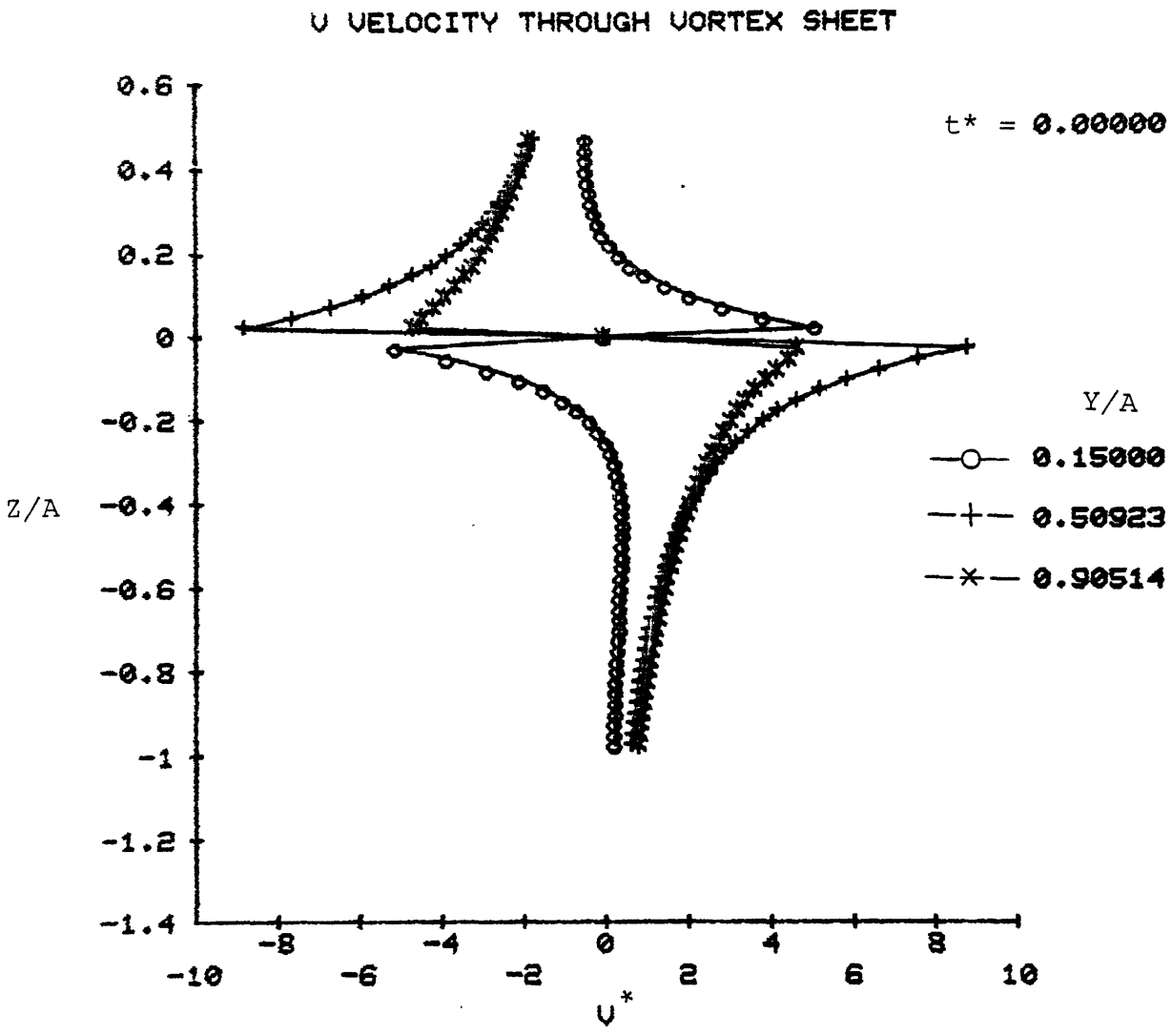

FIGURE 4.27a - SIMULATED FLAP LOADING - V VELOCITY PROFILE, CONSTANT STRENGTH POINT VORTICES, 130 POINTS, GRID = 61x61, t* = 0

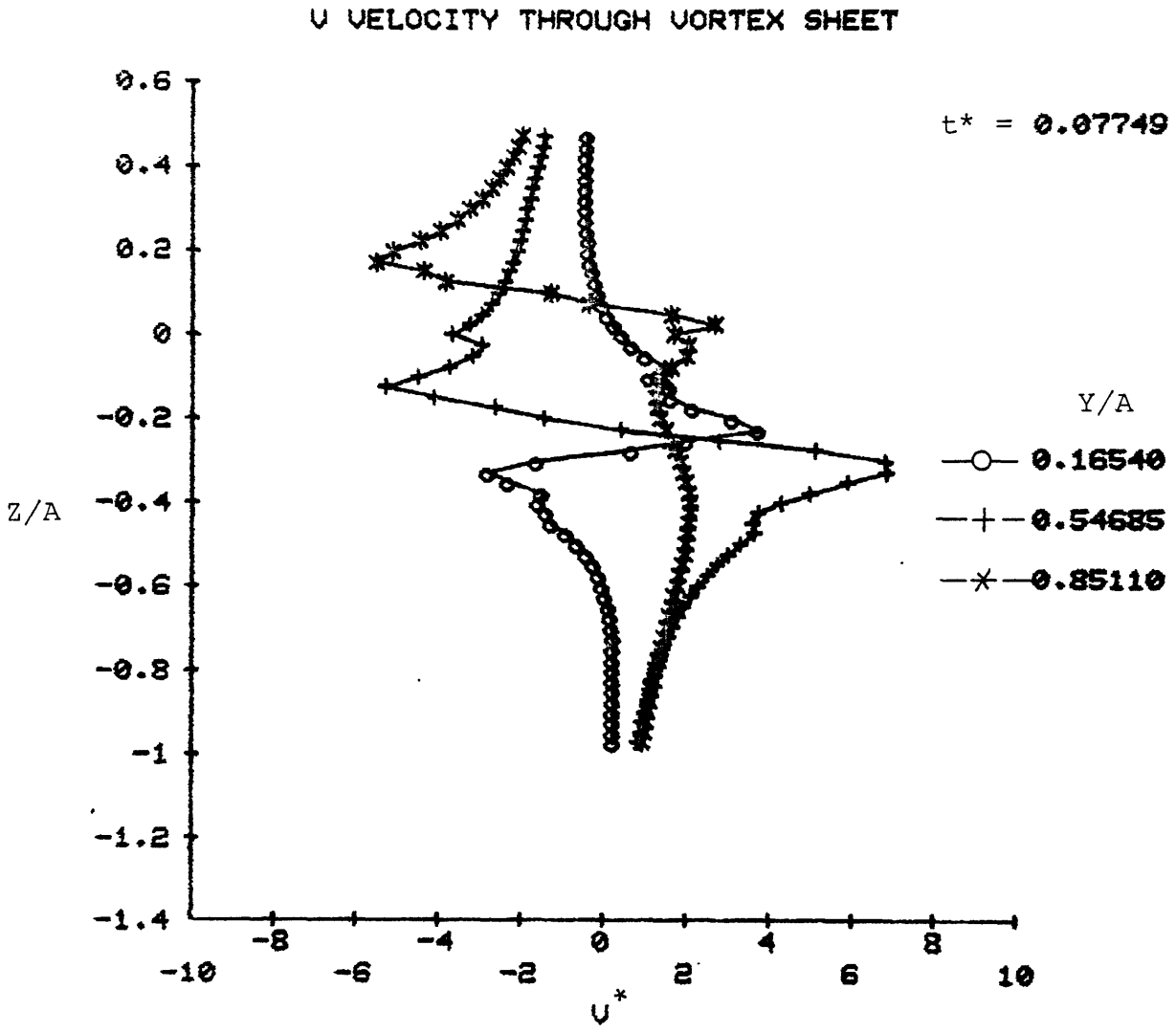

FIGURE 4.27b - SIMULATED FLAP LOADING - V VELOCITY PROFILE, CONSTANT STRENGTH POINT VORTICES, 130 POINTS, GRID = 61x61, t* = .07749

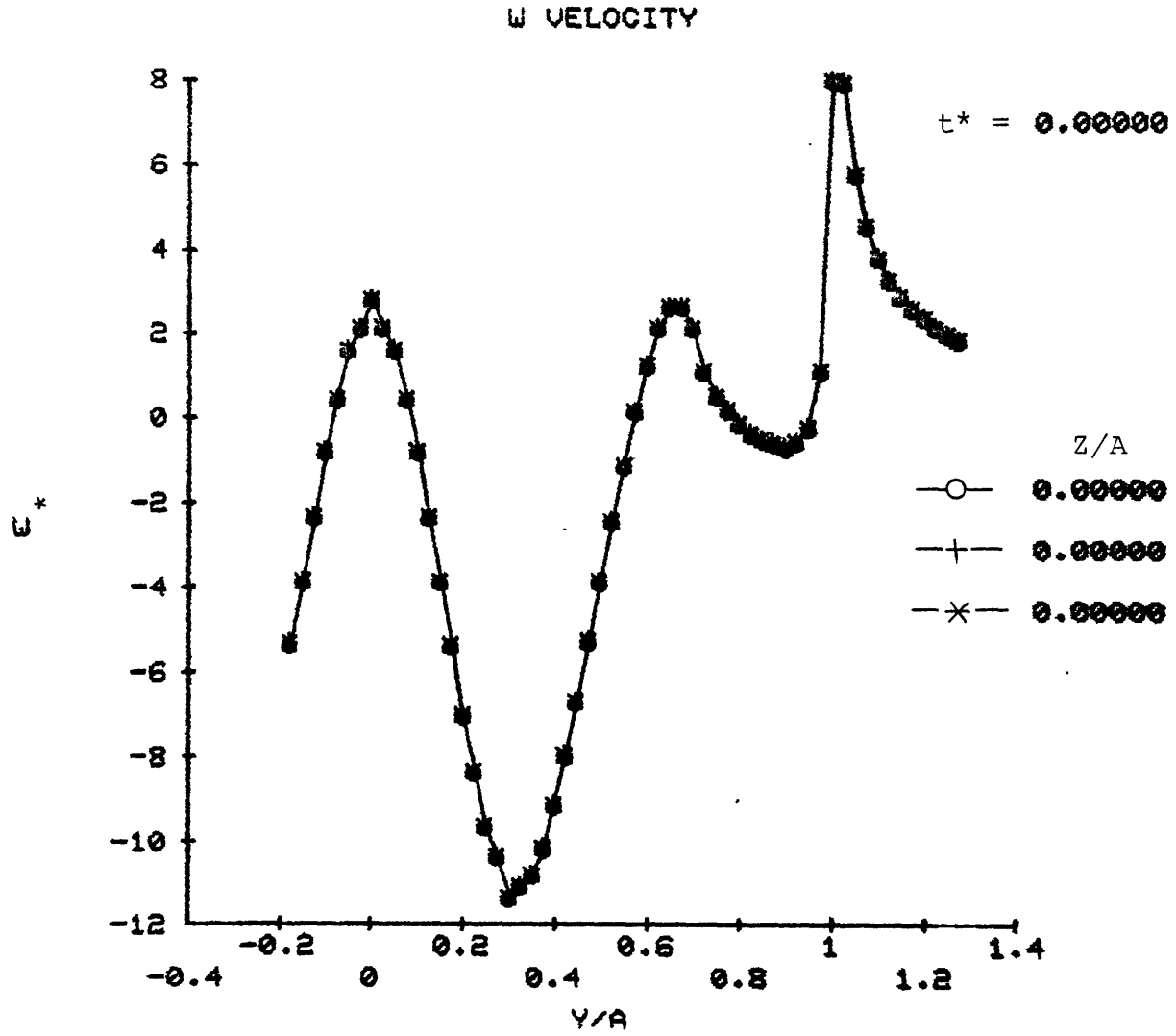

FIGURE 4.28a - SIMULATED FLAP LOADING - W VELOCITY PROFILE, CONSTANT STRENGTH POINT VORTICES, 130 POINTS, GRID = 61x61, t* = 0

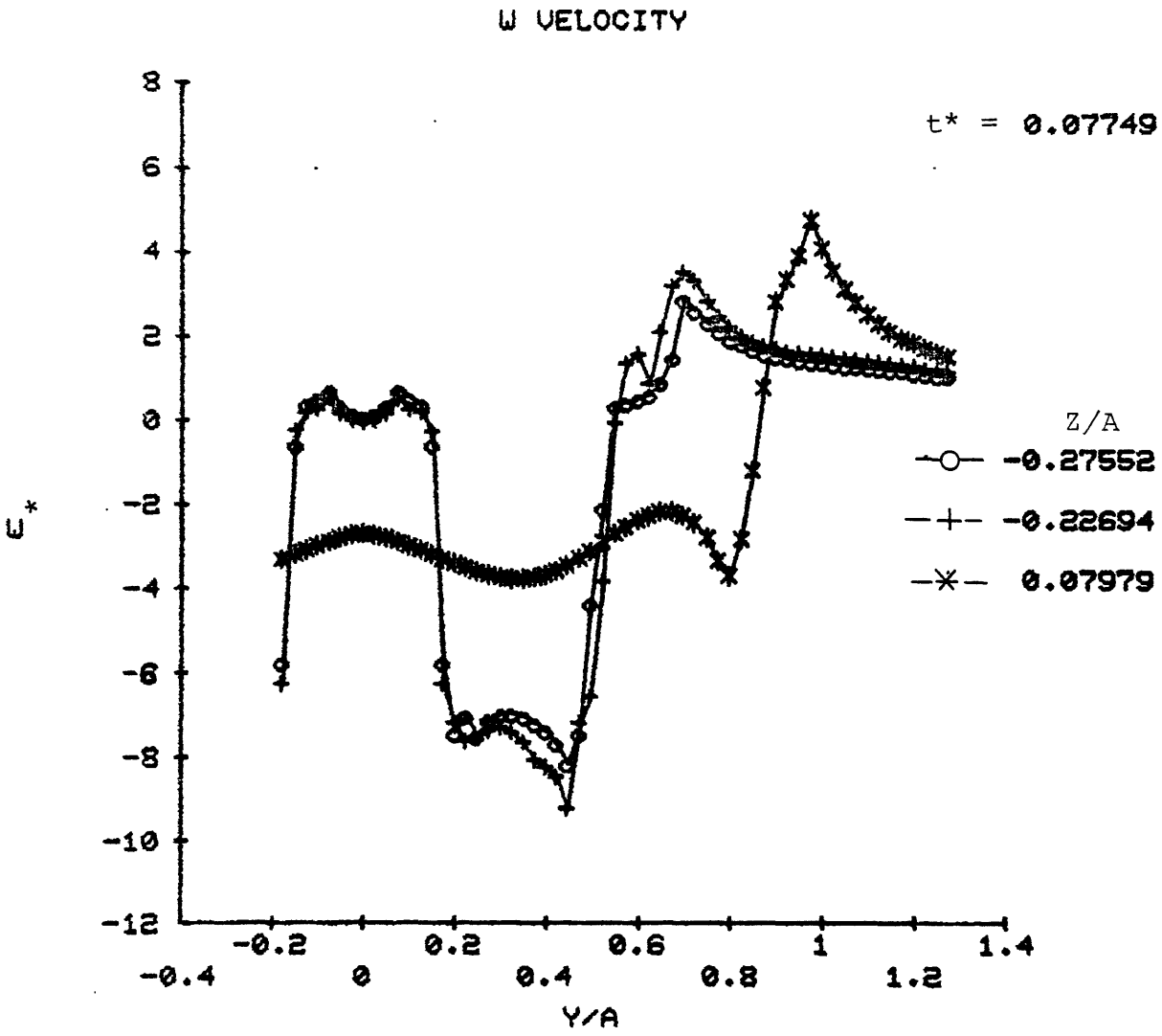

FIGURE 4.28b - SIMULATED FLAP LOADING - W VELOCITY PROFILE, CONSTANT STRENGTH POINT VORTICES, 130 POINTS, GRID = 61x61, t* = .07749

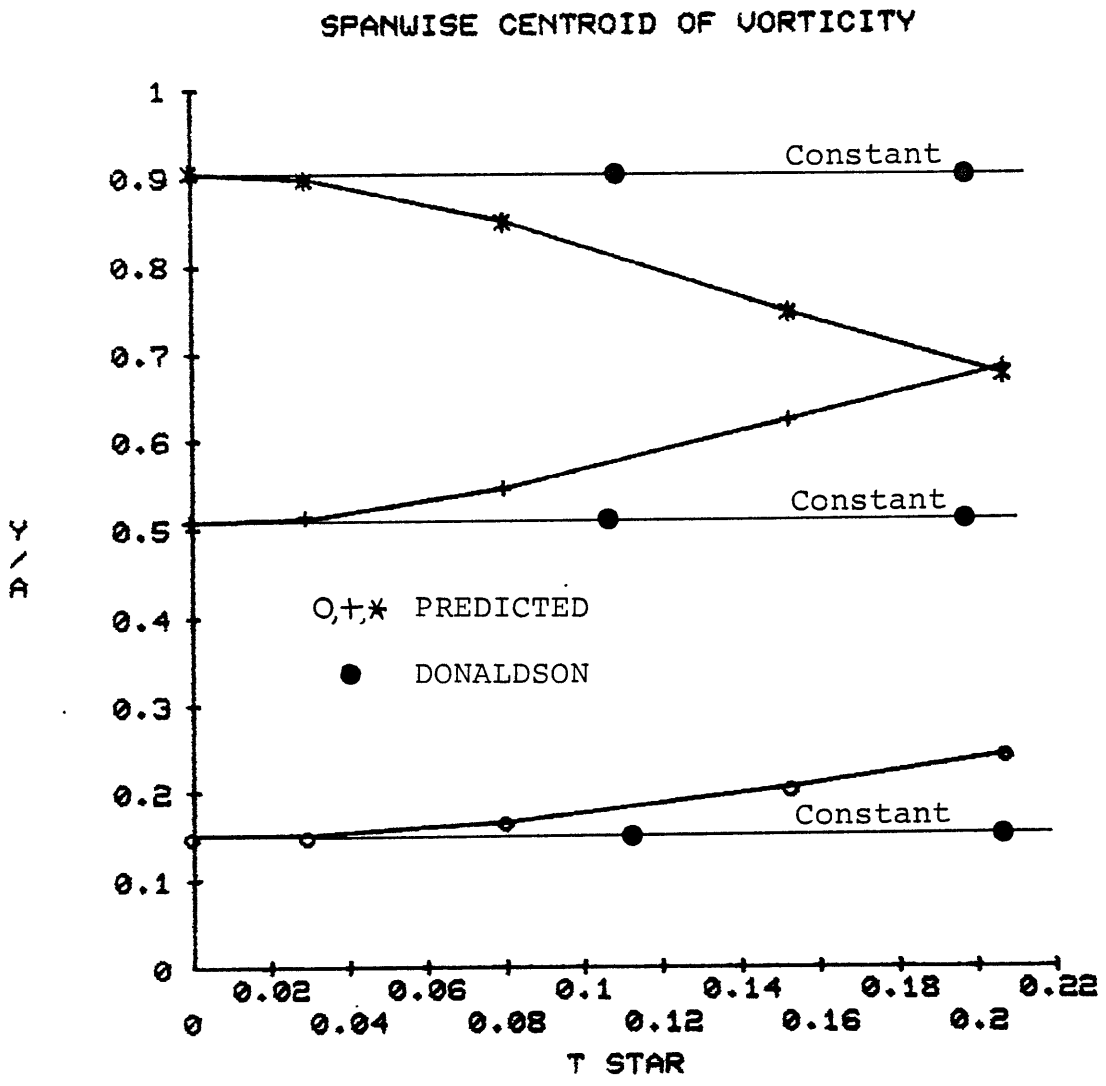

FIGURE 4.29 - SIMULATED FLAP LOADING - SPANWISE VARIATION OF VORTEX CENTROIDS WITH TIME

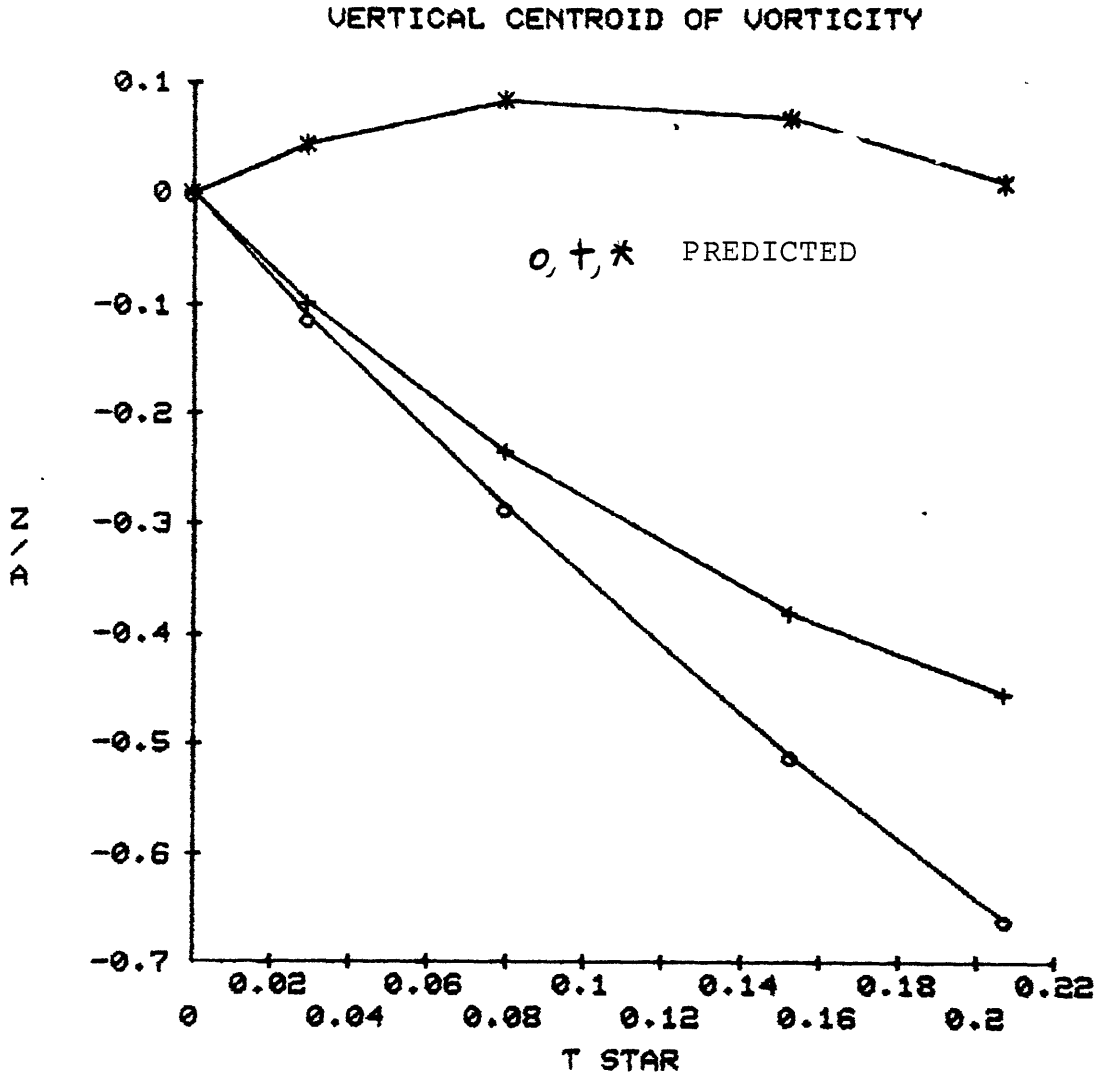

FIGURE 4.30 - SIMULATED FLAP LOADING - VERTICAL VARIATION OF VORTEX CENTROIDS WITH TIME

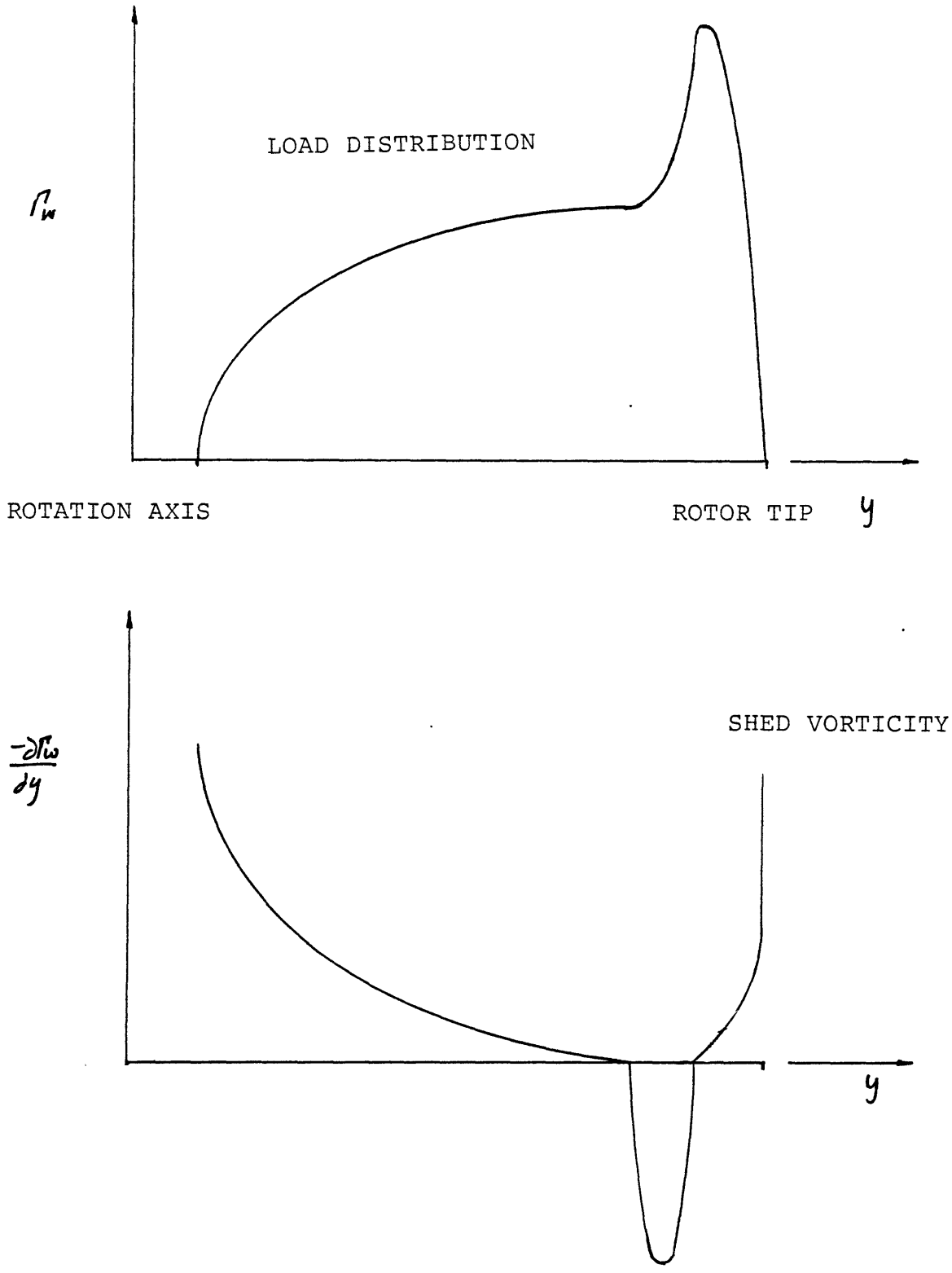

FIGURE 4.31 - WING LOADING AND SHED WAKE STRENGTH - ROTATING WING LOADING

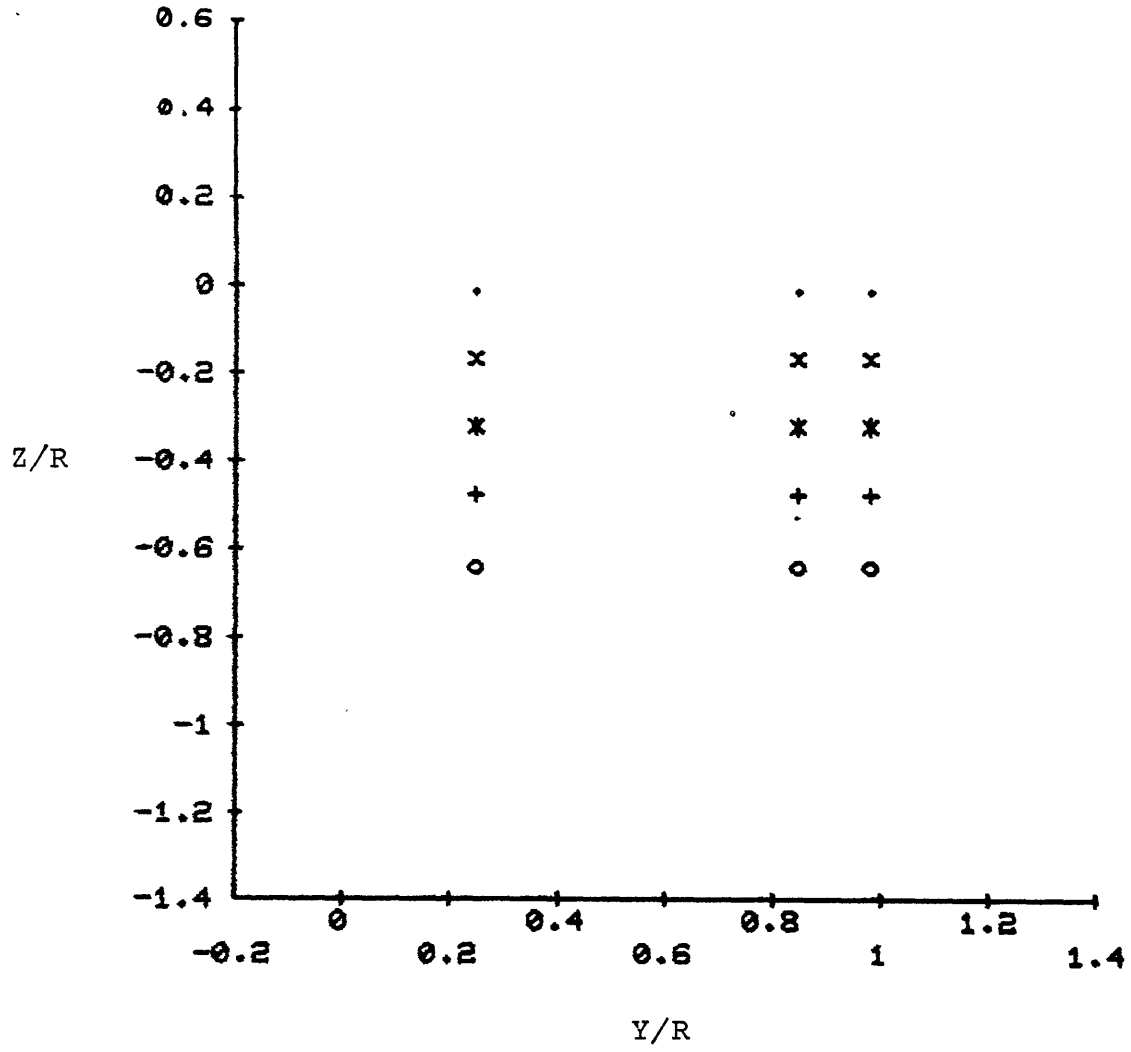

FIGURE 4.32a - ROTATING WING LOAD DISTRIBUTION - VORTEX WAKE GEOMETRY, NEAR WAKE REPRESENTED BY CONCENTRATED POINT VORTICES, 3 POINTS ON EACH VORTEX WAKE, GRID = 61x81, RELAXATION COEFFICIENT = .1

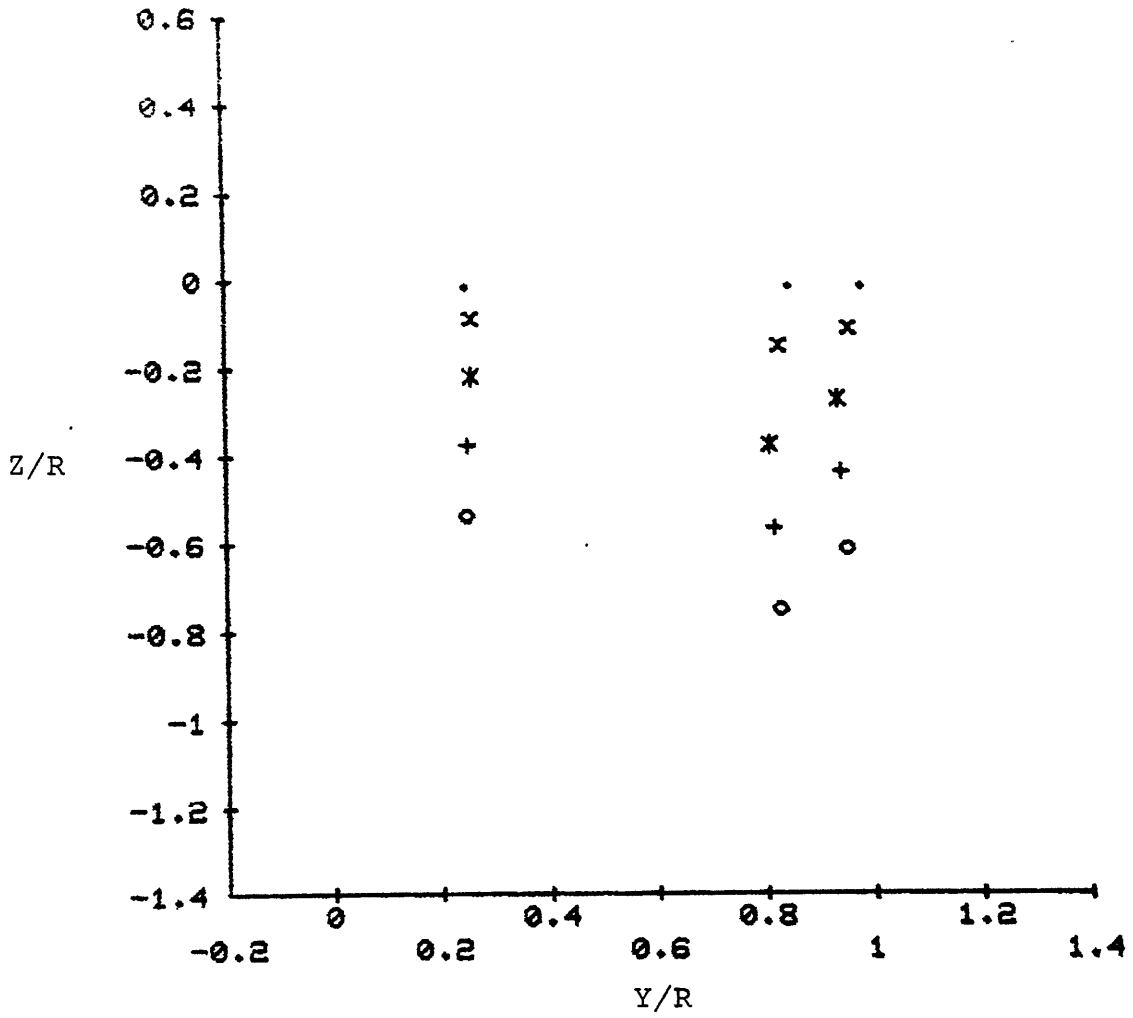

FIGURE 4.32b - WAKE ITERATION = 10

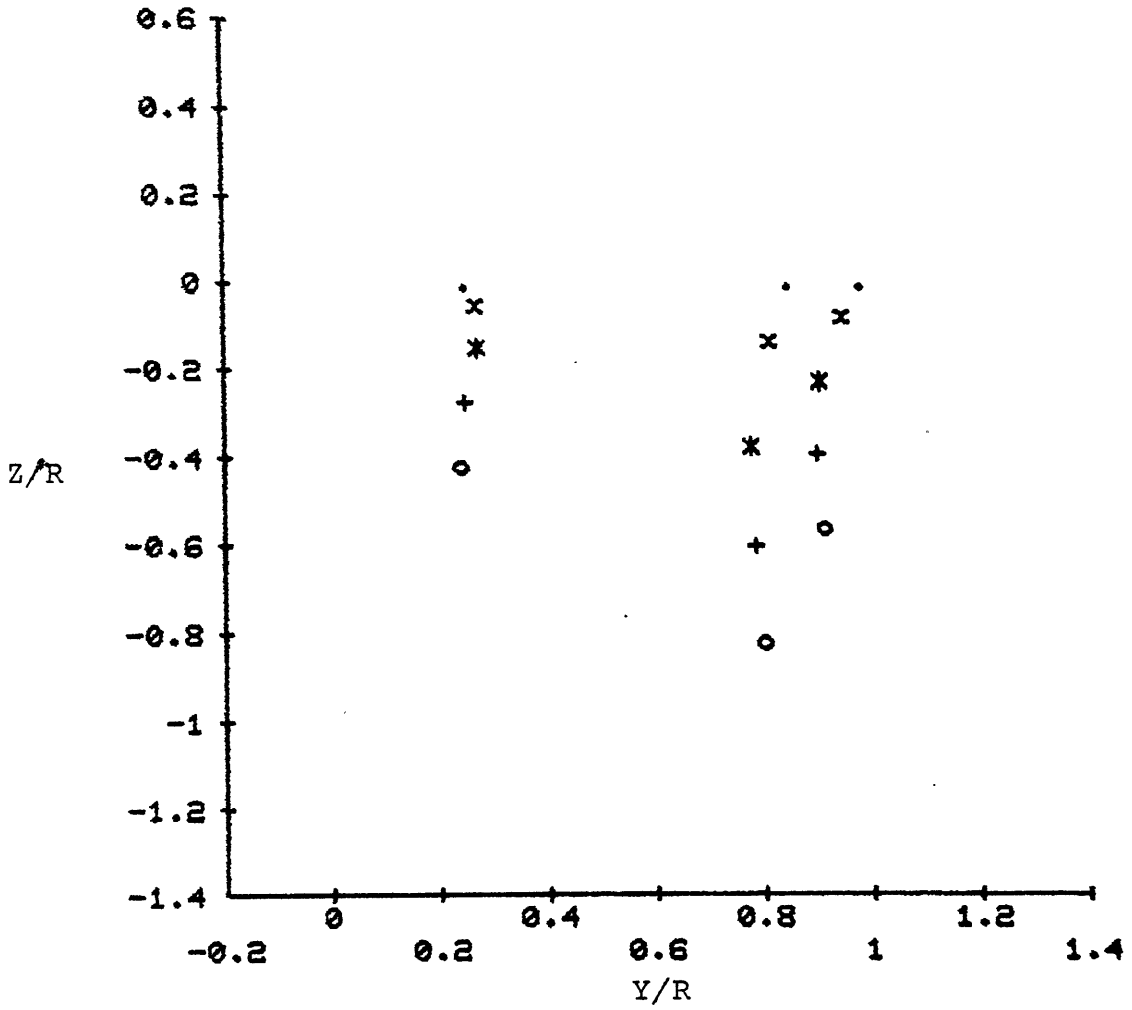

FIGURE 4.32c - WAKE ITERATION = 20

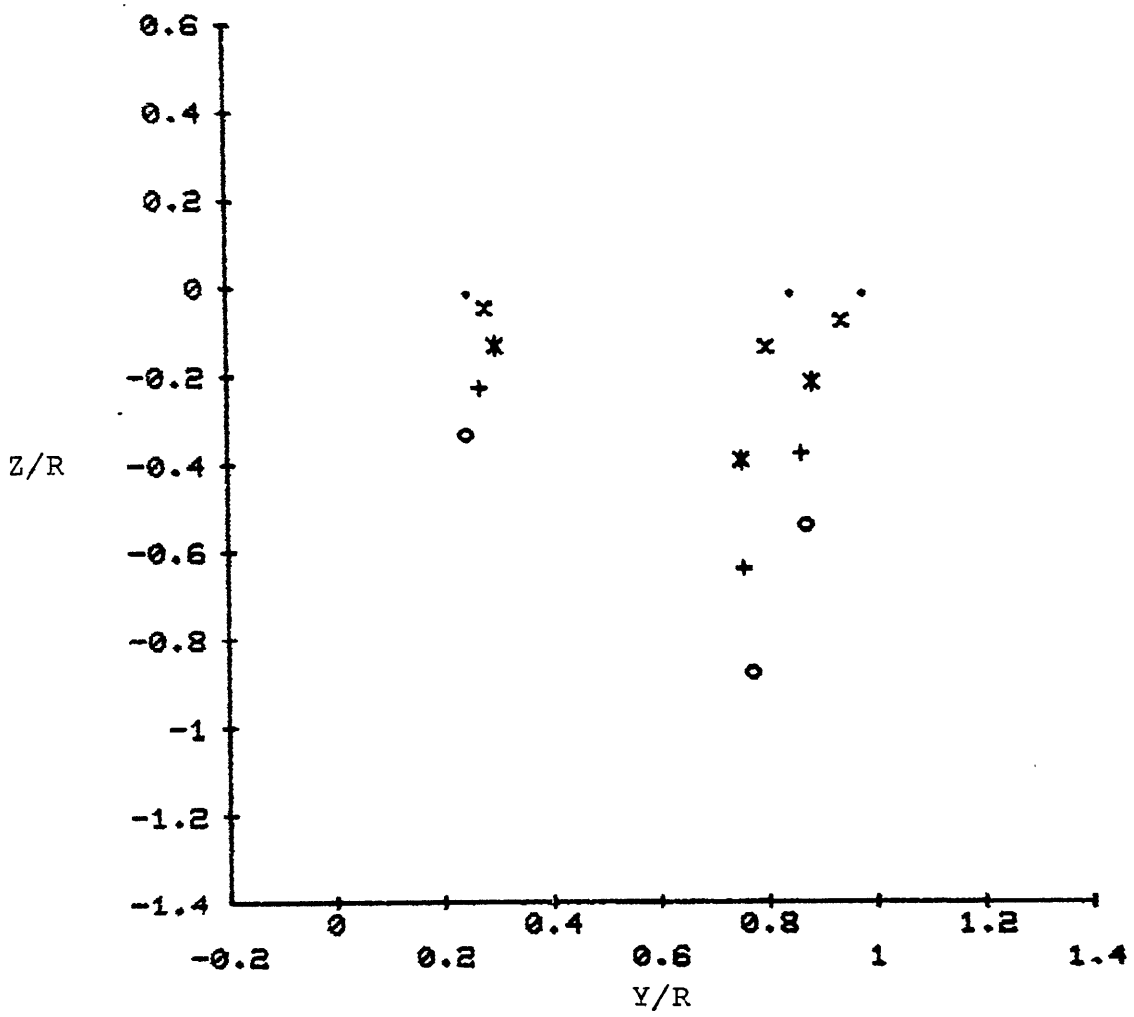

FIGURE 4.32d - WAKE ITERATION = 30

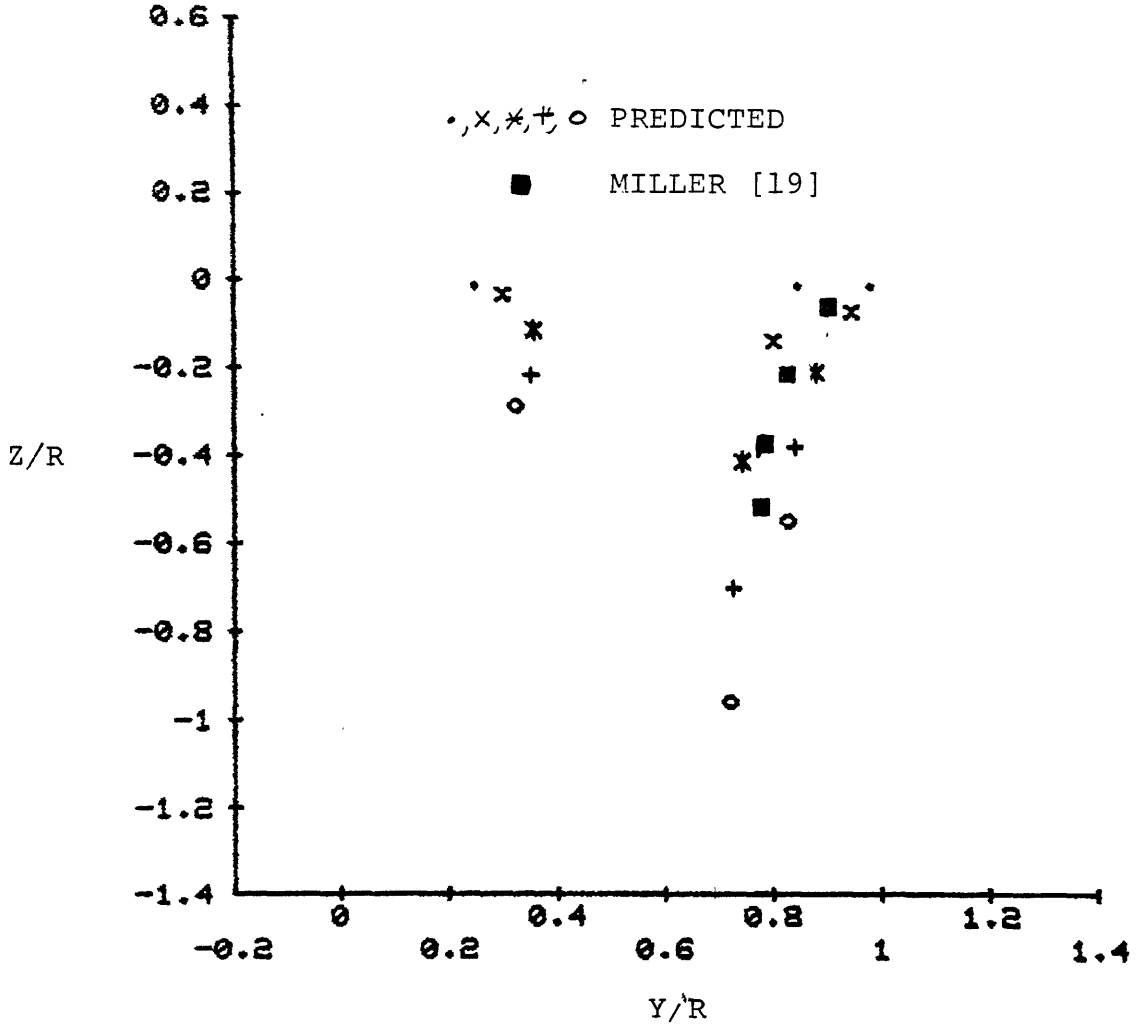

FIGURE 4.32e - WAKE ITERATION = 40

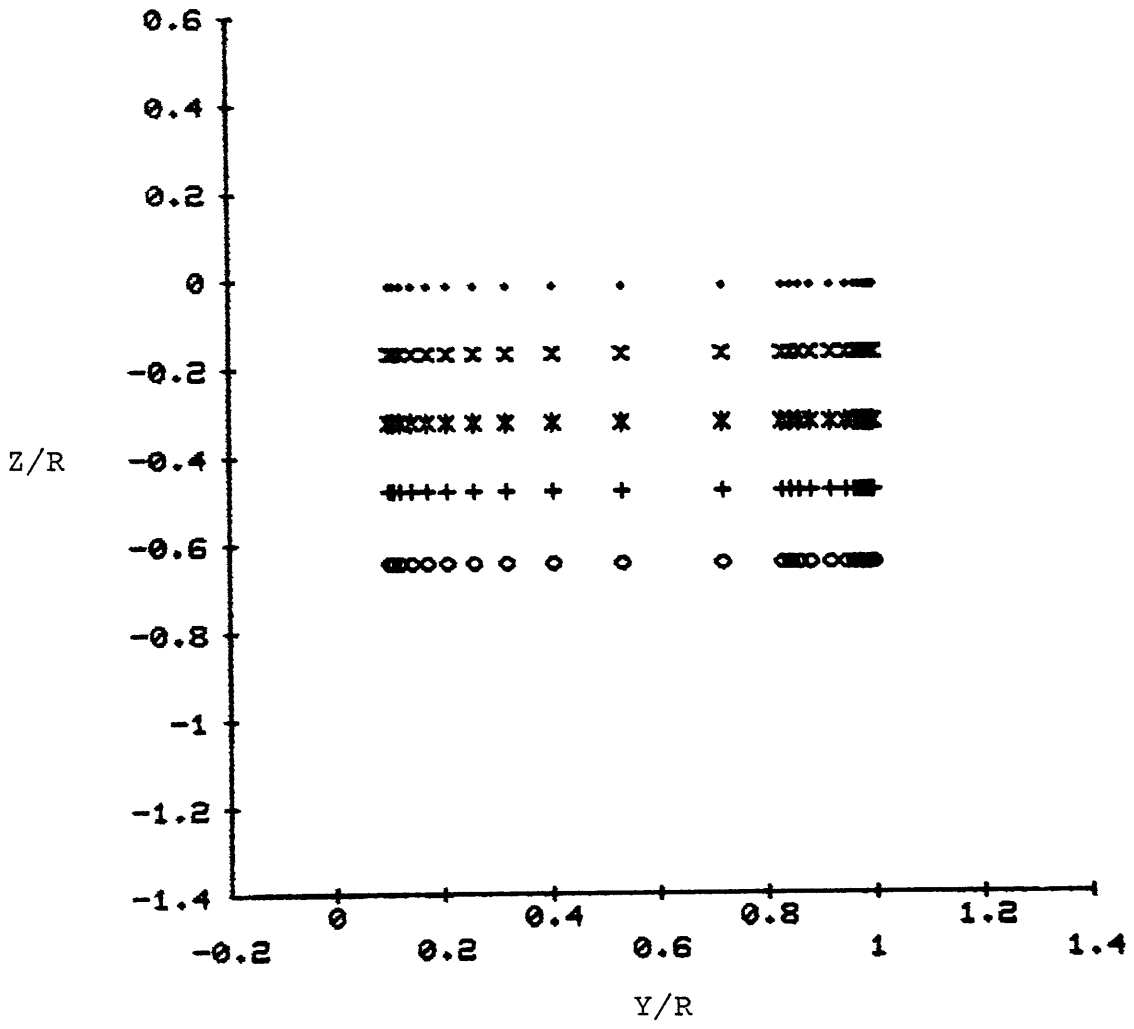

FIGURE 4.33a -ROTATING WING LOAD DISTRIBUTION - VORTEX WAKE GEOMETRY, NEAR WAKE REPRESENTED BY MANY POINT VORTICES, 30 POINTS ON EACH VORTEX WAKE, GRID = 61x81, RELAXATION COEFFICIENT = .2

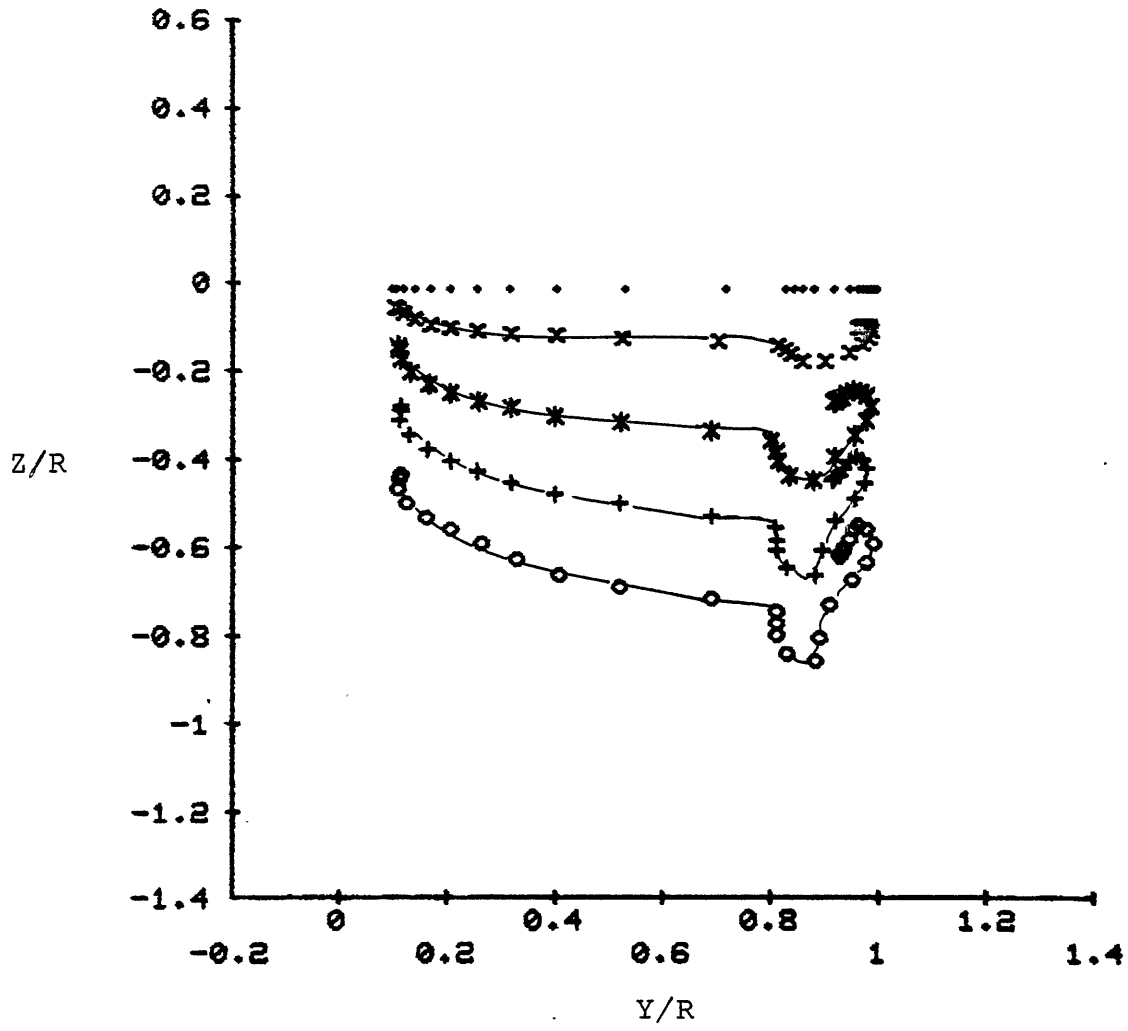

FIGURE 4.33b - WAKE ITERATION = 5

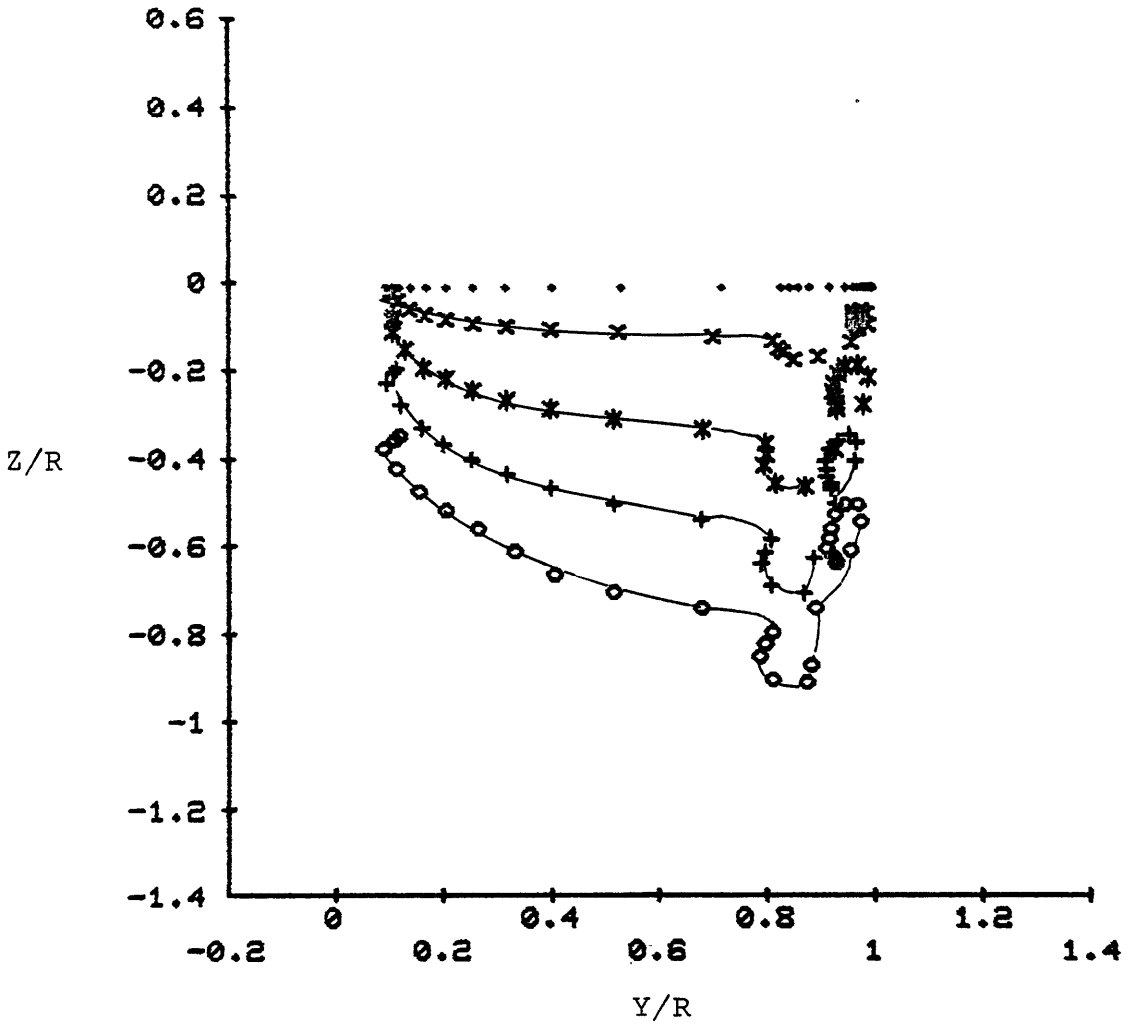

FIGURE 4.33c - WAKE ITERATION = 7

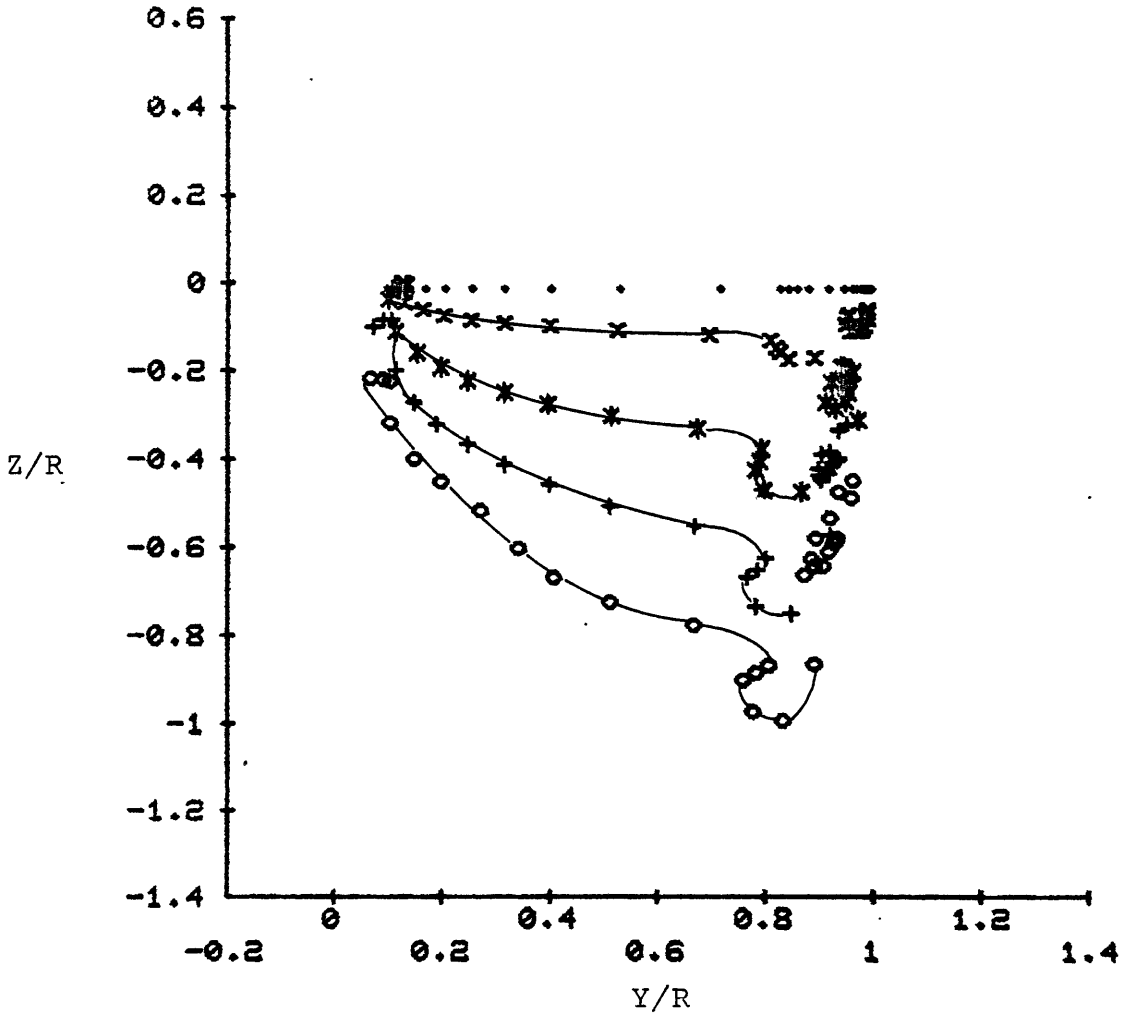

FIGURE 4.33d - WAKE ITERATION = 10

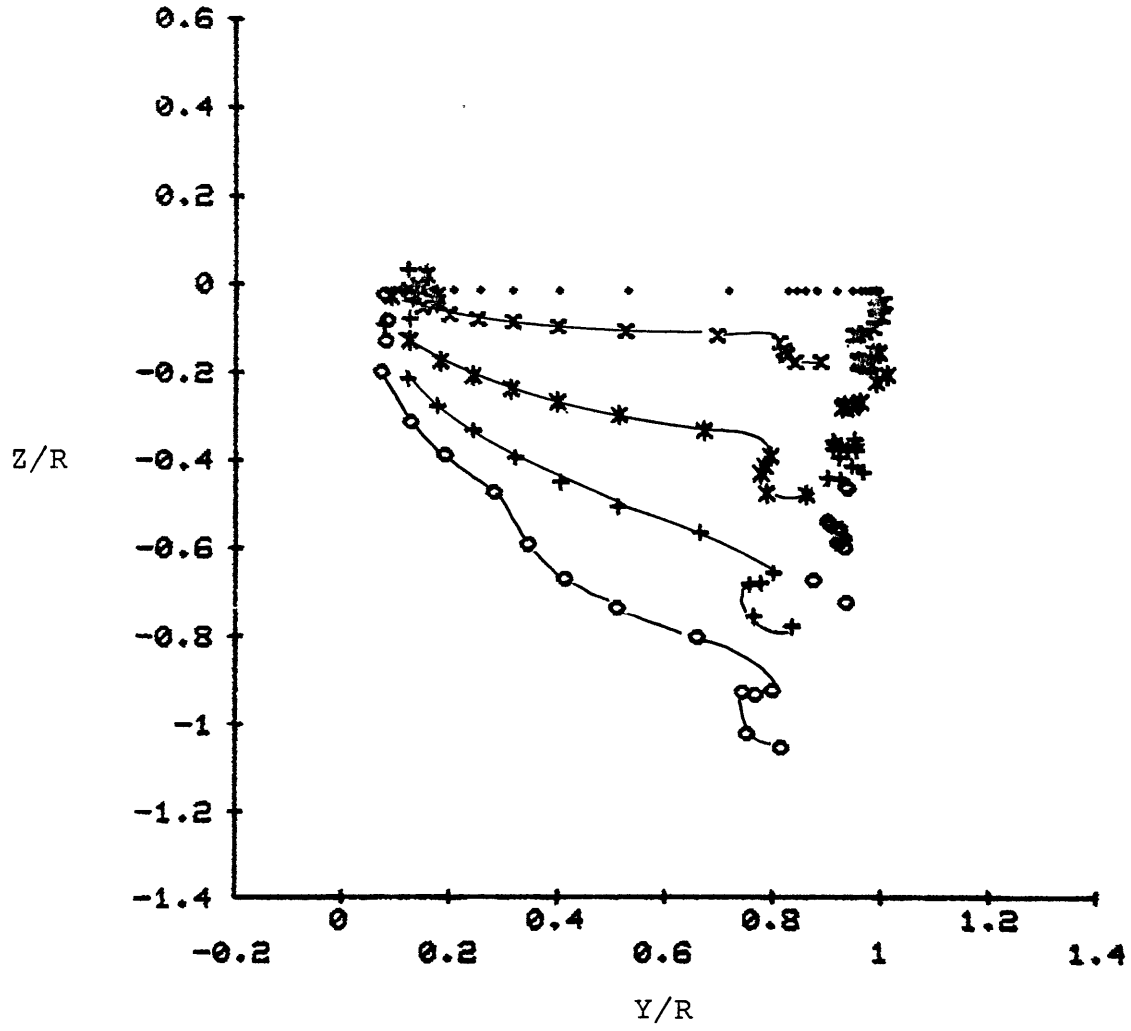

FIGURE 4.33e - WAKE ITERATION = 13

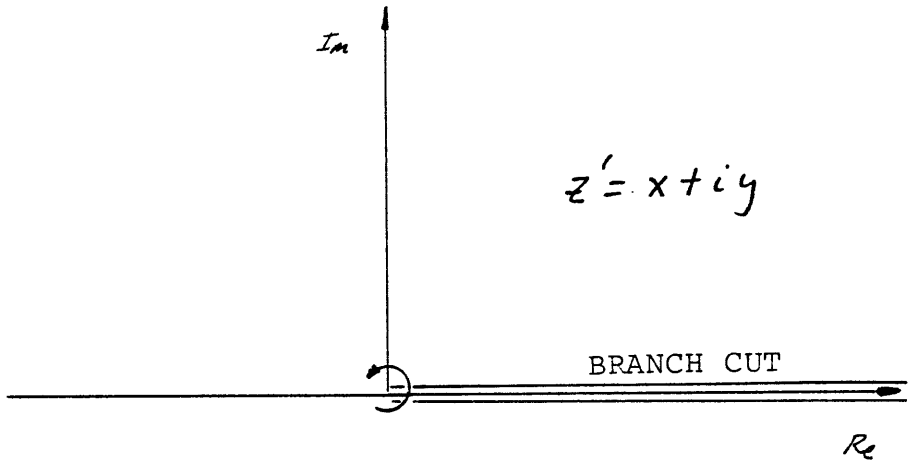

FIGURE A.1 - COMPLEX PLANE REPRESENTATION FOR A POINT VORTEX

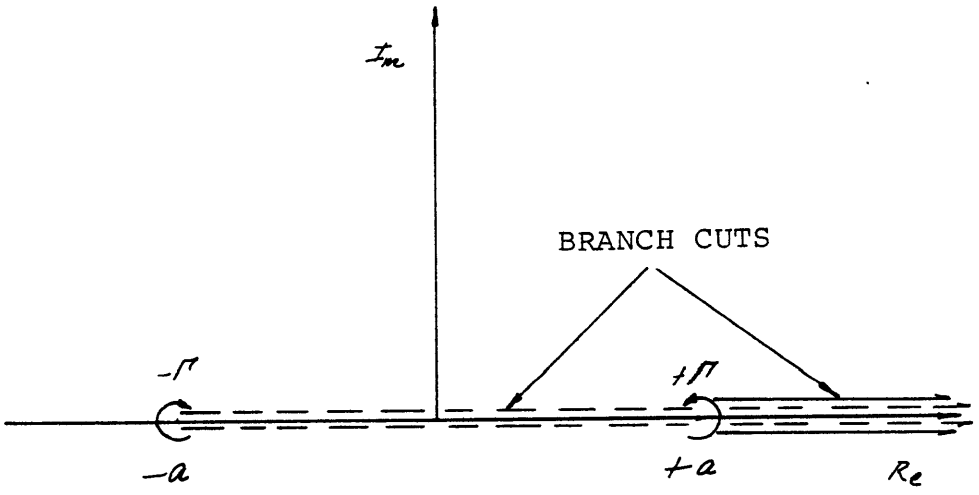

FIGURE A.2 - COMPLEX PLANE REPRESENTATION FOR A PAIR OF REFLECTED VORTICES

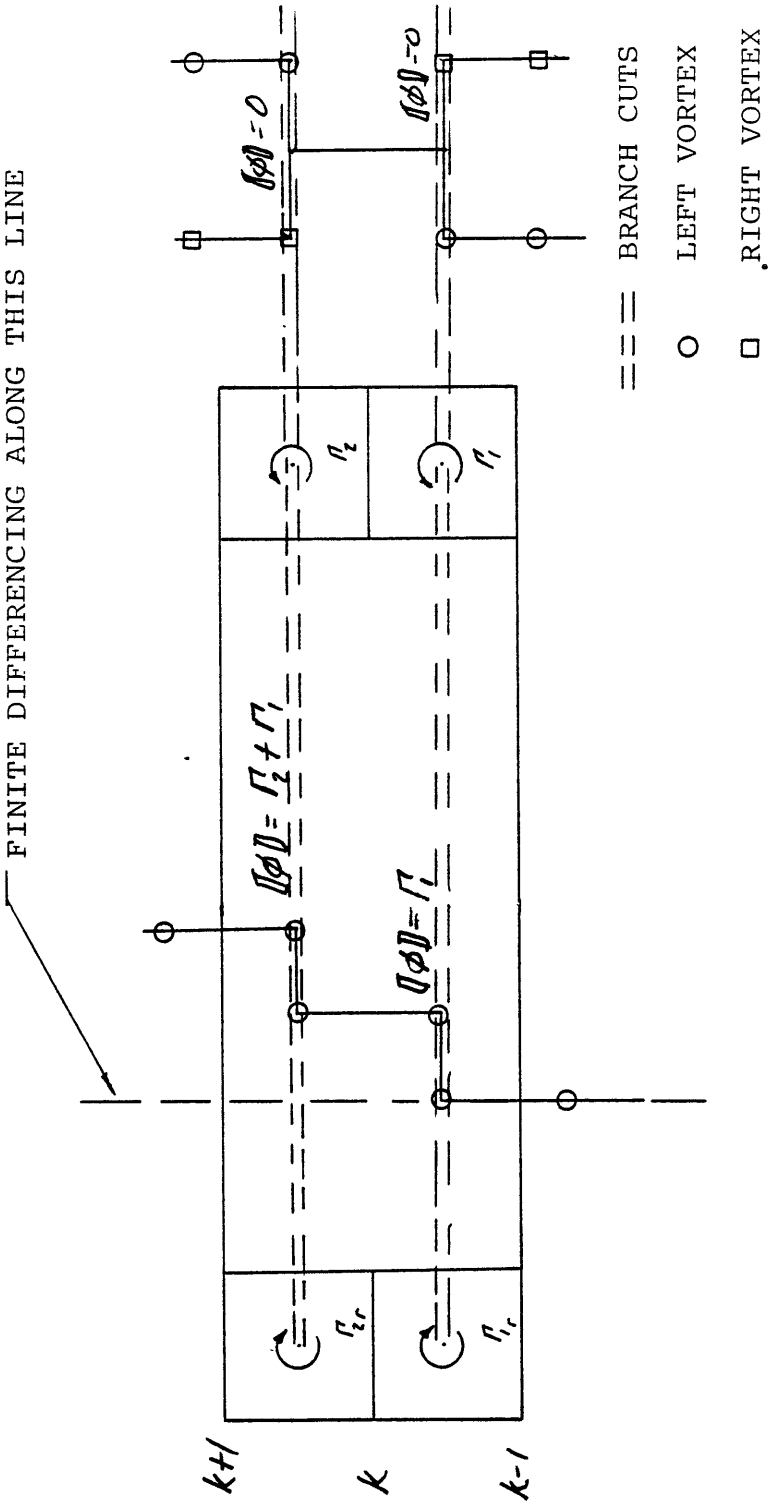

FIGURE A.3 - JUMP CONDITIONS ACROSS SINGULARITY BRANCH CUTS

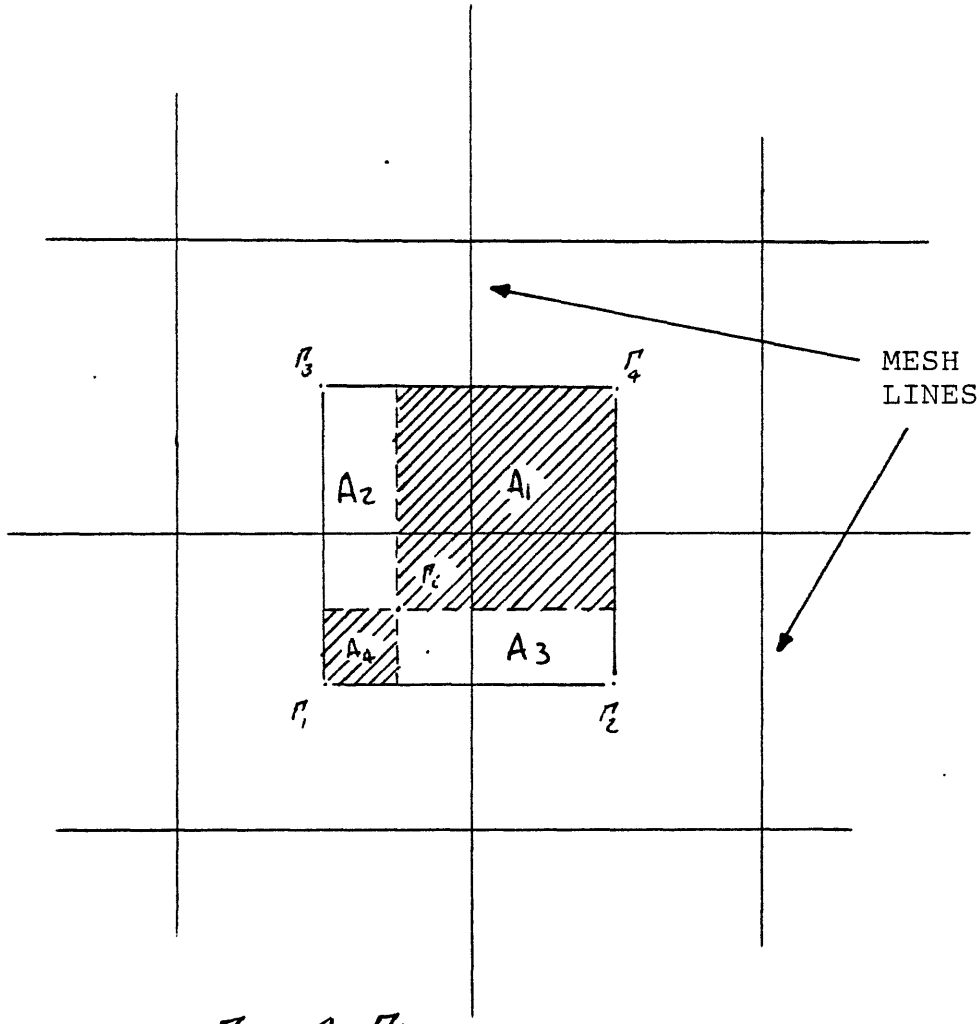

$$\Gamma_1 = A_1 \Gamma_i$$
$$\Gamma_2 = A_2 \Gamma_i$$
$$\Gamma_3 = A_3 \Gamma_i$$
$$\Gamma_4 = A_4 \Gamma_i$$

FIGURE B.1 - SCHEMATIC FOR "CLOUD IN CELL" REDISTRIBUTION SCHEME

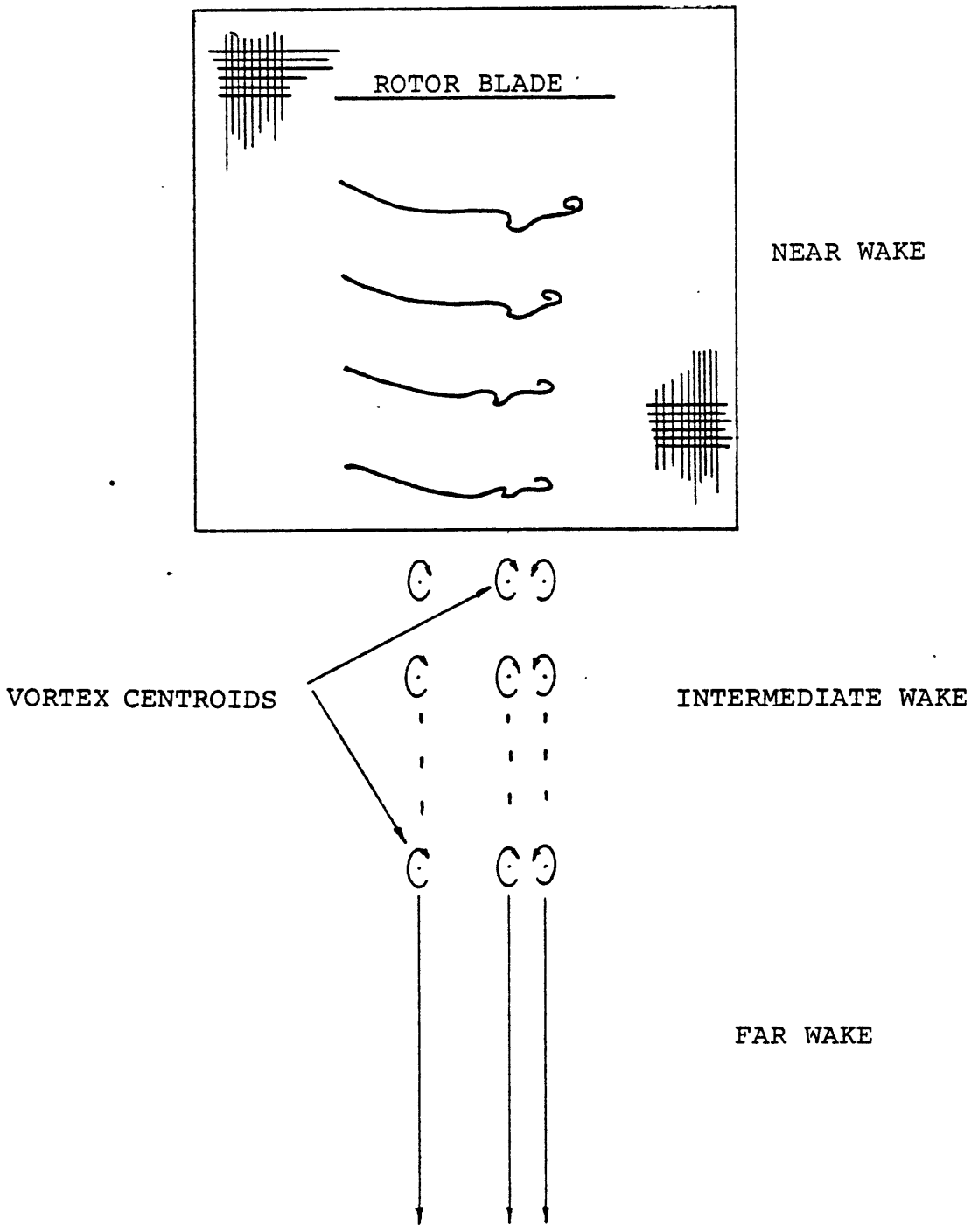

FIGURE C.1 - GEOMETRY OF ROTATING WING WAKE

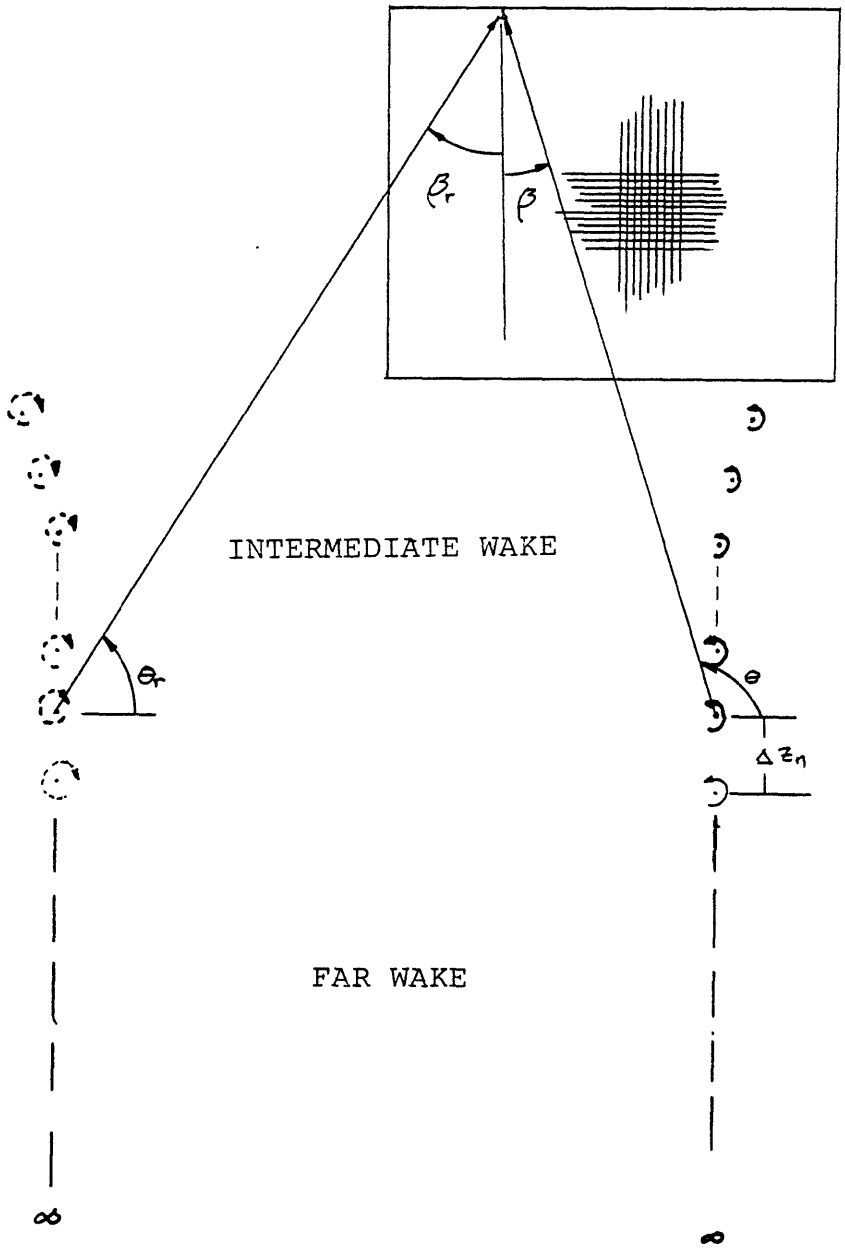

FIGURE C.2 - FAR WAKE MODEL

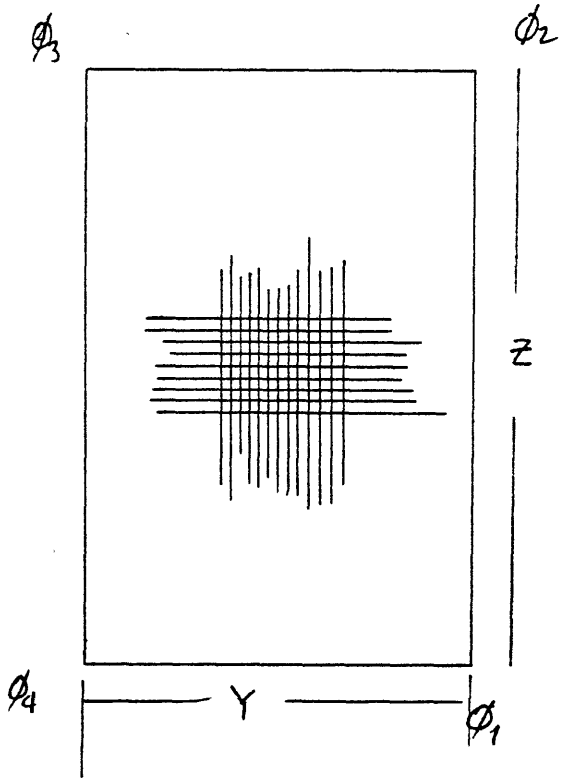

For Linear Velocity Profiles

$$\phi_2 = \phi_1 + (w_2 - w_1)\, z$$
$$\phi_3 = \phi_2 + (v_3 - v_2)\, y$$
$$\phi_4 = \phi_3 + (w_4 - w_3)\, z$$
$$\phi_1 = \phi_4 + (v_1 - v_4)\, y$$

$$\frac{\partial \phi}{\partial y} = v$$
$$\frac{\partial \phi}{\partial z} = w$$

FIGURE C.3 - FAR WAKE BOUNDARY CONDITION - INTEGRATION TECHNIQUES AROUND COMPUTATIONAL BOUNDARY

APPENDIX A

SINGLE VALUE RESTRICTIONS ON THE VELOCITY POTENTIAL

A.1 Jump Conditions

Development of the jump conditions across branch cuts for a single vortex and a reflected pair of vortices will be presented. The outlined procedure is directly applicable to N vortex points.

In the complex plane (see Figure A), consider a point vortex at the origin. Here z'=x+iy and is not to be confused with the use of the variable z in the Trefftz plane.

If, then, the complex potential is written for the single point vortex located at z'=0 in the form:

$$F(z') = \frac{-i\Gamma}{2\pi} \log(z') \tag{A.1}$$

where Γ is real and represents the strength of the vortex. The flow is counterclockwise for $\Gamma > 0$.

The representation of log (z') is written:

$$\log(z') = \log|z'| + i(\theta_p + 2\pi m) \tag{A.2}$$
$$m = 0, \pm 1, \pm 2 \cdots$$

Here, $|z'|$ is the magnitude of the position vector and θ_p is the principal angle measured from the positive real axis.

The complex potential can be expressed in terms of the stream function and velocity potential in the form:

$$F(z') = \phi + i\psi \tag{A.3}$$

Then, from equations A.1-A.3, the stream function and velocity potential become:

$$\psi = \frac{\Gamma}{2\pi} \log|z'|$$

$$\phi = \frac{\Gamma}{2\pi}(\theta_p + 2\pi m), \quad m = 0, \pm 1, \pm 2 \ldots \tag{A.4}$$

The stream function is included here for completeness and will not be discussed further.

There follows from equation A.4:

$$\phi = \frac{\Gamma}{2\pi}\theta_p \quad , \quad m = 0$$
$$\phi = \frac{\Gamma}{2\pi}(\theta_p + 2\pi), \quad m = 1$$
$$\phi = \frac{\Gamma}{2\pi}(\theta_p + 4\pi), \quad m = 2 \quad \text{etc.}$$

Here, the value of the potential is increased by the strength of the vortex after each cycle around a path encircling the vortex. In order to keep ϕ single valued each time, θ_p passes through zero, a branch cut must be introduced and Γ must be subtracted from the potential as θ_p passes from $\theta_p = 0^-$ to $\theta_p = 0^+$.

The jump condition across the branch cut for this flow becomes:

$$[\![\phi]\!] = \phi^+ - \phi^- = -\Gamma \qquad \text{(A.5)}$$

and is enforced all along the branch cut $0 \le y \le \infty$.

Here, ϕ^+, ϕ^- represent the values of the potential above and below the branch cut, respectively.

The extension to a reflected pair of vortices at z'=±a has the following form (see Figure A.2). Equation A.1 for the complex potential has the form:

$$F(z') = \frac{-\Gamma}{2\pi} \log(z'-a) + \frac{\Gamma}{2\pi} \log(z'+a) \qquad \text{(A.6)}$$

then for r_1' = z'-a (position vector from a to z')

r_2' = z'+a (position vector from -a to z')

and with the notation of equation A.2, the stream function and velocity potential take on the form:

$$\Psi = -\frac{\Gamma}{2\pi} \log\left(|r_1'|/|r_2'|\right)$$

$$\phi = \frac{\Gamma}{2\pi}\left[(\theta_1 + 2\pi m) - (\theta_2 + 2\pi n)\right] \qquad \text{(A.7)}$$

m,n = 0, ±1, ±2, ±3, ...

Here, θ_1, θ_2 are the position angles of the vortices and are measured from the positive real axis. Again, the form for the stream function is included for completeness.

Then, for the right vortex (z'=a), equation A.7 takes on the values:

$$\phi = \frac{\Gamma}{2\pi}\theta_1 \quad , \quad m=0$$

$$\phi = \frac{\Gamma}{2\pi}(\theta_1 + 2\pi) \quad , \quad m=1$$

etc.

Here, again, after each cycle, the velocity potential is increased by the vortex strength. However, this jump is only applied on the branch cut extending from z'=a to + infinity along the real axis. The jump condition becomes:

$$[\![\phi]\!] = \phi^+ - \phi^- = -\Gamma \quad , \quad a \le y \le \infty \qquad \text{(A.8)}$$

For the left vortex, equation A.7 has the form:

$$\phi = -\frac{\Gamma}{2\pi}\theta_2 \quad , \quad n=0$$

$$\phi = -\frac{\Gamma}{2\pi}(\theta_2 + 2\pi) \quad , \quad n=1$$

etc.

After each cycle, the velocity potential is decreased by the value of the vortex strength. The jump condition for the left vortex becomes:

$$[\![\phi]\!] = \phi^+ - \phi^- = \Gamma \quad , \quad -a \le y \le \infty \qquad \text{(A.9)}$$

The jump conditions cancel identically on the ray $a \leq y \leq \infty$ and vanish to the left of the left vortex. Between the vortices, the jump conditions are determined by the left vortex only and have the form of equation A.9.

The next section will discuss the application of the jump conditions to the finite difference forms of the governing equation.

A.2 Finite Difference and Non-dimensional Forms

Keeping in mind the results of the previous section and writing equation 2.1 and 2.2b in finite difference forms, the following can be found.

Because the jump condition is normal to the branch cut, this condition will appear in the derivatives normal to the cut only, i.e., derivatives with respect to y are unchanged by the jump conditions.

Consider two reflected vortex pairs, the strengths of these pairs being Γ_1 and Γ_2. Figure A.3 will help to visualize the representation. The jump conditions for the four vortices from equations A.8 and A.9 are represented by the step functions on the figure. Again, notice that the jump conditions cancel to the right of the right vortex. For the positions indicated, k, k+1 and k-1, the second partial derivative of the potential with respect to z in finite difference form, becomes:

$$\bar{\phi}_{zz})_k = \frac{\bar{\phi}_z)_{k+1/2} - \bar{\phi}_z)_{k-1/2}}{\Delta z}$$

$$\bar{\phi}_{zz})_k = \frac{\bar{\phi}_{k+1} - 2\bar{\phi}_k + \bar{\phi}_{k-1}}{\Delta z}$$

The bar is used here to indicate that the finite differences are not taken along a reference line, i.e., a line on which the values of the potential are unique. If, instead, the finite differences are evaluated along the dashed line of Figure A.3, a new form for ϕ_{zz} is obtained.

$$\phi_{zz})_k = \frac{\phi_{k+1} - \Gamma_1 - \Gamma_2 - 2(\phi_k - \Gamma_1) + \phi_{k-1}}{\Delta z^2}$$

$$\phi_{zz})_k = \frac{\phi_{k+1} - 2\phi_k + \phi_{k-1}}{\Delta z^2} + \frac{(\Gamma_1 - \Gamma_2)}{\Delta z^2} \qquad \text{(A.10)}$$

In a similar way, the results at k+1 and k-1 are obtained and have the forms:

$$\phi_{zz})_{k+1} = \frac{\phi_{k+2} - 2\phi_{k+1} + \phi_k}{\Delta z^2} + \frac{\Gamma_2}{\Delta z^2} \qquad \text{(A.11)}$$

$$\phi_{zz})_{k-1} = \frac{\phi_k - 2\phi_{k-1} + \phi_{k-2}}{\Delta z^2} - \frac{\Gamma_1}{\Delta z^2} \qquad \text{(A.12)}$$

The finite difference forms of the w velocity are found similarly and have the forms:

$$w)_k = \frac{\partial \bar{\phi}}{\partial z})_k = \frac{\phi_{k+1} - \phi_{k-1}}{2\Delta z} \qquad \text{(A.13)}$$

$$w)_k = \frac{\phi_{k+1} - \Gamma_1 - \Gamma_2 - \phi_{k-1}}{2\Delta z}$$

$$w)_{k+1} = \frac{\phi_{k+2} - \phi_k}{2\Delta z} - \frac{\Gamma_2}{2\Delta z} \qquad (A.14)$$

and

$$w)_{k-1} = \frac{\phi_k - \phi_{k-2}}{2\Delta z} - \frac{\Gamma_1}{2\Delta z} \qquad (A.15)$$

Using the convention of equation 2.11, the non-dimensional forms of equation 2.12 and 2.13b, in finite difference form, applicable at the branch cut become; @ j,k

$$\frac{\phi^*_{j+1,k} - 2\phi^*_{j,k} + \phi^*_{j-1,k}}{\Delta j^{*2}} + \frac{\phi^*_{j,k+1} - 2\phi^*_{j,k} + \phi^*_{j,k-1}}{\Delta z^{*2}} = \frac{2\pi}{\Delta z^{*2}}\left[\Gamma_2^* - \Gamma_1^*\right] \qquad (A.16)$$

and

$$w^* = \frac{\phi^*_{j,k+1} - \phi^*_{j,k-1}}{2\Delta z^*} - \frac{\pi\left(\Gamma_1^* + \Gamma_2^*\right)}{\Delta z^*} \qquad (A.17)$$

For the rotating wing calculations, with the conventions of equation 2.16, the non-dimensional forms of equations 2.17 and 2.18b, in finite difference form, applicable at the branch cut become; @ j,k

$$\frac{\phi^*_{j+1,k} - 2\phi^*_{j,k} + \phi^*_{j-1}}{\Delta y^{*2}} - \frac{\phi^*_{j,k+1} - 2\phi^*_{j,k} + \phi^*_{j,k-1}}{\Delta z^{*2}} = \frac{1}{\Delta z^{*2}}\left(\Gamma_2^* - \Gamma_1^*\right) \tag{A.18}$$

and

$$w^* = \frac{\phi^*_{j,k+1} - \phi^*_{j,k-1}}{2\Delta z^*} - \frac{\left(\Gamma_1^* + \Gamma_2^*\right)}{2\Delta z^*} \tag{A.19}$$

Equations A.17 and A.19 are applicable to central differencing over two mesh spaces. The forms of A.17 and A.19 for differencing over one mesh cell become, respectively.

$$w^*_{k+\frac{1}{2}} = \frac{\phi^*_{j,k+1} - \phi^*_{j,k}}{\Delta z^*} - \frac{2\pi\left(\Gamma_1^* + \Gamma_2^*\right)}{\Delta z^*} \tag{A.20}$$

$$w^*_{k+\frac{1}{2}} = \frac{\phi^*_{j,k+1} - \phi^*_{j,k}}{\Delta z^*} - \frac{\left(\Gamma_1^* + \Gamma_2^*\right)}{\Delta z^*} \tag{A.21}$$

APPENDIX B

REDISTRIBUTION OF POINT SINGULARITIES

The method outlined here is similar to the "CIC" method. However, the singularity is redistributed to the centroid of the four nearest cells and not the node points (as developed in [4] and [5]). In addition, the velocities of the vortex markers are determined from only the mesh cells affected by the singularity redistribution. The discussion of these two techniques follows.

As outlined in Appendix A, the jump conditions for any point vortex are applied to the mesh nodes adjacent to the branch cut of the singularity. In order to accurately model the branch cut, the point vortex must reside at the centroid of the mesh cell. However, in reality, the point vortex will rarely reside at the centroid of the mesh cell and, therefore, must be redistributed to the centroids of the four nearest mesh cells using bilinear interpolation. The branch cuts are now extended from the newly redistributed vortex markers and the appropriate jump conditions applied across each branch cut. To illustrate this, consider a point vortex of strength Γ_i^* located at position (y_i^*, z_i^*). See Figure B.1.

Let δ_y^*, δ_z^* be the normalized distances from the vortex marker to the mesh node connecting the four nearest mesh cells. Then, if the coordinates of this mesh point are (y_j^*, z_k^*):

$$\delta_y^* = (y_i^* - y_j^*) / \Delta y^*$$

$$\delta_z^* = (z_i^* - z_k^*) / \Delta z^*$$

where $\Delta y^*, \Delta z^*$ represent the mesh spacing.

Then,

$$\begin{aligned} A_1 &= (.5-\delta_y)(.5-\delta_z) \\ A_2 &= (.5+\delta_y)(.5-\delta_z) \\ A_3 &= (.5-\delta_y)(.5+\delta_z) \\ A_4 &= (.5+\delta_y)(.5+\delta_y) \end{aligned} \qquad \text{(B.1)}$$

and

$$\begin{aligned} \Gamma_1^* &= A_1 \Gamma_i^* \\ \Gamma_2^* &= A_2 \Gamma_i^* \\ \Gamma_3^* &= A_3 \Gamma_i^* \\ \Gamma_4^* &= A_4 \Gamma_i^* \end{aligned}$$

The jump conditions of Appendix A can now be applied to the four vortex markers.

The velocity of the point vortex is determined from the velocity potential at the corner nodes of the four nearest mesh cells. The v velocity is determined at the midpoints of the horizontal (z = constant) sides of the mesh cells and the

w velocity at the midpoints of the vertical (y = constant) sides. In determining the velocity components, central difference approximations (over one mesh spacing) to the gradient of the velocity potential are evaluated. When calculating the w velocity component, jump conditions must be applied where appropriate (see equations A.20 and A.21). The value of the velocity at the centroid is determined by averaging the velocities on opposite sides.

Then,

$$V_1^* = .5\left[\left(\frac{\phi^*_{j,k-1} - \phi^*_{j-1,k-1}}{\Delta y^*}\right) + \left(\frac{\phi^*_{jk} - \phi^*_{j-1,k}}{\Delta y^*}\right)\right] \quad \text{(B.2)}$$

and similar expressions for $V2^*$, $V3^*$ and $V4^*$.

With the notation of equation A.20, the following forms are found:

$$W_5^* = \frac{\phi^*_{j-1,k} - \phi^*_{j-1,k-1}}{\Delta z^*} - \frac{2\pi(\Gamma_1^* + \Gamma_2^*)}{\Delta z^*}$$

$$W_6^* = \frac{\phi^*_{jk} - \phi^*_{jk-1}}{\Delta z^*} - \frac{2\pi\Gamma_2^*}{\Delta z^*} \quad \text{(B.3)}$$

with similar expressions for $W7^*$, $W8^*$, $W9^*$ and $W10^*$, see Figure B.1. Similar expressions hold for rotating wing analysis and are determined from equation A.21.

The results of equation B.3 yield:

$$w_1^* = .5(w_5^* + w_6^*)$$

$$w_2^* = .5(w_6^* + w_7^*) \qquad \text{(B.4)}$$

etc.

The velocities at the vortex marker are determined from equations B.1, B.2 and B.4 and become for this case:

$$V_i^* = A_1 V_1^* + A_2 V_2^* + A_3 V_3^* + A_4 V_4^* \qquad \text{(B.5)}$$

$$W_i^* = A_1 W_1^* + A_2 W_2^* + A_3 W_3^* + A_4 W_4^* \qquad \text{(B.6)}$$

This method of singularity distribution and determination of the vortex marker velocity is readily extended to N singularities.

APPENDIX C

ROTATING WING - NEAR AND FAR WAKE MODELS

In hover, a rotating wing generates a semi-infinite helical wake originating at the rotor plane and extending to negative infinity. The wake is divided into three parts: 1) the near wake or wakes inside the computational domain; 2) the intermediate wake; and 3) the far wake. The effects of the intermediate and far wakes on the velocity potential at the computational boundaries will be discussed here. The wake representation is illustrated in Figure C.1.

Intermediate Wake - The intermediate wake is modeled by only a few discrete point vortices instead of the many vortex markers used in the near wake. The intermediate wake consists of ten wakes separated by a wake spacing Δz_w with each wake represented by three concentrated point vortices with strength predicted by Betz's theory (Section 2.1.3). Here, Δz_w represents the z spacing between similar vortex centroids (tip vortices for instance) on the last two wakes in the near wake representation. These three vortices in each wake have the same y location as the corresponding centroid at the last near wake. Using this representation, the boundary condition for the velocity potential due to the intermediate wake can be written (from equation 2.19):

$$\phi^* = \frac{1}{2\pi} \sum_{NI} \Gamma_i \theta_i \qquad \text{(C.1)}$$

where NI is the sum of the concentrated point vortices and the image vortices in the intermediate wake.

Far Wake - Beyond the intermediate wake, the influence of each wake vortex is less dominant and an asymptotic summation may be made. If the far wake was modeled as an infinite number of terms similar to those of the intermediate wake model, the velocity potential calculated by summing the terms would be unbounded. While the velocity potential tends to infinity for an infinite number of terms, the induced flow field velocities for an infinite number of terms would tend to a constant. Therefore, the far wake effects are modeled using relations for the induced velocities. The velocity potential can then be calculated by integrating from the values of the induced velocities along the sides of the computational domain.

Consider the model represented by Figure C.2. This figure illustrates the far wake model and the corresponding reflected images. The method that follows is for the tip vortex and the reflected tip vortex. Extensions to the two remaining pairs of vortices would follow directly.
Then,

$$\theta = \pi/2 - \beta \quad , \quad \theta_r = \pi/2 - \beta_r \qquad \text{(C.2a, b)}$$

and

$$\beta = \tan^{-1}\left(y-y_t / z-z_n \right)$$

$$\beta_r = \tan^{-1}\left(y+y_t / z-z_n \right) \qquad \text{(C.3a, b)}$$

where y_t is the y coordinate of the tip vortex centroid in the far wake and z_n is the z coordinate of the nth shed wake measured from the rotor plane.

The arguments of equations C.3a, b can be expanded to read:

$$\frac{y-y_t}{z-z_n} = \frac{y-y_t}{-z_n}\left[1 + \frac{z}{z_n} + \left(\frac{z}{z_n}\right)^2 + \left(\frac{z}{z_n}\right)^3 + \text{h.o.t.} \right]$$

and

$$\frac{y+y_t}{z-z_n} = \frac{y+y_t}{-z_n}\left[1 + \frac{z}{z_n} + \left(\frac{z}{z_n}\right)^2 + \left(\frac{z}{z_n}\right)^3 + \text{h.o.t.} \right]$$

When β is sufficiently small and the expansions of equations C.3a, b are inserted into equations C.2a, b, the following forms are found:

$$\theta = \frac{\pi}{2} - \frac{y-y_t}{-z_n}\left[1 + \frac{z}{z_n} + \left(\frac{z}{z_n}\right)^2 + \left(\frac{z}{z_n}\right)^3 \right] + \frac{1}{3}\left(\frac{y-y_t}{-z_n}\right)^3 \left[1 + \frac{z}{z_n} + \left(\frac{z}{z_n}\right)^2 + \left(\frac{z}{z_n}\right)^3 \right]^3 \qquad \text{(C.4a)}$$

$$\theta_r = \frac{\pi}{2} - \frac{y+y_t}{-z_n}\left[1 + \frac{z}{z_n} + \left(\frac{z}{z_n}\right)^2 + \left(\frac{z}{z_n}\right)^3 \right] + \frac{1}{3}\left(\frac{y+y_t}{-z_n}\right)^3 \left[1 + \frac{z}{z_n} + \left(\frac{z}{z_n}\right)^2 + \left(\frac{z}{z_n}\right)^3 \right]^3 \qquad \text{(C.4b)}$$

The potential of the nth vortex is represented by the equation:

$$\phi = \frac{\Gamma_t}{2\pi}(\theta - \theta_r)$$

or

$$\phi = \frac{\Gamma_t}{2\pi}\left[-\frac{2y_t}{z_n} - \frac{2y_t z}{z_n^2} - \frac{2y_t z^2}{z_n^3} - \frac{2y_t z^3}{z_n^4} + \frac{2y_t y^2}{z_n^3} + \frac{6y^2 y_t z}{z_n^4} + \frac{2y_t^3}{3z_n^3} + \frac{2y_t^3 z}{z_n^4}\right] \quad (C.5)$$

Here, terms less than $1/\Delta z_n^4$ have been neglected.

The velocity components are determined from equation C.5 as:

$$V = \frac{\partial \phi}{\partial y} = \frac{\Gamma_t}{2\pi}\left[\frac{4y\,y_t}{z_n^3} + \frac{12y\,y_t z}{z_n^4}\right] \quad (C.6)$$

$$W = \frac{\partial \phi}{\partial z} = \frac{\Gamma_t}{2\pi}\left[-\frac{2y_t}{z_n^2} - \frac{4y_t z}{z_n^3} - \frac{6y_t z^2}{z_n^4} + \frac{6y^2 y_t}{z_n^4} + \frac{2y_t^3}{z_n^4}\right] \quad (C.7)$$

The most general expression for the velocity potential is obtained from integrating equations C.6 and C.7 and has the form:

$$\phi = \frac{\Gamma_t}{2\pi}\left[\frac{2y^2 y_t}{z_n^3} + \frac{6y^2 y_t z}{z_n^4} - \frac{2y_t z}{z_n^2} - \frac{2y_t z^2}{z_n^3} - \frac{2y_t z^3}{z_n^4} + \frac{2y_t^3 z}{z_n^4}\right] + C_I \quad (C.8)$$

where C_I is an arbitrary constant of integration.

Let z_n be measured from the blade such that $z_n = (NF)\Delta z$. Where Δz_n is the wake spacing and NF is the wake index. With this convention, equation C.8 can be written in the form:

$$\phi = \frac{\Gamma_t}{2\pi}\left[\frac{2y^2 y_t}{\Delta z_n^3}\sum_{NF}\frac{1}{N^3} + \frac{6y^2 y_t z}{\Delta z_n^4}\sum_{NF}\frac{1}{N^4} - \frac{2y_t z}{\Delta z_n^2}\sum_{NF}\frac{1}{N^2}\right.$$

$$\left. - \frac{2y_t z^2}{\Delta z_n^3}\sum_{NF}\frac{1}{N^3} - \frac{2y_t z^3}{\Delta z_n^4}\sum_{NF}\frac{1}{N^4} + \frac{2y_t^3 z}{\Delta z_n^4}\sum_{NF}\frac{1}{N^4}\right] \quad (C.9)$$

The semi-infinite summations of equation C.9 are readily available (see for example, [25]). Using the convention of equation 2.16, equation C.9 has the dimensionless form:

$$\phi^* = \frac{\Gamma_t^*}{2\pi}\left[\frac{2y_t^*}{\Delta z_n^{*2}}\right]\left[\frac{6y^{*2}}{\Delta z_n^*} + \frac{3cy^{*2}z^*}{\Delta z_n^{*2}} - az^*\right.$$

$$\left. \frac{-bz^{*2}}{\Delta z_n^*} - \frac{cz^*}{\Delta z_n^{*2}} + \frac{cy_t^{*2}z^*}{\Delta z_n^{*2}}\right] + C_I \quad (C.10)$$

where $a = \sum_{15}^{\infty}\frac{1}{N^2}$

$b = \sum_{15}^{\infty}\frac{1}{N^3}$

$c = \sum_{15}^{\infty}\frac{1}{N^4}$

The velocity potential on the computational boundary due to the far wake is then obtained by picking the constant of integration at one point and applying formula C.10. Equation C.10 represents the contribution to the boundary condition for the tip vortex only. Similar forms of equation C.10 are used to define the influence of the remaining two vortices in the far wake model.

APPENDIX D

NUMERICAL ERRORS

In this appendix, numerical errors introduced by the bilinear interpolation scheme are evaluated. Two errors are discussed. First, the induced velocity at the ith point vortex location due to the circulation redistribution is evaluated and second, the errors introduced in the determination of the point vortex velocities using the bilinear interpolation scheme are examined. In addition, the stability restriction on t is presented.

Induced Velocity Due to Circulation Redistribution

Consider a single point vortex positioned within the area of four mesh cells. See figure below.

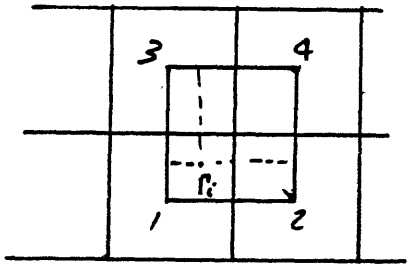

The mesh cells are represented on the x-y plane and have equal dimensions in x and y ($\Delta x = \Delta y = \Delta$). The circulation of the point vortex Γ_i is redistributed to the centroids of the four mesh cells using a bilinear interpolation scheme. Let the coordinates of the point vortex from point 1 be $\delta x, \delta y$ in the x and y directions, respective.

Then, from Appendix B.

$$\Gamma_1 = A_1 \Gamma_i$$
$$\Gamma_2 = A_2 \Gamma_i \qquad \text{(D.1)}$$
etc.

where $A_1 = (\Delta - \delta x)(\Delta - \delta y)$

$A_2 = \delta x(\Delta - \delta y)$

$A_3 = (\Delta - \delta x)\delta y$

$A_4 = \delta x \delta y$

If the previous figure is represented on the complex plane ($z'=x+iy$) with the origin at the point vortex location (see figure below),

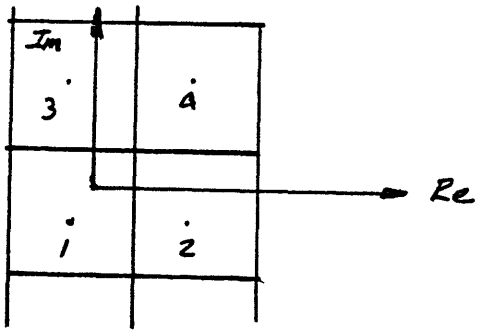

the coordinates of the mesh centroids become,

Point 1 $(-\delta x, -\delta y)$

Point 2 $(\Delta - \delta x, -\delta y)$ (D.2)

Point 3 $(-\delta x, \Delta - \delta y)$

Point 4 $(\Delta - \delta x, \Delta - \delta y)$

The flow field described in the above figure with point vortices defined by equations D.1 and D.2 is represented by the complex potential, $F(z')$. The complex potential has the form:

$$F(z') = -\frac{i\Gamma_1}{2\pi}\log(z'-\text{point1}) - \frac{i\Gamma_2}{2\pi}\log(z'-\text{point2}) - \frac{i\Gamma_3}{2\pi}\log(z'-\text{point3}) - \frac{i\Gamma_4}{2\pi}\log(z'-\text{point4}) \qquad \text{(D.3)}$$

The derivative of equation D.3 dF/dz defines the velocity field and has the form:

$$\frac{dF}{dz} = \frac{-i\Gamma_1}{2\pi}\left[\frac{(x+\delta x)-i(y+\delta y)}{r_1^2}\right] - \frac{i\Gamma_2}{2\pi}\left[\frac{(x-\Delta+\delta x)-i(y+\delta y)}{r_2^2}\right]$$

$$-\frac{i\Gamma_3}{2\pi}\left[\frac{(x+\delta x)-i(y-\Delta+\delta y)}{r_3^2}\right] - \frac{i\Gamma_4}{2\pi}\left[\frac{(x-\Delta+\delta x)-i(y-\Delta+\delta y)}{r_4^2}\right]$$

then, for dF/dz = u-iv and

$$\begin{aligned} r_1^2 &= (x+\delta x)^2 + (y+\delta y)^2 \\ r_2^2 &= (x-\Delta+\delta x)^2 + (y+\delta y)^2 \\ r_3^2 &= (x+\delta x)^2 + (y-\Delta+\delta y)^2 \\ r_4^2 &= (x-\Delta+\delta x)^2 + (y-\Delta+\delta y)^2 \end{aligned} \qquad \text{(D.4)}$$

u and v become:

$$u = \frac{-\Gamma_1}{2\pi}\frac{(y+\delta y)}{r_1^2} - \frac{\Gamma_2}{2\pi}\frac{(y+\delta y)}{r_2^2} - \frac{\Gamma_3}{2\pi}\frac{(y-\Delta+\delta y)}{r_3^2} - \frac{\Gamma_4}{2\pi}\frac{(y-\Delta+\delta y)}{r_4^2} \qquad \text{(D.5)}$$

$$v = \frac{\Gamma_1}{2\pi}\frac{(x+\delta x)}{r_1^2} + \frac{\Gamma_2}{2\pi}\frac{(x-\Delta x+\delta x)}{r_2^2} - \frac{\Gamma_3}{2\pi}\left(\frac{x+\delta x}{r_3^2}\right) - \frac{\Gamma_4}{2\pi}\frac{(x-\Delta+\delta x)}{r_4^2} \qquad \text{(D.6)}$$

where u,v are the velocity components in the x and y directions, respectively.

We introduce, here, dimensionless space variables with respect to Δ for equations D.5 and D.6. Dimensionless variables are represented by an overbar.

For equation D.1:

$$\Gamma_1 = \Delta^2 \bar{A}_1 \Gamma_i$$
$$\Gamma_2 = \Delta^2 \bar{A}_2 \Gamma_i$$

etc.

where $\bar{A}_1 = (1-\bar{\delta}_x)(1-\bar{\delta}_y)$

$\bar{A}_2 = \bar{\delta}_x(1-\bar{\delta}_y)$

etc.

Terms of equation D.4 take the forms:

$$\bar{r}_1^2 = \Delta^2(\bar{x}+\bar{\delta}_x)^2 + \Delta^2(\bar{y}+\bar{\delta}_y)^2$$
$$r_2^2 = \Delta^2(\bar{x}-1+\bar{\delta}_x)^2 + \Delta^2(\bar{y}+\bar{\delta}_y)^2$$

etc.

Equations D.5 and D.6 become:

$$u = \Delta\left[\frac{\Gamma_i}{2\pi}\left(-\frac{\Delta^2\bar{A}_1}{\Delta^2\bar{r}_1^2}(\bar{y}+\bar{\delta}_y) - \frac{\Delta^2\bar{A}_2}{\Delta^2\bar{r}_2^2}(\bar{y}+\bar{\delta}_y) - \frac{\Delta^2\bar{A}_3}{\Delta^2\bar{r}_3^2}(\bar{y}-1+\bar{\delta}_y) - \frac{\Delta^2\bar{A}_4}{\Delta^2\bar{r}_4^2}(\bar{y}-1+\bar{\delta}_y)\right)\right] \quad (D.7)$$

$$v = \Delta\left[\frac{\Gamma_i}{2\pi}\left(\frac{\Delta^2\bar{A}_1}{\Delta^2\bar{r}_1^2}(\bar{x}+\bar{\delta}_x) + \frac{\Delta^2\bar{A}_2}{\Delta^2\bar{r}_2^2}(\bar{x}-1-\bar{\delta}_x) + \frac{\Delta^2\bar{A}_3}{\Delta^2\bar{r}_3^2}(\bar{x}+\bar{\delta}_x) + \frac{\Delta^2}{\Delta^2}\frac{\bar{A}_4}{\bar{r}_4^2}(\bar{x}-1-\bar{\delta}_x)\right)\right] \quad (D.8)$$

Equations D.7 and D.8 are used to evaluate the error in the induced velocity. Ideally, the induced velocity at the ith point vortex location should be identically zero (a point vortex will induce zero velocity at its origin).

Consider the figure below:

Points 1-4 are mesh cell centroids

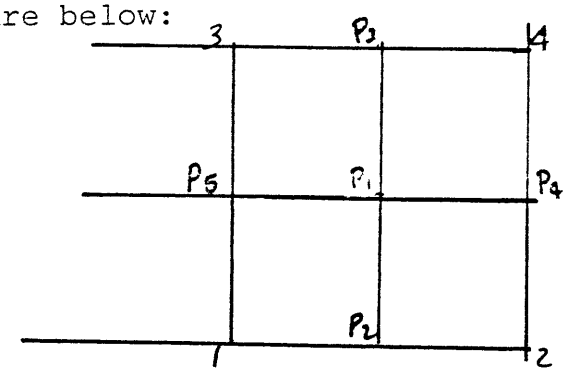

If the mesh cell centroids are again represented by points 1-4, then the following is found from equations D.7 and D.8.

1) If the ith point vortex is at P_1, the u and v velocities are zero and no error is introduced.
2) If the ith point vortex is at P_2 or P_3, the u velocity is zero and the v velocity has error $0(\Delta)$.
3) If the ith point vortex is at P_4 or P_5, the v velocity is zero and the u velocity has error $0(\Delta)$.
4) Elsewhere in the mesh, the error on the u and v is $0(\Delta)$.

Velocity at a Point Vortex

The velocity at a point vortex on the computational mesh is determined by the velocities at the centroids of the four nearest mesh cells. A bilinear interpolation scheme is used to determine the point vortex velocity.

Consider, again, a point vortex on the xy plane and located inside a region formed by the centroids of the four nearest mesh cells. See figure below.

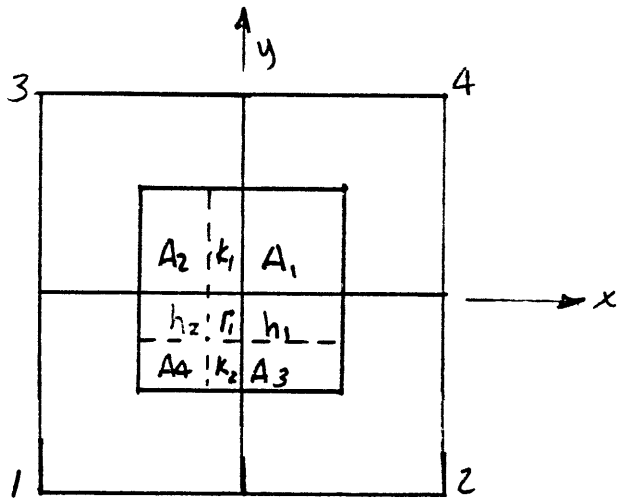

Points 1-4 represent these centroids. The velocity at the ith point vortex has the form:

$$V_i = \frac{A_1 V_1 + A_2 V_2 + A_3 V_3 + A_4 V_4}{\Delta y \, \Delta z}$$

The velocity components V1 through V4 are the velocities at points 1 through 4 and can be represented by Taylor expansions for two variables (see for example, [25]). The expansion for V1 is shown here:

$$V_1 = V_i - h_2 \frac{\partial V}{\partial x} - k_2 \frac{\partial V}{\partial y} + \frac{1}{2}\left(\frac{\partial^2 V}{\partial x^2} h_2^2 + \frac{\partial^2 V}{\partial x \partial y} h_2 k_2 + \frac{\partial^2 V}{\partial y^2} k_2^2 \right)$$

$$- \frac{1}{3!}\left[h_2^3 \frac{\partial^3 V}{\partial x^3} + 3 h_2^2 k_2 \frac{\partial^3 V}{\partial x^2 \partial y} + 3 h_2 k_2^2 \frac{\partial^3 V}{\partial x \partial y^2} + k_2^3 \frac{\partial^3 V}{\partial y^3} \right] + o\left(\Delta x^4, \Delta y^4\right)$$

Similar expressions hold for V2, V3 and V4.

After expansion and collecting terms, the following is found:

$$\frac{A_1V_1 + A_2V_2 + A_3V_3 + A_4V_4}{\Delta x \Delta y} = V_i + \tfrac{1}{2}(\Delta x h_1 - h_1^2)\frac{\partial^2 V}{\partial x^2}$$

$$+\frac{1}{2}(\Delta y k_1 - k_1^2)\frac{\partial^2 V}{\partial y^2} + \frac{1}{6}(2h_1h_2^2 - h_1h_2\Delta x)\frac{\partial^3 V}{\partial x^3}$$

$$+\frac{1}{6}(2k_2k_1^2 - \Delta y\, k_1k_2)\frac{\partial^3 V}{\partial y^3}$$

Therefore,

$$\frac{A_1V_1 + A_2V_2 + A_3V_3 + A_4V_4}{\Delta x \Delta y} = V_i + O(\Delta x^2) + O(\Delta y)^2$$